



Bianca Maria Bresolin

**SYNTHESIS AND PERFORMANCE OF METAL-  
HALIDE PEROVSKITES AS NEW VISIBLE LIGHT  
PHOTOCATALYSTS**



Bianca Maria Bresolin

## **SYNTHESIS AND PERFORMANCE OF METAL- HALIDE PEROVSKITES AS NEW VISIBLE LIGHT PHOTOCATALYSTS**

Dissertation for the degree of Doctor of Science (Technology) to be presented with due permission for public examination and criticism at Lappeenranta-Lahti University of Technology LUT, Lappeenranta, Finland on the 20<sup>th</sup> of January, 2021, at noon.

Acta Universitatis  
Lappeenrantaensis 947

Supervisors Professor Tuomo Sainio  
LUT School of Engineering Science  
Lappeenranta-Lahti University of Technology LUT  
Finland

Assistant Professor Yuri Park  
LUT School of Engineering Science  
Lappeenranta-Lahti University of Technology LUT  
Finland

Reviewers Professor Johan A. Martens  
Centre of Surface Chemistry and Catalysis  
KU Leuven University  
Belgium

Professor Kamila Kočí  
Institute of Environmental Technology  
VSB Technical University of Ostrava  
Czech Republic

Opponent Professor Michael Wark  
Institute of Chemistry, Chemical Technology  
Carl von Ossietzky University Oldenburg  
Germany

ISBN 978-952-335-619-1  
ISBN 978-952-335-620-7 (PDF)  
ISSN-L 1456-4491  
ISSN 1456-4491

Lappeenranta-Lahti University of Technology LUT  
LUT University Press 2021

## Abstract

**Bianca Maria Bresolin**

**Synthesis and performance of metal-halide perovskites as new visible light photocatalysts**

Lappeenranta 2021

97 pages

Acta Universitatis Lappeenrantaesis 947

Diss. Lappeenranta-Lahti University of Technology LUT

ISBN 978-952-335-619-1, ISBN 978-952-335-620-7 (PDF), ISSN-L 1456-4491,

ISSN 1456-4491

Solar-light power, as a sustainable energy source, is renewable, inexhaustible, and available worldwide. The scientific and engineering interest in solar-light based technologies has grown exponentially as a cost-effective and energy-saving approach.

As a green application of converting light into chemical energy, semiconductor-based heterogeneous photocatalysis, represents a suitable approach to address current global issues such as the energy crisis and environmental pollution. This interdisciplinary technology recently experienced a rapid evolution, counting the contribution of semiconductor physics, surface sciences, photo and physical chemistry, material science, and chemical engineering.

Titanium dioxide ( $\text{TiO}_2$ ) is the most employed photocatalyst by far due to its photostability, non-toxicity, and abundance. However,  $\text{TiO}_2$  limits its applicability in the ultraviolet wavelength range, accounting for only about 5% of total solar-light power. The energy's undesired dissipation due to the photogenerated charge carriers' fast recombination rate further reduces its photocatalytic efficiency. Therefore, it seems of great significance to study possible alternative materials to harvest visible light, recognized as the higher energetic part of the solar spectrum.

Metal halide perovskites (MHPs) have recently acquired increasing interest as promising elements in light-driven applications. Their impressive properties, combined with low-cost production, have inspired applications well beyond the photovoltaics field.

In this work, MHPs were proposed as potential visible light photocatalysts, widening the engineering solutions using raw and composite materials.

MHP, as a new generation material, was tested for environmental remediation, particularly for the photodegradation of organic contaminants. Morphological, optical, and electrochemical properties of the as-prepared photocatalysts were investigated to provide insights into their photocatalytic processes. Laboratory-scale conditions were adopted for practical reasons when designing simple reactors and systems.

First, a lead-based  $\text{CH}_3\text{NH}_3\text{PbI}_2$  photocatalyst was prepared due to the photovoltaic field's outstanding efficiency. Then, lead-free  $(\text{CH}_3\text{NH}_3)_3\text{Bi}_2\text{I}_9$  was preferred due to its lower

toxicity, ascribed to the presence of lead. The bismuth-based hybrid organic-inorganic perovskite (HOIP) resulted in a suitable visible light photocatalyst with higher water stability and photocatalytic efficiency than the lead-based counterpart. The HOIP recorded a photodegradation efficiency of 99% and 75% on Rhodamine-B (RhB) in 180 minutes, respectively, under visible light halogen lamp and light emitting diodes (LEDs) lamp irradiations. The photocatalytic activity was further tested on the degradation of different kinds of dyes, such as methyl blue (MB) and reactive blue (RBL). Moreover, a mixture of different dyes, such as crystal violet (CV) and MB, was photodegraded to simulate a realistic industrial wastewater effluent.

On the other hand, the environmental instability of the organic fraction in HOIPs ultimately obstacles the commercialization of these emerging materials. Thus, an all-inorganic material,  $\text{Cs}_3\text{Bi}_2\text{I}_9$ , was prepared and used as a visible light photocatalyst. The complete photodegradation of RhB was achieved in 180 minutes under visible light irradiation. The activity of the recycled photocatalyst confirmed its suitability for multiple uses without evident photocatalytic efficiency decrease. Moreover, the detection of trapped electrons and holes supports the potential of  $\text{Cs}_3\text{Bi}_2\text{I}_9$  as a suitable material for photocatalytic reactions.

In recent years, properly engineered heterojunction photocatalysts have shown higher photocatalytic activity ability, mainly due to photogenerated electron-hole pairs' spatial separation.

Thus, the  $\text{Cs}_3\text{Bi}_2\text{I}_9$  photocatalyst was employed to design appropriate composites. The photocatalytic efficiency was enhanced by coupling  $\text{Cs}_3\text{Bi}_2\text{I}_9$  with more traditional semiconductors such as  $\text{TiO}_2$  and g- $\text{C}_3\text{N}_4$ . The photoelectrochemical studies revealed the composites' synergetic effects, supported by the experimental degradation tests on organic pollutants.

In particular,  $\text{Cs}_3\text{Bi}_2\text{I}_9:\text{TiO}_2$  and  $\text{Cs}_3\text{Bi}_2\text{I}_9:\text{g-C}_3\text{N}_4$  composites demonstrated higher stability and photocatalytic reaction rates than pristine materials. Finally, preliminary tests showed the promising ability of the  $\text{Cs}_3\text{Bi}_2\text{I}_9:\text{g-C}_3\text{N}_4$  composite for hydrogen generation under solar simulator and LED-based visible light irradiation.

This experimental research means to offer new insights into the application of metal halide perovskite and its composites in photocatalytic technologies.

**Keywords:** metal halide perovskites, renewable energy, photocatalysis, material science

## Acknowledgments

The research work was conducted in the laboratory of the Department of Separation Science of LUT, in Mikkeli, in cooperation with the Institute for Technical Chemistry of the Leibnitz University of Hannover, the Department of Industrial Engineering of the University of Padova, and the Department of Industrial Chemistry of the University of Milan.

I want to dedicate my work and to convey my deepest appreciation to my family: my mother, Lia, my father Gianmaria, and my brother Giulio, who supported all my studies and always push me to be a better person, with a relative success.

I want to express my sincere gratitude to all the professors, supervisors, technicians, colleagues, and assistants who walked with me in this chapter of my personal and professional life.

I am grateful to professors and good friends, Paolo Sgarbossa and Mirto Mozzon, who challenged me to the research field and more important to the awareness of my limits and my qualities. I will never forget that ‘Chem-is-try’. I thank prof. Mika Sillanpää and my first supervisor Dr. Samia Ben Hammouda, who gave me the chance to experience the great Finnish research community. I want to express a special thankfulness to prof. Detlef Bahnemann and Dr. Ralf Dillert, of the Leibnitz University of Hannover, who gave me priceless advice on my project work. I thank Dr. Narmina O. Balayeva and her precious friendship for the never-ending support in the laboratory and personal life.

I am grateful to my new and trustful prof. Tuomo Sainio and my new supervisor Yuri Park for the trust in my work, the wise tips and the constant contribution in the last period of my PhD, especially on my thesis work.

I express my sincere appreciation to the Department of Separation Science of the Lappeenranta University of Technology, sited in Mikkeli, and all the staff of LUT University for offering me the chance to live in Finland, the incredible experience of my Ph.D. study, and a lot of professional support.

Special thanks to all my laboratory-mates and closer friends present during this amazing travel and work period.

Bianca Maria Bresolin  
January 2021  
Mikkeli, Finland



# Contents

Abstract

Acknowledgments

Contents

List of publications.....	9
Nomenclature.....	11
<b>1 Introduction (Renewable Energy and Environment) .....</b>	<b>15</b>
1.1 Photocatalysis .....	16
1.1.1. Brief history .....	16
1.1.2. Principles .....	18
1.2 Advanced materials for photocatalytic applications.....	21
1.2.1. Optical and electronic properties: engineering semiconductors ( <i>Eg</i> , aggregation) .....	21
1.2.2. Charge carrier dynamics: Trapping, Recombination, and Transfer.....	23
1.2.3. Driving surface electron transfer and redox reactions .....	23
1.2.4. Analytical methods .....	24
1.2.5. Recent strategies for advanced materials in heterogeneous photocatalysis.....	27
1.3 Research Objectives .....	32
1.4 Hypothesis .....	33
1.5 Scope of study .....	33
1.6 Delimitation of study .....	33
<b>2 Metal halide perovskites .....</b>	<b>35</b>
2.1 Fundamental Structure and Composition .....	35
2.2 History and traditional application (photovoltaics and diodes).....	37



2.2.1.	Photovoltaics.....	38
2.2.2.	Light-emitting diodes.....	39
2.3	Photocatalytic applications .....	39
2.4	Current limitations and future prospective .....	50
<b>3</b>	<b>Materials and Methods .....</b>	<b>53</b>
3.1	Synthesis.....	53
3.1.1.	Hybrid organic-inorganic perovskites (HOIPs).....	53
3.1.2.	All-inorganic MHPs.....	53
3.1.3.	MHP-based composites .....	54
3.2	Characterization.....	55
3.2.1.	Structural and morphological characterization .....	55
3.2.2.	Optical and electrochemical characterization .....	59
3.3	Environmental applications .....	61
3.3.1.	Photocatalytic degradation of organic pollutants.....	61
3.3.2.	The effect of operational parameters .....	69
3.3.3.	The effect of multi-contaminated water solution.....	72
3.3.4.	The recycling effect .....	73
3.3.5.	The effect of the light source .....	75
3.3.6.	Mechanism of photocatalysis.....	77
3.3.7.	Photocatalytic hydrogen production .....	81
3.4	Conclusion.....	83
	<b>References.....</b>	<b>85</b>

**Publications**

## List of publications

I. Bianca-Maria Bresolin, Samia Ben Hammouda and Mika Sillanpää (2019). An Emerging Visible-Light Organic–Inorganic Hybrid Perovskite for Photocatalytic Applications. *Nanomaterials* 10, 115, pp. 1-17.

II. Bianca-Maria Bresolin, Samia Ben Hammouda and Mika Sillanpää (2019). Methylammonium iodo bismuthate perovskite (CH<sub>3</sub>NH<sub>3</sub>)<sub>3</sub>Bi<sub>2</sub>I<sub>9</sub> as new effective visible light-responsive photocatalyst for degradation of environment pollutants. *Journal of Photochemistry & Photobiology A: Chemistry* 376, pp. 116–126.

III. Bianca-Maria Bresolin, Carsten Günnemann, Detlef W. Bahnemann and Mika Sillanpää (2020). Pb-Free Cs<sub>3</sub>Bi<sub>2</sub>I<sub>9</sub> Perovskite as a Visible-Light-Active Photocatalyst for Organic Pollutant Degradation. *Nanomaterials* 10, 763, pp 1-13.

IV. Bianca-Maria Bresolin, Narmina O. Balayeva, Luis I. Granone, Ralf Dillert, Detlef W. Bahnemann and Mika Sillanpää (2020). Anchoring lead-free halide Cs<sub>3</sub>Bi<sub>2</sub>I<sub>9</sub> perovskite on UV100–TiO<sub>2</sub> for enhanced photocatalytic performance. *Solar Energy Materials & Solar Cells* 204, 110214, pp.1-11.

V. Bianca-Maria Bresolin, Paolo Sgarbossa, Detlef W. Bahnemann, Mika Sillanpää. Cs<sub>3</sub>Bi<sub>2</sub>I<sub>9</sub>/g-C<sub>3</sub>N<sub>4</sub> as a new binary photocatalyst for efficient visible-light photocatalytic processes (2020). *Separation and Purification Technology* 251, 117320, pp. 1-12.

## Author's contribution

Bianca Maria Bresolin is the principal author and investigator. Paolo Sgarbossa, Samia Ben Hammouda, Mika Sillanpää, Detlef W. Bahnemann, and Ralf Dillert supervised the work. Carsten Günnemann, Narmina O. Balayeva, and Luis I. Granone helped in the recording and editing of the data.



# 1 Nomenclature

## Abbreviations in order of appearance

$(CH)_3OH$	methanol
$(CH_3NH_3)_3Bi_2I_9$	MAIBI
$\bullet(CH)_2OH$	Hydroxymethyl
$\bullet O_2$	superoxide radicals
$\bullet O_2CH_2OH$	peroxy radical
$\bullet OH$	hydroxyl radical
$0D$	zero dimension
$1D$	one dimension
$^1O_2$	singlet oxygen species
$2D$	two dimensions
$3D$	three dimensions
$ABX_3$	structural formula perovskites
$Ag^+$	silver cation
$AO$	ammonium oxalate
$AOPs$	advanced oxidation processes
$Bi$	bismuth
$BiI_3$	bismuth iodide
$BQ$	p-benzoquinone
$Br^-$	bromide anion
$C$	carbon
$Ca$	calcium
$CaTiO_3$	calcium titanate
$CH_3NH_2$	methylamine
$CH_3NH_3I$	methylammonium iodide
$CH_3NH_3PbI_2$	MAPbI <sub>3</sub>
$Cl^-$	chlorine anion
$CO_2$	carbon dioxide
$Co^{3+}$	cobalt cation
$Cs^+$	cesium inorganic cation
$Cu^{2+}$	copper cation
$CV$	crystal violet
$CV$	cyclic voltammery
$DDL$	diacetyl-dihydro lutidine
$DMF$	N, N-dimethylformamide
$DMSO$	dimethyl sulfoxide

---

<i>DRS</i>	differential reflectance spectroscopy
<i>E/SEM</i>	environmental scanning electron microscopy
$e^-$	electrons
<i>EDS</i>	Energy-dispersive X-ray spectroscopy
<i>EIS</i>	Electrochemical Impedance Spectroscopy
<i>EPR</i>	Electron paramagnetic resonance
$FA^+$	formamidinium organic cation
$Fe^{3+}$	iron(III) cation
<i>GaAs</i>	gallium arsenide
<i>GBL</i>	$\gamma$ -butyrolactone
<i>GC/MS</i>	gas chromatograph-mass spectrometer
<i>g-C<sub>3</sub>N<sub>4</sub></i>	graphitic carbon nitrile
$Ge^{2+}$	germanium inorganic cation
$h^+$	holes
$H_2$	hydrogen
$H_2O$	water
$H_2O_2$	hydrogen peroxide
<i>HCl</i>	hydrogen chloride
<i>HER</i>	hydrogen evolution reaction
<i>Hg lamp</i>	mercury lamp
<i>HI</i>	hydrogen iodide
<i>HOIPs</i>	hybrid organic inorganic perovskites
<i>HPLC</i>	high-pressure liquid chromatograph
$I^-$	iodine anion
<i>IPA</i>	isopropanol
<i>IR</i>	infrared ray wavelength
<i>LEDs</i>	light emitting diodes
$MA^+$	methylammonium organic cation
<i>MB</i>	methyl blue
<i>MHPs</i>	Metal halide perovskites
<i>Mn</i>	manganese
$Mo^{5+}$	molybdenum cation
<i>N</i>	nitrogen
$N_2$	nitrogen (gas)
<i>NaOH</i>	sodium hydroxide
$O_2$	oxygen (gas)
<i>OH</i>	hydroxide diatomic anion

---

$Pb^{2+}$	lead inorganic cation
$PbI_2$	lead iodide
<i>PCE</i>	power conversion efficiency
<i>PEC</i>	photoelectrochemical cell
<i>PL</i>	Photoluminescence
<i>PZC</i>	point of zerocharge
<i>Rb</i>	rubidium
<i>RBL</i>	and reactive blue (RBL)
<i>RhB</i>	Rhodamine B
<i>ROS</i>	reactive oxygen species
$Ru^{3+}$	rhutenium cation
<i>S</i>	sulfur
<i>Si</i>	silicon
$Sn^{2+}$	tin inorganic cation
<i>Sr</i>	strontium
<i>TAS</i>	transient absorption spectroscopy
$TiO_2$	Titanium dioxide
<i>TEM</i>	Transmission electron microscopy
<i>TEMP</i>	2,2,6,6-tetramethylpiperidine
<i>UPS</i>	ultraviolet photoelectron spectroscopy
<i>UV</i>	ultraviolet wavelength
<i>UV-vis DRS</i>	UV–vis diffuse reflectance spectroscopy
<i>Xe lamp</i>	xenon lamp
<i>XRD</i>	x-ray powder diffraction

#### **Mathematical and Physical quantities in order of appearance**

<i>A</i>	depletion area ( $m^{-2}$ )
<i>C</i>	interface capacitance (Farad, $m\ kg\ s\ C$ )
<i>C<sub>i</sub></i>	measured concentration at the time of withdrawal (mg/L)
<i>C<sub>0</sub></i>	initial concentration of dye (mg/L)
<i>CB</i>	conduction band
<i>E<sub>a</sub></i>	activation energy (J/mol)
<i>E<sub>g</sub></i>	band gap (eV)
<i>eV</i>	electron volt
<i>h</i>	Planck's constant ( $J\cdot s$ ; $eV\ s$ )
<i>J</i>	joules
<i>k</i>	reaction rate ( $min^{-1}$ )
<i>k<sub>B</sub></i>	the Boltzmann's constant ( $C\ K^{-1}$ )

---

$\lambda$	wavelength (nm)
$m^2$	square meters
<i>mol</i>	moles
<i>Nd</i>	doping density ( $m^{-3}$ )
<i>nm</i>	nanometers
$R^2$	R-squared value, correlation coefficient
<i>s</i>	seconds
<i>T</i>	temperature (K)
<i>V</i>	the applied potential ( $kg\ m^2\ s^{-2}\ C^{-1}$ ),
<i>W</i>	watts
<i>VB</i>	valence band (eV)
<i>Vfb</i>	the flat band potential ( $kg\ m^2\ s^{-2}\ C^{-1}$ )
$\alpha$	absorption coefficient ( $eV^{-1}\ cm^{-1}$ )
$\varepsilon$	the dielectric constant of semiconductor ( $kg\ m^3\ s^{-2}\ C^{-1}$ )
$\nu$	frequency of the light ( $s^{-1}$ )

## 1 Introduction (Renewable Energy and Environment)

Energy and environmental crises are significant global environmental challenges of the 21<sup>st</sup> century. The intensive employment of renewable energy sources, sustainable technologies, and rigorous respect for the environment and ecosystems are among our society's and the scientific community's most fundamental and ambitious goals [1–3].

Currently, the combustion of non-renewable fossil fuels provides about 80% of the world's energy requirements, promoting global warming and deleterious environmental effects. In increasing population and energy demands, alternative eco-friendly energy sources are urgently required to guarantee a sustainable future [4,5].

On the other hand, the critical concerns of the increasing toxic release of emergent contaminants make environmental pollution one of the significant problems affecting worldwide biodiversity, ecosystems, and human health [6]. For example, wastewater treatment and recovery of agricultural, industrial, and domestic effluents have significant importance for future freshwater availability. The combination of rapid urbanization, increasing population, and related wastewater production will lead to a critical situation if we do not rethink pollution management. The uncontrolled discharge of wastewater in water bodies remarkably affects our planet's future, spreading the disease to humans and damaging living ecosystems.

In particular, synthetic organic dyes, usually discharged by the textile, tannery, and printing industries, are considered hazardous and toxic to the environment due to their mutagenic and carcinogenic effects. Industrial wastewater contaminated by organic dyes can cause undesired impacts on human health and the quality of the receiving water bodies, the aquatic ecosystem, and biodiversity [7]. Thus, it seems urgent to preserve our water and reduce pollution with suitable and effective methods.

In the previously mentioned critical scenario, solar light represents a green, inexhaustible, cheap, and globally available energy resource that could positively affect pollution mitigation. Solar light has been successfully employed in several applications, such as photovoltaics, thermal energy, artificial photosynthesis, and photocatalysis.

Sunlight, as a portion of electromagnetic radiation, can be generally divided into ultraviolet (UV, 100–380 nm), visible light (380–700 nm), and infrared wavelength ranges (IR, 700 nm–1 mm). In terms of total solar radiation, visible light provides about 40%, UV radiation makes up about 8%, and the remaining 52% belongs to IR [8,9] (**Figure 1**).

In general, a tiny portion of total sunlight irradiation reaches the Earth's surface due to its absorption by atmospheric layers and reflection back into space. However, global solar irradiation with approximately 1040 W/m<sup>2</sup> would provide more power than a hundred times the current human needs [7]. Moreover, widespread utilization of clean and renewable solar energy may increase energy security and sustainability, decreasing the costs of mitigation of climate change and pollution treatment.

Photocatalysis, converting light into chemical energy, is a potential technology with great potential to simultaneously face energy and environmental issues. Photocatalytic processes initiated by light absorption have recently attracted much attention as promising technologies able to address different endeavors, such as advanced oxidation processes (AOPs), hydrogen (H<sub>2</sub>) evolution, carbon dioxide (CO<sub>2</sub>) reduction, and desired organic synthesis. Photocatalysis has also received particular attention because it offers multifarious advantages, such as chemical-physical stability, low cost, and environmental-friendliness [10–13].



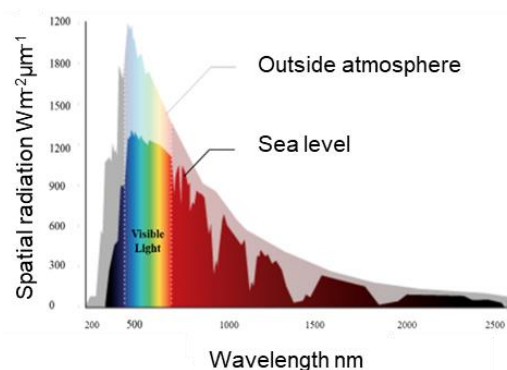


Figure 1: Representation of solar-light radiation as a function of wavelengths.

## 1.1 Photocatalysis

### 1.1.1. Brief history

The term “*catalysis*” dates from 1836 when Jöns Jakob Berzelius (1779-1848) noticed the ability of certain materials to induce chemical reactions on other substances while remaining unchanged [14,15]. At the end of the century, Ostwald revised the definition of catalysis as the acceleration of chemical reactions without changing the energetic situation in the presence of a foreign substance, removable after process [16]. In the following centuries, many advancements in the catalytic mechanism's comprehension were possible, primarily due to the development of surface science tools and the cooperation between disciplines [17].

Nowadays, the modern catalytic concept depends on two principles: the unchanged thermodynamics of the overall reaction and the catalyst's ability to influence the reaction coordinate and the nature of transition states or intermediates. IUPAC defines the term ‘catalyst’ as both a reactant and a product able to increase the reaction rate without modifying the overall standard Gibbs energy [18]. **Figure 2** shows a simple scheme to understand the catalytic process, where  $E_a$  represents the activation energy lowered by the catalyst's presence.

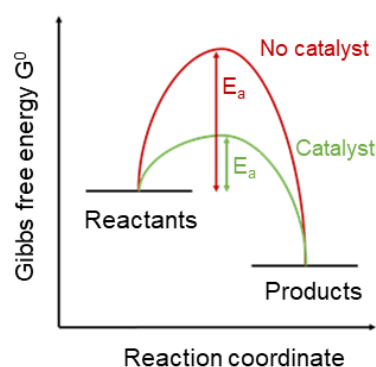


Figure 2: Free-energy diagram of catalysis processes.

It took nearly a century before a clear understanding of the molecular principles of catalytic processes due to its multidisciplinary character and its dependence on the coordination of different disciplines, including chemical engineering, inorganic chemistry, and organic chemistry, which previously developed in a reasonably independent way. The chemical legacy of the nineteenth century culminated in the Nobel Prize for Sabatier with catalytic hydrogenation. Sabatier formulated the intermediate stability of the reaction species formed at the surface of a catalyst to be active but not decomposing [19]. From a modern perspective, he considered the catalytic process as a cycle of reaction steps, where intermediates may be formed before decay.

Photocatalysis is a type of catalysis that accelerates a chemical reaction rate, starting from light absorption by one or more reacting species. The substance that participates in the chemical reactions without being consumed or modified is usually called a photocatalyst. In 1972, Fujishima and Honda announced the first-ever electrophotocatalytic water splitting of n-type titanium dioxide ( $\text{TiO}_2$ ) [20]. This result represented a groundbreaking discovery and is usually considered the birth of the so-called photocatalytic process. The phenomenon was not immediately accepted, but later, it attracted considerable attention from many scientists in a remarkable number of related disciplines [21]. The extensive and multidisciplinary research in chemistry, chemical engineering, and physics paved the way for developing a new chemistry branch called photo-electrochemistry [22]. The topic has recently sparked interest within different academic fields, yielding thousands of peer-reviewed articles in the last four decades, as shown in **Figure 3**. As a combination of photochemistry and heterogeneous catalysis, photocatalysis has attracted remarkable attention in the chemistry community in the past decades, boasting great success in environmental and energy-related applications. Its advantages, described in the following chapters, allowed rapid and spontaneous growth in a multidisciplinary scientific and industrial field. Photocatalysis can be considered one of the major expressions of sustainable and green chemistry applicable to several energy-related and environmental systems due to its attractive properties, such as high efficiency, cost-effectiveness, and renewable energy utilization sources.

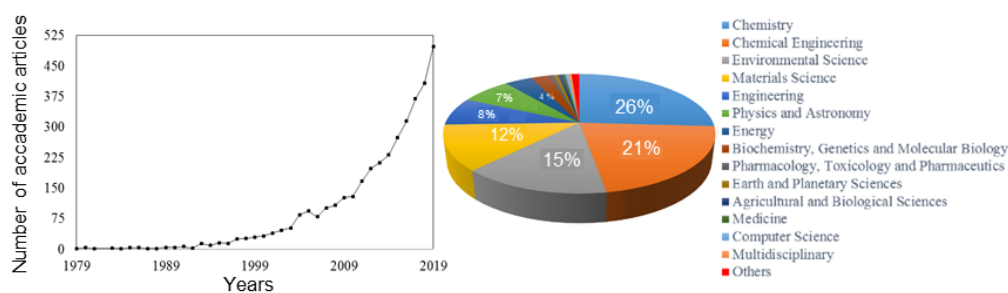


Figure 3: Trends of the published scientific articles in heterogeneous photocatalytic processes and academic fields (Analyses search results by Scopus.com).

### 1.1.2. Principles

The word “*photocatalysis*”, from the Greek language, is a conflation of photo, which stands for the use of light as an energy source, and catalysis, a process where the activation energy is reduced and the chemical reaction rate increase. In a simple form, the photocatalytic process can be briefly described by the following reaction:



where  $A$  and  $B$  denotatively, the product and reagent of reaction, respectively.  $Cat$  refers to the catalyst that absorbs light energy ( $h\nu$ ) and increases the photochemical reaction rate.

There are two main categories of photocatalytic processes: *homogeneous* and *heterogeneous photocatalysis*. Homogeneous photocatalysis, such as ozone and photo-Fenton systems, refers to a process where the reactants and the photocatalysts exist in the same phase. Homogenous photocatalysis has received tremendous attention, offering high activity and selectivity with atomically dispersed catalytic sites and tunable light absorption. On the other hand, the homogenous process was limited by its relatively high costs and the difficulty of extracting and recycling the catalyst after use. The main disadvantage of homogeneous photocatalysts turns out to be the strength in the counterpart, heterogeneous processes. In heterogeneous photocatalysis, the catalyst can be easily separated from the reaction products, assuring continuous applicability and recyclability, resulting in a desirable process for practical and industrial applications.

Semiconductors are considered the most suitable materials for the photocatalytic process because of their favorable electronic structure. In general, solids can be classified as *metals*, *semiconductors*, or *insulators* based on conductivity or resistivity and energy bands. The electronic band structure is a convention to describe the conductivity of materials consisting of two energy bands, valence and conduction band, and a potential gap in between called band gap. In the valence (VB), electrons are at the ground state and serve as potential charge carriers for the conduction band (CB) that is empty. The energy gap between the two energy bands, whose width influences materials' conductivity, is called the band gap ( $E_g$ ) [3]. In the crystalline structure of a metal, the electrons can move freely, leading to high conductivity and low resistivity. In terms of band structure, the valence band overlaps with the empty conduction band, partially filled, leaving the electrons to move without obstacle.

Conversely, an insulator is characterized by high resistivity and low conductivity because the electrons cannot freely move. The valence band is fully occupied with electrons in covalent bonds that lock them up between the atoms. Electron-free conduction cannot be achieved due to the band gap lying between the two energy bands. In a semiconductor, it is possible to distinguish a fully occupied low-energy level (VB) and a higher empty level (CB). In-between VB and CB, the  $E_g$  stands. In comparison to insulators, the  $E_g$  is such small that the electrons, when excited, can jump from VB to CB and can move freely and act as charge carriers. The excited electron leaves a hole in the VB that can pair with other electrons.

When light with sufficient energy, higher than the  $E_g$ , hits a semiconductor in the photocatalytic process, the electron, forcibly in the VB, can be excited into the CB (**Figure 4**). The previous property makes crucial whether or not there are electrons in the conduction band.

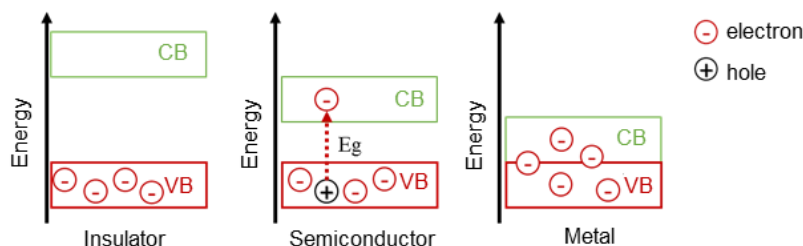


Figure 4: Simplified illustration of the energy bands theory: the difference between insulator, semiconductor and metal, representation of the band gap ( $E_g$ ) including Valence Band (VB) and Conduction Band (CB).

The band gap of a semiconductor ( $E_g$ ), according to its nature, can be defined as *indirect* or *direct* (**Figure 5**). In indirect band gap material, the two energetic peaks are not aligned; thus, the radiative recombination process entails emitting a phonon or the involvement of a crystallographic defect. In a direct band gap material, the lower energy level of CB is placed right over the highest part of the VB, fastening the radiative recombination process. The band gap is influenced by different parameters, including its morphology, such as its particle size [23].

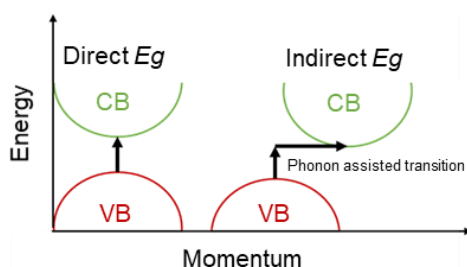


Figure 5: Illustration of a direct and indirect band gap ( $E_g$ ) of semiconductors, valence band (VB), and conduction band (CB).

The heterogeneous photocatalytic process is based on electrons' excitation in a semiconductor by light irradiation with energy at least equal to that of the semiconductor band gap ( $E_g$ ). The process, while varying the details in terms of reactions and mechanisms, can be summarized in the following stages:

- (I) Absorption of light energy to generate electron-hole pairs;
- (II) Separation of the photogenerated charges;
- (III) Transfer of electrons and holes to the surface of semiconductor;
- (IV) Consumption of photogenerated charges for redox reactions on the surface of the catalyst (reductive, *A* or oxidative *D*, **Figure 6a**).

Among the limits of such a mechanism, either on the surface or on the photocatalyst's bulk sites, the potential electrostatic recombination (III<sup>a</sup>) of the photogenerated charges may dissipate the harvested energy in the form of radiative and non-radiative recombination, such as light and heat, respectively. The mechanism is displayed in **Figure 6a**.

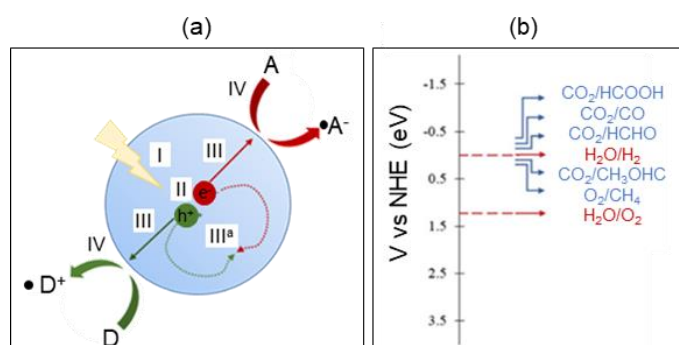


Figure 6: (a) Steps in photocatalytic reaction process: (I) light absorption, (II) separation of photogenerated charges, (III) transfer of electrons and holes, (III<sup>a</sup>) eventual recombination of charges; (IV) redox reactions where R and O mean chemicals in reductive and oxidative reactions, respectively. (b) Energy levels of the important photocatalytic reactions concerning NHE at pH = 0.

In general, there are two categories of approaches to enhance the activity of a photocatalyst: increase the charge carrier density as a function of the absorbed light or increase the charge carrier separation, improving their utilization. According to the indexed mechanism, there are three target parameters to consider to improve photocatalyst activity. First, the light absorption process determines the number of excited charges: a higher light-energy absorbed leads to a higher number of charge carriers, likely accumulated on the surface of the semiconductor, providing higher photocatalytic ability. Therefore, improving the optical absorption properties has become a primary challenge to enhance semiconductors' overall activity [3]. Second, the decrease in photogenerated species' recombination rate favors their separation, maximizing their utilization, and enhancing photocatalytic performance [3,24]. Third, the relationship between the semiconductor band gap, valence band, and conduction band energy positions concerning the target redox reactions (**Figure 6b**) [25]. In general, semiconductor-based photocatalysts can generate simultaneously oxidizing and reducing reactions on the surface of a particle, having the potential to provide a wide range of redox reactions.

In summary, a suitable semiconductor for photocatalytic applications should be: i) photoactive in the broadest region of the sun emission; ii) chemically and biologically inert and stable toward corrosion and photo-corrosion; iv) available, inexpensive, or easy to prepare; and v) non-toxic.

In this work, the photocatalytic efficiency of prepared materials has been studied based on three main fundamentals: optical absorption, the generation of charge carriers, and their subsequent availability for chemical reactions.

---

## 1.2 Advanced materials for photocatalytic applications

### 1.2.1. Optical and electronic properties: engineering semiconductors

As remarked in the previous paragraphs, light absorption represents a critical factor in designing new photocatalytic advanced materials. As a principle, light absorption initiates the photocatalytic process; thus, the optical properties, including absorption, extinction, and scattering coefficients, play prominent roles in the overall photocatalytic process. In heterogeneous photocatalysis, the material should absorb most of the available light energy to maximize its activity. Considering the total sunlight irradiation portion reaching the Earth's surface, 4% belongs to UV, 45% to visible, and 51% to IR wavelengths.

UV irradiation-based technologies have found success in many applications, but on the other hand, they are limited both in terms of feasibility and environmental benefits on an industrially relevant scale [26]. On the other hand, the low energy of IR, unable to activate most organic reactions, makes visible-based photocatalysis more desirable [27].

Thus, visible light benefits comprise its predominance in the solar spectrum, a large window of available wavelengths, a harmless character concerning UV radiation, and a higher energy amount concerning IR. The photocatalysts' design with the potential to be activated in the spectrum's visible light region can achieve heterogeneous photocatalytic applications' cost-effectiveness by using the full sun-light power.

Accounting for all the previous considerations, a consistent investigation has recently been dedicated to new advanced materials to increase their light absorption ability, especially in the visible range of solar irradiation. Recently, a new trend in heterogeneous photocatalysis has dealt with the formulation of new semiconductors active in the presence of visible light (380-700 nm) [28–31].

From the perspective of a green and sustainable future, the development of efficient and environmentally friendly photocatalysts with visible light response represents a research focus with exceptional advantages, offering many opportunities to revolutionize light-driven applications [32,33]. **Figure 7** shows the exponential enhancement in academic interest in visible light-based photocatalytics over the last 50 years.

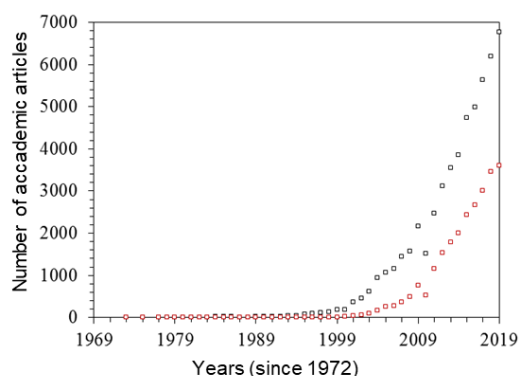


Figure 7: Trends of the published scientific articles on photocatalysis (black squares) and visible light photocatalysis (red squares), data by Scopus.com

In semiconductor-based photocatalysis, the optical excitation of the electron from the VB to the CB may lead to the generation of an electron-hole pair, initiating potential redox reactions beyond the initial light absorption. The process of light absorption obeys the energy and momentum conservation laws; thus, the minimum quantum energy necessary for the electron to jump from the VB to the CB must be equal to or higher than the semiconductor band gap ( $E_g$ ). The  $E_g$ , as the red edge of the fundamental absorption, determines one of the most critical parameters in the design of suitable semiconductors for photocatalytic applications. In principle, only photons with energies greater or equal to the semiconductor  $E_g$  can effectively promote the photogeneration of charge carriers (electrons and holes). The previous principle should always be included when the research aims to design new photocatalysts [34]. To date, the fabrication of efficient photocatalysts active under visible light irradiation and based on an individual semiconductor remains a great challenge for the research community. As a reference, titanium dioxide ( $\text{TiO}_2$ ) has shown great potential as a powerful and ideal photocatalyst for many reasons, including chemical stability, nontoxicity, and availability, leading to a considerable number of research papers [35–39].

Moreover,  $\text{TiO}_2$  has already reached not only pilot-scale but also practical applications. However, despite the great results, the wide  $E_g$ , with a value between 3.0–3.2 eV, restricts its use only to the narrow light-response range of UV irradiation ( $\lambda < 400$  nm), leading to inefficient utilization of the potential solar power (approximately 4 %) [34,40]. Many efforts have recently been made to develop visible light-response semiconductors with suitable  $E_g$  value-engineered to achieve more efficient solar light utilization. Band-gap engineering applied to photocatalytic processes mainly acted on the compositional modifications or the morphology of the crystal structure of semiconductors and their composition. Several methods have been applied to narrow the  $E_g$  to trigger the semiconductor's photoactivity under visible light irradiation, as much efficient radiation respects UV and IR. Some of these are discussed in the following chapter (1.3.4).

### 1.2.2. Charge carrier dynamics: Trapping, Recombination, and Transfer

After they have been photogenerated, the charge carriers may undergo trapping, recombination, and interfacial transfer. The fate and dynamics of photogenerated electrons and holes are critical investigations since they govern the redox reactions' reaction, the target of the overall photocatalytic process [41,42]. It can be assumed that, in many cases, the fast recombination rate of the photogenerated charges mainly determines the efficiency of photocatalysts [43]. In general, the absorption of light by the semiconductor induces the initial charge carrier separation. In terms of time, this process occurs in *femtoseconds*, and afterward, the photogenerated charge carriers may undergo recombination driven by electrostatic forces, releasing energy in the form of heat or light. However, the more desirable fate for the photogenerated charge carriers is the migration on the photocatalyst's surface, where it can be trapped before undergoing interfacial charge transfer processes. The subsequent charge transfer and redox reactions strongly depend on the energetic position of the as-formed trapped states.

By considering the time-scale of the single events, the photocatalytic performance can be considered the competition between the recombination and trapping processes that drive the photogenerated free charge carriers [3,38,44]. **Figure 8** shows a scheme of the process.

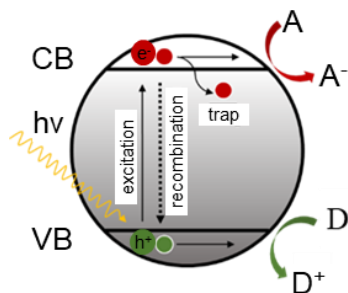


Figure 8: Charge carrier dynamics in a photocatalyst particle. At the surface electrons react with electron acceptors (A) and holes with electron donors (D).

### 1.2.3. Driving surface electron transfer and redox reactions

Electron transfer reactions constitute one of the main pillars of chemistry: driving forces of several natural processes and technological applications. Photosynthesis is an example of a natural light-driven process. It uses specialized complexes, such as pigments, to transfer the absorbed light energy to an efficient hierarchy of proteins and generate an energetic cascade that finally leads to fixing solar energy in chemical bonds once it reaches the reaction centers [45]. An example of an energy transfer process can be summarized as:



The excited donor,  $D^*$ , quenched at its ground state ( $D$ ), releases energy, subsequently absorbed by the acceptor ( $A$ ), which is promoted to its excited state  $A^*$ .



Similarly, in heterogeneous photocatalysis, energy transfer photo-induced reactions are fundamental for the overall process's proper proceeding.

These reactions may occur on the irradiated photocatalyst's surface, which can be suspended in liquid or gaseous media, or immobilized, as when coated on a support.

As electron transfer processes, redox reactions constitute one of the broadest and most important classes of chemistry and biochemistry reactions. The redox reactions involve a full or partial transfer of electrons between substrates. In previous literature, the role of electrochemical properties of semiconductors used as catalysts in redox reactions in natural environments and engineered systems designed to convert light-energy has been recognized [46,47]. A semiconductor's suitability for a target photocatalytic application can be verified by its ground and excited states' redox ability. In the first approximation, the interfacial charge transfer processes occurring on the photocatalyst's surface strictly depended on the energy position of the CB and VB edges [3,48]. In principle, both in the case of reversible (dye-sensitized solar cells) and irreversible (pollutant oxidation) processes, in redox reactions, suitable level energies (CB, for electrons, and VB, for holes) are required to assure the overall process.

The determination of redox properties and the corresponding energy band levels of semiconductors, often underestimated by researchers, is crucial to investigate the photo-induced electron transfer that drives the overall photocatalytic process. However, despite examples of induced photocatalytic reactions and their mechanistic aspects being widely investigated, they have yet to be clarified [49–53]. A deep understanding of the energy (electron) transfer phenomena in engineered materials is still required, and the design of suitable materials that provide efficiency and selectivity in transfer processes is gaining increasing attention. Unfortunately, measuring uncertainties and complex interpretation of the data may be why such analyses are often missing in many reports.

#### 1.2.4. Analytical methods

##### a. Optical properties

The determination of the optical absorption ability and the band gap of semiconductor-based photocatalysts was considered essential to understanding the as-prepared photocatalysts' potential efficiency.

UV-vis diffuse reflection spectroscopy (UV-vis DRS) measures the reflection ability of a solid sample hit by a suitable light beam; thus, indirectly, it provides useful information on the ability of photocatalysts to harvest light. Generally speaking, when a material can absorb in the visible light range, its UV-vis DRS spectrum shows an absorption edge over 380 nm, exhibiting blue-shifting over longer wavelengths [54,55]. Thus, UV-vis DRS analysis is fundamental when the goal is the design of visible light-based photocatalysts. According to theory, the ability to absorb light and the corresponding band gap,  $E_g$ , can be estimated with UV-vis DRS using the Tauc plot extracted by the Kubelka-Munk equation:

$$\alpha hv = \beta (hv - E_g)^{n/2} \quad (1.4)$$

where  $\alpha$  is the absorption coefficient ( $\text{eV}^{-1}\cdot\text{cm}^{-1}$ ),  $h$  is the Planck constant ( $\text{eV}\cdot\text{s}$ ),  $\nu$  the photon frequency ( $\text{s}^{-1}$ ),  $\beta$  is the proportionality constant,  $E_g$  the band gap energy (eV), and the value of  $n$  depends on the transition properties of the semiconductor. The  $n$ -value is equal to 1 for direct and 4 for the indirect nature of transitions [56]. The  $E_g$  value can be calculated by plotting  $(\alpha h\nu)^2$  vs  $h\nu$  and extrapolating the curve's straight-line portion to the x-axis.

The previous approach measured the photocatalyst materials' absorption ability synthesized in Papers I, II, III, and IV. For further information, see **Paper II**.

Alternatives to the mentioned method include x-ray (XRD) and ultraviolet photoelectron spectroscopy (UPS). These measurements can give information on the value of VB that, combined with UV-Vis spectroscopy, can estimate the energy level of CB and the  $E_g$  [57]. Also, cyclic voltammetry analysis (CV) can measure the redox potentials, from which it is possible to extrapolate the  $E_g$  [58].

### **b. Charge carrier dynamics**

Transient absorption spectroscopy (TAS), as an extension of absorption spectroscopy, is an established method for observing charge carrier kinetics by studying their dynamics using an ultrafast pulsed laser as excitation. During TAS analyses, photogenerated electrons and holes are isolated and monitored by a delayed continuous probe beam. The signals can be measured as a function of wavelengths and time until equilibrium is reached. The charge carrier population is evaluated according to the intensity of the obtained transient signals, and the lifetime of photogenerated species can be measured according to time. Based on these parameters and the employed experimental conditions (i.e., air,  $\text{N}_2$ , or  $\text{O}_2$  atmosphere), the measurements can reveal the formation, the consumption, and the different types of photogenerated charge carriers [39,59–61].

Moreover, it is possible to evaluate the photocatalyst's electronic structure, including the position of energy levels, VB and CB, and the corresponding charge densities employing the density functional theory (DFT). For example, DFT measurements are useful tools to investigate the structural units responsible for trapping the excited electrons, prolonging the charge carriers' lives. Moreover, this method can reveal the formation of localized mid-gaps, which spatially separated from the CB electrons are beneficial in limiting recombination losses [37,62]. A possible alternative is the study of charge carrier dynamics by using the photoluminescence technique (PL). In general, charge recombination releases energy in the form of light or heat. PL spectra can thus estimate the recombination rate of charge carriers directly by measuring the energy-released intensity [63–65].

TAS measurement has been selected as a suitable approach to clarify the charge-carrier dynamics in the current work; comprehensive information is reported in **Paper III**.

### **c. Driving surface electron transfer and redox reactions**

In general, two critical parameters in the electronic structure of the material should be considered to design new efficient photocatalysts: the forbidden  $E_g$ , that influence the absorption spectrum, and the flat band potential,  $V_{fb}$ , that affects the probability of charge recombination [66]. The equilibrium of Fermi levels of a semiconductor at the interface with

an electrolyte solution (or another semiconductor) leads to bending band edges. This phenomenon consists of a charge transfer from one side to the other side of the interface. The flat band potential  $V_{fb}$  is defined as the potential required to bring the semiconductor band edges back to their flat band positions. Thus, this parameter study leads to evaluating the charge carriers involved in the process [67].

The flat band potential can be evaluated by Electrochemical Impedance Spectroscopy (EIS) by plotting the capacitance versus voltage measurements, and under specific circumstances ( $EF > EF_{(redox)}$ ), the Mott–Schottky model can be used to determine the  $V_{fb}$  of a semiconductor:

$$\frac{1}{C^2} = \frac{2}{\epsilon\epsilon_0 A^2 e N_D} \left( V - V_{fb} - \frac{k_B T}{e} \right) \quad (1.5)$$

where  $C$  is the interface capacitance (Farad,  $m \cdot kg \cdot s \cdot C$ ),  $\epsilon$  the dielectric constant of semiconductor ( $kg \cdot m^3 \cdot s^{-2} \cdot C^{-1}$ ),  $V$  the applied potential ( $kg \cdot m^2 \cdot s^{-2} \cdot C^{-1}$ ),  $V_{fb}$  the flat band potential ( $kg \cdot m^2 \cdot s^{-2} \cdot C^{-1}$ ),  $N_D$  the doping density ( $m^{-3}$ ),  $A$  the charge depletion area ( $m^2$ ),  $k_B$  the Boltzmann's constant ( $C \cdot K^{-1}$ ),  $T$  the room-temperature (K). In general, the Mott Schottky equation results are obtained by plotting the inverse square of the space charge layer capacitance versus semiconductor electrode potential and extrapolating the straight line of the curve. The Mott Schottky model yields two direct details. First, the value of the slope of the line provides information on the doping density of the semiconductor: the decrease in the slope corresponds to an increase in donor density. Second, the intercept of the line with the electrode potential (eV) on the x-axis provides an estimation of the value of  $V_{fb}$ . Allowing the measurements of the semiconductor CB energy level related to the reference potential. **Figure 9** shows an example of a plotted Mott–Schottky model. The measurement is performed in a photoelectrochemical cell. A thin film of the photocatalyst is coated on the glass-based photoanode and immersed in a liquid electrolyte under controlled conditions, using a potentiostat as electronic hardware. More details are provided in **Paper IV**.

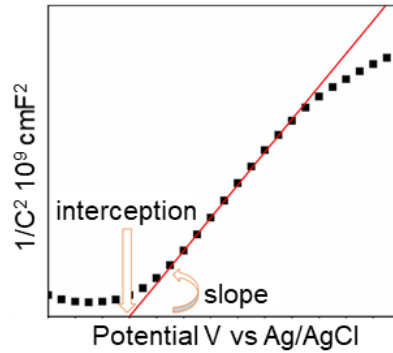


Figure 9: Representative Mott–Schottky data.

Many oxidative and reducing species are usually formed through radical-chain processes initiated by photogenerated holes and electrons. Briefly, at this stage, the photocatalytic activity depends on the catalyst's ability to create electron-hole pairs, which subsequently generate free radicals to undergo different secondary reactions.

In recent years, several methods have been studied to reveal the generation of reactive radicals. Electron paramagnetic resonance (EPR) or electron paramagnetic spectroscopy (EPS) is one method for detecting reactive radicals as intermediates in photocatalytic redox reactions [3,68]. EPR, revealing the analyte's unpaired electrons, represents a useful tool to establish the photogenerated charge carriers' transference mechanism between surfaces or environmental interfaces. This method was employed during this study, and more details can be found in **Paper I**.

As a more straightforward approach, radical trapping experiments in the gas or liquid phase may also detect the reactive radicals that play the principal roles' redox reaction. The method is based on chemical reactions employing selected scavengers [35]. This approach was applied in this study, and more information is presented in **Paper II**.

### 1.2.5. Recent strategies for advanced materials in heterogeneous photocatalysis

Photocatalysis has proven a remarkable development since Fujishima and Honda's breakthrough discovery in 1972 [21]. Nevertheless, there are some limits concerning its efficiency, feasibility, and environmental benefits, particularly on an industrially relevant scale [26,69]. Much effort has been dedicated to the eco-friendly enhancement of some common photocatalysts' fundamental properties from this perspective. **Figure 10** shows some of the most popular approaches.

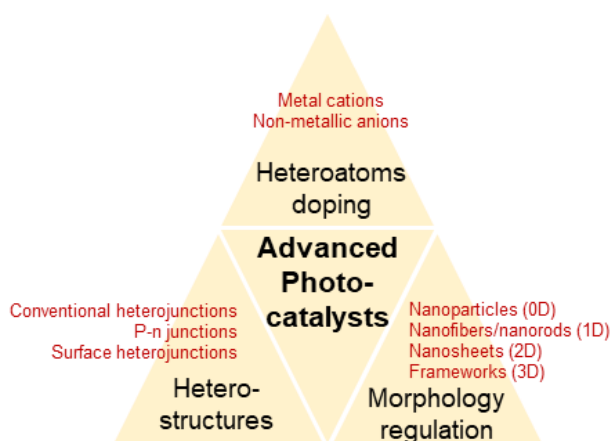


Figure 10: A synthetic illustration showing the design strategies for advanced photocatalysts.

#### a. Advanced material: morphology regulation and nanoscience

The advent of nanotechnology and nanoscience has recently succeeded in many fields, such as environmental, energy, and biological engineering, representing a new trend in developing highly active and functional materials [70]. Nanomaterials are defined according to their dimensions and shapes, which vary from dots (0D), tube, rod, and wire particles (1D), sheets (2D), or arrays of 1D structures (3D). The morphology and the dimensions vary the properties of materials, providing potentially optimal solutions in practical applications.

In the past decades, the effect of nanosize in photocatalysts has been investigated, discovering unique photophysical and catalytic properties [71]. Nanoscience expands from conventional bulk and colloidal materials (10–100 nm) to nanosized or small clusters (1–10 nm). At the nano-scale, material properties are governed by quantum confinement and cluster surface chemistry: the physical properties strictly depend on the surface area, and the dimension and the structural morphology influence the electronic behavior. First, nanosized photocatalysts, with a higher surface area, generally provide high light absorption. Second, nanotechnology offers the possibility to explore the new phenomena observed when the material size and the electromagnetic field (light wavelength) match [71]. The nano-atoms' size and shape allow fine-tuning of the energy in discrete electronic states and optical transitions, resulting in controlled light absorption and further optical properties. According to their strong photoluminescence, nanosized semiconductors should be considered poor photocatalyst candidates.

On the contrary, due to the minimized structural distances, the charge carriers' diffusion time is so fast that the normal recombination processes lose importance concerning the transport and trapping effects. Nanoscale architectures exhibit unique optical and electronic properties required in many photo-functional materials and their applications [72,73]. Third, as a practical consideration, modified nano-based photocatalysts can be prepared with simple approaches such as sol-gel, hydrothermal, and solvothermal methods [36,74,75]. It is useful to highlight that reproducible and straightforward synthetic methods are desirable, especially for their potential industrial utilization feasibility.

Finally, the easy functionalization of nanoparticles can provide a further implementation in advanced material science. New routes to design nanohybrid systems are ideal methods to enhance light-harvesting properties and charge-transfer processes [76–79]. Moreover, nanostructure assembly behavior is easier to control, leading to photocatalyst preparation with specific properties, functions, and applications. In conclusion, nanoscience and nanotechnology open a conceptual direction for developing new efficient photocatalysts. However, a higher level of understanding is still needed, for example, on the correlations between sizes and photocatalytic properties [80].

#### **b. Advanced materials: heteroatoms doping**

The effects of chemical composition, such as heteroatom doping, have been widely recognized as valid approaches to enhance photocatalytic processes. These methods alter their electrical, optical, and structural properties by adding impurities into the intrinsic semiconductors, leading to attracting superior activities. Nowadays, many doped materials have been developed, such as the use of metal cations, non-metal anions, or non-metal molecules, demonstrating enhancement in the absorption ability and beneficial influence of the electronic structure of the pure semiconductor [81–83].

The most employed metal cations used in heteroatom doping for semiconductors include transition metal ions ( $\text{Fe}^{3+}$ ,  $\text{Co}^{3+}$ ,  $\text{Mo}^{5+}$ ,  $\text{Ru}^{3+}$ ,  $\text{Ag}^+$ ,  $\text{Cu}^{2+}$ ) [84]. The redox energy states of metal cations, lying within the semiconductor's band gap states, can introduce intra-band states near the CB or VB edge of the precursor, leading to a redshift in band gap absorption. This effect may contribute to charge carrier migration between the doped cations' electrons and the corresponding semiconductors' bands. Moreover, in some cases, the metal cations may act as

charge carrier traps, regulating the equilibrium concentration of electrons and holes in the overall photocatalytic process. Additionally, some transition metal cations, providing new energy levels, improve the corresponding semiconductor activity by acting as electron donors or acceptors. This approach's disadvantages include the relative structural instability, expensive precious metals, and the increase in recombination rate, making this strategy limited in particular circumstances.

As an alternative, appropriate non-metal doping has proven to be a valuable option to modify semiconductors' electronic structure and improve photocatalytic performance [85]. For example, the introduction of non-metal impurities, such as N, C, and S, can introduce energy levels above the photocatalyst VB, resulting in beneficial photocatalytic performance [86–88]. In general, the availability, stability, and nontoxicity of such dopant ions are among the advantages of non-metal over metal elements [89]. Briefly, great photocatalytic performances have been reported by doping semiconductors; thus, this successful approach merits continuing efforts.

### c. Advanced materials: heterostructures

Properly engineered composite photocatalysts have also shown successfully increased photocatalytic activities. The approach provides a combination of multiple materials. The materials' synergetic actions improve photogenerated electron-hole pairs' spatial separation, decrease their recombination rate, and enhance photocatalytic performance. The principle stands in forming interfaces between semiconductors with unequal band level structures that may lead to the formation of band alignments [90]. In general, different configurations were developed and classified in *conventional* or *new generation heterostructures*. The conventional heterojunctions are sorted into three types according to the relative position of the semiconductors' energy levels: type I with a straddling gap, type II with a staggering gap, and type III a broken gap (**Figure 11**).

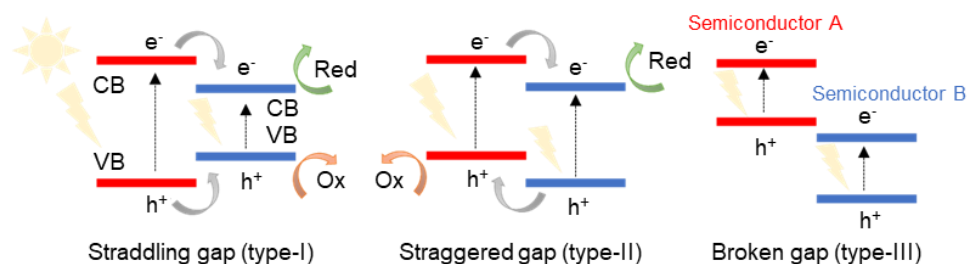


Figure 11: Schematic illustration of the three types of conventional light-responsive heterojunction photocatalysts.

In **type I heterojunctions**, the redox reactions performed on the second semiconductor's surface with a lower redox potential generally suppress the whole photocatalyst's efficiency. In **type II heterojunctions**, the energy levels of the first semiconductor, VB, and CB are higher than those of the second material. The photogenerated electrons tend to migrate from the first to the second material, which reduces potential. The holes migrate from the second to the first material, which has a lower oxidation potential. In this case, the beneficial spatial separation of electron-hole pairs assures high photocatalytic performance. The electron-hole transfer

results are unsuitable in type III heterojunctions due to the semiconductor energy levels' configuration. In summary, the type II heterojunction is considered the most effective structure to improve semiconductor performance in light-driven catalysis, and, for this reason, it has received greater attention in many photocatalytic applications [91].

In general, traditional heterostructures' redox ability may result in sacrifice because the redox processes at the surfaces occur on the semiconductor with lower reduction and oxidation potentials. To overcome the mentioned problem, **Z-scheme photocatalysts** were first proposed by Bard [92] and then further improved by other researchers [93,94]. In brief, a Z-scheme photocatalytic system is based on two different semiconductors (P1 and P2) that are not in direct contact and a pair of acceptor/donor (A and D), which interact in the charge transfer process (Figure 12). However, conventional Z-scheme photocatalysts are mainly applicable in the liquid phase, limiting specific applications. As an alternative, **all-solid Z-scheme photocatalysts** can provide a solid electron mediator between the two semiconductors. This structure was employed in liquid, gas, and solid media. However, the solid mediators required are very expensive, limiting large-scale applications [95,96] **Figure 12**. However, the conventional Z-scheme photocatalysts are mainly applicable in the liquid phase, limiting specific applications. As an alternative **all-solid Z-scheme photocatalysts** can provide a solid electron mediator between the two semiconductors. This structure was employed in liquid, gas, and solid media. However, the solid mediators required are very expensive, limiting large-scale applications [95,96] (**Figure 12**).

**Hierarchical direct Z-scheme photocatalyst** was prepared, with a relatively cheap method, combining two different semiconductors, without the electron mediator **Figure 12**. The electrostatic attraction formed between electrons and holes favored the charge transfer optimizing the overall redox potential concerning conventional heterojunctions [97–100].

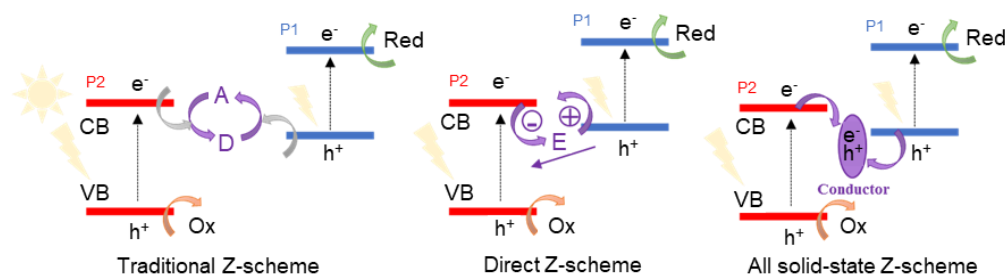


Figure 12: Schematic illustration of the most popular Z-scheme light-responsive photocatalysts.

As an efficient alternative, **p–n heterojunction photocatalysts** can be considered (**Figure 13**). The advantage of such a system includes the suitability of the separation process, from a thermodynamic point of view, due to the specific configuration of the energy levels [101]. The system results in higher and faster separation charges concerning the traditional type-II heterojunction photocatalysts due to a synergetic effect between the internal electric field and band alignment. Moreover, the p–n heterojunction photocatalyst morphologies' easy tunability results in enhanced specific surface area and amount of active surface sites, leading to improved photocatalytic activity [102].

Finally, the **surface heterojunctions** are a valuable alternative due to the unique phenomenon of charge separations observed on the crystal facets using a single semiconductor (**Figure 13**). Different crystal facets were employed in the system to contain separated band structures [103]. This engineered design enables a positive charge separation characterized by affordable fabrication costs to face economic feasibility because only one semiconductor can be employed. Notably, the redox potential loss can also be minimized with a suitable small difference in the band structure of the material facets [104,105].

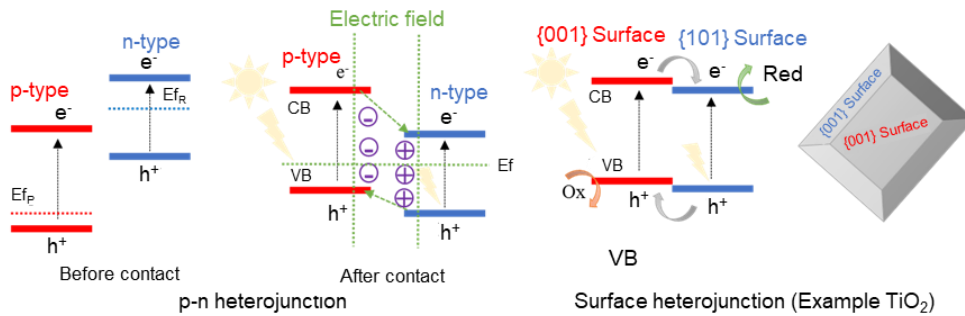


Figure 13: Schematic illustration of p-n heterojunction and surface heterojunction light-responsive photocatalysts.

To date, practical applications and commercialization of heterojunction photocatalysts still require further insights and progress. Future research should probably focus on developing facile, efficient, and economic preparation methods, especially on a large scale for practical industrial applications. Advancements in morphological control, contact-interfaces, crystallization, and hierarchical assembly may lead to potential developments parallel with nanoscience and nanotechnology. A study on the photogenerated charges' migration pathways is required to confirm the reason for the success of the different types of heterojunctions. Theoretical calculations and modeling methods should attract relatively more attention to better comprehend the processes' kinetics. Finally, more efforts to design materials for heterojunction photocatalysts also seem favorable to optimize morphological and optoelectric properties, fulfilling requirements such as visible light activity, high solar-conversion efficiency, structured redox reactions, photostability, and scalability for industrial commercialization.



### 1.3 Research Objectives

This research project aims to develop new semiconductors or composites with enhanced photocatalytic activity under visible light irradiation. This work aimed to perform fundamental experiments to investigate new photocatalysts' performance, focusing on their preparation, characterization, and potential applications. **Figure 14** describes the approach schematically.

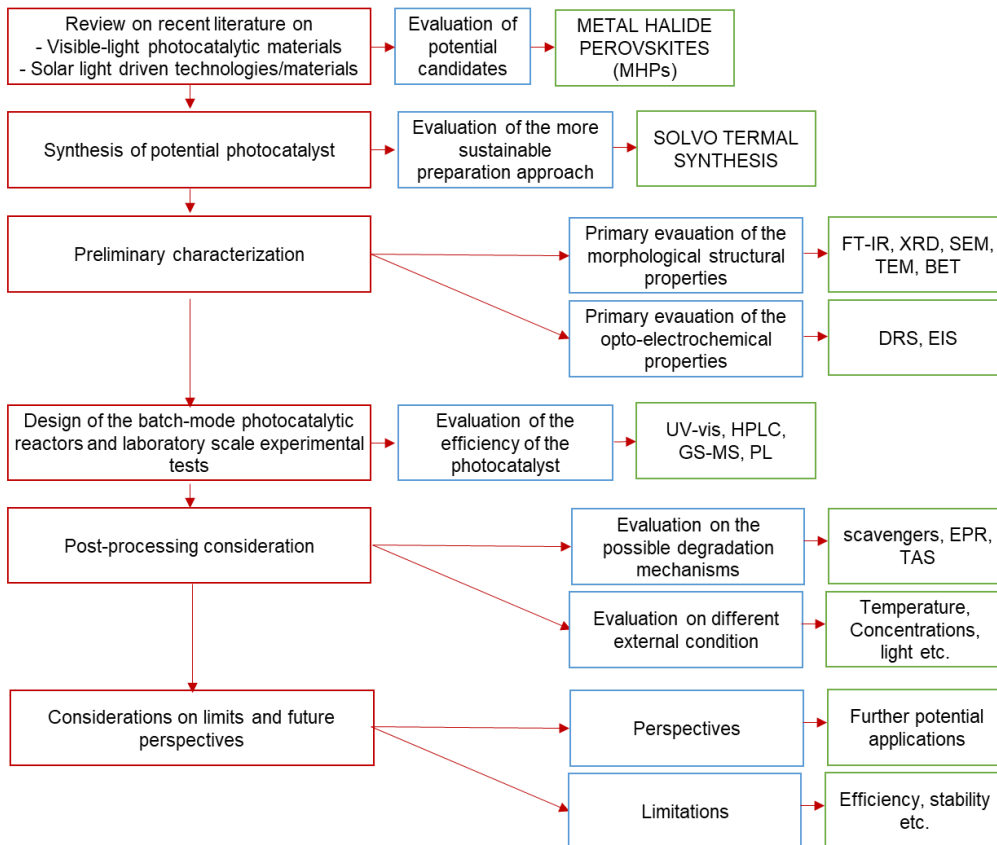


Figure 14: Schematic representation of the research approach adopted.

## 1.4 Hypothesis

Metal halide perovskites recently emerged as new frontier materials, and they were efficiently used in multiple photoelectrochemical applications due to their particular properties. For this reason, MHPs were employed in this research work based on two principal hypotheses:

- MHPs are considered a new promising class of cheap and easy-to-make semiconductors, useful for different visible-light-driven photocatalytic applications.
- A heterostructured photocatalyst may provide higher photocatalytic activity when properly engineered due to multiple materials' synergetic action.

## 1.5 Scope of study

This work studies the synthesis of metal-halide perovskite-based photocatalysts and their potential in particular for visible-light-driven applications. The efficiencies of the materials were tested in different photocatalytic reactions and conditions. The photocatalytic mechanisms, including the correlations between the achieved results and the photocatalysts' optoelectric properties, were discussed. All measurements and experiments employed laboratory-scale reactors. In the system, the metal-halide perovskites were first tested alone rather than in composition with other materials used as supports. All photocatalysts were characterized in their morphological, optical, and electrochemical properties using different advanced techniques. The as-prepared materials were applied for wastewater treatments and hydrogen production. However, the research mainly focused on wastewater experiments. In the particular case of photodegradation experiments, the by-products and the involved reactive oxygen species (ROS) were detected and examined to highlight the hypothetical mechanisms of degradation.

## 1.6 Delimitation of study

Research on new photocatalytic materials is a field in continuous expansion due to their environmental and energy impacts. To date, an enormous number of materials and systems have been reported in the scientific literature as potential photocatalysts. The paper aims to highlight methodological considerations in the design of a new photocatalyst. Due to the relative novelty of the employed material, some former research limits should be discussed.

The solvothermal approach was selected for its synthetic simplicity and reproducibility to obtain the desired products. However, further studies on parameter optimization could influence the photocatalytic efficiency of the resulting materials.

A similar principle should be applied to choosing a simple reactor that was selected to avoid complicated design. The current research was conducted on a lab-scale; thus, pilot-scale reactor construction was not considered at this stage. Finally, the current research was based on experimental tests and analytical approaches. The mathematical modeling of the involved processes was not considered at this stage.



## 2 Metal halide perovskites

Recent years have witnessed an incredibly high fever in perovskites as a new family of advanced materials for different light-based technologies. Metal halide perovskites (MHPs) have attracted academic interest due to their easy production and excellent optical and electrochemical properties. Remarkably rapid development and comprehensive studies involve MHPs, due to the great results achieved in photovoltaics and photochemical applications. MHPs are considered promising candidates in different light-driven technologies, such as light-emitting diodes, photodetectors, lasers, X-ray detectors, or luminescent solar concentrators. These materials' advantages include high extinction coefficients, suitable band gaps, high photoluminescence quantum yields, and long electron/hole diffusion lengths [1,106–108]. Pioneer reports first appeared in the photovoltaic field, where MHPs were used to enhance the performance of self-organization dye-sensitized solar cells supported on nanoporous TiO<sub>2</sub> layers [109,110]. The extinction coefficients of MHPs, across the entire visible range, and the enhanced conversion efficiency, comparable to the traditional solar cells, make this family of materials very appealing [111].

Moreover, MHPs have shown other distinct advantages, such as structural simplicity and flexibility and optical and electrochemical properties tenability, leading to remarkable attention in different fields [106,112]. Therefore, due to the several properties presented, MHPs have also been considered great candidates for photocatalytic applications. As first, Park et al. [107] succeeded in the employment of methylammonium lead iodide (CH<sub>3</sub>NH<sub>3</sub>PbI<sub>3</sub>, MAPbI<sub>3</sub>) for generating hydrogen via light-driven splitting from hydrogen iodide solution. Later, other researchers investigated the potential of MHPs in different photocatalytic reactions [113–118].

In this work, different types of MHPs were prepared and tested as visible light active photocatalysts. The photoelectrochemical properties of MHPs, considered driving forces for successful photocatalysis, are considered the research work guidelines. The exciting results achieved in many recent research works seemed good reasons to investigate this family of materials for potential photocatalytic applications. These promising materials' limitations are discussed to explore their real potential utilization, economic feasibility, and environmental sustainability.

### 2.1 Fundamental Structure and Composition

The exceptional morphological and photoelectrochemical properties of MHPs were among the main factors that motivated considerable attention to this class of materials for light-based applications. Generally, MHPs have a structure defined as ABX<sub>3</sub>. The A-site contains a hybrid organic-inorganic monovalent cation (methylammonium MA<sup>+</sup>, formamidinium FA<sup>+</sup>), an inorganic cation (cesium Cs<sup>+</sup>), or a mixing of these ions. The B-site generally consists of a metal element of the XIV group of the periodic table in a divalent oxidation state (lead Pb<sup>2+</sup>, tin Sn<sup>2+</sup>, germanium Ge<sup>2+</sup>...) or mixing of them. The X-site usually consists of a halide anion (iodine I<sup>-</sup>, bromide Br<sup>-</sup>, or chlorine Cl<sup>-</sup>) or mixing of them. In general, the cations in the A-site determine the structural orientation between the main cage's layer, leading to transitions in the optoelectronic properties, the interfacial energy levels, and the absorption abilities [119–121]. In particular, the A-cation size can affect the structure's symmetry, causing distortions on the B-X bonds, influencing the framework's electronic features [122]. Among the hybrid organic-

inorganic MHPs,  $\text{MA}^+$  has been widely employed as a cation in the A-site due to its size, which allows lower packing symmetry, higher band gap, and higher efficiency concerning other cations [119]. In hybrid organic-inorganic MHPs (HOIPs), an organic cation occupies the A-site position. Recently, researchers replaced the organic fraction with inorganic metals to overcome the long-term and environmental instability of hybrid materials. The commercialization of hybrid MHPs has demonstrated that environmental stability represents a fundamental requirement; thus, temperature, light, and humidity conditions should always be considered during the tests. The organic components in MHPs, such as  $\text{MA}^+$  and  $\text{FA}^+$  ions, may undergo various degradation and decomposition pathways due to the different environmental factors [123,124]. All-inorganic MHPs have emerged as a valuable alternative and new class for optoelectric devices and in other applications. Therefore, many researchers have successfully replaced the organic fraction with inorganic components, such as  $\text{Cs}^+$ , to increase the devices' long-term stability [125,126].

Moreover, in the A-site position, mixed organic and inorganic cations can enhance the stability of hybrid MHPs toward thermal and moisture stresses [127,128]. In general, by proceeding through the periodic table's IV group elements, B-site modulation was affected by reducing the divalent oxidation state stability. Moreover, enhancing the elements' electronegativity and covalent characters decreases the band gap and electron pair effect [24,129]. Among all-inorganic MHPs, lead-based material has received considerable attention, overcoming stability issues, and maintaining remarkable electrochemical properties [130]. Many researchers have focused their interest on Pb-based MHPs, eventually doped with Cs or Rb, because they showed relatively higher power conversion and stability in the air atmosphere [131]. However, to provide a more environmentally friendly solution, other ions have been employed to replace lead. For example, lead, known as a toxic element, was substituted or partially substituted by tin (Sn) with interesting results in solar-cell devices [132]. From a similar perspective, calcium (Ca) [133,134], manganese (Mn) [135,136], strontium (Sr) [137], and bismuth (Bi) [138] have been employed in B-site, resulting in relatively higher environmental stability and, in some cases, even higher application performance. B-sites play an essential role in environmental stability, and divalent ions in this position are desirable [139]. The selection of the halogen element in the X-site has also demonstrated a significant impact, particularly on both the optical and electrochemical properties of the MHPs. In general, along with the XVII group of the periodic table, going from chloride (Cl) to I (iodide) elements, the bond strength between the A-site cation and the halogen element decreases, and the valence and conduction band tend to move closer, decreasing the value of the optical band gap [140,141]. This effect can be considered beneficial for the enhancement of visible light photocatalytic performance.

Moreover, X-site modulation with mixed halogen ions has demonstrated enhanced stability and reduced charge carrier recombination, leading to superior application performance compared to the single ion-based counterparts [109,130,142–144]. Band gap engineering and compositional modulation were also considered. For example, the cover of almost the entire visible spectral region was achieved by employing a suitable Cl/Br ratio (410–527 nm) and Br/I ratio (527–700 nm) [140].

In conclusion, the morphology and composition of MHPs influence several factors, such as environmental stability, activity performance, and toxicity, and they must be carefully

considered to produce breakthrough perovskite-based materials according to the target application [145–147].

## 2.2 History and traditional application (photovoltaics and diodes)

In the current society, the discovery and implementation of materials for energy storage and production using solar light as renewable energy resources have an important impact as a sustainable source of power with low environmental impact. In this context, the last century has witnessed the advent of a new generation of materials, MHPs, which emerged for their remarkable properties useful for many applications. In very few years, MHP-based solar cells showed an incredibly rapid increase in power conversion efficiency from 3.8% up to 23.3%. This discovery opened the way to further light-energy-related applications as challenges of the century [1,148]. The halide perovskite-based materials are easy to prepare, and they have a characteristic versatility in terms of composition. According to morphology and composition, the easily tunable properties of MHPs lead to a new avenue for many applications. The term *perovskite* was created in 1839, when Perovski, a Russian mineralogist, discovered the structure of calcium titanate ( $\text{CaTiO}_3$ ) [149,150]. In the last decades, these materials have increased their employment in numerous academic fields with hundreds of peer-reviewed publications (**Figure 15**).

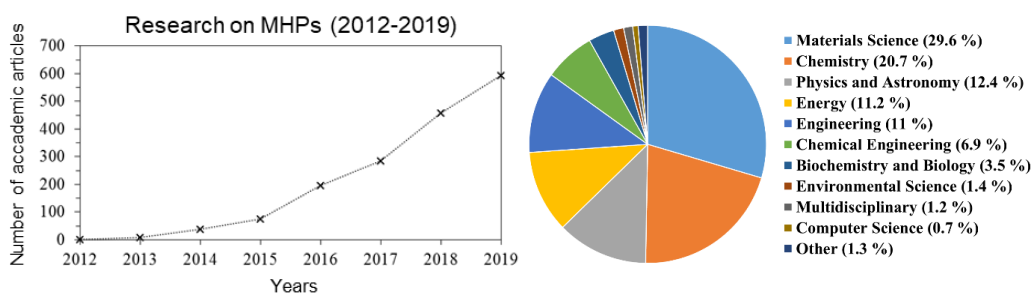


Figure 15: Trends of the published scientific articles on metal halide perovskites and academic fields (Scopus.com).

Around one century later, the born of the term perovskite, the first employment of MHPs, highlighted their crystal size effects in particular on the excitonic optical spectra of copper nanocrystals and silver colloids [151,152]. In the beginning, for many decades, MHPs did not receive relevance despite pioneering studies, probably due to their defective applicability [153–155]. More recently, the remarkable photoelectrochemical properties of MHPs have found relevance in many technologies [109,156–158]. Among the first successful applications, the Miyasaka group in 2005 [159] applied MHPs on mesoporous  $\text{TiO}_2$  electrodes, inspired by quantum photochemistry studies of Teshima and Kojima [160,161]. HOIPs initially achieved remarkably positive results due to their enhanced absorption in the visible light range. In 2014, solution-based colloidal approaches were employed by Schmidt et al. [162], achieving similar benefits in the use of MHPs. However, the relative instability of HOIPs, especially in humid conditions, opened up the way for alternatives, including the fabrication of all-inorganic MHPs. Among all-inorganics MHPs,  $\text{CsPbX}_3$  ( $X = \text{Cl}, \text{Br}, \text{I}$ ) is to date the most investigated due to its ability to cover the entire visible spectrum and its high quantum efficiency [163]. The discovery

of the rare properties of MHPs has expanded their studies on other applications, such as light-emitting diodes (LEDs), photodetectors, X-ray detectors, memory devices, and more. The incredibly fast progress achieved in MHP-based applications can be related to their interdisciplinary nature, which required the cooperation of chemists, physicists, and engineers, gaining the interest of a large community of researchers worldwide. However, despite the enthusiastic achievements, the practical relevance, limits, and potentials of MHPs remain unclear or partially unexplored, leaving researchers a lot to discover. Among the most traditional investigations based on MHPs, photovoltaic solar cells and light emission diodes (LEDs) are discussed before exploring the more recent MHP-based photocatalytic applications.

### 2.2.1. Photovoltaics

As previously discussed, MHPs were initially used as an alternative to dye molecule-based sensitized solar cells due to their exceptional absorption coefficients and the ability to extend the absorption in the visible light range of the solar spectrum [108,164,165]. MHPs have long carrier diffusion lengths, and remarkable performance was achieved in planar heterojunction architectures [166,167]. In 2014, the power conversion efficiency (PCE) of perovskite-based solar cells led up to 19.3% when applied in sandwich-structure in between n-type electrons collector layer ( $\text{TiO}_2$ ) and p-type holes transporting materials (organic Spiro-OMeTAD) [2]. Only one year later, the inconvenient large hysteresis exhibited by the previously mentioned structure was reduced using a thin layer of mesoporous  $\text{TiO}_2$ , preserving the great stability [168]. Moreover, this system recorded a high charge extraction and low electron accumulation, which are usually considered beneficial effects for solar power conversion [107]. In the same year, an efficient alternative was provided by Yang et al. [169] substituting  $\text{TiO}_2$  with an organic n-type layer in the so-called p-i-n perovskite cells. The decrease in the density defects led to the beneficial effect of the organic materials.

Moreover, in this configuration, all the advantages of organic photovoltaics were maintained, for example, the low-temperature solution process and the easy energy level alignment tenability at the interfaces [170]. There is no doubt that all the reported advantages have predicted a successful perspective for the employment of MHPs in future technologies. Multi-junction hybrid devices also provide a cost-effective and efficient MHP-based solar cell. The perovskites were supported on silicon, copper, or indium gallium selenide in these configurations, leading to valuable opportunities in the commercial field [107]. The adaptability and processability of MHPs make them easy to display on multiple layers via solution or vapor deposition, leading to the construction of flexible formats. In the future, many technologies would take advantage of employing MHPs, including lightweight and high-power photovoltaics, space applications, air transportation, and military industries.

Moreover, the ability of MHPs to range from rigid to flexible and from semi-transparent to colored solar-powered systems are advantageous technological features to be considered an evident and rich toolbox in the next generation of photovoltaic devices [171–173]. Nowadays, MHP-based solar cells have achieved a certified PCE of 25.2% for small and 16.1% for large-area solar modules, comparable with the most traditional commercialized devices such as Si or GaAs-based devices [111]. Moreover, the convenient costs of fabrication revealed the further advantages of MHP-based devices compared with traditional ones. Finally, one should mention that many challenges remain; for example, the development of studies for MHP-based device cost analysis may guarantee their future commercialization [174–176].

### 2.2.2. Light-emitting diodes

Besides the recent advancement in photovoltaics, MHPs also promise a bright future for light-emitting diodes (LEDs). Their advantageous properties, such as high color purity, high luminance yield, low non-radiative recombination rates, and suppressed defect formation, have recently gained the attention of many researchers [112]. LED technology uses light energy to produce electricity; thus, it is useful in several modern applications, such as lighting, flat-panel displays, medical devices, and more. In general, non-radiative recombination mainly limits the efficiency of LED. The photogenerated charge carriers tend to recombine without releasing photons, trapping the light; thus, considerable improvements in the device's efficiency are still required. Traditional approaches usually involve complicated fabrication processes or may face application complications, such as distortion of the output-spectrum or light-direction, leading to lower efficiency of the devices [177,178]. In general, heterostructure-based semiconductor LEDs have shown many advantages by controlling fundamental parameters such as the electronic band structure, the band gaps, refractive indices of material, and the effective mass and mobility of charge carriers. In particular, the development of MHP-based semiconductors in photovoltaics prompted engineers to re-focus their application in other emerging fields, such as LEDs, lasers [179], and even radiation detectors [180,181]. Recently, MHPs have been successfully employed in bright LEDs due to their impressive photophysical properties, such as high defect tolerance and excellent photoluminescent quantum yield.

Moreover, their photoluminescent emissions and band gaps can easily be tuned by changing their compositions [182–184]. The rapid increase in the number of studies on MHP-based LEDs has made a remarkable progression in merely five years, comparable to the development of MHP-related photovoltaics [185]. On the other hand, MHP-based LEDs, as an early-stage technology, present some issues and require further developments, such as higher quality of the perovskite films and higher charge injection efficiency. Finally, the long-term stability and lifetime of MHP-based LEDs are still limited to commercialization.

Thus, the MHP-based LEDs demonstrated outstanding advantages and, despite some challenges to be addressed, they can be considered valuable alternatives to the traditional LEDs, gaining merits for further study to understand their full and real potential.

## 2.3 Photocatalytic applications

The development of green and economically sustainable approaches to convert solar irradiation to chemical energy is a cornerstone challenge within the current society. Solar irradiation is by far the largest renewable source providing every year total power of about  $2 \times 10^5$  TW at the Earth's surface that it is about 6,000 times the current human consumption [186]. Semiconductor-based photocatalysis is a sustainable technology efficiently used in many processes, such as hydrogen production, CO<sub>2</sub> conversion, raw organic material transformations, and wastewater organic compound photodegradation. Different semiconductors have been studied for photocatalytic applications, but many times with a significant lack of efficiency. Photocatalytic applications are powerful tools able to convert light into available chemical energy and have currently attracted extensive scientific interest. Some of the expectations of such advantageous technology include:

- i) The conversion of sunlight directly into chemical energy using the charge carriers,



- ii) The potential of green energy production
- iii) The environmental friend degradation of undesirable pollutants.

Heterogeneous photocatalysis is a powerful and sustainable technology for energy and environmental challenges at a global level. This explains academics' interest, pushing for productive efforts, especially for commercializing such green technology. To date, MHPs, as a new generation class of cheap and easy-to-prepare semiconductors, have a relatively restricted widespread in applications concerning their potential. Indeed, MHPs have emerged as a new promising class of cheap and easy-to-make photocatalysts, even though their unstable bounds and crystal structures have restricted widespread applications. MHPs, due to their recent breakthrough as remarkable light-harvesting materials, are considered potential photocatalysts suitable for solar power conversion applications. The intensive research on MHPs led to rapid employment growth, making it one of the fastest-developed histories [180]. The advantages of MHPs include a direct band gap, efficient charge transport, long carrier lifetimes, and long charge diffusion lengths of photogenerated charges. This argument makes MHPs excellent candidates for photocatalytic applications.

Among the critical issues pressing the current era, one should mention the increasing energy demand due to population and industrialization's fast growth. Nowadays, many challenges need to be critically faced, such as the depletion of limited fossil fuel sources and the predicted climate change, mainly due to CO<sub>2</sub> emission originated from the abusing of carbon-based fuels [187]. Photovoltaic technologies, which account for about 18% of the world's energy demand, play a principal role. However, synthetic solar fuels such as hydrogen evolution reaction (HER) are considered a promising alternative. One of these technology's main advantages is their renewability and sustainability, representing a significant source from a post-fossil fuel point of view [188]. The instability towards water and moisture represented one of the significant limits in the MHP-based HER technology. To overcome the mentioned issue, the researchers focused on two main approaches: protecting the material or the medium solution's substitution. Stable MHP-based photocatalytic systems included the encapsulation or the use of capping agents on MHPs. Fusible alloys such as InBiSn may enable the use of MHPs immersed in an aqueous solution for hydrogen production [187]. A more recent report found a sandwich-like structure CH<sub>3</sub>NH<sub>3</sub>PbI<sub>3</sub>-based photocathode supported on metal foils, providing superior performance and good stability in a water medium and under continuous illumination [189]. An alternative suitable method involves H<sub>2</sub> generation from saturated halo acid solutions. The adopted approach provided an improved understanding of the photocatalytic potential of MHPs, contributing to the development of efficient solar-driven hydrogen fuel production [190].

Moreover, structural, compositional, and doping engineering have been recently widely developed to provide new strategies for modulating the photocatalytic activity of MHP hydrogen production [118,191–197]. **Table 1** reports a summary of some recent MHPs used in photocatalytic HER application compared to the TiO<sub>2</sub>, considered the most employed material in light-driven field applications [198]. The mentioned studies highlight the great potential of MHPs in promoting photocatalytic HER, opening the way for the alternative utilization of their use towards efficient solar energy conversion.

Table 1: MHPs used in photocatalytic HER

Photocatalyst	Specifics	Irradiation	Medium	Results	Ref.
$\text{CH}_3\text{NH}_3\text{PbI}_3$	Photocathode encapsulated metal alloyed layer	Solar simulator 150W, $100\text{mWcm}^{-2}$ , AM 1.5G and IR filters	aqueous electrolyte solution	Faradaic efficiency 95.1%	[187]
$\text{CH}_3\text{NH}_3\text{PbI}_3$	Sandwich-like Photocathode	Solar simulator $100\text{mWcm}^{-2}$ , AM 1.5G	phosphate buffer solution	Faradaic efficiency 100%	[189]
$\text{CH}_3\text{NH}_3\text{PbI}_3$	Pt/ $\text{CH}_3\text{NH}_3\text{PbI}_3$	Solar simulator 100W, $\lambda > 475$	hydroiodic acid solution $\text{H}_3\text{PO}_2$ stabilizer	Apparent quantum efficiency 0.81%	[190]
$\text{CH}_3\text{NH}_3\text{PbI}_3$	Pt/TiO <sub>2</sub> /MAPBI Heterojunction photocatalyst	Solar simulator 100W, AM 1.5G	hydroiodic acid solution	H <sub>2</sub> evolution apparent quantum efficiency 70% (420 nm) HI splitting efficiency 0.86%	[118]
$\text{CH}_3\text{NH}_3\text{PbI}_3$	hybridizing with Pt/Ta <sub>2</sub> O <sub>5</sub> and PEDOT:PSS nanoparticles film	Xe lamp 300 W, $150\text{mWcm}^{-2}$ , $\lambda > 420$ nm	hydroboric acid/hypophosphorous acid solution	Apparent quantum efficiency 16.4% (440 nm)	[196]
$\text{CH}_3\text{NH}_3\text{PbI}_3$	CoPi/BiVO <sub>4</sub> - $\text{CH}_3\text{NH}_3\text{PbI}_3$ architecture	Xe lamp, 300 W, $120\text{mW cm}^{-2}$ , $\lambda \geq 420$ nm	sodium sulfate/sodium sulfite phosphate buffered aqueous solution	Solar-to-hydrogen conversion efficiency of 2.5% at neutral pH	[195]
$\text{CH}_3\text{NH}_3\text{PbI}_3$	$\text{CH}_3\text{NH}_3\text{PbI}_3$ /rGO photocatalyst powder	Xe lamp, 300 W, $100\text{mWcm}^{-2}$ , AM 1.5G	hydroiodic acid solution $\text{H}_3\text{PO}_2$ stabilizer	Apparent quantum efficiency 1.40% (450 nm)	[194]
$\text{CH}_3\text{NH}_3\text{PbI}_3$	Ni <sub>3</sub> C decorated $\text{CH}_3\text{NH}_3\text{PbI}_3$	Xe lamp, 300 W, $\lambda > 420$ nm	hydroiodic acid solution $\text{H}_3\text{PO}_2$ stabilizer	Apparent quantum efficiency 16.6% (420nm), 16.5% (450nm), 14.3% (500nm)	[193]
$\text{CH}_3\text{NH}_3\text{PbI}_3$	Pt/ $\text{CH}_3\text{NH}_3\text{PbI}_3$ Photocatalyst	Solar simulator 100W, AM 1.5G	hydroiodic/hydroboric acid solution	Apparent quantum efficiency 8.10% (450 nm) HI splitting efficiency 1.06%	[192]
$\text{CsPbBr}_3$	$\text{CsPbBr}_3$ perovskite nanocrystals Ru@TiO <sub>2</sub> in toluene	Laser, 50mW, 445 nm	Triethylamine, trifluoroacetic acid	Apparent quantum efficiency about 1% (455 nm)	[197]
$\text{CsPbBr}_3$	Pt/ $\text{CH}_3\text{NH}_3\text{PbBr}_3$ Photocatalyst	Xe lamp 300 W, $\lambda > 420$ nm	aqueous hydroboric/KI solution	Apparent quantum efficiency 2.15% (450 nm)	[191]
P25 TiO <sub>2</sub> /Pt	-	250W Hg lamp (300-400 nm)	Pure water	Apparent quantum efficiency 1.40%	[198]

On the other hand, fossil fuel processing and their abuse have generated a critical amount of hazardous emissions, such as the notorious greenhouse gas CO<sub>2</sub> that heavily contributed to current climate change. About 20% of global emitted air pollution consists of CO<sub>2</sub>, resulting from the combustion of natural gas used for heating, electricity, or chemical feedstock [4,68]. Pioneering works have recently attracted remarkable attention to photocatalytic CO<sub>2</sub> conversion. The properties of MHPs have recently stimulated their employment in CO<sub>2</sub> photoreduction. As for the other technologies, the relatively low stability of MHPs at room conditions represents one of the primary limits. Structural and morphological modifications were applied to enhance the activity and selectivity of MHPs. Capping and encapsulation approaches were employed to address the stability problem. On the other hand, suitable low polar media, such as ethyl acetate, were considered to reduce the dissociation of MHPs during the reduction process. **Table 2** provides a brief overview of MHP-based photocatalytic CO<sub>2</sub> reduction compared to the more employed photocatalyst TiO<sub>2</sub> [199].

In summary, highly active MHP- and MHP-based materials have been successfully prepared as photocatalysts for the CO<sub>2</sub> reduction process, exhibiting good activity and stability and proving that this family of materials represents a promising candidate for a great range of practical applications.

Table 2: MHPs used in photocatalytic CO<sub>2</sub> photoreduction

Photocatalyst	Specifics	Irradiation	Conditions	Products	Electron consumption rate $\mu\text{mol g}^{-1} \text{h}^{-1}$	Selectivity %	Ref.
CsPbBr <sub>3</sub>	nanocrystals	Xe lamp, 300 W, AM 1.5G	ethyl acetate solution	CO, CH <sub>4</sub> , H <sub>2</sub>	20.9	99.0	[200]
CsPbBr <sub>3</sub>	nanocrystals	Xe lamp, 100 W, 150 mW cm <sup>-2</sup> , AM 1.5G	ethyl acetate solution	CO, CH <sub>4</sub> , H <sub>2</sub>	23.7	99.3	[201]
CsPbBr <sub>3</sub> /GO	CsPbBr <sub>3</sub> /GO	Xe lamp, 100 W, 150 mW cm <sup>-2</sup> , AM 1.5G	ethyl acetate solution	CO, CH <sub>4</sub> , H <sub>2</sub>	29.8	99.1	[201]
CsPb(Br <sub>0.5</sub> /Cl <sub>0.5</sub> ) <sub>3</sub>	CO <sub>2</sub> and ethyl acetate	Xe lamp, 300 W, AM 1.5G	ethyl acetate solution	CO, CH <sub>4</sub>	85.2	99.0	[202]
Cs <sub>2</sub> AgBiBr <sub>6</sub>		Xe lamp, 100 W, AM 1.5G	ethyl acetate solution	CO, CH <sub>4</sub>	17.5	100.0	[203]
CsPbBr <sub>3</sub> QDs/Pd nanosheets	CsPbBr <sub>3</sub> nanocrystal/Palladium nanosheet	Xe lamp, 150 W, visible light (>420 nm)	nonaqueous ethyl acetate	CO, CH <sub>4</sub> , H <sub>2</sub>	33.1	93.5	[204]
CsPbBr <sub>3</sub> @ZIF-8	CsPbBr <sub>3</sub> @Zeolitic Imidazolate Framework Nanocomposite	Xe lamp, 100 W, 150 mW cm <sup>-2</sup> , AM 1.5G	CO <sub>2</sub> +H <sub>2</sub> O	CO, CH <sub>4</sub>	15.5	100.0	[205]
CsPbBr <sub>3</sub>	nanocrystals	Xe lamp, 100 W, visible light (>420 nm)	CO <sub>2</sub> +H <sub>2</sub> O	CO, CH <sub>4</sub>	8.3		[205]
CsPbBr <sub>3</sub> @ZIF-8	CsPbBr <sub>3</sub> @Zeolitic Imidazolate Framework Nanocomposite	Xe lamp, 100 W, visible light (>420 nm)	CO <sub>2</sub> +H <sub>2</sub> O	CO, CH <sub>4</sub>	12.4		[205]
CsPbBr <sub>3</sub> @ZIF-67	CsPbBr <sub>3</sub> @Zeolitic Imidazolate Framework Nanocomposite	Xe lamp, 100 W, 150 mW cm <sup>-2</sup> , AM 1.5G	CO <sub>2</sub> +H <sub>2</sub> O	CO, CH <sub>4</sub>	29.6	100.0	[205]
CsPbBr <sub>3</sub> @ZIF-67	CsPbBr <sub>3</sub> @Zeolitic Imidazolate Framework Nanocomposite	Xe lamp, 100 W, visible light (>420 nm)	CO <sub>2</sub> +H <sub>2</sub> O	CO, CH <sub>4</sub>	27.5		[205]
CsPbBr <sub>3</sub>	nanocrystals	Xe lamp, 100 W, 150 mW cm <sup>-2</sup> , AM 1.5G	ethyl acetate solution	CO, CH <sub>4</sub> , H <sub>2</sub>	8.6	90.3	[206]
a-TiO <sub>2</sub> /CsPbBr <sub>3</sub>	amorphous-TiO <sub>2</sub> encapsulated CsPbBr <sub>3</sub> Nanocrystal Composite	Xe lamp, 100 W, 150 mW cm <sup>-2</sup> , AM 1.5G	ethyl acetate solution	CO, CH <sub>4</sub> , H <sub>2</sub>	64.5	95.5	[206]
CsPbBr <sub>3</sub>	CsPbBr <sub>3</sub> Nanocrystal Decorated ZnO Nanowires/Macroporous Graphene	Xe lamp, 100 W, 150 mW cm <sup>-2</sup> , AM 1.5G	Gas CO <sub>2</sub> +H <sub>2</sub> O	CO, CH <sub>4</sub>	52.0	100.0	[207]
CsPb(Br <sub>0.5</sub> /Cl <sub>0.5</sub> ) <sub>3</sub>	CO <sub>2</sub> and ethyl acetate	Xe lamp, 300 W, AM 1.5G filter	ethyl acetate solution	CO, CH <sub>4</sub>	85.2	99.0	[202]

CsPbBr <sub>3</sub> -Ni(tpy)	CsPbBr <sub>3</sub> Perovskite Nanocrystals by Immobilizing Metal Complexes	Xe lamp, 300 W, visible light $\lambda > 400$ nm, 100 mW cm <sup>-2</sup> ,	ethyl acetate/water	CO, CH <sub>4</sub>	1252.0	100.0	[208]
CsPbBr <sub>3</sub>	nanocrystals	Xe lamp, 300 W, 100 mW cm <sup>-2</sup> , AM 1.5G	Gas CO <sub>2</sub> +H <sub>2</sub> O	CO, CH <sub>4</sub> , H <sub>2</sub>	8.1	99.5	[204]
Cu/CsPbBr <sub>3</sub> @rGO	Cu-loaded reduced graphene oxide (Cu-RGO)	Xe lamp, 300 W, 100 mW cm <sup>-2</sup> , AM 1.5G	Gas CO <sub>2</sub> +H <sub>2</sub> O	CO, CH <sub>4</sub> , H <sub>2</sub>	103.0	98.5	[204]
CsPbBr <sub>3</sub> QDs/PCN	CsPbBr <sub>3</sub> perovskite quantum dots on porous g-C <sub>3</sub> N <sub>4</sub>	Xe lamp, 150 W, AM 1.5G	acetonitrile/water	CO	297.8	100.0	[209].
CsPbBr <sub>3</sub> QDs /UiO- 66(NH <sub>2</sub> )	Perovskite-type CsPbBr <sub>3</sub> quantum dots/UiO-66(NH <sub>2</sub> ) nanojunction	Xe lamp, 300 W, $\lambda$ >400 nm	ethyl acetate/water	CO, CH <sub>4</sub>	18.5	100.0	[210]
MAPbI <sub>3</sub> QDs/Fe- MOF	Perovskite Quantum Dots in Iron- Based Metal–Organic Frameworks (MOFs)	Xe lamp, 300 W, 100 mW cm <sup>-2</sup> , $\lambda$ >420 nm	ethyl acetate/water	CO, CH <sub>4</sub>	112.0	100.0	[211]
TiO <sub>2</sub> P25	-	Xe lamp, 100 W	Gas CO <sub>2</sub> +H <sub>2</sub> O	-	10.0	56.0	[199]
TiO <sub>2</sub> P25	-	Xe lamp, 100 W	Solution H <sub>2</sub> O	-	13.0	19.0	[199]

The sunlight power as a unique natural energy resource has increased researchers' interest in many fields beyond the HER or CO<sub>2</sub> reduction processes. A visionary idea has recently addressed the employment of sustainable photocatalytic technology in organic synthesis. Photocatalytic organic synthesis aims to replace traditional hazardous processes with sustainable and energy-efficient methods to reduce toxic chemicals to minimize the final residues and by-products. Recent reviews have highlighted the green aspects expected by synthetic organic photochemistry, recognizing the economic and ecological benefits achievable in the industrial field with the potential for the large-scale production of fine chemicals [212–214].

Recent literature has reported remarkable results, with extraordinary and unexpected results in MHP-based photocatalytic organic synthesis under visible light [215–219]. An exciting advantage of the use of MHPs includes the variants that were reported for many photocatalytic transformations using both HOIPs [220] and all-inorganic MHPs [216,217]. In particular, the most impressive results have been achieved with lead-free Cs<sub>3</sub>Bi<sub>2</sub>Br<sub>9</sub> photocatalyst that exhibited good stability and excellent conversion, mainly ascribed to the combination of the photocatalytic ability and the presence of suitable Lewis-acidic centers on the surface of the bismuth-based material [216]. MHPs were directly employed in organic solvents showing high efficiency on  $\alpha$ -alkylation of aldehydes under the irradiation of a single-wavelength blue LED light [218]. The main advantages recorded in the MHPs-based photocatalytic synthesis are the requirement of only readily available and cheap non-noble materials, the high catalytic activity, the simple preparation of the catalysts, the potential activation of a broader range of organic substrates due to easy band edge-tuning, and the employment at room condition without the necessity of further parameters control. The environmental benefit achievable by employing MHP-based photochemical synthesis represents a hot topic in the current academic field.

**Table 3** summarized some of the most recent works on MHP-based photocatalytic organic synthesis.

Table 3: MHPs used in photocatalytic organic synthesis

Photocatalyst	Irradiation	Photocatalytic Reaction	Conversion %	Ref.
FAPbBr <sub>3</sub>	Simulated solar lamp, AM1.5G	oxidation of benzylic alcohol	15	[220]
nano-FAPbBr <sub>3</sub>	Simulated solar lamp, AM1.5G	oxidation of benzylic alcohol	11	[220]
FAPbBr <sub>3</sub> /TiO <sub>2</sub>	Simulated solar lamp, AM1.5G	oxidation of benzylic alcohol	63	[220]
FAPbBr <sub>3</sub> /SiO <sub>2</sub>	Simulated solar lamp, AM1.5G	oxidation of benzylic alcohol	13	[220]
FAPbBr <sub>3</sub> /TiO <sub>2</sub>	Simulated solar lamp, $\lambda > 500$ nm	oxidation of benzylic alcohol	13	[220]
CsPbI <sub>3</sub>	Vis LED 420-700 nm	thiophenol coupled to disulfide	58	[215]
CsPbBr <sub>3</sub>	Vis LED 420-700 nm	thiophenol coupled to disulfide	98	[215]
CsPbBr <sub>2</sub> Cl	Vis LED 420-700 nm	thiophenol coupled to disulfide	98	[215]
CsPbBr <sub>0.5</sub> Cl <sub>0.5</sub>	Vis LED 420-700 nm	thiophenol coupled to disulfide	68	[215]
CsPbBrCl <sub>2</sub>	Vis LED 420-700 nm	thiophenol coupled to disulfide	35	[215]
CsPbCl <sub>3</sub>	Vis LED 420-700 nm	thiophenol coupled to disulfide	12	[215]
CsPbCl <sub>3</sub>	UV LED max 400 nm	thiophenol coupled to disulfide	93	[215]
CsPbCl <sub>3</sub> + Br <sub>2</sub>	Vis LED 420-700 nm	thiophenol coupled to disulfide	62	[215]
Cs <sub>3</sub> Bi <sub>2</sub> Br <sub>9</sub>	visible light $\geq 420$ nm	alcoholysis of styrene oxide in IPA	> 99	[216]
Cs <sub>3</sub> Bi <sub>2</sub> Br <sub>9</sub>	visible light $\geq 420$ nm	alcoholysis of styrene oxide in IPA	> 99	[216]
CsPbI <sub>3</sub>	visible light $\geq 495$ nm	polymerization of 3,4-ethylenedioxythiophene	32.6	[217]
CsPbBr <sub>3</sub>	Blue LED 455 nm	$\alpha$ -alkylation of aldehydes	> 99	[218]
CsPbBr <sub>3</sub> NCs	Blue LED 12 W 455 nm	synthesis aldehyde	85	[219]
CsPbBr <sub>3</sub> NCs	Blue LED, 12W, 455 nm	synthesis tertiary amines	90	[219]
CsPbBr <sub>3</sub> NCs	Blue LED, 12W, 455 nm	cyclization of benzaldehyde phenylhydrazone	88	[219]
MAPbBr <sub>3</sub>	Blue LED, 12W, 455 nm	cyclization of benzaldehyde phenylhydrazone	75	[219]
CsPbBr <sub>3</sub> NCs	Blue LED, 12W, 455 nm	cyclization of ethyl (Z)-3-phenyl-3-(phenylamino)acrylate	93	[219]
MAPbBr <sub>3</sub>	Blue LED, 12W, 455 nm	cyclization of ethyl (Z)-3-phenyl-3-(phenylamino)acrylate	65	[219]
CsPbBr <sub>3</sub> NCs	Blue LED, 12W, 455 nm	coupling of benzoic acid with 4-bromotrifluorobenzene	78	[219]
CsPbBr <sub>3</sub>	Blue LED, 4.6 W	photopolymerized styrene	12	[221]

Increasing human industrial, agricultural, and municipal activities have alarmingly increased hazardous pollution in the environment. Uncontrolled industrialization has introduced numerous new contaminants that have become challenging to remove with the currently available technologies. Moreover, nearly a third of the worldwide population is estimated to lack safe drinking water access. The mentioned deficiency is mainly addressed to developing and less populated regions, but a critical future of urban water treatment systems was also recognized in developed countries [222]. Usually, municipal drinking water and wastewater are treated in centralized facilities, and then they are transported through large and old pipe networks. Therefore, beyond the pollution coming from the industrial and personal care product effluents, the aging infrastructure and the limited resiliency against the current growing population is challenging the wastewater facilities.

Moreover, unsuitable implementation in isolated communities needs shifts towards decentralized treatments with a smaller-scale approach, closer to the point of consumption. From this perspective, heterogeneous photocatalysis is a suitable option to address the previously presented management and practical issues. For example, photocatalytic-based wastewater treatments may enable the development of highly effective materials capable of a large variety of pollutant degradation under light irradiation. In particular, this technology produces strong oxidizing species (such as reactive oxygen species (ROS)) capable of degrading toxic organic pollutants, non-biodegradable matter, and recalcitrant residues in ambient conditions. Moreover, this application may reduce the costs of energy demands, employing modular target systems; thus, it can satisfy specific needs for water supply, the wastewater treatment plants, and the final users. MHPs can be considered a promising material among the different photocatalysts because of their efficient light-absorption performance, high catalytic efficiency, structural simplicity, and flexibility. To date, only a few studies have reported the use of MHPs for wastewater treatments. Generally, this is mainly due to their relative environmental instability, especially in water mediums. However, two considerations should be considered to supplement our understanding of the importance of current research. First, successful methods were previously presented to overcome the environmental instability of MHPs, such as capping agents, encapsulation, and coupled-materials systems with stable bonds [223]. Secondly, MHP-based photocatalytic applications for organic pollutant degradation are in their very early stages, and many developments are expected in the future. The MHPs-based photocatalysts for organic contaminants lead to remarkable results due to the visible light absorption ability, remarkable charge transport, and reduced recombination rate of the photogenerated electrons and holes. In general, due to the environmental stability, all-inorganic MHPs [114,224–228] have been preferred to HOIPs [229,230] because the organic fraction may induce the instability of the overall systems.

Moreover, the combination of MHPs in heterogeneous systems showed an enhancement in the degradation efficiency due to the increased separation of photogenerated charge carriers [116,225]. Nowadays, the approach of MHPs and MHP-based photocatalysts for organic pollutant degradation is in its early stage. However, the preliminary results seem to provide great promises for future developments.

**Table 4** briefly summarizes some of the recent applications of MHP-based materials for photocatalytic organic contaminant degradation.



Table 4: MHPs used in photocatalytic wastewater treatments

Photocatalyst	Specifics	Pollutant	Irradiation	Ref.
TiCdI <sub>3</sub>	nanoparticles	methylene blue dye	UV Light	[224]
CsSnBr <sub>3</sub>	all-inorganic perovskite	crystal violet dye	Visible-Light	[227]
CsSnBr <sub>3</sub>	all-inorganic perovskite	methyl orange dye	500 W Xe lamp, visible light	[226]
CsPbCl <sub>3</sub>	quantum dots	methyl orange dye	500 W Xe lamp, visible light	[226]
CsPbBr <sub>3</sub>	quantum dots	tetracycline hydrochloride in ethanol	300 W Xe lamp, 420 nm cut-off filter	[114]
CsPbBr <sub>3</sub>	quantum dots	tetracycline hydrochloride in water	300 W Xe lamp, 420 nm cut-off filter	[114]
CsPbBr <sub>3</sub>	quantum dots	tetracycline hydrochloride in isopropanol	300 W Xe lamp, 420 nm cut-off filter	[114]
CsPbBr <sub>3</sub>	quantum dots	methyl orange dye in ethanol	300 W Xe lamp, 420 nm cut-off filter	[114]
OHNH <sub>3</sub> PbI <sub>2</sub> Cl	hybrid organic-inorganic MHPs	dye Direct Yellow 27	Solar light lamp	[229]
OHNH <sub>3</sub> PbCl <sub>3</sub>	hybrid organic-inorganic MHPs	dye Direct Yellow 27	Solar light lamp	[229]
Cs <sub>3</sub> Bi <sub>2</sub> I <sub>9</sub> -OA		methylene blue in water	Visible light lamp	[225]
Cs <sub>3</sub> Bi <sub>2</sub> I <sub>9</sub> -OA/Ag <sub>2</sub> S	heterostructure	methylene blue in water	Visible light lamp	[225]
Cs <sub>3</sub> Bi <sub>2</sub> I <sub>9</sub> -OA/TiO <sub>2</sub>	heterostructure	methylene blue in water	Visible light lamp	[225]
Cs <sub>3</sub> Bi <sub>2</sub> Br <sub>9</sub> -OA	heterostructure	methylene blue in water	Visible light lamp	[225]
Cs <sub>3</sub> Bi <sub>2</sub> Br <sub>9</sub> -OA/Ag <sub>2</sub> S	heterostructure	methylene blue in water	Visible light lamp	[225]
Cs <sub>3</sub> Bi <sub>2</sub> Br <sub>9</sub> -OA/TiO <sub>2</sub>	heterostructure	methylene blue in water	Visible light lamp	[225]
Cs <sub>3</sub> Bi <sub>2</sub> Br <sub>9</sub>	nanoparticles	methylene blue in isopropanol	Visible light lamp	[225]
Cs <sub>3</sub> Bi <sub>2</sub> Br <sub>9</sub> -OA NCs	heterostructure	methylene blue in isopropanol	Visible light lamp	[225]
IO-CsPbBr <sub>3</sub>	Inverse Opal Structured perovskite	Rhodamine 6G	Solar light lamp (AM 1.5)	[228]
Cs <sub>3</sub> Bi <sub>2</sub> I <sub>9</sub> perovskite on UV100-TiO <sub>2</sub>	heterostructure	Methanol	LED 455nm lamp	[116]
(CH <sub>3</sub> NH <sub>3</sub> ) <sub>3</sub> Bi <sub>2</sub> I <sub>9</sub>	hybrid organic-inorganic MHPs	Rhodamine B	150 W Halogen lamp, visible light	[230]
(CH <sub>3</sub> NH <sub>3</sub> ) <sub>3</sub> Bi <sub>2</sub> I <sub>9</sub>	hybrid organic-inorganic MHPs	Rhodamine B	LED Visible light lamp	[230]

---

$(\text{CH}_3\text{NH}_3)_3\text{Bi}_2\text{I}_9$	hybrid organic-inorganic MHPs	Methylene Blue	150 W Halogen lamp, Visible light	[230]
$(\text{CH}_3\text{NH}_3)_3\text{Bi}_2\text{I}_9$	hybrid organic-inorganic MHPs	Reactive Blue	150 W Halogen lamp, Visible light	[230]
$(\text{CH}_3\text{NH}_3)_3\text{Bi}_2\text{I}_9$	hybrid organic-inorganic MHPs	Mix Crystal violet – Methylene Blue	150 W Halogen lamp, Visible light	[230]

---

## 2.4 Current limitations and future prospective

The past years have witnessed a phenomenal rapid development of MHP-based light-driven applications. The remarkable performance achieved can be ascribed to their suitable band gaps and strong absorption coefficients, matching the visible portion of the solar spectrum, high charge carrier mobility, long photogenerated carrier lifetime, and diffusion. This research study focused attention on the potential of this new generation class of materials in photocatalytic processes, aware of the remarkable results and fast development achieved in traditional applications such as solar cells and LEDs. Several promising approaches have been identified to overcome some of the limits in MHP-based photocatalysis. First, in future research, the improvement for long-term catalytic cycling and operational stability of MHPs should be addressed. Partial or total substitution of Pb in B-site with similar medium-sized metallic particles (such as Sn and Bi) seemed to maintain similar performances with an increase in environment stability without compromising efficiency. Doping methods were also recognized as beneficial to provide higher stability in MHP structures, beneficially enhancing the interaction between the ions and the crystal frame. Capping layers or encapsulation methods can limit contact of the MHPs with the solvent, providing resistance toward material degradation. The design of suitable chemical structures and engineering device architectures have also gained significant attention to provide higher stability to MHP-based devices.

Furthermore, these approaches can facilitate charge carrier separation and transportation, increasing the overall system's performance. Reactions in halo acids or solutions with relatively low polarity provided useful alternatives to overcome the instability of MHPs towards the water, particularly in HER processes. Second, new strategies to improve the photocatalytic efficiency of MHP are also fundamental. Higher photocatalytic efficiency was recorded using composite systems. However, there are several alternatives to increase MHP photocatalysis activity, such as metal-based co-catalysts to accelerate the surface reaction rate, nanostructure morphologies such as nano-sheet nano-platelets to increase the surface area and density of reaction sites, and novel heterojunctions to enhance charge separation. The organic chemistry field seems beneficial to enlarge the target raw organic material transformations and develop new chemical reactions. The previously reported MHP-based transformations appeared to be relatively narrow in comparison to most employed semiconductor photocatalysts. For example, extended reactions by combining MHPs with other materials seemed a promising approach for high value-added organic syntheses.

Moreover, high specificity and selectivity is a further promising direction to enhance MHP-based photo-redox catalysis applications. Finally, the improvement of the redox abilities of MHP-based photocatalysts is a required future challenge. The relatively narrow band gaps of MHPs may result in relatively weak redox abilities specifically related to the VB edge and low oxidation efficiency. New photocatalytic reactions, such as water oxidation or volatile organic compound mineralization, may also represent new potential MHP-based applications. Combining other semiconductors can be considered a potential pathway to enhance the light absorption and redox ability of MHPs. Alternatively, encapsulating the perovskite layer in a solar cell architecture with applied voltage can enhance the redox ability of MHP-based photocatalysts.

In conclusion, the introduction of MHP-based photocatalysts in practical applications is far from optimal, and, to date, it is limited to the current energy demand and environmental issues. However, the revised state-of-the-art demonstrates that MHPs represent an emerging material for several light-driven technologies. One definitively holds strong motives to consider MHPs as new generation materials due to their easy preparation, low-cost materials processing, and remarkable optical, electrochemical, and photo-physical properties. Despite the relatively early stage of discovery, the field of MHP-photocatalysts is highly promising, and this research work is intended to be a preliminary guide to study their potential.



## 3 Materials and Methods

### 3.1 Synthesis

#### 3.1.1. Hybrid organic-inorganic perovskites (HOIPs)

Hybrid organic-inorganic perovskite is easy with a reproducible, one-step, solvothermal method. The organic precursor, methylammonium iodide ( $\text{CH}_3\text{NH}_3\text{I}$ ), was synthesized by mixing methylamine ( $\text{CH}_3\text{NH}_2$ ) and hydrogen iodide (HI) for two hours in an ice bath at  $0\text{ }^\circ\text{C}$ . After the solution evaporation at  $50\text{ }^\circ\text{C}$ , the solid was recovered and washed with diethyl ether to remove the residues and dried on a hot plate. The organic precursor was mixed in about in an organic solvent ( $\gamma$ -butyrolactone or N, N-dimethylformamide) with the selected iodide ( $\text{PbI}_2$  or  $\text{BiI}_3$ ) at  $60\text{ }^\circ\text{C}$  until evaporation, and finally ground to obtain a homogenous powder. In **Paper I** and **Paper II**, methylammonium iodide ( $\text{CH}_3\text{NH}_3\text{I}$ ) was selected as an organic precursor because, according to the literature, its radius was structurally more suitable, resulting in low packing symmetry [231]. The lead was selected as iodide, due to the previously reported harvesting performance and efficiency achieved in the photovoltaic field [232]. The IV group elements of the periodic table, starting from Pb to Ge, generally showed lower stability in the divalent oxidation state, leading to a decrease in band gap value combined with reduced inert electron pair effects [233].  $\text{CH}_3\text{NH}_3\text{PbI}_3$  demonstrated great harvesting ability, but, unfortunately, its low humidity stability can lead to the leaching of  $\text{Pb}^{2+}$ , as a toxic bioavailable cation, making it disadvantageous for many applications, before further protection of the particles. On the contrary, bismuth-based HOIPs can be suitable candidates as photocatalysts for environmental stability [234]. For this reason, hybrid organic-inorganic methylammonium iodobismuthate perovskite ( $\text{CH}_3\text{NH}_3$ ) $_3\text{Bi}_2\text{I}_9$  was synthesized and applied as a visible light photocatalyst (**Paper II**).

#### 3.1.2. All-inorganic MHPs

Hybrid organic-inorganic halide perovskites demonstrated promising results as visible light photocatalysts. However, the relatively low water stability and possible decomposition due to the labile organic components usually required further modification to provide efficient environmental remediation materials. All-inorganic MHPs have recently gained attention as potential alternatives, partially solving the stability and toxicity issues related to lead-based HOIPs [235,236]. Recently, replacing the organic cation by cesium,  $\text{Cs}^+$ , to form completely inorganic perovskite structure resulted materials with light harvesting efficiencies as high as those of the analogous HOIP ones, solving both the stability and toxicity [235,236].

Cesium bismuth iodide ( $\text{Cs}_3\text{Bi}_2\text{I}_9$ ), selected for its low toxic and environmental stability, was tested as a promising visible light photocatalyst (**Paper III**). All-inorganic  $\text{Cs}_3\text{Bi}_2\text{I}_9$  perovskite was synthesized by mixing cesium and bismuth iodides using dimethylformamide as an organic solvent at  $60\text{ }^\circ\text{C}$ . After the solvent's complete evaporation, the recovered solid was washed with diethyl ether to remove the organic residues. The sample was dried and finally ground in a mortar to obtain a fine homogenous powder.

### 3.1.3. MHP-based composites

TiO<sub>2</sub> is the most investigated photocatalyst due to its advantageous properties, such as oxidative efficiency, chemical stability, nontoxicity, and low cost [237,238]. However, its photocatalytic ability can be improved due to slow catalytic reactions and low visible light absorption [239]. In particular, TiO<sub>2</sub> exhibits a wide band gap ( $E_g \cong 3.2$  eV), thus only UV or higher-energy photons are effective, accounting for only 5% of the total solar radiation energy [40]. Moreover, charge generation and separation efficiency are still considered limiting factors, leading to a fast recombination rate of the photogenerated charge carriers and low photocatalytic efficiency [237]. The increase in photocatalytic activity and the extension of the light absorption range of TiO<sub>2</sub> represents a current challenge in the academic field. Recently, semiconductor heterostructures have been investigated for their ability to enhance the separation efficiency of photogenerated charges [240]. In a heterostructure configuration, band bending may induce the photogenerated charge carriers to migrate from one semiconductor to the other, resulting in more efficient separation of charges. The former mechanism can reduce the recombination rate of electrons and holes, increasing the charge carrier lifetime and finally improving photocatalytic efficiency [241]. Moreover, the coupled optoelectric properties can further extend the light-harvesting range and efficiency, improving solar energy utilization [242].

In this study, all-inorganic MHPs, Cs<sub>3</sub>Bi<sub>2</sub>I<sub>9</sub>, and anatase-TiO<sub>2</sub> (UV100) were combined in a heterostructured material for photocatalytic applications (Paper IV). The Cs<sub>3</sub>Bi<sub>2</sub>I<sub>9</sub>:TiO<sub>2</sub> composite was synthesized by applying a simple impregnation method. The solids were prepared in deionized water under sonication. The obtained powder was recovered from the suspension by centrifugation and calcined at 400 °C for 4 hours. Before the characterization, the material was ground in a fine and homogenous powder. The relationship between aggregation, agglomeration, and photocatalytic activity was studied employing four different weight ratios of the pristine materials. **Figure 16** shows a simple scheme of applied synthesis.

Graphitic carbon nitride (g-C<sub>3</sub>N<sub>4</sub>) has recently been a hot spot for intensive investigation as a potential material for sustainable energy conversion and photocatalytic applications [243]. Moreover, remarkable scientific efforts have been made to combine this carbon-based material with other semiconductors to fabricate nanocomposites with excellent visible light photocatalytic performance for environmental remediation [244]. In this study, an all-inorganic MHP was combined with g-C<sub>3</sub>N<sub>4</sub> in different ratios to evaluate the potential increase in photocatalytic ability (Paper V). In the preparation method of the composite, the g-C<sub>3</sub>N<sub>4</sub> sheets were dispersed in hexane under ultra-sonication. Afterward, Cs<sub>3</sub>Bi<sub>2</sub>I<sub>9</sub> was added, in different loads, to the suspension and ultra-sonicated for about half an hour. The material was collected by centrifugation and dried at 40 °C. **Figure 16** shows a simple scheme of syntheses. **Table 5** shows a summary of the prepared materials investigated in the next chapters.

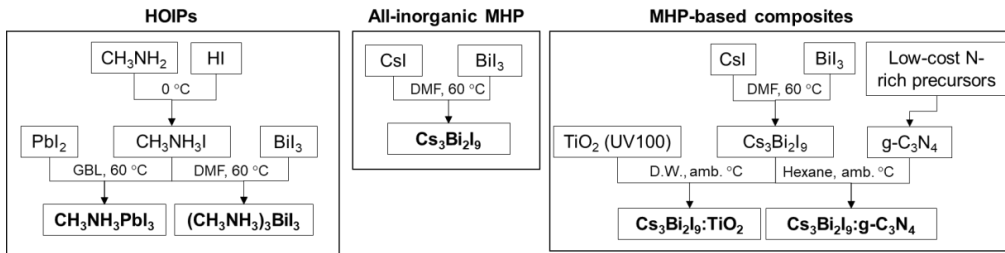


Figure 16: Schemes of the synthesis of the prepared materials.

Table 5: Summary of the as-prepared materials.

Metal Halide Perovskite	Photocatalyst	Organic precursor	Inorganic precursor	Solvent	Paper
HOIP	$\text{CH}_3\text{NH}_3\text{PbI}_3$	$\text{CH}_3\text{NH}_2$	$\text{PbI}_2$	GBL	Paper I
		HI			
Inorganic MHP	$(\text{CH}_3\text{NH}_3)_3\text{BiI}_9$	$\text{CH}_3\text{NH}_2$	$\text{BiI}_3$	DMF	Paper II
		HI			
MHP-based composites	$\text{Cs}_3\text{Bi}_2\text{I}_9$	-	CsI	DMF	Paper III
			$\text{BiI}_3$		
MHP-based composites	$\text{Cs}_3\text{Bi}_2\text{I}_9:\text{TiO}_2$	-	$\text{Cs}_3\text{Bi}_2\text{I}_9$	DI water	Paper IV
			$\text{TiO}_2$ Hombikat UV100		
MHP-based composites	$\text{Cs}_3\text{Bi}_2\text{I}_9:\text{g-C}_3\text{N}_4$	-	$\text{Cs}_3\text{Bi}_2\text{I}_9$	Hexane	Paper V

## 3.2 Characterization

### 3.2.1. Structural and morphological characterization

X-ray diffraction (XRD) was used to analyze the materials' structure to identify the samples' crystalline phases and reveal their chemical composition. **Figure 17a, b,** and **c** present the collected XRD patterns of the bare MHPs. The results were supplemented by comparison to the available literature, leading to the successful preparation of  $\text{CH}_3\text{NH}_3\text{PbI}_3$  [245],  $(\text{CH}_3\text{NH}_3)_3\text{BiI}_9$  [246], and  $\text{Cs}_3\text{Bi}_2\text{I}_9$  [247].

In **Papers I-II-III**, the analyses are reported in detail. The novel composites (i.e.,  $\text{TiO}_2$  and  $\text{g-C}_3\text{N}_4$ ), with different molar ratios of MHPs showed a consistent change in the structure of the XRD patterns, respectively, in  $\text{Cs}_3\text{Bi}_2\text{I}_9:\text{TiO}_2$  (UV100) (**Figure 17d**) and  $\text{Cs}_3\text{Bi}_2\text{I}_9:\text{g-C}_3\text{N}_4$  (**Figure 17e**). See **Papers IV-V** for further details.



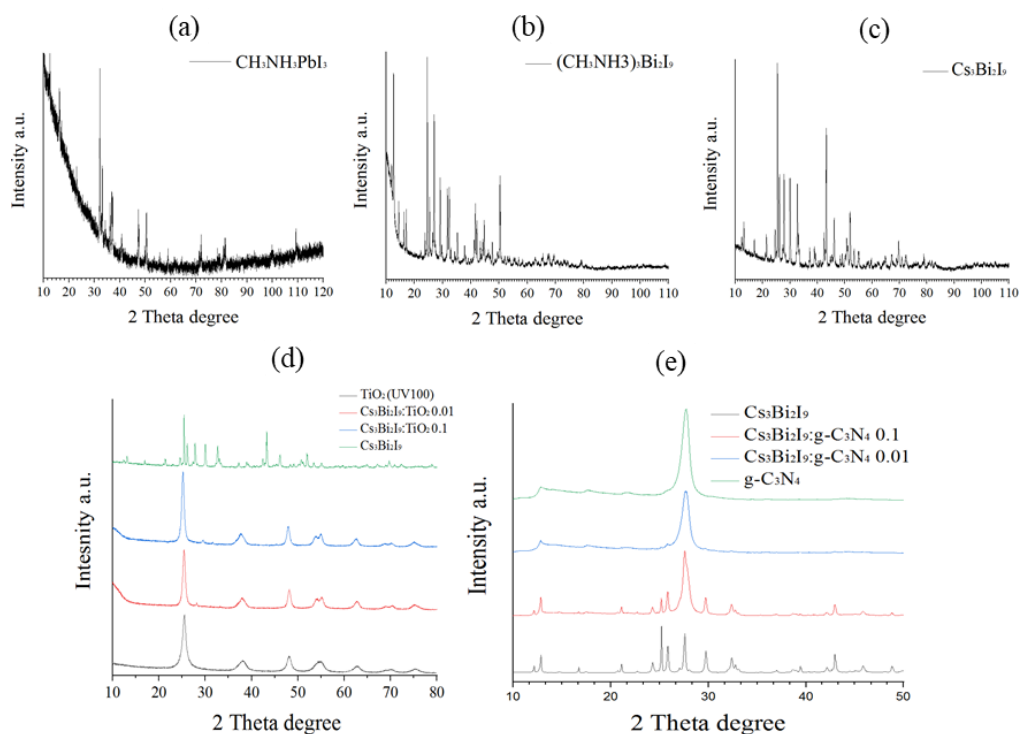


Figure 17: XRD spectra of (a)  $\text{CH}_3\text{NH}_3\text{PbI}_3$ , (b)  $(\text{CH}_3\text{NH}_3)_3\text{BiI}_3$ , (c)  $\text{Cs}_3\text{Bi}_2\text{I}_9$ , (d)  $\text{Cs}_3\text{Bi}_2\text{I}_9:\text{TiO}_2$ , and (e)  $\text{Cs}_3\text{Bi}_2\text{I}_9:\text{g-C}_3\text{N}_4$ .

The morphological characterizations of the prepared materials were carried out using scanning electron microscopy (SEM), respectively, for  $\text{CH}_3\text{NH}_3\text{PbI}_3$  (**Figure 18a**),  $(\text{CH}_3\text{NH}_3)_3\text{BiI}_3$  (**Figure 18b**), and  $\text{Cs}_3\text{Bi}_2\text{I}_9$  (**Figure 18c**). SEM analyses provided insights into the morphological properties, including the particle size, crystallinity, and homogeneity in shape and size in the powdered samples. The bare MHPs crystallized well, maintaining a homogenous distribution of the size of the particles. Particle size distribution measurements were found to be in the order of nanometres for  $\text{CH}_3\text{NH}_3\text{PbI}_3$ , micrometers for  $(\text{CH}_3\text{NH}_3)_3\text{BiI}_3$ , and  $\text{Cs}_3\text{Bi}_2\text{I}_9$ . Energy-dispersive X-ray spectroscopy (EDX) was applied to investigate the elemental analysis and the samples' chemical characterization (**Figure 18d-f**), confirming the successful synthesis. Further details are presented in **Papers I-III**.

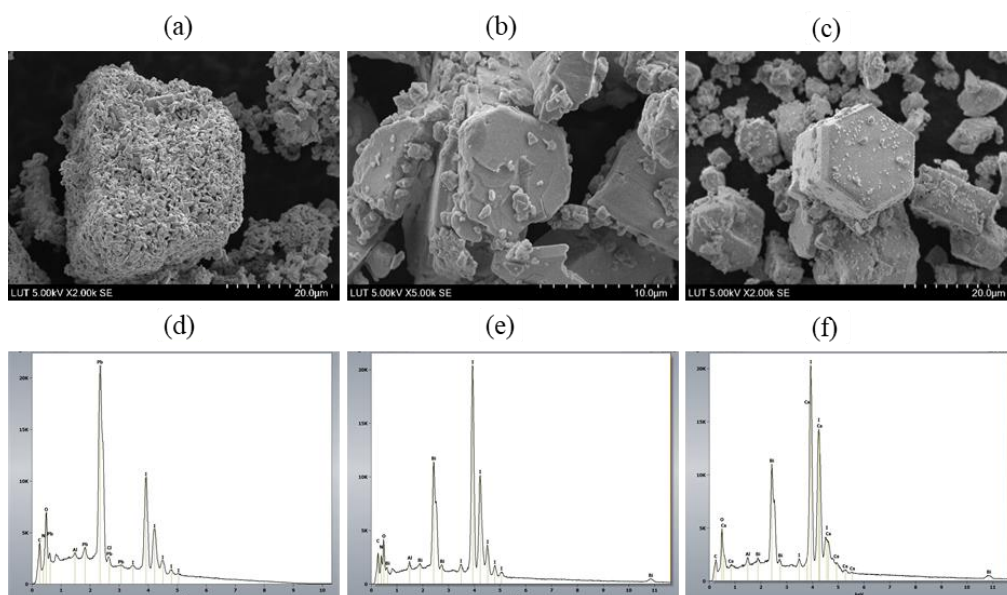


Figure 18: SEM and EDX analyses for (a,d)  $\text{CH}_3\text{NH}_3\text{PbI}_3$ , (b,e)  $(\text{CH}_3\text{NH}_3)_3\text{BiI}_3$ , and (c,f)  $\text{Cs}_3\text{Bi}_2\text{I}_9$ .

The SEM images of the  $\text{Cs}_3\text{Bi}_2\text{I}_9$ : $\text{TiO}_2$  composite are shown in **Figure 19a**.  $\text{TiO}_2$  (Hombikat UV100) exhibited a narrow range of homogeneous particles in shape and size, with a surface rich in pores. The high specific surface area of  $\text{TiO}_2$ , as found in Brunauer–Emmett–Teller measurements (BET), can facilitate the implant of functional species on its surface. The presence of  $\text{Cs}_3\text{Bi}_2\text{I}_9$  on the surface of  $\text{TiO}_2$  was revealed by enhancement in the samples' roughness.

Transmission electron microscopy (TEM) was employed to confirm that the single components exhibited similar precursors' morphology, remaining unchanged after the treatment in the organic solvent (**Figure 19b**). The different lattice fringes of the MHPs on the UV100 revealed the formation of the target composite. EDX results confirmed the coexistence of  $\text{TiO}_2$  and  $\text{Cs}_3\text{Bi}_2\text{I}_9$  without exhibiting any remarkable contamination by other chemical species (**Figure 19c**). For further details, see **Paper IV**.

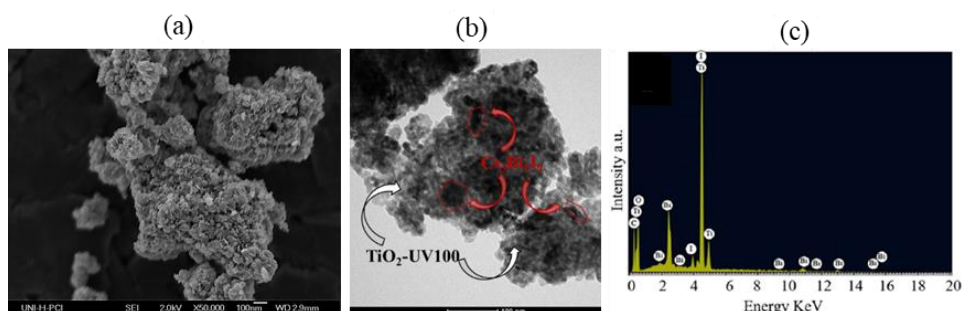
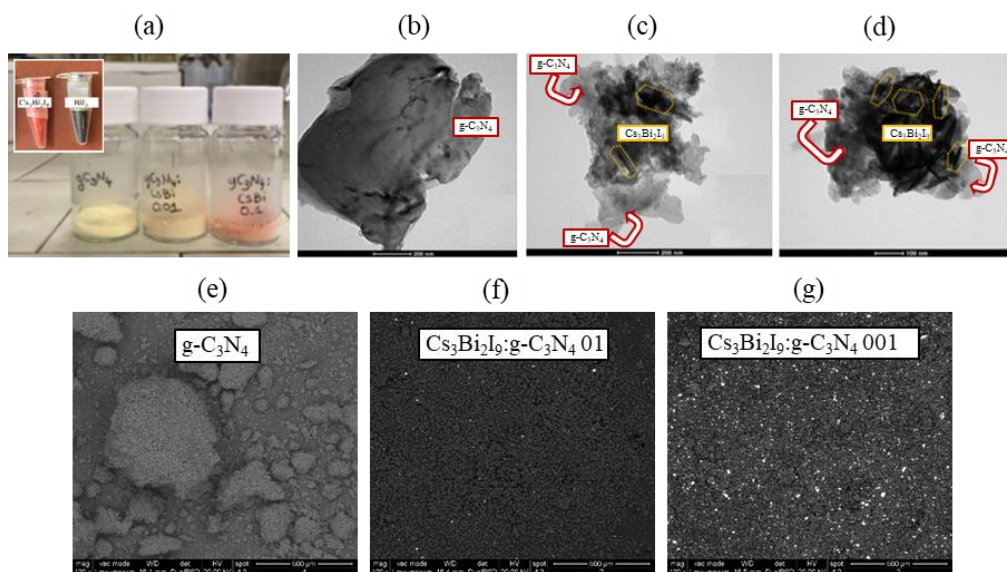


Figure 19: (a) SEM image, (b) TEM image, and (c) EDX analysis for  $\text{Cs}_3\text{Bi}_2\text{I}_9$ : $\text{TiO}_2$ .

Photograph of g-C<sub>3</sub>N<sub>4</sub> and composites prepared with different amounts of 0.1 and 0.01% of MHPs are presented in **Figure 20a**. It shows the change in the colour of the original carbon-based material that is usually light yellow. After the composition, the colour turned into purple, accordingly with the presence of Cs<sub>3</sub>Bi<sub>2</sub>I<sub>9</sub>. The interfacial interactions between g-C<sub>3</sub>N<sub>4</sub> and MHPs in the Cs<sub>3</sub>Bi<sub>2</sub>I<sub>9</sub>:g-C<sub>3</sub>N<sub>4</sub> composite were confirmed by TEM analysis (**Figure 20b-d**). The pristine materials' structures were maintained: the layered sheets of g-C<sub>3</sub>N<sub>4</sub> and the hexagonal configuration of the Cs<sub>3</sub>Bi<sub>2</sub>I<sub>9</sub>, indicating negligible changes after the solvent treatment. The smooth surface of the Cs<sub>3</sub>Bi<sub>2</sub>I<sub>9</sub> particles, about 45–50 nm in size, became rougher after anchoring the carbon-based sheets. The different lattice fringes detected between the materials confirmed the successful formation of the target composite.

Moreover, environmental-SEM (ESEM) analyses were performed for further morphological information on the samples. Back-scattered electrons were used in analytical SEM because the signal's intensity is strongly related to the element's atomic weight in the specimen. The presence of the two materials was confirmed: the higher molecular weight material in a lighter color, (Cs<sub>3</sub>Bi<sub>2</sub>I<sub>9</sub>), and the lower, (g-C<sub>2</sub>N<sub>4</sub>), in a darker color (**Figure 20e-g**), a further demonstration of the successful synthesis. Finally, EDX analysis confirmed the nature of the darker spots, carbon, nitrogen, and the lighter spots, bismuth, and iodine (**Figure 20h**). For further details, see **Paper V**.



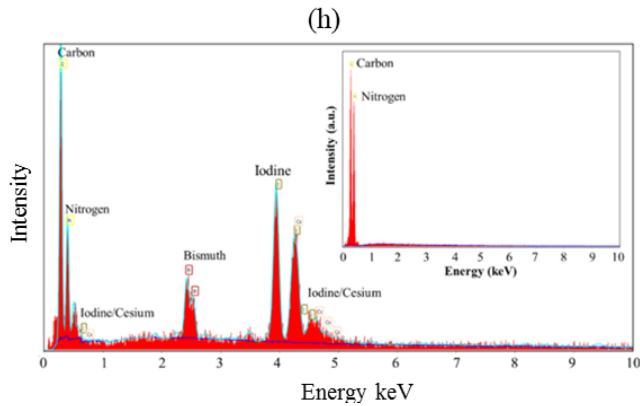
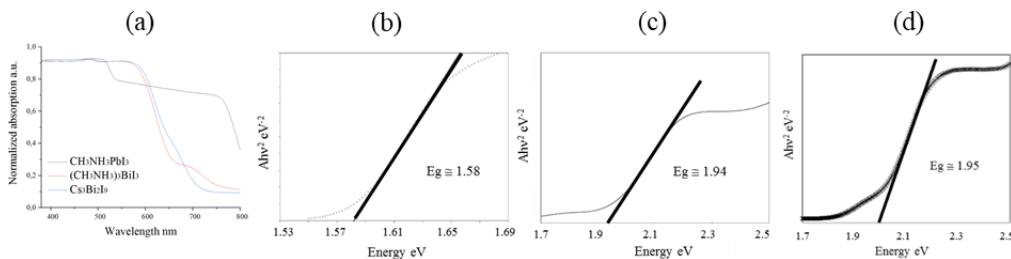


Figure 20: (a) Powders photographs, (b-d) TEM images, (e-g) ESEM images, and (h) EDX analysis for  $\text{Cs}_3\text{Bi}_2\text{I}_9\text{:g-C}_3\text{N}_4$ .

### 3.2.2. Optical and electrochemical characterization

Differential reflectance spectroscopy (DRS) is a well-known surface analytical technique to evaluate irradiation light and solid photocatalysts' interaction, revealing the samples' harvesting abilities. In general, all MHP-based photocatalysts show an excellent ability to harvest visible light (**Figure 21a**). Absorption spectra were measured in the visible range, from 380 nm to 800 nm, demonstrating multi-absorption phenomena due to multi-absorption effects [248]. The absorption spectra of the samples were processed with the Kubelk-Munk model to reveal the values of the band gaps of  $\text{CH}_3\text{NH}_3\text{PbI}_3$  ( $\text{CH}_3\text{NH}_3$ ) $_3\text{BiI}_3$ , and  $\text{Cs}_3\text{Bi}_2\text{I}_9$ , respectively equal to 1.58 eV (**Figure 21b**), 1.94 eV (**Figure 21c**), and 1.95 eV (**Figure 21d**). The results were consistent with recent literature [248–250]. In **Papers I-II-III**, more details are presented.

The values of the optical band gaps of the composites were measured. As expected, light absorption intensity in the visible light was enhanced with the increasing load of  $\text{Cs}_3\text{Bi}_2\text{I}_9$ , with a redshift respectively to 580 and 620 nm for  $\text{Cs}_3\text{Bi}_2\text{I}_9\text{:TiO}_2$  (**Figure 21e**) and  $\text{Cs}_3\text{Bi}_2\text{I}_9\text{:g-C}_3\text{N}_4$  composites (**Figure 21f**). More details can be found in **Papers IV–V**.



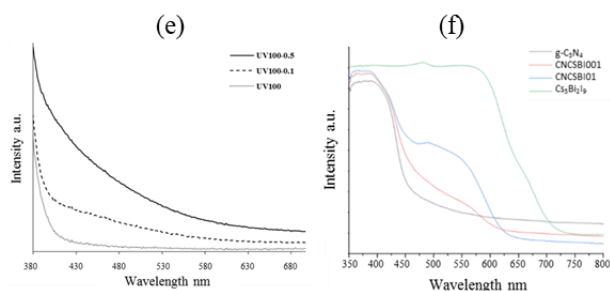
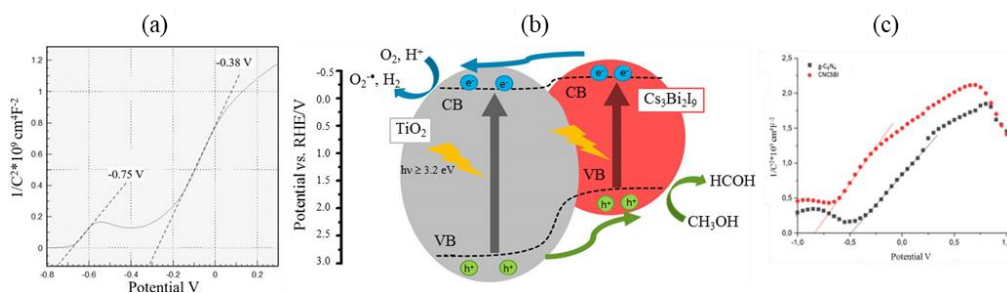


Figure 21: Adsorption spectra comparison for  $\text{CH}_3\text{NH}_3\text{PbI}_3$ ,  $(\text{CH}_3\text{NH}_3)_3\text{BiI}_3$ , and  $\text{Cs}_3\text{Bi}_2\text{I}_9$  (A), and  $\text{Cs}_3\text{Bi}_2\text{I}_9:\text{TiO}_2$  (E), and  $\text{Cs}_3\text{Bi}_2\text{I}_9:\text{g-C}_3\text{N}_4$  (F); Kubelk-Munk model application for the determination of the bandgaps of  $\text{CH}_3\text{NH}_3\text{PbI}_3$  (B),  $(\text{CH}_3\text{NH}_3)_3\text{BiI}_3$  (C), and  $\text{Cs}_3\text{Bi}_2\text{I}_9$  (D).

In semiconductor electrochemistry, the Mott-Schottky plot can evaluate important information on the system, such as flat band potential and other photoelectrical properties. In this study, the Mott-Schottky plot's linear portion was employed to determine the composite materials' energy levels' positions. In all the composites,  $\text{Cs}_3\text{Bi}_2\text{I}_9:\text{TiO}_2$  (**Figure 22a**) and  $\text{Cs}_3\text{Bi}_2\text{I}_9:\text{g-C}_3\text{N}_4$  (**Figure 22b**), Mott-Schottky analysis evidenced the junction features of heterostructures that strengthen the separation of electrons and holes. The energetic configuration of  $\text{Cs}_3\text{Bi}_2\text{I}_9:\text{TiO}_2$  composite is presented in **Figure 22b**. According to the energy band alignment, the photogenerated electrons are transferred from the VB of  $\text{TiO}_2$  into the CB of  $\text{Cs}_3\text{Bi}_2\text{I}_9$ . Different semiconductors provided a more efficient charge separation to respect the pristine materials, leading to higher photocatalytic efficiency.

A similar analytic approach was applied to the  $\text{Cs}_3\text{Bi}_2\text{I}_9:\text{g-C}_3\text{N}_4$  composite. The configuration of the energetic band position is shown in **Figure 22d**. Two contributions of the enhancement in photocatalytic ability were considered. In the conventional heterojunction configuration, the photogenerated charges are effectively separated due to the staggered band structures. In the Z-scheme, the electrons may flow from the CB of  $\text{g-C}_3\text{N}_4$ , they may combine with the holes of  $\text{Cs}_3\text{Bi}_2\text{I}_9$ , acting as scavengers. The former double-charge transfer mechanism can enhance charge separation. Both mechanisms are expected to lead to higher photocatalytic activity.



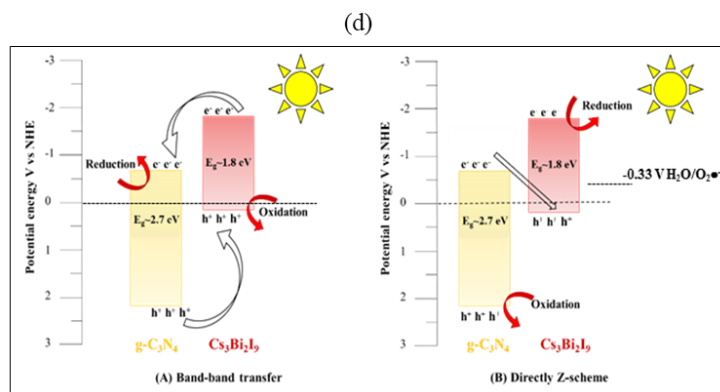


Figure 22: (a) Mott–Schottky plots for  $\text{Cs}_3\text{Bi}_2\text{I}_9:\text{TiO}_2$ , and (c)  $\text{Cs}_3\text{Bi}_2\text{I}_9:\text{g-C}_3\text{N}_4$ ; (b) band alignment schemes of  $\text{Cs}_3\text{Bi}_2\text{I}_9:\text{TiO}_2$ , and (d) of  $\text{Cs}_3\text{Bi}_2\text{I}_9:\text{g-C}_3\text{N}_4$ .

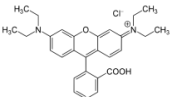
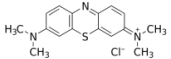
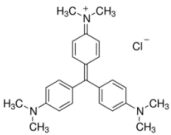
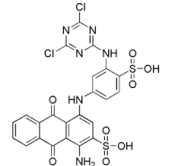
### 3.3 Environmental applications

#### 3.3.1. Photocatalytic degradation of organic pollutants

Water pollution and scarcity are definitively global issues with negative impacts on the environment and society. The environmental contamination of the last centuries has led to the leaching of dangerous persistent contaminants. Among these substances, organic dyes are considered highly toxic, and their uncontrolled discharge has a considerable impact on human health and ecosystems [251]. Dye contamination was found in a broad range of products, such as furniture, clothes, and accessories. They are often employed in many manufactures in dyeing, textile, leather, tanning, ink, and paint factories. More than 10,000 different types of dyes are estimated to be globally produced annually [252]. During their processing, up to 12% of dyes are wasted, of which 20% usually enter the environment, mainly discharged in the water bodies [253]. Most of the organic dyes are soluble in water. The potential bioavailability of these substances leads to harmful effects for aquatic animals and plants.

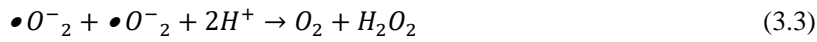
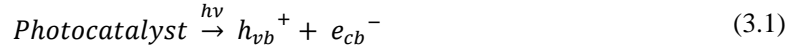
Moreover, organic dyes are recalcitrant and resistant to most conventional chemical and biological treatments, representing a threat to the environment and human health [254]. Organic dyes are commonly classified in thiazine dyes, such as methylene blue, xanthenes, rhodamine B, and azo dyes, such as reactive blue 4. This research work investigated the degradation of a variety of organic dyes with different chemical structures. The preliminary test was based on a single dye solution, but typical industrial effluents contain contaminated mixtures. For this reason, the treatment of a solution with mixed contaminants was investigated to simulate potential real industrial wastewater. **Table 6** summarized the properties of the organic dyes investigated in this research work.

Table 6: Characteristics of the investigated dyes.

Name	Structure	$\lambda$ max (nm)	MW (g/mol)
Rhodamine B		554	479.01
Methylene Blue		664	319.85
Crystal Violet		583	407.98
Reactive Blue 4		598	637.44

Different methods to achieve effective dye removal have been investigated, such as biodegradation, coagulation, adsorption, and membrane. The main limitations of traditional methods include operating costs, non-biodegradable products, time-consuming processes, and dye stability on treatments. Advanced oxidation processes (AOPs) are efficient methods for the near-ambient degradation of soluble organic dyes from waters and soils, with an almost total degradation of the contaminant [255]. Semiconductor-based heterogeneous photocatalysis is considered one of the more effective AOPs due to its inexpensive character and its efficiency in mineralizing various organic compounds. The photocatalytic process starts with the irradiation of a solid photocatalyst by an appropriate external light source. When the electrons are excited about the conduction band's valence, an electron-hole pair is formed as a separation between positive (holes), and negative (electrons) charges. Both the electrons ( $e^-$ ) and holes ( $h^+$ ) entities tend to migrate to the photocatalyst surface, where they can perform redox reactions with other species present on the surface. In general, the holes react with  $H_2O$  to produce hydroxyl radicals, and electrons with  $O_2$  generating superoxide radicals. The free radicals react with the organic dye, degrade its structure until the eventual mineralization to  $CO_2$  and water. A pathway of RhB photocatalytic degradation was proposed (3.1-3.5). The electrons and holes are separated under light illumination (3.1), photogenerating them as pairs. The charge carriers, interacting with the external environment, can produce hydroxyl free radicals and superoxide free radicals, (3.2). The superoxide radicals further react with protons

and produce  $H_2O_2$  (3.3), as a secondary source for the formation of hydroxyl radicals (3.4). The free radicals have a high oxidative capacity and can oxidize dye-based organic compounds such as RhB, MB, and MO to complete mineralization, finally release  $CO_2$ , and  $H_2O$  (3.5).



The experimental techniques for recording dye degradation are different and can be divided into qualitative and quantitative analyses. These methods usually involve UV-vis spectrophotometer, gas chromatograph-mass spectrometer (GC/MS), high-pressure liquid chromatography (HPLC), ion chromatography, capillary electrophoresis, and radiometry. In most techniques, a prior filtration procedure is required to collect the photocatalyst to analyze the solution.

In a typical experiment, photocatalytic efficiency was evaluated based on the degradation of the target dyes as a function of time. The tests were carried out in Pyrex vessels filled on a volume of dye-contaminated solution. A specified amount of solid photocatalyst was dispersed in the solution. After a dark period to reach equilibrium, the solution was irradiated with a specific light source, and samples were withdrawn at regular time intervals and analyzed with the UV-vis spectrophotometer. The efficiency of dye removal is commonly determined as follows:

$$\text{Removal efficiency} = 100 * \left(1 - \frac{C_i}{C_0}\right) (\%) \quad (3.6)$$

where  $C_0$  is the initial concentration of dye, and  $C_i$  is the measured concentration at the time of withdrawal.

**Figure 23** shows the time-dependent degradation of RhB using  $CH_3NH_3PbI_3$  (a),  $(CH_3NH_3)_3Bi_2I_9$  (b), and  $Cs_3Bi_2I_9$  (c) irradiated by visible light. Briefly, some considerations are highlighted in the following bullets.

- Photolysis, the decomposition of dyes only due to the presence of light, was negligible. This means that the presence of photocatalysts was required for an efficient photodegradation of the target compound.

- In dark conditions, as an indicator of the photocatalyst's adsorption ability, no relevant decrease in the dye concentration was recorded. This means that the photocatalytic procedure was not directly that photocatalytic degradation is not mainly driven by adsorption.



- For the experiment with  $\text{CH}_3\text{NH}_3\text{PbI}_3$ , around 90% of the RhB photodegradation was achieved in 180 minutes (**Figure 23a**). When  $(\text{CH}_3\text{NH}_3)_3\text{BiI}_2$ , the lead-free HOIP, was employed, almost complete degradation of RhB was achieved in 180 minutes under halogen visible light irradiation (**Figure 23b**). Moreover, around 90% of the degradation of MB was reordered in the same period. Similarly, in the presence of the all-inorganic MHP, perovskite  $\text{Cs}_3\text{Bi}_2\text{I}_9$ , nearly complete degradation of about 93% of RhB was observed (**Figure 23c**). All the presented results revealed the potential of the as-prepared HOIPs as visible light photocatalysts. More details on the degradation efficiency of bare HOIPs and all-inorganic MHPs are reported in **Papers I-II-II**.

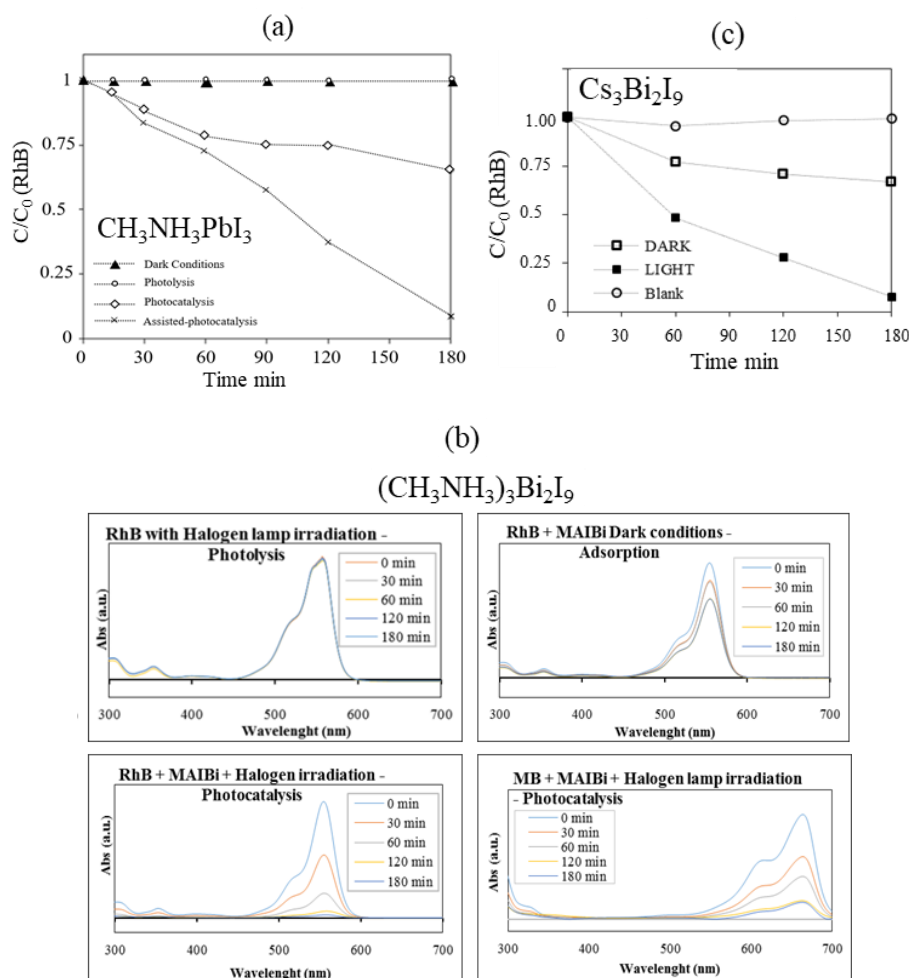


Figure 23: (a) Photocatalytic dye degradation using  $\text{CH}_3\text{NH}_3\text{PbI}_3$ , (b)  $(\text{CH}_3\text{NH}_3)_3\text{BiI}_2$ , and (c)  $\text{Cs}_3\text{Bi}_2\text{I}_9$ .

A first-order kinetic model was found to properly describe the photocatalytic reactions. The reaction rate constant  $k$  is determined by linearizing the integrated form of the mass balance in the batch reactor:

$$\ln(C_i) = \ln C_0 - k * t \quad (3.7)$$

where  $k$  is the reaction rate ( $\text{min}^{-1}$ ),  $C_0$  is the initial concentration ( $\text{mg/L}$ ), and  $C_i$  is the concentration a time  $t$ . The logarithm of the concentrations' ratios was plotted versus the time resulting in a straight line. The slope of the linear regression is equal to the first-order rate constant  $k$ . The R-squared value, denoted by  $R^2$ , verified the correlation. **Table 7** reports an example of applying the first-order kinetic model for the lead-free HOIP  $(\text{CH}_3\text{NH}_3)_3\text{Bi}_2\text{I}_9$  in the degradation of RhB, MB, and RBL in comparison with the bare  $\text{BiI}_3$  iodide. The results show a good correlation for the first-order kinetic model, with an  $R^2 \geq 0.95$ . The hybrid organic-inorganic perovskite provided a higher first-order kinetic rate equal to  $0.0221 \text{ min}^{-1}$ . Details are reported in **Paper II**.

Table 7: Parameters included in the evaluation of the photocatalytic process

Dye	Catalyst	Dye concentration (mg/L)	Catalyst load (g/L)	Reaction rate constant ( $\text{min}^{-1}$ )	$R^2$
RhB	$\text{BiI}_3$	20	0.5	0.0048	0.95
RhB	$(\text{CH}_3\text{NH}_3)_3\text{Bi}_2\text{I}_9$	20	0.5	0.0221	0.98
MB	$(\text{CH}_3\text{NH}_3)_3\text{Bi}_2\text{I}_9$	20	0.5	0.0129	0.97
RBL	$(\text{CH}_3\text{NH}_3)_3\text{Bi}_2\text{I}_9$	20	0.5	0.0006	0.98

The effectiveness of the synergetic effect of the  $\text{Cs}_3\text{Bi}_2\text{I}_9\text{:g-C}_3\text{N}_4$  were compared to the precursors materials  $\text{Cs}_3\text{Bi}_2\text{I}_9$  and  $\text{g-C}_3\text{N}_4$ , in the photocatalytic degradation of RhB. The total degradation of RhB was achieved after 120 minutes, the red line represents the rate of the composite with lower amount of MHP respect the blue line (**Figure 24a**). This demonstrated the higher performance achieved with the composites respect the bare perovskite and carbon-based material. The composite material was also tested for the degradation of different pollutants. MO was completely degraded 180 minutes (**Figure 24b**), partial degradation of MO was recorded in 300 minutes (**Figure 24c**). The higher activity on MB was correlated with the substrates' binding affinity, in terms of available active sites, and environmental conditions. The results confirmed the visible light-based photocatalytic ability of the material on the degradation of different organic dyes' degradation under visible light irradiation. More details can be found in **Paper V**.

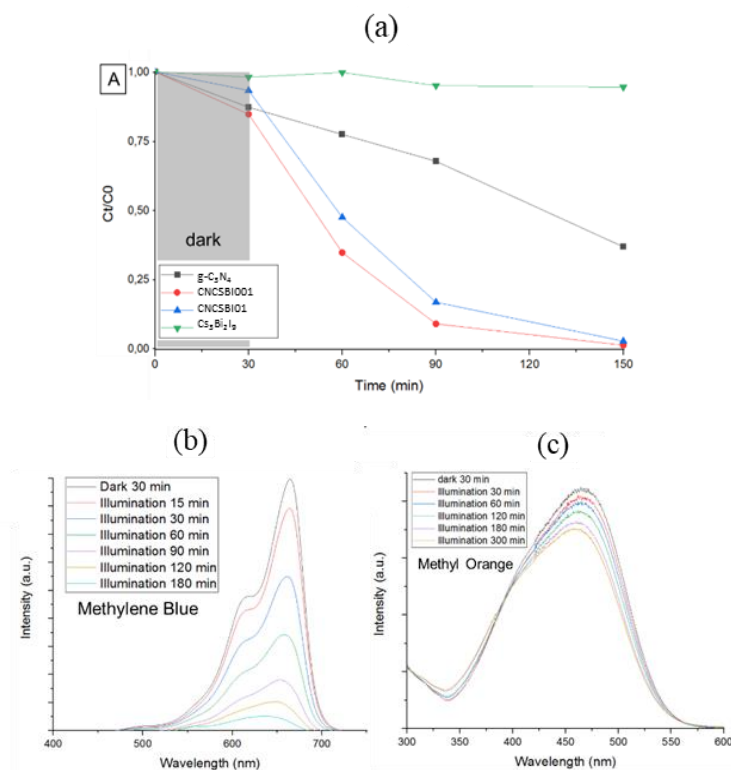


Figure 24: (a) Photocatalytic degradation of RhB, (b) MB, and (c) MO under visible light irradiation.

An alternative and useful method to evaluate organic and inorganic compounds' photodegradation is high-performance liquid chromatography (HPLC), an analytical chemistry technique to separate, identify, and quantify a mixture's components. Intermediates were identified using HPLC on the degradation of RhB at different time intervals. The photocatalyst was separated using a reversed-phase column. RhB was associated with the peak at the retention time equal to 7.5 minutes. The further peaks were associated with N-deethylation process of the dye (**Figure 25a**), producing N,N,N-diethyl-N0-ethylrhodamine (I), N,N-diethylrhodamine (II), N-ethyl-N0-ethylrhodamine (III), and N-ethylrhodamine (IV), as reported in literature [256]. The chromatographs, corresponding to different time interval withdraws, show a diminishing RhB peak. The decrease in the main peak indicated the progressive photodegradation of the target compound, RhB (**Figure 25b**).

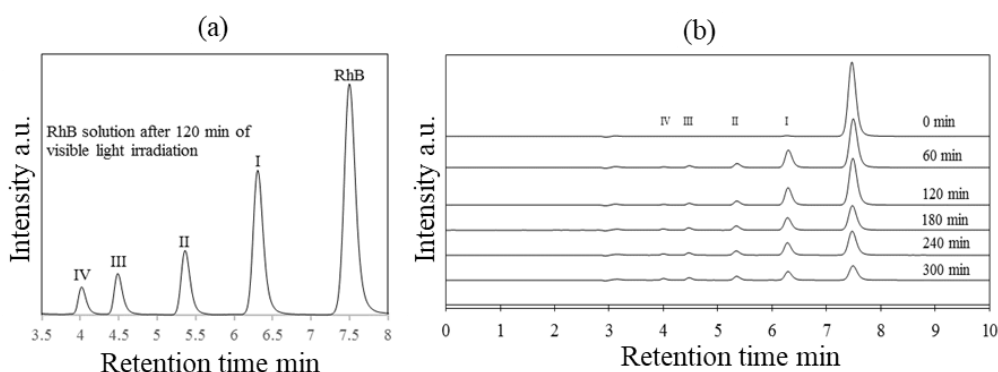


Figure 25: (a) HPLC chromatogram of RhB peak and its associated by-products' peak, (b) HPLC results of RhB photodegradation in function of time.

In photocatalytic processes, methanol is a chemical not only employed usually as a scavenger of holes but also as a model system for heterogeneous photocatalysis for formaldehyde production. The generation of formaldehyde via photocatalytic oxidation of methanol is desirable to respect the conventional methods due to the ambient reaction temperature and pressure, the sustainability of the light energy source, and the simplicity of the design of the reactive system. The methanol conversion to formaldehyde was investigated under visible light irradiation using all-inorganic MHP-based composites, named  $\text{Cs}_3\text{Bi}_2\text{I}_9:\text{TiO}_2$ .

The experiment was conducted using a typical quartz reactor containing a methanol aqueous solution. After a dark period to reach the adsorption equilibrium, a single-wavelength LED source at 406 and 455 nm was used. The liquid samples were withdrawn at regular time intervals, and filtered to separate the photocatalyst from the solution prior to the analysis. The produced formaldehyde was determined by fluorescent analyses of the formed yellow-coloured diacetyl-dihydro lutidine (DDL), produced by the prior addition of the Nash reagent (0.02 M acetylacetone, 0.05 M acetic acid, and 2 M ammonium acetate) [257]. The evaluation of photolysis and adsorption processes was previously investigated. The MHP-based composite performance as photocatalyst for methanol oxidation was compared under UV and visible light irradiation (**Figure 26**). Under UV light irradiation (**Figure 26a**), the reaction activity was attributed to  $\text{TiO}_2$ , a well-known UV-light photocatalyst. The photocatalytic activity of the composite  $\text{Cs}_3\text{Bi}_2\text{I}_9:\text{TiO}_2$ , was enhanced in comparison to the commercial  $\text{TiO}_2$  (UV100). Moreover, the positive result showed the composite as a promising visible light photocatalyst (**Figure 26b**). A decrease in efficiency was recorded when the weight-ratio  $\text{Cs}_3\text{Bi}_2\text{I}_9:\text{TiO}_2$  was increased from 0.05 % to 0.5 %, probably due to the different degrees of aggregation: the MHPs occupying the adsorption site on the  $\text{TiO}_2$  surface decreased its adsorption ability. The composites showed a reaction rate of 50% and 44% higher compared to the pristine  $\text{TiO}_2$  (UV100). The efficiencies of the photo-oxidation of methanol in formaldehyde were further compared by measuring the processes' reaction rates, as shown in **Table 8**.

Similarly, the photocatalytic efficiency of the  $\text{Cs}_3\text{Bi}_2\text{I}_9:\text{g-C}_3\text{N}_4$  was evaluated (**Figure 26c**) and compared in different environmental conditions (**Figure 26d**). The oxidation from methanol to formaldehyde was described as follows:

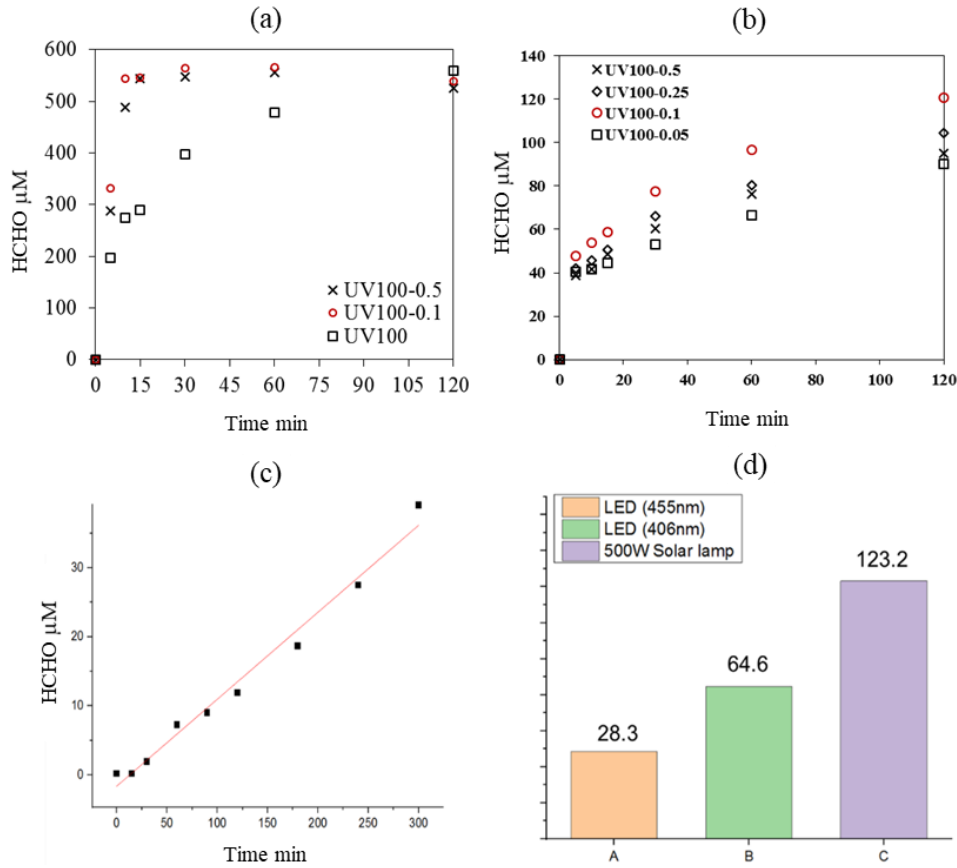
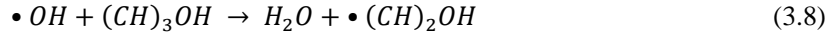


Figure 26: (a)  $\text{Cs}_3\text{Bi}_2\text{I}_9:\text{TiO}_2$ -based methanol photooxidation under UV light, (b)  $\text{Cs}_3\text{Bi}_2\text{I}_9:\text{TiO}_2$ -based methanol photooxidation under visible light, (c)  $\text{Cs}_3\text{Bi}_2\text{I}_9:g\text{-C}_3\text{N}_4$ -based methanol photooxidation under visible-light, (d) comparison of  $\text{Cs}_3\text{Bi}_2\text{I}_9:g\text{-C}_3\text{N}_4$  performances in the photodegradation of methanol as formaldehyde production.

Table 8: Reaction rate constants Cs<sub>3</sub>Bi<sub>2</sub>I<sub>9</sub>:TiO<sub>2</sub>-based photooxidation of methanol.

	Cs <sub>3</sub> Bi <sub>2</sub> I <sub>9</sub> :TiO <sub>2</sub> (UV100-0.1)	Cs <sub>3</sub> Bi <sub>2</sub> I <sub>9</sub> :TiO <sub>2</sub> (UV100-0.5)	TiO <sub>2</sub> UV100
$k$ (min <sup>-1</sup> ) – UV light	1.51	1.72	0.84
$R^2$	0.99	0.99	0.95
$k$ (min <sup>-1</sup> ) – visible light	0.05	0.03	-
$R^2$	0.95	0.98	-

### 3.3.2. The effect of operational parameters

In photocatalytic processes, the pH can influence the process efficiency, especially in organic-dye degradation. In particular, the initial pH of the solution modified the surface charges of the photocatalyst. In photocatalysis, the photocatalyst's absorption efficiency as a function of the charges on its surface is a crucial process. A typical method to evaluate this effect is the point of zerocharge analyses (PZC). The pH at the point of zero charge indicates the photocatalysts' net surface charges that subsequently affect the photocatalytic activity. The dye-contaminated solutions' pH was altered by incrementally adding either dilute HCl solution, enhancing the acidic conditions, or diluted NaOH solution for an alkaline effect. The removal rate was found to increase in acidic media when CH<sub>3</sub>NH<sub>3</sub>PbI<sub>3</sub> was employed under visible light irradiation (**Figure 27a**). In an alkaline medium, new oxidizing species can be formed, such as hydroperoxy anions. These species can react with both reactive oxygen species, lowering the reaction rate.

Similarly, the MB-contaminated solution's initial pH was modified when lead-free HOIPs, (CH<sub>3</sub>NH<sub>3</sub>)<sub>3</sub>BiI<sub>3</sub> was employed as photocatalyst. **Figure 27b** shows the photocatalytic results at different initial pH values. At extreme pH values, complete photodegradation was recorded (95%). In alkaline conditions, the presence of large quantities of hydroxide ions OH<sup>-</sup> favored ROS formation, principal oxidizing species, leading to a directly reducing reaction of MB into leucomethylene blue. At a strongly acidic pH, the photocatalyst was in a beneficial condition of zero-point charge; thus, the enhanced adsorption led to increased photocatalytic efficiency. Secondly, in acidic conditions, the aromatic structure of organic dyes can be cleaved easily. The details are presented in **Papers I–II**.

The photodegradation efficiency is also influenced by the amount of photocatalyst loaded in the solution. Generally, an enhancement of the photocatalytic reaction rate is associated with an increase in catalyst load. The effect is associated with the increment of the number of active sites on the photocatalyst surface, leading to an enhancement in the number of adsorption sites available. On the other hand, the photocatalyst load also influences the turbidity of the solution. Turbidity quantifies the scattering effect of suspended solids on light irradiation. The optimal photocatalyst concentration depends on the balance between active sites' availability and the scattering effect of the suspended solids in the solution [258].

**Figure 27e** and **Figure 27f** show the effects of the photocatalyst load on the ability to remove RhB and MB in aqueous solution, respectively, for  $\text{CH}_3\text{NH}_3\text{PbI}_3$  and  $(\text{CH}_3\text{NH}_3)_3\text{Bi}_2\text{I}_9$ .

As expected, the photocatalytic performance increased with the catalyst load up to a certain amount and then decreased for previously mentioned reasons. Moreover, an overload of photocatalysts can further induce particle deactivation by collision with ground-state molecules, reducing the reaction rate [259].

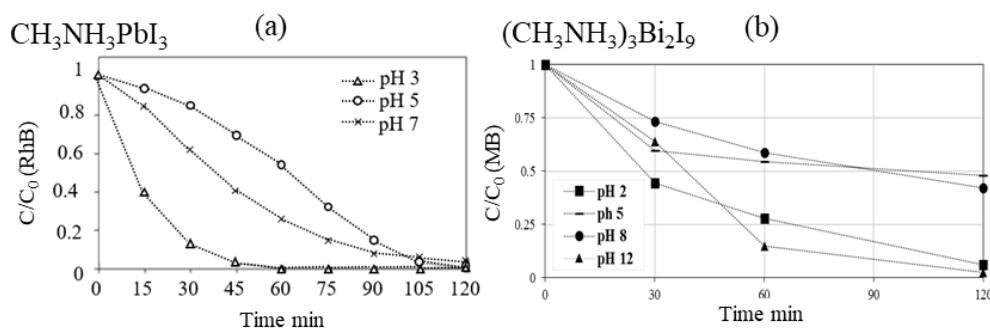
Similarly, the concentration of contaminants is a parameter to be considered in photocatalytic processes [258]. In general, more molecules are adsorbed on the surface of the photocatalyst when the concentration of dye is enhanced. At a high concentration of the contaminant, the generation of radicals on the photocatalyst's surface is reduced by the active sites' potential competition. Moreover, the turbidity of the solution is influenced by the concentration of pollutants. As reported in **Figure 27c** and **Figure 27d**, an enhancement of the pollutant concentration decreased the photocatalytic reaction rate. More details are available in **Papers I–II**.

The photocatalytic mineralization of organic contaminants is often tricky, and it is typically prolonged to complete. A potential approach to overcome this drawback is to assist the photocatalytic processes with external electron acceptors, such as  $\text{H}_2\text{O}_2$ . Assisted  $\text{H}_2\text{O}_2$ -photocatalysis can influence the overall photocatalytic efficiency by increasing the reaction rate and accelerating the process. The oxidant's photolysis generates free radicals (3.10) as a fundamental part of the photocatalytic process's reaction rate improvement (3.11).



Moreover,  $\text{H}_2\text{O}_2$  as an electron acceptor can reduce the recombination rate of photogenerated charge carriers, a desirable effect in photocatalysis.

**Figure 27g** shows the effect of  $\text{H}_2\text{O}_2$ -assisted photocatalytic degradation of RhB by increasing the oxidant concentration. A comparison of the reaction rates is presented in **Table 9**. More details are presented in **Paper I**.



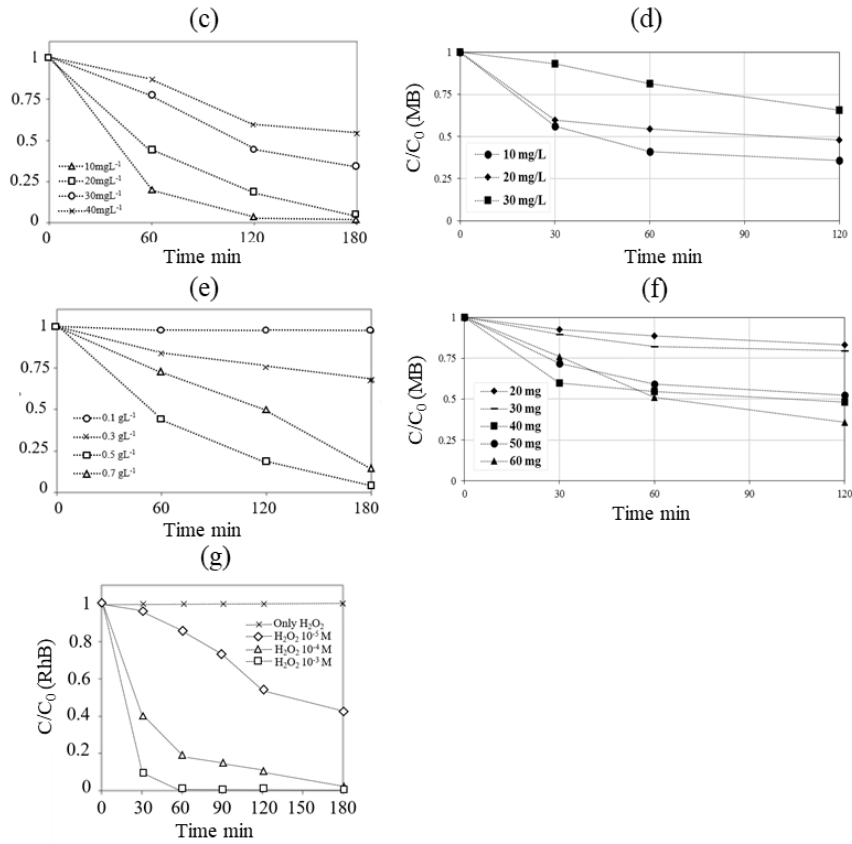


Figure 27: pH effects  $\text{CH}_3\text{NH}_3\text{PbI}_3$  (A),  $(\text{CH}_3\text{NH}_3)_3\text{BiI}_3$  (B); Initial dye concentration effects  $\text{CH}_3\text{NH}_3\text{PbI}_3$  (C),  $(\text{CH}_3\text{NH}_3)_3\text{BiI}_3$  (D); photocatalyst load effects  $\text{CH}_3\text{NH}_3\text{PbI}_3$  (E),  $(\text{CH}_3\text{NH}_3)_3\text{BiI}_3$  (F); hydrogen peroxide dose effect (G).

Table 9: Reaction rate constants as a function of hydrogen peroxide dosage.

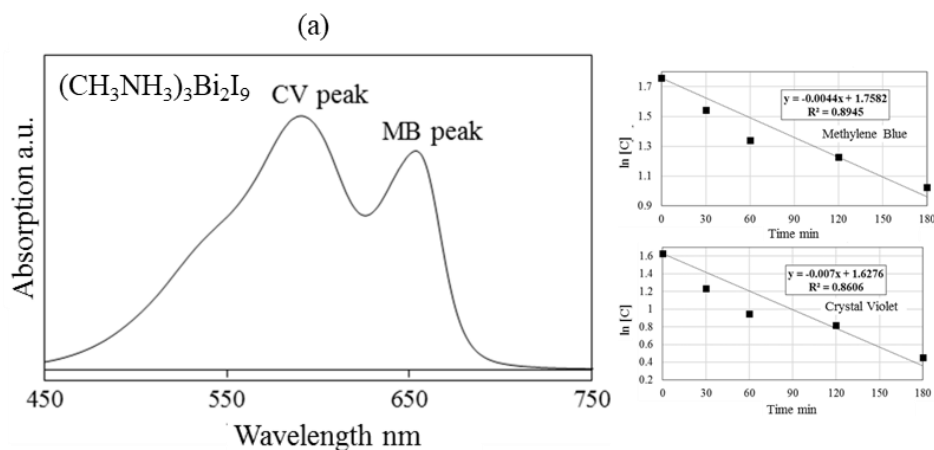
Experiment	Reaction rate constant ( $\text{min}^{-1}$ )	$R^2$
$\text{CH}_3\text{NH}_3\text{PbI}_3$ assisted photocatalysis $\text{H}_2\text{O}_2$ $10^{-5}$ mol·L $^{-1}$	0.27	0.94
$\text{CH}_3\text{NH}_3\text{PbI}_3$ assisted photocatalysis $\text{H}_2\text{O}_2$ $10^{-4}$ mol·L $^{-1}$	1.29	0.92
$\text{CH}_3\text{NH}_3\text{PbI}_3$ assisted photocatalysis $\text{H}_2\text{O}_2$ $10^{-3}$ mol·L $^{-1}$	6.52	0.92



### 3.3.3. The effect of multi-contaminated water solution

In industrial wastewater, it is hardly possible that contaminate steam consists of single dye contamination. Therefore, realistic studies were performed in a mixture of different dyes, simulating wastewater that can belong, for example, to textile or printing industries where more dyes are discharged in the same basin. In terms of simplicity, it is useful to select the type of contaminants that can be detected separately, for example, dyes with different emission wavelengths. The photodegradation of a mixed aqueous solution of CV and MB was evaluated in the presence of lead-free HOIP under visible light irradiation. The well-distinguishable characteristic peaks are shown in **Figure 28a**. The relatively low photocatalytic efficiency, concerning single-dye degradation, is associated with the two contaminants' competition for the photocatalyst adsorption surface sites. The effect of a multi-contaminated solution was also investigated under visible light irradiation on a mixture of MB and MO in the presence of the  $\text{Cs}_3\text{Bi}_2\text{I}_9\text{:g-C}_3\text{N}_4$  composite (**Figure 28b**).

The total degradation of MB was achieved in 180 minutes, and a partial degradation of MO in 300 min, the different reaction rate were correlated with the types of available active sites and binding affinity on the substrates' surfaces towards the specific contaminant. More details can be found in **Papers II** and **V**.



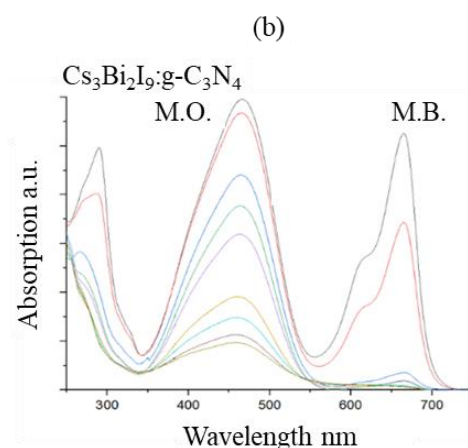


Figure 28: (a) UV-vis spectra for the mixture of CV and MB, and reaction rate constants measurements, for  $(\text{CH}_3\text{NH}_3)_3\text{BiI}_3$ ; (b) UV-vis spectra decreasing along time irradiation for the mixture of MO and MB, for  $\text{Cs}_3\text{Bi}_2\text{I}_9\text{:g-C}_3\text{N}_4$  (B).

### 3.3.4. The recycling effect

The stability of the photocatalyst and its reuse are fundamental properties in photocatalysis. Recyclability represents a sustainable aspect and, along with its stability, can be evaluated as a function of the decrease in efficiency over several photocatalytic cycles. After the first treatment in a typical experiment, the photocatalyst is recovered, washed several times to remove eventual residues, and reused for many cycles.

**Figure 29a, b, c, d, and f** show the resulting recycle of respectively  $\text{CH}_3\text{NH}_3\text{PbI}_3$ ,  $(\text{CH}_3\text{NH}_3)_3\text{BiI}_9$ ,  $\text{Cs}_3\text{Bi}_2\text{I}_9$  and the as-prepared composites  $\text{Cs}_3\text{Bi}_2\text{I}_9\text{:TiO}_2$ , and  $\text{Cs}_3\text{Bi}_2\text{I}_9\text{:g-C}_3\text{N}_4$ . The negligible efficiency was recorded in the recycling tests. For further details, see **Papers I–V**.

The XRD patterns before and after reactions were recorded for  $\text{Cs}_3\text{Bi}_2\text{I}_9\text{:TiO}_2$  to further demonstrate its stability. **Figure 29e** shows the XRD patterns for the as-prepared composite before and after treatment. The XRD pattern of pristine UV100 was also recorded as a reference. Negligible changes were recorded, indicating the photocatalyst's stability in structure not influenced by the photocatalytic processes. The  $\text{Cs}_3\text{Bi}_2\text{I}_9\text{:g-C}_3\text{N}_4$  sample was further analyzed, and FTIR spectra before and after the treatment are shown in **Figure 29g**. Negligible changes were observed in the existing stretching and bending frequencies. Further details are reported in **Papers IV and V**.

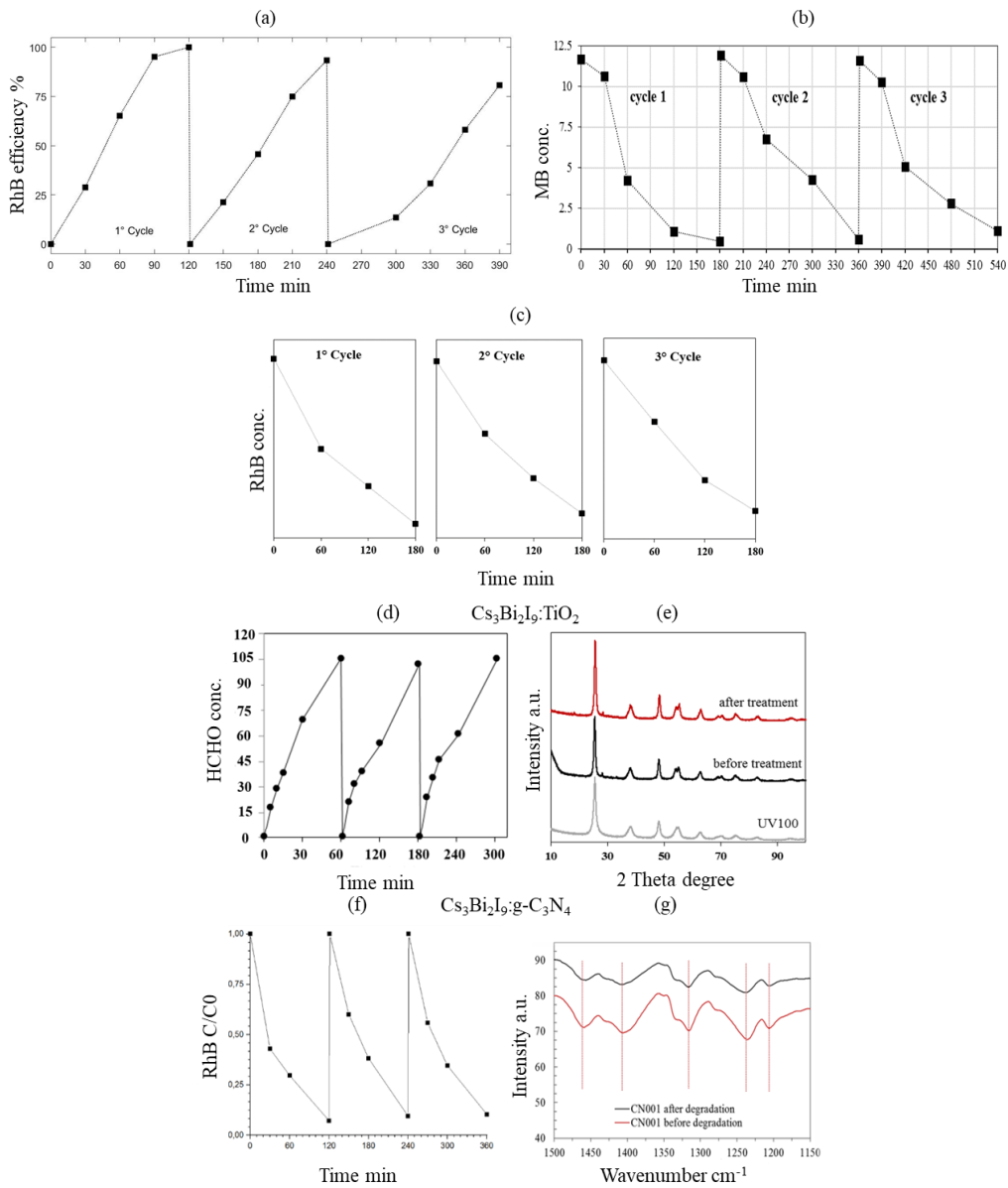


Figure 29: (a) Recycle test for  $\text{CH}_3\text{NH}_3\text{PbI}_3$ , (b)  $(\text{CH}_3\text{NH}_3)_3\text{BiI}_3$ , (c)  $\text{Cs}_3\text{Bi}_2\text{I}_9$ , (d)  $\text{Cs}_3\text{Bi}_2\text{I}_9:\text{TiO}_2$ , and (e)  $\text{Cs}_3\text{Bi}_2\text{I}_9:\text{g-C}_3\text{N}_4$ ; (f) XRD patterns before and after treatment; (g) FT-IR spectra before and after treatment.

### 3.3.5. The effect of the light source

The recent advancement of industries and technology has led to substantial environmental pollution and increased energy demand [260]. The supply of sustainable and clean sources of energy sources has become a key factor in parallel to environmental protection to preserve life on our planet. From this perspective, technologies based on solar energy, due to its availability, accessibility, and cleanliness, could represent a sustainable way to address both energy and environmental issues. In particular, the visible light portion of the solar spectrum is due to the reason presented in previous paragraphs. Among the typical instruments to simulate the visible range of solar light, halogen and LED sources were considered in this research work. Halogen lamps are incandescent lamps consisting of a tungsten filament contained in a compact transparent tube filled with a mixture of inert gas and halogen element content, for example, iodine or bromine. The chemical reaction between the halogen element and the inert gas leads to the production of light. These lamps' main properties include the operation at high temperature, respect for the standard incandescent lamps, maintaining similar power, and operating life.

Moreover, halogen lamps produce higher luminous efficacy at different color temperatures. Halogen lamps permit their employment in compact optical systems due to their smaller size. On the other hand, LED lamps have shown higher light efficiency concerning standard and halogen incandescent bulbs. In recent years, LEDs have become cheaper and more available. The advantages of LEDs include their heat emissions. The halogen bulbs lost almost all the energy as heat, making them harder to replace and hazardous to nearby combustible materials. LEDs dissipate only 10% or 20% of their energy as heat, making them cooler and safer concerning halogen sources. Nowadays, some conventions enforce regulations on halogen light sources due to safety issues and power consumption. The lifespan of LED lights lasts around 40 times longer than halogen bulbs, making them more sustainable. In general, LEDs cost more per unit, but considering the overall lifespan, they remain more advantageous to respect halogen lamps. It is fundamental to consider ideal action spectra irradiation in photocatalytic systems to select the excitation source. Comparing the absorbance spectrum of the prepared photocatalyst and the light emission spectrum from the selected lamps is a useful tool to achieve real efficiency in the photocatalytic process. An overlap of catalyst absorbance ability and emission of light sources represent one contribution to the photoreaction activity. In this research work, visible light irradiation was provided with different types of lamps:

- A 150 W halogen lamp (Visilight CL150, Lutterworth, UK) with an emission in the visible range (380–400 nm) (**Figure 30a**).

- A 36 W LED-visible light lamp (VisiLight LED3, Lutterworth, UK), with a luminous intensity of 730 lm, with an emission presented in **Figure 30c**.

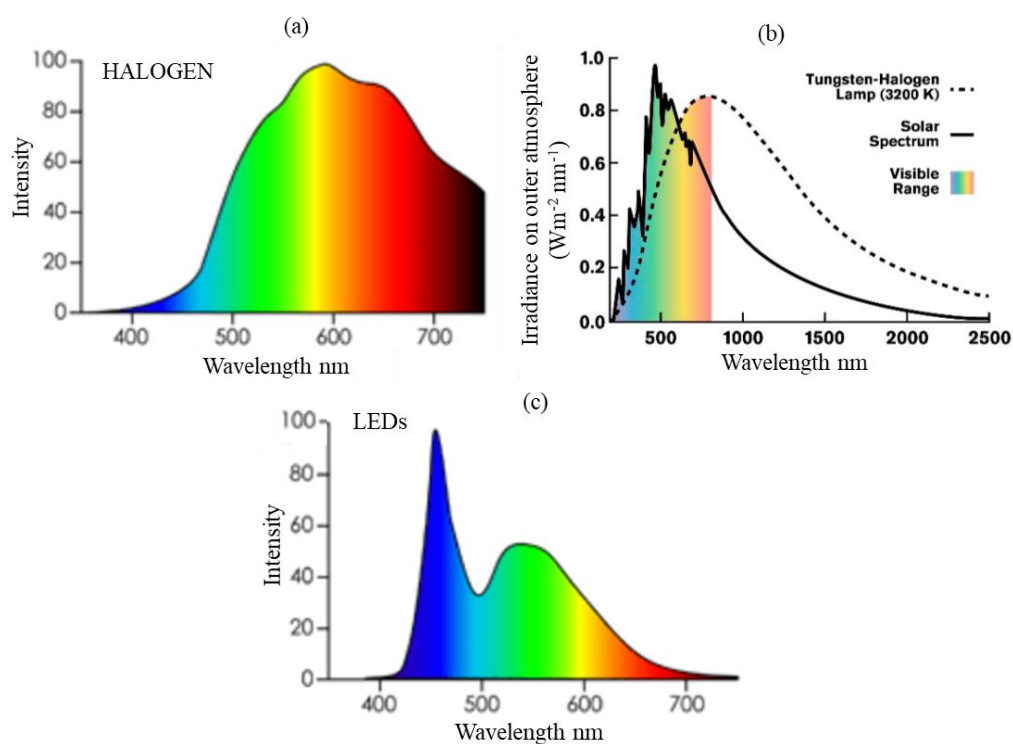
- Two single-wavelength emission LEDs: LED 455 nm and LED 365 nm (Thorlabs, Newton, New Jersey, U.S.) with emissions presented in **Figure 30d,e**

Visilight CL150 and VisiLight LED3 were both provided by VWR. **Table 10** shows a comparison between the main characteristics of the two kinds of lamps. LED and halogen light cover visible light in the spectrum of 380 nm–780 nm with different intensities. The halogen

lamp shows a homogeneous emission intensity between 550 and 650 nm, and the LED lamp shows two relatively isolated peaks at 450 nm and 550 nm (**Figure 30a** and **Figure 30c**). Halogen and LED light sources were compared on the photocatalytic behavior of the lead-free HOIPs. LED irradiation provided a first-order kinetic rate of  $0.0072 \text{ min}^{-1}$  (**Figure 30f**), lower of about 35% concerning the halogen lamp. The halogen lamp showed higher photocatalytic efficiency due to the better fitting between its emission and the adsorption ability of the selected photocatalyst (**Figure 30b**). For more details, see **Papers II** and **IV**.

Table 10: Comparison of the properties of halogen and LED light-sources.

Lamp	Power consumption (W)	Luminous efficacy (lumens/watt)	Colour temperature (K)	Average Lifespan (hours)
Visilight CL150	150	16-24	3270	1.000
Visilight LED 3	36	80-100	5700	55.000



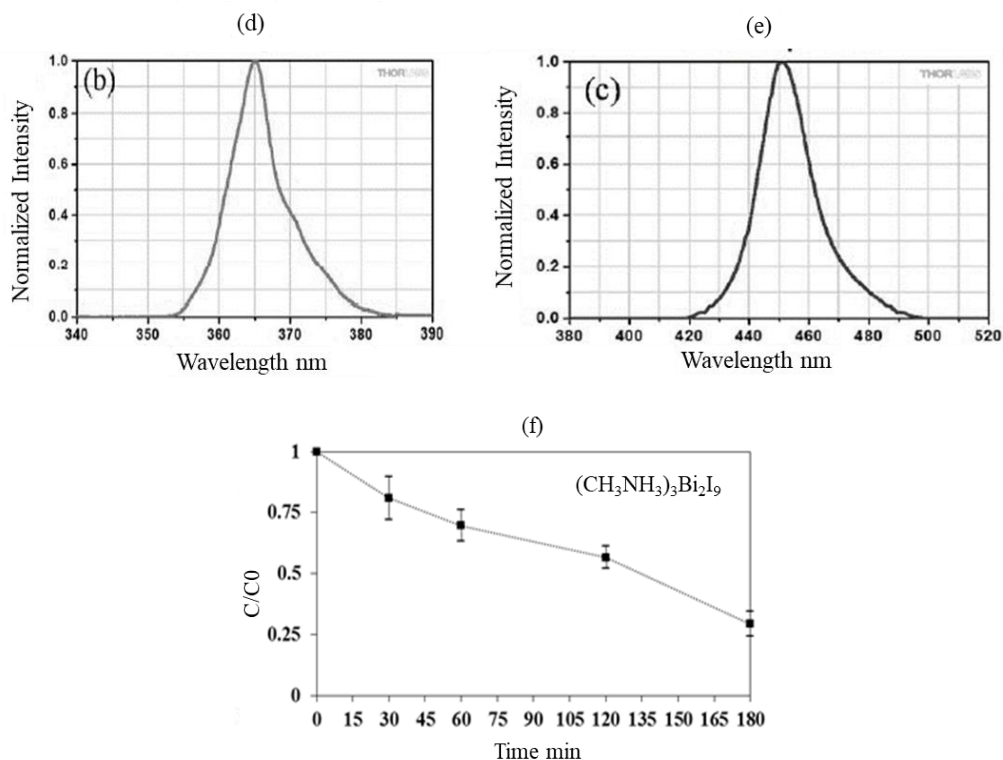


Figure 30: (a,b) Emission spectra for halogen and (c) LED light-sources; (d) emission spectra for single-wavelength LEDs 365 nm and (e) 455 nm; (f) photocatalytic efficiency for lead-free HOIPs under LED illumination.

### 3.3.6. Mechanism of photocatalysis

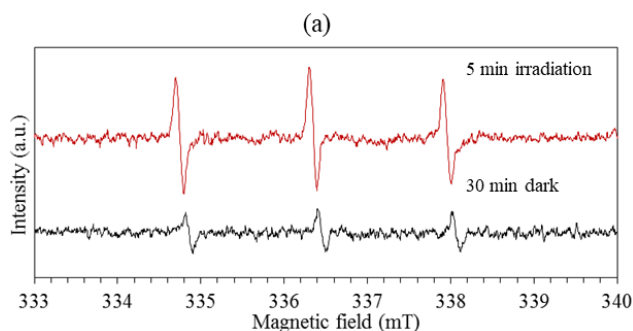
Several different techniques can obtain insight into the nature of the photocatalytic process. One example is the electron spin resonance (ESR) approach. Even at its early stage, this approach has been widely and successfully used to characterize the electronic structure and reveal the photocatalyst's active sites [264]. Generally, in photocatalytic applications, when a semiconductor is excited by irradiation with an equivalent or greater light-energy concerning its band gap, the electrons ( $e^-$ ) in the valence band (VB) are excited into the conduction band (CB), and the holes ( $h^+$ ) remain in the valence band (VB). These species, known as charge carriers, trigger the redox reaction. The charge carriers and reactive oxygen species (ROS), including  $O_2^{\cdot-}$ , and  $\cdot OH$ , are widely considered the main active species responsible for the degradation of organic contaminants. In this research work, ESR, with proper spin traps, was used to determine the presence of reactive oxygen species (ROS) as main actors in the photocatalytic degradation of organic compounds. TEMP (2,2,6,6-tetramethylpiperidine) was used as a spin trap for singlet oxygen and DMSO (dimethyl sulfoxide) for superoxide and hydroxyl radicals [264,265]. Under visible light photoexcitation of the mixture of the lead-based HOIPs and TEMP solution, three lines with equal intensities were observed in the ESR spectrum (**Figure 31A, red line**), indicating the generation of TEMPO radicals due to the

presence of singlet oxygen species ( $^1\text{O}_2$ ). The intensity of the peaks decreased when the time of irradiation was increased, suggesting that the radical generation occurred only in the very first intervals of the photocatalytic process [266,267] (**Figure 31a, black line**). DMPO solution was selected as a spin trap of superoxide and hydroxyl radicals (**Figure 31b, red line**). The four typical peaks appeared in the spectrum, revealing the presence of the target radicals.

Like the previous experiment, the signal recorded after 30 min showed a decrease in peaks' intensity, implying that radicals' generation stopped after a certain period (**Figure 31b, black line**). Finally, a solution of equal content of RhB and DMPO was prepared, irradiated, and analyzed by the ESR technique. After 5 minutes of irradiation, the ESR spectrum recorded radicals' presence (**Figure 31c, red line**). The generation of radicals was not recorded in the analysis of the mixed solution of RhB and DMPO without the photocatalyst. More details can be found in **Paper I**.

A direct and straightforward alternative to evaluate ROS's presence and relevance is the reaction with organic and inorganic scavengers, chemicals able to interfere with reactive species' formation. Scavengers can react quickly and on target radicals, generating stable products that do not interfere with the reaction's proceeding, eventually eliminating the reactive species' effect on the degradation. Different molecules have been used as radical scavengers in heterogeneous photocatalysis, targeting species such as the VB hole, the electron, and the other ROS [268].

In this thesis work, to investigate the RhB mechanism of photodegradation, different scavengers were employed to determine the reactive species involved in the process. Ammonium oxalate (AO) reacts with holes ( $\text{h}^+$ ), isopropanol (IPA) with hydroxyl radicals ( $\bullet\text{OH}$ ), p-benzoquinone (BQ) with superoxide radicals ( $\bullet\text{O}_2^-$ ) [269]. **Figure 31d** shows the scavenger reaction results in the visible light photodegradation of RhB using  $\text{Cs}_3\text{Bi}_2\text{I}_9\text{:g-C}_3\text{N}_4$  composite. Briefly, AO or IPA did not influence the photocatalytic efficiency, meaning that both the holes and the hydroxyl radicals were negligible reactive species. On the contrary, BQ's addition led to a decrease in photodegradation efficiency, leading to the conclusion that  $\bullet\text{O}_2^-$  was the major reactive species involved in the system's photocatalytic degradation irradiated by visible light. The reactive oxygen radicals' intrinsic and nonselective character follows their consideration as the main actors of the RhB chromophore structure's cleavage.



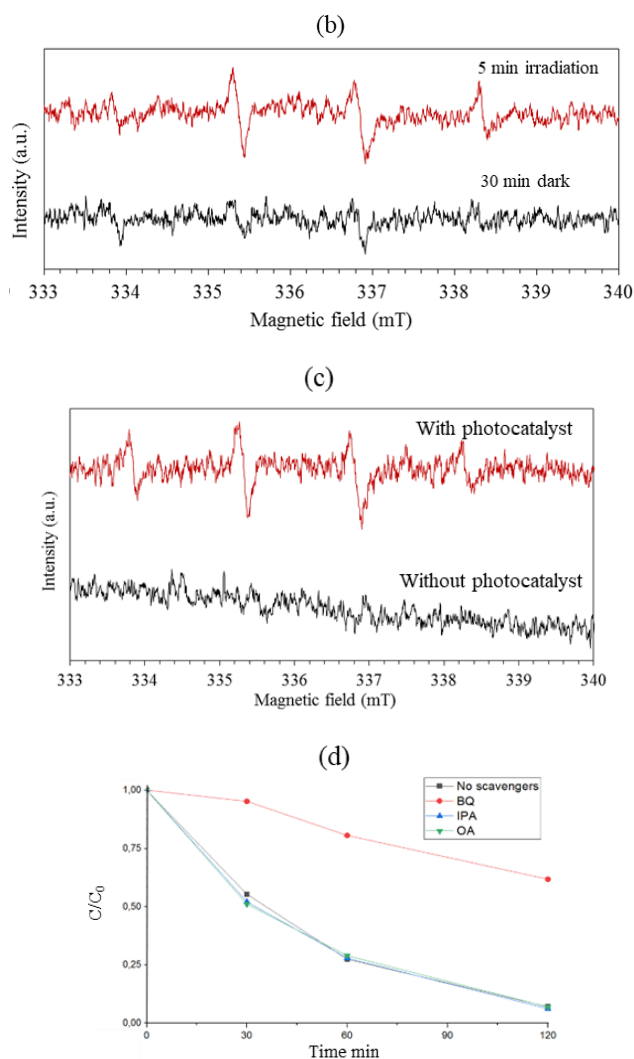


Figure 31: (a) Spin traps-based ESR analyses TEMP, (b) DMPO; (c) ESR analysis with and without photocatalyst; (d) scavengers experiments.

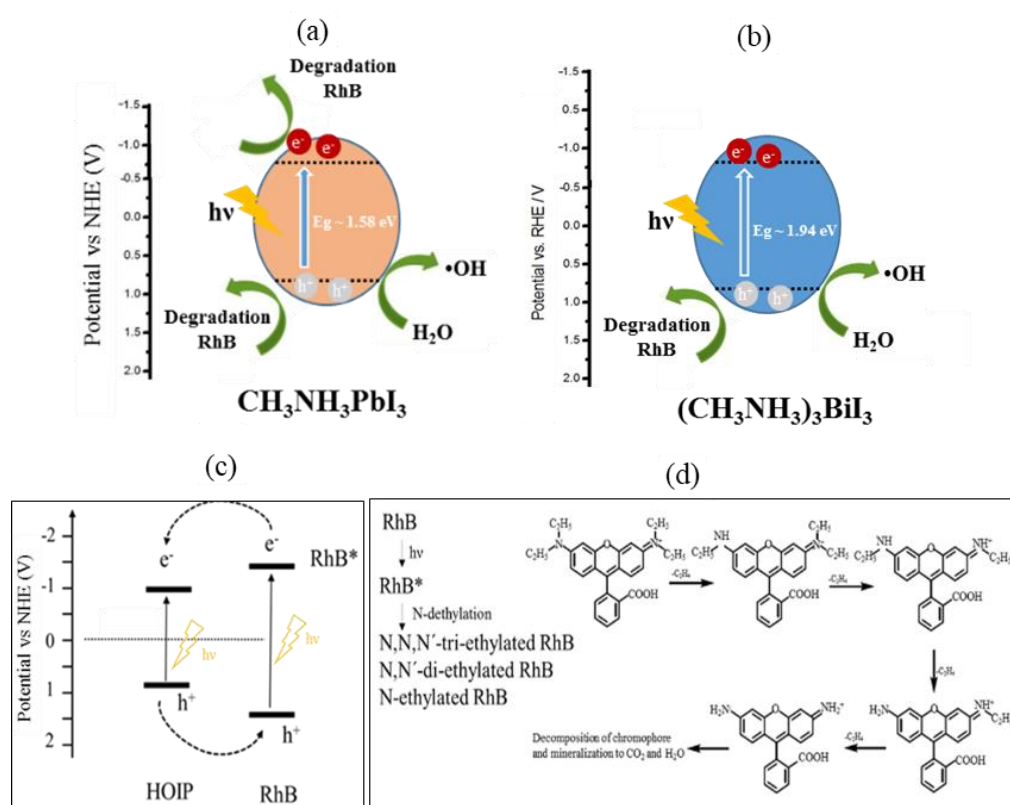
The main processes responsible for initiating the photodegradation of dyes are direct semiconductor excitation and indirect dye sensitization [270]. According to the self-sensitized mechanisms, illumination can induce an electron transfer process from the dye molecules to the photocatalyst (**Figure 32C**). On the other hand, as previously mentioned, the electrons in the VB of the photocatalyst can be excited and photogenerated charge carriers. In both cases, reactive free radical species will initiate photocatalytic reactions. Both HOIPs and all-inorganic MHPs have demonstrated photocatalytic abilities, primarily due to their suitable absorption coefficient, favorable band gap, high charge carrier mobility, reduced surface recombination, and long electron-hole diffusion length. In this research work, the optoelectric analyses explained the potential photodegradation mechanism in recent literature [271]. **Figure 32A-B**



show the energy diagrams for the as-prepared HOIP-based photocatalysts, respectively  $\text{CH}_3\text{NH}_3\text{PbI}_3$  and  $(\text{CH}_3\text{NH}_3)_3\text{BiI}_3$ .

Heterojunction formation has been considered a critical factor in the enhancement of photocatalytic activity [93,272]. The photogenerated charge carriers' transfer direction depends on the energetic levels' position in a composite material. **Figure 22a** and **Figure 22b** show the energy levels' mechanism and positions, respectively, for  $\text{Cs}_3\text{Bi}_2\text{I}_9:\text{TiO}_2$  and  $\text{Cs}_3\text{Bi}_2\text{I}_9:\text{g-C}_3\text{N}_4$  composites. In general, when two semiconductors are combined, spatial charge transfer and separation occur, leading to a lower recombination rate and higher photocatalytic activity. For more insights, see Paper IV and Paper V.

In the specific case of the photodegradation of RhB, two degradation pathways were considered (**Figure 32D**). A first possible degradation occurs by the de-ethylation of  $\text{RhB}^{++}$  by the N-ethyl group's attack, leading to de-ethylated intermediates (N,N,N'-tri-ethylated rhodamine, N,N'-di-ethylated rhodamine, N-ethylated rhodamine, and rhodamine). A second pathway involves the degradation of RhB chromophore by the attack of  $\bullet\text{OH}$  radicals on the chromophoric structure, leading to the formation of organic acids and alcohol-intermediates and finally to  $\text{CO}_2$  and  $\text{H}_2\text{O}$  [273,274]. The photocatalytic degradation of RhB under visible light is further represented in **Figure 32E**. More information is reported in **Papers I–V**.



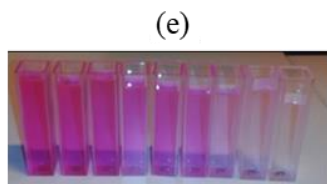


Figure 32: (a) Energy level position for  $\text{CH}_3\text{NH}_3\text{PbI}_3$ , (b)  $(\text{CH}_3\text{NH}_3)_3\text{BiI}_3$ ; (c) representation of the self-sensitized mechanisms; (d) example of photodegradation of RhB; (e) photograph representing the removal of RhB as a function of time intervals.

### 3.3.7. Potential application of MHPs in photocatalytic hydrogen

Awareness of the current energy crisis has led to considering the hydrogen-based energy source as a clean and sustainable form of energy. Increasing the employment of hydrogen fuels recently arises for the high yield of energy production concerning the more common combustion process, typically based on fossil fuels, well known for their dangerous pollution emissions [261]. The photocatalytic hydrogen generation is a sustainable method through non-PEC water splitting that employs the photocatalyst's excitons with light energy to dissociate water [262]. This approach is environmentally friendly because it does not produce any harmful by-products. Nowadays, available processes for hydrogen generation involve the emission of  $\text{CO}_2$  production. Therefore, alternatives, excluding the production of greenhouse gases, are desirable [263]. Photocatalytic applications are one of the promising approaches to resolving the current energy and environmental crisis.

The photocatalytic efficiency of MHPs was further investigated for photochemical hydrogen production under solar light irradiation. In a typical experiment, a platinum layer was deposited on the surface  $\text{Cs}_3\text{Bi}_2\text{I}_9\text{:g-C}_3\text{N}_4$  composite using a photo-deposition method described in Paper V. Methanol aqueous solution was used as a hole scavenger in a closed quartz reactor. The suspension was degassed with argon to remove undesired air. After a dark period to reach the solution-photocatalyst equilibrium, the sample was irradiated with a 450W Xe-lamp, equipped with a water-filter and a WG320-filter to block UV-B and UV-C. The spectral irradiance measured by a SpectraRad (BWTEK) is shown in **Figure 33a**. The hydrogen generation analysis was measured periodically using a gas chromatograph equipped with a TCD detector and a 5 Å molecular sieve packed column. **Figure 33b** shows the photogeneration of hydrogen. The results demonstrated a continuous hydrogen production occurring along the irradiation period. An enhancement in hydrogen production of about 46% was recorded employing the composite photocatalyst compared to the pristine material,  $\text{g-C}_3\text{N}_4$  (**Figure 33c**). An increasing light absorption and separation charge abilities of the newly designed material were considered responsible for the enhanced photocatalytic performance. Finally, **Figure 33d** demonstrated that the hydrogen evolution was achieved under visible light irradiation LED 455 nm. Although they must be considered only a preliminary study, the previously described results confirmed the potential of the as-prepared material in multiple photocatalytic applications. In **Paper V**, more details are repo

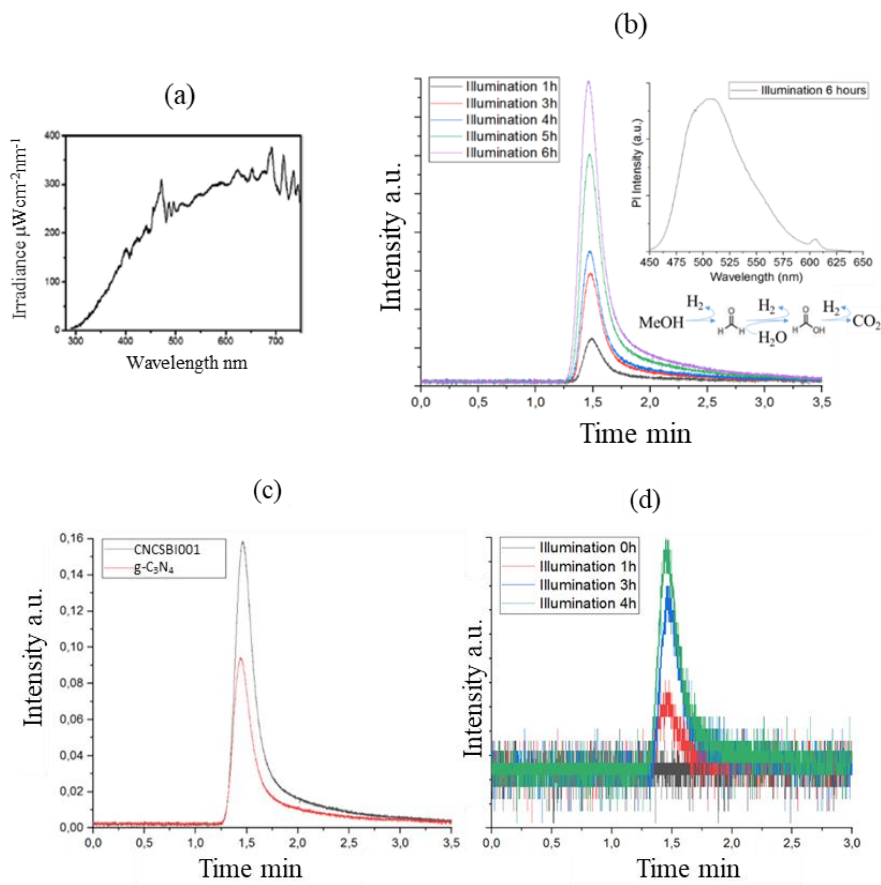


Figure 33: (a) Solar simulator light emission spectrum; (b) Hydrogen evolution results of the composite; (c) comparison between pristine material and composite sample in the photogeneration of hydrogen; (d) MHP-based composite photogeneration of hydrogen under visible-light irradiation.

### 3.4 Conclusion

Heterogeneous photocatalysis has been demonstrated to be an effective method for light-to-chemical energy conversion and green applications. Thus, it is a desirable approach to address current global challenges, such as energy crises and environmental pollution. On the other hand, the transition from widely explored lab-scale systems to real commercialization is still limited, in particular, due to the lack of efficiently designed photocatalysts. Remarkable advancements were achieved after 1972 when the first report on TiO<sub>2</sub> used as a UV-light photocatalyst for water-splitting appeared [21]. Nevertheless, most traditional photocatalysts still show several limitations, such as wide band gap, rapid recombination of photogenerated charge carriers, and low photo-redox ability. Thus, the development of new semiconductor photocatalysts with suitable properties continues to motivate the scientific community. In recent years, MHPs have attracted several research groups, mainly due to their remarkable properties, such as low production costs, easy processability, and favorable optical and electrochemical properties. More specifically, MHPs have emerged as promising photocatalysts due to their superior optoelectrical properties.

In this thesis, three bare MHPs were synthesized and employed as photocatalysts. First, HOIPs were considered due to the high efficiency reached in the photovoltaic field. The lead-based perovskite (CH<sub>3</sub>NH<sub>3</sub>PbI<sub>3</sub>) proved to be an active, visible light photocatalyst, performing the complete assisted removal of a hazardous xanthene dye, known as RhB, in 180 minutes (**Paper I**). Despite the promising result, the relatively low stability of the mentioned material and the non-environmentally friendly presence of lead prompted lead-free HOIPs to be considered more sustainable candidates. As reported previously, Bi-based photocatalysts possess a unique configuration with superior photocatalytic activity [247]. Bi-based HOIP ((CH<sub>3</sub>NH<sub>3</sub>)<sub>3</sub>Bi<sub>2</sub>I<sub>9</sub>) was selected and employed in visible light photocatalytic applications. The impressive results demonstrated for aqueous dye removal were comparable to the lead-based photocatalyst. Complete dye degradation was reached in 180 minutes under visible light LED irradiation without oxidant assistance (H<sub>2</sub>O<sub>2</sub>). The material was employed for the degradation of methylene blue (MB) and reactive blue (RBL), showing its potential over the removal of dyes with different chemical structures. Moreover, the photocatalytic treatment of mixed MB and crystal violet (CV) was also investigated, simulating a real industrial effluent that usually contains a mixture of contaminants. The previously mentioned studies highlighted the potential of the as-prepared photocatalyst for wastewater treatment, for example, in the textile or printing industries (**Paper II**).

A well-designed photocatalyst's key factors include evaluating its environmental stability and its ability to withstand various external stresses, such as light-dark cycles, moisture, and air. In HOIPs, the organic fraction was reported to destabilize the material's overall structure due to its sensitivity to moisture, UV light, oxygen, and temperature. For this reason, all-inorganic MHPs were considered for their outstanding environmental stability. Thus, all-inorganic Bi-based MHP (Cs<sub>3</sub>Bi<sub>2</sub>I<sub>9</sub>) was proposed as a visible light photocatalyst. The photocatalytic experiments exhibited the competitive photodegradation of RhB in 180 minutes under monochromatic 455-visible light irradiation. The recycling tests and after-treatment structural analyses highlighted the photocatalyst's expected stability to the treatment (**Paper III**). Transient absorption spectroscopy measurements confirmed the photogeneration of charge

---

carriers, highlighting the advantageous photoelectrochemical properties of the MHP photocatalyst.

Recognized the potential of  $\text{Cs}_3\text{Bi}_2\text{I}_9$  as a visible light photocatalyst, its photocatalytic activity was enhanced by designing two heterostructures, employing the synergetic actions of coupled semiconductors. Two traditional semiconductors,  $\text{TiO}_2$  nanoparticles and g- $\text{C}_3\text{N}_4$  nanosheets were selected as supports for the  $\text{Cs}_3\text{Bi}_2\text{I}_9$ -based composites. Anchored- $\text{Cs}_3\text{Bi}_2\text{I}_9$  on  $\text{TiO}_2$  (UV100) nanoparticles exhibited enhanced visible light absorption ability, charge carrier transportation, and chemical stability. The photo-oxidation of MeOH was compared under UV and visible light irradiation. As the main actors of the redox reactions, hydroxyl radicals were demonstrated by terephthalic acid fluorescence analysis. The two semiconductors' simultaneous contribution led to the increased photocatalytic activity under UV light irradiation compared to the bare- $\text{TiO}_2$  powder. On the other hand, under visible light irradiation, MHPs were found to act as redox mediators. The as-prepared composite exhibited excellent stability and visible light activity and a convenient simplicity in the preparation as a critical factor for green photocatalysts (**Paper IV**).

Graphitic carbon nitride (g- $\text{C}_3\text{N}_4$ ) is considered an excellent candidate for photocatalytic applications due to its tunable electronic structure and excellent physicochemical stability. In this research work, its low charge transportation efficiency was overcome by anchoring  $\text{Cs}_3\text{Bi}_2\text{I}_9$  on the graphitic nanosheets by nitrogen-iodine chemical bonds. The as-prepared composite showed an outstanding yield for visible light photocatalytic degradation of different contaminants, such as organic-dyes and methanol. RhB was found to be degraded after 150 minutes under monochromatic 455-LED irradiation. Further, the as-prepared photocatalyst was tested for hydrogen photocatalytic evolution under simulated solar light and visible light irradiation, showing positive preliminary results (**Paper V**).

Practically, the as-described experimental research aims to provide new insights into the use of MHPs and MHP-based heterostructures as visible light photocatalysts for wastewater treatments. Currently, the photocatalytic performance and environmental stability of MHP-based photocatalysts are far from optimal. MHP-based applications are still limited to fulfill global energy and environmental challenges. Nevertheless, the current state-of-the-art MHPs demonstrate their potential as new generation materials for different emerging light-driven applications.

---

## REFERENCES

- [1] W. Zhang, G.E. Eperon, H.J. Snaith, *Nat. Energy* 1 (2016) 1–8.
- [2] H. Zhou, Q. Chen, G. Li, T. Song, H.-S. Duan, Z. Hong, Y. You; Yongsheng, Liu; Yang, *Science* 345 (2014) 542–546.
- [3] M.R. Hoffmann, S.T. Martin, W. Choi, D.W. Bahnemann, *Chem. Rev.* 95 (1995) 69–96.
- [4] A. Jäger-Waldau, *Energy* 12 (2019) 1–7.
- [5] A. Kumar, V. Sharma, S. Kumar, A. Kumar, V. Krishnan, *Surfaces and Interfaces* 11 (2018) 98–106.
- [6] L.M.M.F. Cans, A. Kleidon, *Earth Syst. Dyn.* 2 (2011) 1–12.
- [7] N. Mathur, P. Bhatnagar, P. Nagar, M.K. Bijarnia, *Ecotoxicol. Environ. Saf.* 61 (2005) 105–113.
- [8] Y. Sang, H. Liu, A. Umar, *ChemCatChem* 7 (2015) 1–16.
- [9] X. Hu, Y. Li, J. Tian, H. Yang, H. Cui, *J. Ind. Eng. Chem.* 45 (2017) 189–196.
- [10] S. Linic, P. Christopher, D.B. Ingram, *Nat. Mater.* 10 (2011) 911–921.
- [11] U. Ulmer, T. Dingle, P.N. Duchesne, R.H. Morris, A. Tavasoli, T. Wood, G.A. Ozin, *Nat. Commun.* 10 (2019) 1–12.
- [12] T.P. Yoon, M.A. Ischay, J. Du, *Nat. Chem.* 2 (2010) 527–532.
- [13] T. Hisatomi, K. Domen, *Nat. Catal.* 2 (2019) 387–399.
- [14] J.G. McCarty, *Nature* 403 (2000) 35–36.
- [15] B.A.J.B. Robertson, L.J. Thnard, *Platin. Met. Rev.* 19 (1975) 64–69.
- [16] W. Ostwald, *Phys. Chem.* 15 (1984) 705–706.
- [17] G. Ertl, *Surf. Sci.* 6 (1967) 208–232.
- [18] K.J. Laidler, *Pure Appl. Chem.* 68 (1996) 149–192.
- [19] C. Vogt, M. Monai, G.J. Kramer, B.M. Weckhuysen, *Nat. Catal.* 2 (2019) 188–197.
- [20] K. Fujishima, A., and Honda, *Nature* 238 (1972) 37–38.
- [21] A. Fujishima, K. Honda, *Nature* 238 (1972) 37–38.
- [22] K.J. Bachmann, *Nature* 305 (1983) 615–616.
- [23] R. Vijayalakshmi, V. Rajendran, *Arch. Appl. Sci. Res.* 4 (2012) 1183–1190.

- 
- [24] S. Zhu, D. Wang, *Adv. Energy Mater.* 7 (2017) 1–24.
- [25] M. Yasmina, K. Mourad, S.H. Mohammed, C. Khaoula, *Energy Procedia* 50 (2014) 559–566.
- [26] D.M. Schultz, T.P. Yoon, D.M. Schultz, T.P. Yoon, *Science* 343 (2014) 1–8.
- [27] J. Chen, J. Cen, X. Xu, X. Li, *Catal. Sci. Technol.* 6 (2016) 349–362.
- [28] M. Mohsen, Z. Nazari, *Ceram. Int.* 42 (2016) 8691–8697.
- [29] K. Dai, T. Peng, D. Ke, B. Wei, *Nanotechnology* 20 (2009) 1–6.
- [30] Q. Lin, W. Zhang, Y.U. Shao, Y. Chen, M. Sun, X. Fu, *Environ. Sci. Technol.* 43 (2009) 4164–4168.
- [31] H. Park, M.R. Hoffmann, *J. Mater. Chem.* 18 (2008) 2379–2385.
- [32] N.S. Lewis, *Science* 315 (2007) 798–802.
- [33] K. Takanabe, *ACS Catal.* 7 (2017) 8006–8022.
- [34] G.C. Turner, P. Debbage, *Molecular Imaging with Nanoparticles: The Dwarf Actors Revisited 10 Years Later*, Springer Berlin Heidelberg, 2018.
- [35] X. Van Doorslaer, P. Heynderickx, K. Demeestere, K. Debevere, *Appl. Catal. B Environ.* 111–112 (2011) 150–156.
- [36] R. Habchi, M. Bechelany, *ChemSusChem* 11 (2018) 3023–3047.
- [37] F.M. Pesci, G. Wang, D.R. Klug, Y. Li, A.J. Cowan, *J. Phys. Chem. C* 117 (2013) 25837–25844.
- [38] D.K. Pallotti, L. Passoni, P. Maddalena, F. Di Fonzo, S. Lettieri, *J. Phys. Chem. C* 121 (2017) 9011–9021.
- [39] S. Shen, X. Wang, T. Chen, Z. Feng, C. Li, *J. Phys. Chem. C* 118 (2014) 12661–12668.
- [40] S.B. Rewal, S. Bera, D. Lee, D.-J. Jang, W.I. Lee, *Catal. Sci. Technol.* 3 (2013) 1822–1830.
- [41] L.R. Baker, C.M. Jiang, S.T. Kelly, J.M. Lucas, J. Vura-Weis, M.K. Gilles, A.P. Alivisatos, S.R. Leone, *Nano Lett.* 14 (2014) 5883–5890.
- [42] J. Tang, J.R. Durrant, D.R. Klug, *J. Am. Chem. Soc.* 127 (2008) 13885–13891.
- [43] H. Yan, X. Wang, M. Yao, X. Yao, *Prog. Nat. Sci. Mater. Int.* 23 (2013) 402–407.
- [44] R. Qian, H. Zong, J. Schneider, G. Zhou, T. Zhao, Y. Li, *Catal. Today* 335 (2019) 78–90.
- [45] J. Ihssen, A. Braun, G. Faccio, K. Gajda-schranz, L. Thöny-meyer, *Curr. Protein Pept. Sci.* 15 (2014) 374–384.
- [46] M.A.A. Schoonen, Y. Xu, D.R. Strongin, *J. Geochemical Explor.* 62 (1998) 201–215.
- [47] V.A. Online, *Phys. Chem. Chem. Phys.* 15 (2013) 14256–14261.

- 
- [48] J. Herrmann, *Catal. Today* 53 (1999) 115–129.
- [49] D.L. Dexter, *J. Chem. Phys.* 21 (1953) 836–849.
- [50] R. Va, P. Jungwirth, *P. Chem, C. Phys, Phys. Chem. Chem. Phys.* 12 (2010) 14364–14366.
- [51] E.R. Goldman, H. Mattoussi, *Nat. Mater.* 4 (2005) 435–446.
- [52] J.C. Claussen, N. Hildebrandt, K. Susumu, M.G. Ancona, I.L. Medintz, *ACS Appl. Mater. Interfaces* 6 (2013) 3771–3778.
- [53] P. V Kamat, *J. Phys. Chem. C* 112 (2008) 18737–18753.
- [54] L. Lin, C. Hou, X. Zhang, Y. Wang, Y. Chen, T. He, *Appl. Catal. B Environ.* 221 (2018) 312–319.
- [55] R. Dadigala, R. Bandi, B.R. Gangapuram, V. Guttena, *J. Photochem. Photobiol. A Chem.* 342 (2017) 42–52.
- [56] A.R. Zanatta, *Sci. Rep.* (2019) 1–12.
- [57] M. Ghaffari, H. Huang, O.K. Tan, M. Shannon, *CrystEngComm* 14 (2012) 7487.
- [58] S.N. Inamdar, P.P. Ingole, S.K. Haram, *ChemPhysChem* 9 (2008) 2574–2579.
- [59] H.H. Mohamed, D.W. Bahnemann, *Appl. Catal. B Environ.* 128 (2012) 91–104.
- [60] D. Gong, V.P. Subramaniam, J.G. High, Y. Tang, Y. Lai, Z. Chen, *ACS Catal.* 2 (2011) 864–871.
- [61] A.M. Pennington, A.I. Okonmah, D.T. Munoz, G. Tsilomelekis, F.E. Celik, *J. Phys. Chem. C* 122 (2018) 5093–5104.
- [62] N. Feng, Q. Wang, A. Zheng, Z. Zhang, J. Fan, S. Liu, J. Amoureux, F. Deng, *J. Am. Chem. Soc.* 135 (2013) 1607–1616.
- [63] W. Gao, J. Lu, S. Zhang, X. Zhang, Z. Wang, W. Qin, *Adv. Sci.* 6 (2019).
- [64] N.C. Greenham, X. Peng, A.P. Alivisatos, *Phys. Rev. B* 54 (1996) 628–637.
- [65] A. You, M.A.Y. Be, I. In, *Appl. Phys. Lett.* 1745 (2004) 1–4.
- [66] M. Radecka, M. Rekas, A. Trenczek-zajac, K. Zakrzewska, *J. Power Sources* 181 (2008) 46–55.
- [67] K. Gelderman, L. Lee, S.W. Donne, *J. Chem. Educ.* 84 (2007) 685–688.
- [68] S. Albrecht, B. Rech, *Nat. Energy* 2 (2017) 1–2.
- [69] R.B.P. Marcelino, C.C. Amorim, *Environ. Sci. Pollut. Res.* 26 (2019) 4155–4170.
- [70] R. Subbiah, M. Veerapandian, K.S. Yun, *Curr. Med. Chem.* 17 (2010) 4559–4577.



- 
- [71] D. Beydoun, R. Amal, G. Low, S. Mcevoy, *J. Nanobiotechnology* 1 (1999) 439–458.
- [72] B. Yong, S. Zhao, H. Fu, A. Peng, Y. Ma, D. Xiao, J. Yao, *Adv. Mater.* 20 (2008) 2859–2876.
- [73] H. Zhou, Y. Qu, X. Duan, *Energy Environ. Sci.* 5 (2012) 6732–6743.
- [74] W. Jiang, Y. Zhu, G. Zhu, Z. Zhang, X. Chen, W. Yao, *J. Mater. Chem. A* 5 (2017) 5661–5679.
- [75] Y. Zhang, S. Park, *J. Solid State Chem.* 253 (2017) 421–429.
- [76] S. Cao, J. Yu, *J. Phys. Chem. Lett.* 5 (2014) 2101–2107.
- [77] X. Wang, K. Maeda, A. Thomas, K. Takanabe, G. Xin, J.M. Carlsson, K. Domen, M. Antonietti, *Nat. Mater.* 8 (2008) 76–80.
- [78] P. Niu, L. Zhang, G. Liu, H. Cheng, *Adv. Funct. Mater.* 22 (2012) 4763–4770.
- [79] Y. Zheng, J. Liu, J. Liang, M. Jaroniec, S.Z. Qiao, *Energy Environ. Sci.* 5 (2012) 6717–6731.
- [80] Y. Chen, A. Li, Z. Huang, L. Wang, F. Kang, *Nanomaterials* 6 (2016) 1–17.
- [81] J. Li, B. Shen, Z. Hong, B. Lin, B. Gao, Y. Chen, *Chem. Commun.* 48 (2012) 12017–12019.
- [82] D.R. Paul, W.J. Koros, R.Y.F. Liu, Y.S. Hu, E. Baer, A. Hiltner, H.D. Keith, R.Y.F. Liu, A. Hiltner, E. Baer, R.E. Cohen, A. Bellare, R.J. Albalak, W. Hu, G. Reiter, *Science* 323 (2009) 760–763.
- [83] X. Zheng, Y. Wei, L. Wei, B. Xie, M. Wei, *Int. J. Hydrogen Energy* 35 (2010) 11709–11718.
- [84] J. Ge, Y. Zhang, Y. Heo, *Catalysts* 9 (2019).
- [85] R. Marschall, L. Wang, *Catal. Today* 225 (2014) 111–135.
- [86] R. Asahi, *Science* 269 (2012) 269–271.
- [87] T. Umebayashi, T. Yamaki, H. Itoh, K. Asai, *Appl. Phys. Lett.* 81 (2002) 454–455.
- [88] S. Sakthivel, H. Kisch, *Angew. Chemie - Int. Ed.* 42 (2003) 4908–4911.
- [89] A.O. Ibadon, P. Fitzpatrick, *Catalysts* 3 (2013) 189–218.
- [90] V. V Afanas, *Adv. Condens. Matter Phys.* 2014 (2014) 1–30.
- [91] W. Chen, T. Liu, T. Huang, X. Liu, G. Duan, X. Yang, S. Chen, *RSC Adv.* 5 (2015) 101214–101220.
- [92] A.J. Bard, *J. Photochem.* 10 (1979) 59–75.
- [93] K. Maeda, *ACS Catal.* 3 (2013).
- [94] P. Zhou, J. Yu, M. Jaroniec, *Adv. Mater.* 26 (2014) 4920–4935.
- [95] H. Tada, T. Mitsui, T. Kiyonaga, T. Akita, K. Tanaka, *Science* 5 (2006) 782–786.

- 
- [96] Q. Huang, Q. Zhang, S. Yuan, Y. Zhang, M. Zhang, *Appl. Surf. Sci.* 353 (2015) 949–957.
- [97] J. Yu, S. Wang, J. Low, W. Xiao, *Phys. Chem. Chem. Phys.* 15 (2013).
- [98] J. Jin, J. Yu, D. Guo, C. Cui, W. Ho, *Small* 11 (2015) 5262–5271.
- [99] J. Zhang, Y. Hu, X. Jiang, S. Chen, S. Meng, *J. Hazard. Mater.* 280 (2014) 713–722.
- [100] M. Munoz, Z.M. De Pedro, J.A. Casas, J.J. Rodriguez, *Appl. Catal. B Environ.* 176–177 (2015) 249–265.
- [101] Y. Peng, M. Yan, Q.-G. Chen, C.M. Fan, H.-Y. Zoou, A.-W. Xu, *J. Mater. Chem. A* 2 (2014) 8517–8524.
- [102] J. Yu, W. Wang, B. Cheng, *Chem. Asian J.* 5 (2010) 2499–2506.
- [103] J. Yu, J. Low, W. Xiao, P. Zhou, M. Jaroniec, *J. Am. Chem. Soc.* 136 (2014).
- [104] G. Liu, H.G. Yang, J. Pan, Y.Q. Yang, G. Qing, M. Lu, H. Cheng, *Chem. Rev.* 114 (2014) 9559–9612.
- [105] H. Lin, L. Li, M. Zhao, X. Huang, X. Chen, G. Li, R. Yu, *J. Am. Chem. Soc.* 134 (2012) 1–4.
- [106] C. Zhang, D. Kuang, W. Wu, *Small* 4 (2019) 1–30.
- [107] N. Park, M. Grätzel, T. Miyasaka, K. Zhu, K. Emery, *Nat. Energy* 1 (2016) 1–8.
- [108] T. Song, Q. Chen, H. Zhou, C. Jiang, H. Wang, M. Yang, Y. Liu, *J. Mater. Chem. A Mater. Energy Sustain.* 3 (2015) 9032–9050.
- [109] M.M. Lee, J. Teuscher, T. Miyasaka, T.N. Murakami, H.J. Snaith, *Science* 338 (2012) 643–648.
- [110] A. Kojima, K. Teshima, Y. Shirai, T. Miyasaka, *J. Am. Chem. Soc.* 131 (2009) 6050–6051.
- [111] T. Leijtens, G.E. Eperon, N.K. Noel, S.N. Habisreutinger, A. Petrozza, H.J. Snaith, *Adv. Energy Mater.* 5 (2015) 1–23.
- [112] S.A. Veldhuis, P.P. Boix, N. Yantara, M. Li, T.C. Sum, N. Mathews, S.G. Mhaisalkar, *Adv. Mater.* 28 (2016) 6804–6834.
- [113] F. Reyes-pérez, J.J. Gallardo, T. Aguilar, R. Alcántara, C. Fernández-lorenzo, J. Navas, *Chem. Sel.* 3 (2018) 10226–10235.
- [114] X. Qian, Z. Chen, X. Yang, W. Zhao, C. Liu, T. Sun, D. Zhou, Q. Yang, G. Wei, M. Fan, *J. Clean. Prod.* 249 (2019) 119335.
- [115] G. Do Park, C.W. Lee, K.T. Nam, *Curr. Opin. Electrochem.* (2018) 1–7.
- [116] B. Bresolin, N.O. Balayeva, L.I. Granone, R. Dillert, *Sol. Energy Mater. Sol. Cells* 204 (2020) 1–11.
- [117] B.M. Bresolin, S. Ben Hammouda, M. Sillanpää, *Nanomaterials* 10 (2020) 1–17.

- 
- [118] X. Wang, H. Wang, H. Zhang, W. Yu, X. Wang, Y. Zhao, X. Zong, C. Li, *ACS Energy Lett.* 3 (2018) 1159–1164.
- [119] Y. Ogomi, A. Morita, S. Tsukamoto, T. Saitho, N. Fujikawa, Q. Shen, T. Toyoda, K. Yoshino, S.S. Pandey, T. Ma, S. Hayase, *J. Phys. Chem. Lett.* 5 (2014) 1004–1011.
- [120] W.J. Yin, T. Shi, Y. Yan, *Adv. Mater.* 26 (2014) 4653–4658.
- [121] J.P. Correa-Baena, L. Nienhaus, R.C. Kurchin, S.S. Shin, S. Wieghold, N.T. Putri Hartono, M. Layurova, N.D. Klein, J.R. Poindexter, A. Polizzotti, S. Sun, M.G. Bawendi, T. Buonassisi, *Chem. Mater.* 30 (2018) 3734–3742.
- [122] Q. Chen, N. De Marco, Y. Yang, T. Bin Song, C.C. Chen, H. Zhao, Z. Hong, H. Zhou, Y. Yang, *Nano Today* 10 (2015) 355–396.
- [123] E.J. Juarez-Perez, L.K. Ono, M. Maeda, Y. Jiang, Z. Hawash, Y. Qi, *J. Mater. Chem. A* 6 (2018) 9604–9612.
- [124] B. Brunetti, C. Cavallo, A. Ciccioli, G. Gigli, A. Latini, *Sci. Rep.* 6 (2016) 1–10.
- [125] L. Iagher, L. Etkar, *ACS Energy Lett.* 3 (2018) 366–372.
- [126] A.F. Akbulatov, S.Y. Luchkin, L.A. Frolova, N.N. Dremova, K.L. Gerasimov, I.S. Zhidkov, D. V Anokhin, E.Z. Kurmaev, K.J. Stevenson, P.A. Troshin, *J. Phys. Chem. Lett.* 8 (2017) 1211–1218.
- [127] D.P. McMeekin, G. Sadoughi, W. Rehman, G.E. Eperon, M. Saliba, M.T. Hörantner, A. Haghighirad, N. Sakai, L. Korte, B. Rech, M.B. Johnston, L.M. Herz, H.J. Snaith, *Science* (80-.). 351 (2016) 151–155.
- [128] M. Perovskites, Y. Hu, M.F. Aygu, M.L. Petrus, T. Bein, P. Docampo, *ACS Energy Lett.* 2 (2017) 2212–2218.
- [129] C.C. Stoumpos, C.D. Malliakas, M.G. Kanatzidis, *Inorg. Chem.* 52 (2013) 9019–9038.
- [130] S.F. Hoefler, G. Trimmel, T. Rath, *Monatshefte Fur Chemie* 148 (2017) 795–826.
- [131] B. Li, L. Fu, S. Li, H. Li, L. Pan, L. Wang, B. Chang, L. Yin, *J. Mater. Chem. A* 7 (2019) 20494–20518.
- [132] J. Liang, P. Zhao, C. Wang, Y. Wang, Y. Hu, G. Zhu, L. Ma, J. Liu, Z. Jin, *J. Am. Chem. Soc.* 139 (2017) 14009–14012.
- [133] M. Pazoki, T.J. Jacobsson, A. Hagfeldt, G. Boschloo, T. Edvinsson, *Phys. Rev. B* 93 (2016) 1–10.
- [134] C.F.J. Lau, X. Deng, J. Zheng, J. Kim, Z. Zhang, M. Zhang, J. Bing, B. Wilkinson, L. Hu, R. Patterson, S. Huang, A. Ho-Baillie, *J. Mater. Chem. A* 6 (2018) 5580–5586.
- [135] S. Zou, Y. Liu, J. Li, C. Liu, R. Feng, F. Jiang, Y. Li, J. Song, H. Zeng, M. Hong, X. Chen, *J. Am. Chem. Soc.* 139 (2017) 11443–11450.

- 
- [136] J. Liang, Z. Liu, L. Qiu, Z. Hawash, L. Meng, Z. Wu, Y. Jiang, L.K. Ono, Y. Qi, *Adv. Energy Mater.* 8 (2018) 1–7.
- [137] T.J. Jacobsson, M. Pazoki, A. Hagfeldt, T. Edvinsson, *J. Phys. Chem. C* 119 (2015) 25673–25683.
- [138] C. Cuhadar, S.G. Kim, J.M. Yang, J.Y. Seo, D. Lee, N.G. Park, *ACS Appl. Mater. Interfaces* 10 (2018) 29741–29749.
- [139] W. Wang, M.O. Tadé, Z. Shao, *Chem. Soc. Rev.* 44 (2015) 5371–5408.
- [140] Q. Zhang, R. Su, X. Liu, J. Xing, T.C. Sum, Q. Xiong, *Adv. Funct. Mater.* 26 (2016) 6238–6245.
- [141] E.T. Hoke, D.J. Slotcavage, E.R. Dohner, A.R. Bowring, H.I. Karunadasa, M.D. McGehee, *Chem. Sci.* 6 (2015) 613–617.
- [142] Z. Xiao, C. Bi, Y. Shao, Q. Dong, Q. Wang, Y. Yuan, C. Wang, Y. Gao, J. Huang, *Energy Environ. Sci.* 7 (2014) 2619–2623.
- [143] M. Yang, T. Zhang, P. Schulz, Z. Li, G. Li, D.H. Kim, N. Guo, J.J. Berry, K. Zhu, Y. Zhao, *Nat. Commun.* 7 (2016) 2–10.
- [144] J.H. Noh, S.H. Im, J.H. Heo, T.N. Mandal, S. Il Seok, *Nano Lett.* 13 (2013) 1764–1769.
- [145] T.M. Koh, K. Thirumal, H. Sen Soo, N. Mathews, *ChemSusChem* 9 (2016) 2541–2558.
- [146] E.T. McClure, M.R. Ball, W. Windl, P.M. Woodward, *Chem. Mater.* 28 (2016) 1348–1354.
- [147] M.C. Brennan, S. Draguta, P. V. Kamat, M. Kuno, *ACS Energy Lett.* 3 (2018) 204–213.
- [148] Y. Dong, Y. Zhao, S. Zhang, Y. Dai, L. Liu, Y. Li, Q. Chen, *J. Mater. Chem. A* 6 (2018) 21729–21746.
- [149] G. Rose, Berlin AG Schade (1839).
- [150] A.R. Chakhmouradian, P.M. Woodward, *Phys. Chem. Miner.* 41 (2014) 387–391.
- [151] C.R. Berry, *Phys. Rev.* 161 (1967) 848–851.
- [152] Q.A. Akkerman, G. Rainò, M. V. Kovalenko, L. Manna, *Nat. Mater.* 17 (2018) 394–405.
- [153] T. Itoh, T. Kirihara, *J. Lumin.* 32 (1984) 120–122.
- [154] A.L. Efros, A.A. Onushchenko, *JETP Lett.* 34 (1981) 345–349.
- [155] A.L. Éfros, *Sov. Phys. Usp.* 16 (1974) 789–805.
- [156] M.A. Green, A. Ho-Baillie, H.J. Snaith, *Nat. Photonics* 8 (2014) 506–514.
- [157] M. Grätzel, *Nat. Mater.* 13 (2014) 838–842.
- [158] N.G. Park, *J. Phys. Chem. Lett.* 4 (2013) 2423–2429.

- 
- [159] A.K. Jena, A. Kulkarni, T. Miyasaka, *Chem. Rev.* 119 (2019) 3036–3103.
- [160] Y. Takeoka, K. Asai, M. Rikukawa, K. Sanui, *Chem. Commun.* 1 (2001) 2592–2593.
- [161] T. Kondo, S. Iwamoto, S. Hayase, K. Tanaka, J. Ishi, M. Mizuno, K. Ema, R. Ito, *Solid State Commun.* 105 (1997) 503–506.
- [162] L.C. Schmidt, A. Pertegás, S. González-Carrero, O. Malinkiewicz, S. Agouram, G. Mínguez Espallargas, H.J. Bolink, R.E. Galian, J. Pérez-Prieto, *J. Am. Chem. Soc.* 136 (2014) 850–853.
- [163] G. Nedelcu, L. Protesescu, S. Yakunin, M.I. Bodnarchuk, M.J. Grotevent, M. V. Kovalenko, *Nano Lett.* 15 (2015) 5635–5640.
- [164] S.D. Stranks, H.J. Snaith, S.D. Stranks, P.K. Nayak, W. Zhang, T. Stergiopoulos, H.J. Snaith, *Angew. Chemie - Int. Ed.* 54 (2015) 2–11.
- [165] H. Kim, C. Lee, J. Im, K. Lee, T. Moehl, A. Marchioro, S. Moon, R. Humphry-baker, J. Yum, J.E. Moser, M. Gra, *Sci. Rep.* 2 (2012) 1–7.
- [166] S.D. Stranks, G.E. Eperon, G. Grancini, C. Menelaou, M.J.P. Alcocer, T. Leijtens, L.M. Herz, A. Petrozza, H.J. Snaith, *Science* 342 (2013) 341–344.
- [167] M. Liu, M.B. Johnston, H.J. Snaith, *Nature* 501 (2013) 395–398.
- [168] W. Van Schalkwijk, N. Mater, *Science* 348 (2015) 2013–2017.
- [169] J.H. Heo, H.J. Han, D. Kim, T.K. Ahn, S.H. Im, *Energy Environ. Sci.* 8 (2015) 1602–1608.
- [170] Y. Shao, Z. Xiao, C. Bi, Y. Yuan, J. Huang, *Nat. Commun.* (2014) 1–7.
- [171] G.E. Eperon, V.M. Burlakov, A. Goriely, H.J. Snaith, *ACS Nano* 8 (2013) 591–598.
- [172] A. Cannavale, G.E. Eperon, P. Cossari, A. Abate, H.J. Snaith, G. Gigli, *Energy Environ. Sci.* 8 (2015) 1578–1584.
- [173] W. Zhang, M. Anaya, G. Lozano, M.E. Calvo, M.B. Johnston, *Nano Lett.* 15 (2015) 1698–1702.
- [174] Z. Li, Y. Zhao, Y. Li, Q. Chen, Z. Li, Y. Zhao, X. Wang, Y. Sun, Z. Zhao, Y. Li, H. Zhou, *Joule* 2 (2018) 1559–1572.
- [175] M. Saliba, T. Buonassisi, M. Grätzel, A. Abate, W. Tress, A. Hagfeldt, *Science* 358 (2017) 739–744.
- [176] M. Cai, Y. Wu, H. Chen, X. Yang, Y. Qiang, L. Han, *Adv. Sci.* 4 (2017) 1–6.
- [177] Y. Cao, N. Wang, H. Tian, J. Guo, Y. Wei, H. Chen, Y. Miao, W. Zou, K. Pan, Y. He, H. Cao, Y. Ke, M. Xu, Y. Wang, M. Yang, K. Du, Z. Fu, D. Kong, D. Dai, Y. Jin, G. Li, H. Li, Q. Peng, J. Wang, W. Huang, *Nature* 562 (2018).
- [178] M. Schaper, J. Schmidt, H. Plagwitz, R. Brendel, *Prog. Photovoltaics Res. Appl.* 13 (2005) 381–386.

- 
- [179] S. Yakunin, L. Protesescu, F. Krieg, M.I. Bodnarchuk, G. Nedelcu, M. Humer, G. De Luca, M. Fiebig, W. Heiss, M. V Kovalenko, *Nat. Commun.* 6 (2015) 1–8.
- [180] S. Yakunin, M. Sytnyk, D. Kriegner, S. Shrestha, M. Richter, G.J. Matt, H. Azimi, C.J. Brabec, J. Stangl, M. V Kovalenko, W. Heiss, *Nat. Photonics* 10 (2016) 1–7.
- [181] H. Wei, D. Desantis, W. Wei, Y. Deng, D. Guo, T.J. Savenije, L. Cao, J. Huang, *Nat. Mater.* 16 (2017) 1–9.
- [182] V.D. Innocenzo, A. Ram, S. Kandada, M. De Bastiani, M. Gandini, A. Petrozza, *J. Am. Chem. Soc.* 136 (2014) 17730–17733.
- [183] V.D. Innocenzo, G. Grancini, M.J.P. Alcocer, A. Ram, S. Kandada, S.D. Stranks, M.M. Lee, G. Lanzani, H.J. Snaith, A. Petrozza, *Nat. Commun.* 5 (2014) 1–6.
- [184] J. Luo, X. Wang, S. Li, J. Liu, Y. Guo, G. Niu, L. Yao, Y. Fu, L. Gao, Q. Dong, C. Zhao, M. Leng, F. Ma, W. Liang, L. Wang, S. Jin, J. Han, L. Zhang, J. Etheridge, J. Wang, Y. Yan, E.H. Sargent, J. Tang, *Nature* (2018).
- [185] L. Zhang, Y. Liu, Z. Yang, S. Frank, *J. Energy Chem.* 37 (2019) 97–110.
- [186] N. Armaroli, V. Balzani, *Angew. Chemie - Int. Ed.* 46 (2007) 52–66.
- [187] M. Crespo-Quesada, L.M. Pazos-ouo, J. Warnan, M.F. Kuehnel, R.H. Friend, E. Reisner, *Nat. Commun.* 7 (2016) 1–7.
- [188] N. Armaroli, V. Balzani, *Angew. Chemie - Int. Ed.* (2007) 52–66.
- [189] H. Zhang, Z. Yang, W. Yu, H. Wang, W. Ma, X. Zong, C. Li, *Adv. Energy Mater.* 1800795 (2018) 1–7.
- [190] S. Park, W.J. Chang, C.W. Lee, S. Park, H.Y. Ahn, K.T. Nam, *Nat. Energy* 2 (2017) 1–8.
- [191] Z. Guan, Y. Wu, P. Wang, Q. Zhang, Z. Wang, Z. Zheng, Y. Liu, Y. Dai, M. Whangbo, B. Huang, *Appl. Catal. B Environ.* 245 (2019) 522–527.
- [192] Y. Wu, P. Wang, Z. Guan, J. Liu, Z. Wang, Z. Zheng, S. Jin, Y. Dai, M. Whangbo, B. Huang, *ACS Catal.* 8 (2018) 10349–10357.
- [193] Z. Zhao, J. Wu, Y. Zheng, N. Li, X. Li, X. Tao, *ACS Catal.* 9 (2019) 8144–8152.
- [194] Y. Wu, P. Wang, X. Zhu, Q. Zhang, Z. Wang, Y. Liu, *Adv. Mater.* 1704342 (2018) 2–7.
- [195] P. V Kamat, *J. Am. Chem. Soc.* 137 (2015).
- [196] H. Wang, X. Wang, R. Chen, H. Zhang, X. Wang, *ACS Energy Lett.* 4 (2019) 40–47.
- [197] M. V Pavliuk, M. Abdellah, J. Sá, *Mater. Today Commun.* 16 (2018) 90–96.
- [198] S. Tabata, H. Nishida, Y. Masaki, K. Tabata, *Catal. Letters* 34 (1995) 245–249.
- [199] L. Liu, H. Zhao, J. Andino, Y. Li, *J. Accepted, ACS Catal.* 2 (2012) 1817–1828.

- 
- [200] J. Hou, S. Cao, Y. Wu, Z. Gao, J. Hou, S. Cao, Y. Wu, Z. Gao, F. Liang, Y. Sun, *Chem. - A Eur. J.* 23 (2017) 9481–9485.
- [201] Y. Xu, M. Yang, B. Chen, X. Wang, H. Chen, D. Kuang, C. Su, *J. Am. Chem. Soc.* 139 (2017) 5660–5663.
- [202] S. Guo, J. Zhou, X. Zhao, C. Sun, S. You, X. Wang, Z. Su, *J. Catal.* 369 (2019) 201–208.
- [203] L. Zhou, Y.-F. Xu, B.-X. Chen, D.-B. Kuang, C.-Y. Su, *Small* 14 (2018) 1–7.
- [204] S. Kumar, M. Regue, M. Isaacs, E. Freeman, S. Eslava, *ACS Appl. Energy Mater.* (2020).
- [205] C. Shell, C. Zeolitic, *ACS Energy Lett.* 3 (2018) 2656–2662.
- [206] Y. Xu, X. Wang, J. Liao, B. Chen, H. Chen, *Adv. Mater. Interfaces* (2018) 1–8.
- [207] D. Kuang, X. Wang, *J. Mater. Chem. A Mater. Energy Sustain.* 7 (2019) 13762–13769.
- [208] Z. Chen, Y. Hu, J. Wang, Q. Shen, Y. Zhang, C. Ding, Y. Bai, G. Jiang, Z. Li, N. Gaponik, *Chem., Chem. Mater.* 32 (2020) 1517–1525.
- [209] M. Ou, W. Tu, S. Yin, W. Xing, S. Wu, H. Wang, S. Wan, Q. Zhong, R. Xu, *Angew. Chemie - Int. Ed.* 130 (2018).
- [210] S. Wan, M. Ou, Q. Zhong, X. Wang, *Chem. Eng. J.* 358 (2019) 1287–1295.
- [211] L. Wu, Y. Mu, X. Guo, W. Zhang, Z. Zhang, M. Zhang, T. Lu, *Angew. Chemie - Int. Ed.* 131 (2019) 9591–9595.
- [212] S. Protti, M. Fagnoni, *Photochem. Photobiol. Sci.* 8 (2009) 1499–1516.
- [213] M. Oelgemöller, C. Jung, J. Mattay, *Pure Appl. Chem.* 79 (2007) 1939–1947.
- [214] M. Fagnoni, D. Dondi, D. Ravelli, A. Albin, *Chem. Rev.* 107 (2007) 2725–2756.
- [215] W.-B. Wu, Y.-C. Wong, Z.-K. Tan, J. Wu, *Catal. Sci. Technol.* 8 (2018) 4257–4263.
- [216] Y. Dai, H. Tüysüz, *ChemSusChem* 12 (2019) 2587–2592.
- [217] K. Chen, X. Deng, G. Dodekatos, *J. Am. Chem. Soc.* 139 (2017) 12267–12273.
- [218] X. Zhu, Y. Lin, Y. Sun, M.C. Beard, Y. Yan, Y. Lin, Y. Sun, M.C. Beard, Y. Yan, *J. Am. Chem. Soc.* 141 (2019) 773–738.
- [219] X. Zhu, Y. Lin, J. San Martin, Y. Sun, D. Zhu, Y. Yan, *Nat. Commun.* 10 (2019) 1–10.
- [220] H. Huang, H. Yuan, K. Janssen, G. Solís-fernández, Y. Wang, C.Y.X. Tan, D. Jonckheere, E. Debroye, J. Long, J. Hendrix, J. Hofkens, J.A. Steele, M.B.J. Roeffaers, *ACS Energy Lett.* 3 (2018) 755–759.
- [221] Y. Wong, J.D.A. Ng, Z. Tan, *Adv. Mater.* 1800774 (2018) 1–6.
- [222] L. Duen, M. Elimelech, X. Huang, G. Jiang, J. Kim, B.E. Logan, D.L. Sedlak, P. Westerho,

- P.J.J. Alvarez, *Environ. Sci. Technol.* 51 (2017) 10274–10281.
- [223] H. Huang, B. Pradhan, J. Hofkens, M.B.J. Roefsaers, J.A. Steele, *ACS Energy Lett.* 5 (2020) 1107–1123.
- [224] M. Ghanbari, F. Ansari, M. Salavati-niasari, *Inorganica Chim. Acta* 455 (2017) 88–97.
- [225] S. Bhattacharjee, S.P. Chaudhary, S. Bhattacharyya, *ChemRxiv* (2019).
- [226] S. Wan, M. Ou, Q. Zhong, X. Wang, *Chem. Eng. J.* 358 (2019) 1287–1295.
- [227] K.A. Huynh, L. Tri, V. Nguyen, D.N. Vo, Q. Thang, *J. Chem. Technol. Biotechnol.* (n.d.).
- [228] S. Schünemann, H. Tüysüz, *Eur. J. Inorg. Chem.* (2018) 2350–2355.
- [229] M. Aamir, Z. Hussain, M. Sher, A. Iqbal, *Mater. Sci. Semicond. Process.* 63 (2017) 6–11.
- [230] B.-M. Bresolin, S. Ben Hammouda, M. Sillanpää, *J. Photochem. Photobiol. A Chem.* 376 (2019) 116–126.
- [231] J.H. Im, J. Chung, S.J. Kim, N.G. Park, *Nanoscale Res. Lett.* 7 (2012) 1–7.
- [232] J. Navas, A. Sánchez-Coronilla, J.J. Gallardo, N. Cruz Hernández, J.C. Piñero, R. Alcántara, C. Fernández-Lorenzo, D.M. De Los Santos, T. Aguilar, J. Martín-Calleja, *Nanoscale* 7 (2015) 6216–6229.
- [233] N.K. Noel, S.D. Stranks, A. Abate, C. Wehrenfennig, S. Guarnera, A.A. Haghighirad, A. Sadhanala, G.E. Eperon, S.K. Pathak, M.B. Johnston, A. Petrozza, L.M. Herz, H.J. Snaith, *Energy Environ. Sci.* 7 (2014) 3061–3068.
- [234] M. Lyu, J.H. Yun, M. Cai, Y. Jiao, P. V. Bernhardt, M. Zhang, Q. Wang, A. Du, H. Wang, G. Liu, L. Wang, *Nano Res.* 9 (2016) 692–702.
- [235] N.G. Park, *Mater. Today* 18 (2015) 65–72.
- [236] M. Leng, Y. Yang, K. Zeng, Z. Chen, Z. Tan, S. Li, J. Li, B. Xu, D. Li, M.P. Hautzinger, Y. Fu, T. Zhai, L. Xu, *Adv. Funct. Mater.* (2017) 1–11.
- [237] D. Friedmann, C. Mendive, D. Bahnemann, *Appl. Catal. B Environ.* 99 (2010) 398–406.
- [238] V. Dal Santo, A. Naldoni, *Catalysts* 8 (2018) 1–21.
- [239] J.C. Yu, L. Zhang, Z. Zheng, J. Zhao, *Chem. Mater.* 15 (2003) 2280–2286.
- [240] R. Wang, G. Jiang, Y. Ding, Y. Wang, X. Sun, X. Wang, W. Chen, *ACS Appl. Mater. Interfaces* 3 (2011) 4154–4158.
- [241] H. McDaniel, P.E. Heil, C.L. Tsai, K. Kim, M. Shim, *ACS Nano* 5 (2011) 7677–7683.
- [242] Z. Jiang, K. Qian, C. Zhu, H. Sun, W. Wan, J. Xie, H. Li, P.K. Wong, S. Yuan, *Appl. Catal. B Environ.* 210 (2017) 194–204.



- 
- [243] H. Zhang, L. Zhao, F. Geng, L.H. Guo, B. Wan, Y. Yang, *Appl. Catal. B Environ.* 180 (2016) 656–662.
- [244] S.M. Lam, J.C. Sin, A.R. Mohamed, *Mater. Sci. Semicond. Process.* 47 (2016) 62–84.
- [245] E. Grabowska, *Appl. Catal. B Environ.* 186 (2016) 97–126.
- [246] Z. Zhang, X. Li, X. Xia, Z. Wang, Z. Huang, B. Lei, Y. Gao, *J. Phys. Chem. Lett.* 8 (2017) 4300–4307.
- [247] B. Park, B. Philippe, X. Zhang, H. Rensmo, G. Boschloo, E.M.J. Johansson, *Adv. Mater.* 27 (2015) 6806–6813.
- [248] C. Lan, J. Luo, S. Zhao, C. Zhang, W. Liu, S. Hayase, T. Ma, *J. Alloys Compd.* 701 (2017) 834–840.
- [249] K. Eckhardt, V. Bon, J. Getzschmann, J. Grothe, F.M. Wisser, S. Kaskel, *Chem. Commun.* 52 (2016) 3058–3060.
- [250] A.J. Lehner, D.H. Fabini, H.A. Evans, C.A. Hébert, S.R. Smock, J. Hu, H. Wang, J.W. Zwanziger, M.L. Chabiny, R. Seshadri, *Chem. Mater.* 27 (2015) 7137–7148.
- [251] E. Forgacs, T. Cserhádi, G. Oros, *Environ. Int.* 30 (2004) 953–971.
- [252] C.I. Pearce, J.R. Lloyd, J.T. Guthrie, *Dye. Pigment.* 58 (2003) 179–196.
- [253] M.A. Rauf, S.S. Ashraf, *Chem. Eng. J.* 151 (2009) 10–18.
- [254] S. Song, J. Yao, Z. He, J. Qiu, J. Chen, *J. Hazard. Mater.* 152 (2008) 204–210.
- [255] M.A. Rauf, S.B. Bukallah, A. Hamadi, A. Sulaiman, F. Hammadi, *Chem. Eng. J.* 129 (2007) 167–172.
- [256] W. Wang, M.O. Tadé, Z. Shao, *Chem. Soc. Rev.* 44 (2015) 5371–5408.
- [257] T. Salthammer, S. Mentese, R. Marutzky, *Chem. Rev.* 110 (2010) 2536–2572.
- [258] K. Nagaveni, G. Sivalingam, M.S. Hegde, G. Madras, *Appl. Catal. B Environ.* 48 (2004) 83–93.
- [259] A.T. Toor, A. Verma, C.K. Jotshi, P.K. Bajpai, V. Singh, *Dye. Pigment.* 68 (2006) 53–60.
- [260] W. Zhang, Q. Zhao, X. Wang, X. Yan, J. Xu, Z. Zeng, *Catal. Sci. Technol.* 7 (2017) 2753–2762.
- [261] P. Ganguly, M. Harb, Z. Cao, L. Cavallo, A. Breen, S. Dervin, D.D. Dionysiou, S.C. Pillai, *ACS Energy Lett.* 4 (2019) 1687–1709.
- [262] H. Yu, W. Liu, X. Wang, F. Wang, *Appl. Catal. B Environ.* 225 (2018) 415–423.
- [263] P. Nikolaidis, A. Poullikkas, *Renew. Sustain. Energy Rev.* 67 (2017) 597–611.
- [264] M. Fittipaldi, D. Gatteschi, P. Fornasiero, *Catal. Today* 206 (2013) 2–11.
- [265] Z. Li, Y. Han, Z. Gao, F. Wang, *ACS Catal.* 7 (2017) 4676–4681.

- 
- [266] Y. Zhang, A.N. Barnes, X. Zhu, N.F. Campbell, R. Gao, J. Photochem. Photobiol. A Chem. 224 (2011) 16–24.
- [267] S.P. Jovanović, Z. Syrgiannis, Z.M. Marković, A. Bonasera, D.P. Kepić, M.D. Budimir, D.D. Milivojević, V.D. Spasojević, M.D. Dramićanin, V.B. Pavlović, B.M. Todorović Marković, ACS Appl. Mater. Interfaces 7 (2015) 25865–25874.
- [268] J.T. Schneider, D.S. Firak, R.R. Ribeiro, P. Peralta-Zamora, Phys. Chem. Chem. Phys. 22 (2020) 15723–15733.
- [269] S. Chen, Y. Hu, S. Meng, X. Fu, Appl. Catal. B Environ. 150–151 (2014) 564–573.
- [270] T. Wu, G. Liu, J. Zhao, H. Hidaka, N. Serpone, J. Phys. Chem. B 102 (1998) 5845–5851.
- [271] M. Beija, C.A.M. Afonso, J.M.G. Martinho, Chem. Soc. Rev. 38 (2009) 2410.
- [272] O. Ola, M.M. Maroto-Valer, J. Photochem. Photobiol. C Photochem. Rev. 24 (2015) 16–42.
- [273] S.K. Yadav, P. Jeevanandam, J. Alloys Compd. 649 (2015) 483–490.
- [274] K. Yu, S. Yang, H. He, C. Sun, C. Gu, Y. Ju, J. Phys. Chem. A 113 (2009) 10024–10032.



## **Publication I**

Bresolin, B.M., Ben Hammouda, S., and Sillanpää, M.  
**An Emerging Visible-Light Organic–Inorganic Hybrid Perovskite for Photocatalytic Applications**

Reprinted with permission from  
*Nanomaterials*  
Vol. 10 (115), pp. 1-17, 2019  
© 2019, MDPI



Article

# An Emerging Visible-Light Organic–Inorganic Hybrid Perovskite for Photocatalytic Applications

Bianca-Maria Bresolin <sup>1,\*</sup> , Samia Ben Hammouda <sup>1</sup> and Mika Sillanpää <sup>1,2</sup>

<sup>1</sup> Laboratory of Green Chemistry, School of Engineering Science, Lappeenranta University of Technology, Sammonkatu 12, 50130 Mikkeli, Finland; samiabenhammouda@gmail.com (S.B.H.); Mika.Sillanpaa@lut.fi (M.S.)

<sup>2</sup> Department of Civil and Environmental Engineering, Florida International University, Miami, FL 33174, USA

\* Correspondence: biancabresolin@yahoo.it or Bianca-maria.Bresolin@lut.fi

Received: 23 October 2019; Accepted: 28 December 2019; Published: 7 January 2020



**Abstract:** The development of visible-light active photocatalysts is a current challenge especially energy and environmental-related fields. Herein, methylammonium lead iodide perovskite (MAIPb) was chosen as the novel semiconductor material for its ability of absorbing visible-light. An easily reproducible and efficient method was employed to synthesize the as-mentioned material. The sample was characterized by various techniques and has been used as visible-light photocatalyst for degradation of two model pollutants: rhodamine B (RhB) and methylene-blue (MB). The photo-degradation of RhB was found to achieve about 65% after 180 min of treatment. Moreover, the efficiency was enhanced to 100% by assisting the process with a small amount of H<sub>2</sub>O<sub>2</sub>. The visible-light activity of the photocatalyst was attributed to its ability to absorb light as well as to enhance separation of photogenerated carriers. The main outcome of the present work is the investigation of a hybrid perovskite as photocatalyst for wastewater treatment.

**Keywords:** halide perovskite; photocatalysis; visible-light; Rhodamine B; oxidation

## 1. Introduction

Nowadays, environment pollution and energy related issues captured the attention of new century researchers [1–5]. In particular, accelerated release of pollutants because of a combination of growing population and a rapid industrial development have dramatically increased the water pollution in many parts of the world. On the other hand, it is equally urgent to answer the increasing energy demand and mitigate the negative effect of global warming by means of renewable energy sources. Thus, efficient and eco-friendly methods for the degradation of organic pollutants based on renewable energy source, such as solar light, have become an imperative task worldwide [6–11].

Heterogeneous photocatalysis consists in the dispersion of a solid material, usually a semiconductor, that when irradiated at appropriated wavelengths is capable to generate highly reactive oxygen species (ROS) which can degrade organic pollutants [12,13]. Photocatalysis main advantages are: the room temperature operation, the utilization of clean and renewable solar light as the driving force and any production of hazardous residues after mineralization to align with the “zero” waste scheme for industries [14,15].

Recently, hybrid organic–inorganic halide perovskites (HOIPs) have gain a lot of attention, especially in photovoltaics, because of their remarkable properties. It was 2009 when for the first time Miyasaka and his colleagues employed hybrid perovskites in photovoltaic devices [16]. Then, the studies of the HOIPs have stunned the research community with their remarkable performance and rapid progress [17].

Perovskite general formula is  $ABX_3$ . HOIP A-site is occupied by an organic cation, B-site by a metal of group IVA in a divalent oxidation state and X-site by a halogen anion [18]. As reported in previous studies, the electronic properties of the mentioned perovskites is mainly governed by the B-X bonds [19]. Electronic properties are fundamental in the understanding of heterogeneous photocatalysis [20].

Herein, focusing on the compositional, structural, optical, and charges transportation properties, we investigated this class of materials as promising candidate for photocatalytic applications [18,21–25]. First, the advantageous properties are a favorable mobility of the photogenerated charges, a reduced surface recombination and long electron–hole diffusion length because of the strong defect tolerance, the shallow point defects and the benign grain boundary. Second, these materials are known to own an enhanced visible-light shift absorption ability and suitable band gap [23,24]. Moreover, they can be produced by low cost solution processes [26].

According to literature, lead-based HOIPs (MAIPb) has achieved the best efficiency among all the studied hybrid perovskites [27–31]. In MAIPb, A-site is occupied by methyl ammonium cation ( $CH_3NH_3^+$ ), the B-site by lead cation ( $Pb^{2+}$ ), and the X-site by iodine anion ( $I^-$ ) (Figure 1) [32,33].

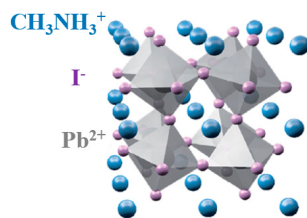


**Figure 1.** Hybrid organic inorganic perovskite tetragonal structure.

Herein, we propose to determine the feasibility of MAIPb, as one of the most promising HOIPs, as visible-light photocatalyst for the degradation of some dyes having different chemical structures. In particular we investigate the photocatalytic degradation on rhodamine B (RhB, fluorone dye) and methylene blue (MB, thiazine dye) because these dyes are extensively used in industries and medicines [34,35]. Moreover, the effect of key operating conditions on degradation efficiency were studied: catalyst loading, addition of hydrogen peroxide, radiation intensity, solution pH, solution temperature, pollutant initial concentration, and potential recycling test.

## 2. Experimental

### 2.1. Materials

Methylamine ( $CH_3NH_2$ , 33 wt% in ethanol), hydriodic acid distilled (HI 57 wt% in water), diethyl ether (DE purity  $\geq 99.8\%$ ), lead (II) iodide ( $PbI_2$  purity 99%),  $\gamma$ -butyrolactone (GBL purity  $\geq 99\%$ ) were purchased from Sigma Aldrich (Darmstadt, Germany) and used as received. The target dye pollutants RhB, was obtained from Sigma Aldrich (Darmstadt, Germany).

### 2.2. Photo-Catalyst Synthesis

Hybrid organic-inorganic perovskite was prepared with a one-step, solution-processed method as described in previous literature report [18].  $CH_3NH_2$  (11.39 mL, 0.09 mol) and HI (10 mL, 0.08 mol) were stirred for 2 h in an ice bath kept at  $0^\circ C$  to synthesize the precursor,  $CH_3NH_3I$ . The solution was evaporated at  $50^\circ C$  and the solid was washed three times with DE and dried at  $50^\circ C$  on a hot plate. The  $CH_3NH_3I$  (0.39 g) and  $PbI_2$  (1.16 g) were mixed in GBL (10 mL). Finally, the sample was dried at  $60^\circ C$  for 6 h until the solution was completely evaporated. Before performing photo-catalytic oxidation process, the catalyst was washed several time with deionized water. It should be mentioned that methylammonium was selected as precursor because it is most widely used as A-site cation

since its radius appeared to be the more suitable resulting in low packing symmetry and high band gap [36,37]. In comparison to other elements of group IV, Pb was selected because of its performance and stability [18,38–40]. In particular, along group IV from Pb to Ge, it was previously reported a decrease in stability of the divalent oxidation state and a consequent decrease in band gap value combined with a reduced inert electron pair effects [41]. Among the halogens, iodide was selected for its higher efficiency compared to other elements [16]. Moreover, in the periodic table iodide lies close to Pb, thus, they result in more stable structure by sharing similar covalent character [18]. However, we must notice that many factors remain not entirely understood. Moreover, some barriers are still to overcome as stability and toxicity in large-scale implementation.

### 2.3. Photo-Catalyst Characterization

The X-ray powder diffraction (XRD) spectrum of the catalyst was recorded by PANalytical instrument with the empyrean program (PANalytical, Cambridge, UK) with Co-K $\alpha$  ( $\lambda = 1.7809 \text{ \AA}$ ) as the radiation source, 40 kV generator voltage and 40 mA tube current. The diffraction angle ( $2\theta$ ) ranged from  $20^\circ$  and  $80^\circ$  with intervals of  $0.05^\circ$ . The sample functional groups were characterized by Fourier transform infrared spectra (FT-IR) (Bruker, Solna, Sweden) in the region from  $400$  to  $4000 \text{ cm}^{-1}$  at room temperature using Horiba FT-730 FT-IR spectrometer. The microstructure and morphology of the material were defined using scanning electron microscope (SEM) Hitachi SU3500 (Chiyoda, Tokyo, Japan). Energy dispersive spectroscopy (EDS) (Thermo Scientific, Waltham, MA, USA) detected the elemental composition of the pure hybrid organic-inorganic perovskite. The surface composition and the electronic states of elements in the valence-band region were determined by ESCALAB 250 X-ray photoelectron spectroscopy (XPS) (ThermoFisher Scientific, Waltham, MA, USA) with Al-K $\alpha$  ( $1486.6 \text{ eV}$ ) as the X-ray source. Absorption spectra were measured with a PerkinElmer Lambda 1050 spectrophotometer (UV-vis) (PerkinElmer, Waltham, MA, USA) to establish the absorption spectrum and band gap of the sample.

### 2.4. Procedure for Photo-Catalysis

The visible-light photocatalytic efficiency was evaluated based on the degradation of RhB. All experiments were carried out in Pyrex vessels (100 mL) with 50 mL of RhB ( $20 \text{ mg}\cdot\text{L}^{-1}$ ). Specified amount of reaction mixture was withdrawn at regular time intervals and analyzed with UV-vis spectrophotometer at emission wavelength of  $554 \text{ nm}$  [42]. The efficiency of RhB removal was determined as follow:

$$\text{Removal efficiency \%} = C/C_0 \quad (1)$$

where  $C_0$  is the initial concentration of RhB and  $C$  is the measured concentration at the time of withdrawal [43,44]. Electron spin resonance (ESR) technique with proper spin traps was used to determine the presence of reactive oxygen species (ROS). TEMP (2,2,6,6-tetramethylpiperidine) was used as spin trap for singlet oxygen and DMSO (dimethyl sulfoxide) for superoxide and hydroxyl radicals [45,46]. The specifics of the visible-light device, used in the current research, are reported in the Supporting Information (Table S1 and Figure S1).

## 3. Results and Discussion

### 3.1. Photo-Catalyst Characterization

The morphology of the material was investigated with SEM, the results, shown in Figure 2A,B, suggest an aggregation of nanoparticles with hexagonal shape domains with nanometers size. The specific morphology of the crystal lattice is mainly influenced by the synthesizing temperature and may affect the optical, electrical, and transmission properties of the material, as confirmed in the study of Li et al. [47].



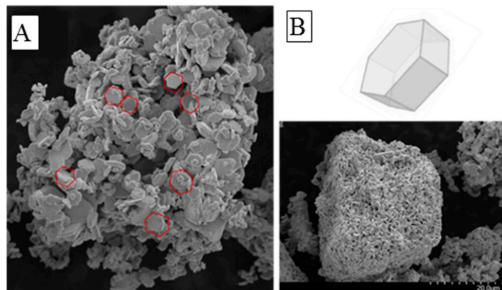


**Figure 2.** (A,B) Scanning electron microscopy (SEM) image of the as-prepared MAIPb (methylammonium lead iodide perovskite).

In order to access the sorption behavior of these materials in aqueous phase,  $N_2$  sorption can provide some useful information for the characterization and evaluation of the performance of the photocatalyst [48]. As indicated by the analysis in Figure S2, the sample showed type III according to IUPAC classification.

Figure S3 shows EDS spectra of the sample. The analysis confirms the presence of C, N, O, Pb, and I. The ratio C:N:I:Pb was found to be 4.06:0.58:42.33:49.62. Lower signals for carbon and nitrogen can be assigned to their lighter atomic weights. XRD pattern of the sample is presented in Figure 3A. Hexagonal crystal system was mainly detected with space groups  $P3m1$ . Dominant diffraction peaks at  $2\theta = 14.7, 30.2, 40, 46.26,$  and  $53.01^\circ$  were assigned respectively to the (002), (012), (104), (110), and (106) facets of the hexagonal crystalline structure. Peaks at  $14.7$  and  $30.2^\circ$  were also indexed to (110) and (220) facets of the tetragonal structure of perovskite according to literature [49]. It should be noted the diffraction peaks of  $PbI_2$ , assigned at  $2\theta$  equals to  $12.8^\circ$ . The miller indexes (h, k, l) recorded suggested more than one preferred crystal orientation in our samples.

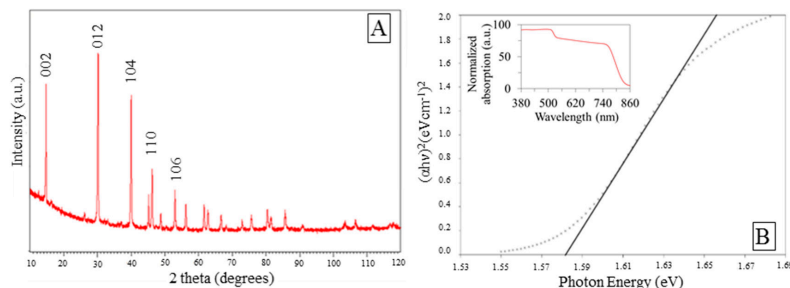


**Figure 3.** (A) X-ray diffraction (XRD) spectrum of the as-prepared MAIPb, (B) UV-vis spectrum and Tauc plot of the as prepared MAIPb.

Figure S4 displays FT-IR spectrum of the synthesized organo-halide perovskite. The sample showed broad vibrations N-H from  $2800$  to  $3350\text{ cm}^{-1}$ , the characteristic features of hydrogen bonds overlapped the C-H vibrations signs. The peaks at  $1450\text{ cm}^{-1}$  and around  $650\text{--}750\text{ cm}^{-1}$  belong to the organic cation vibrations since the Pb-I and Pb-I-Pb appeared in very lower energy [50,51]. Peaks displayed at  $1500$  and  $956\text{ cm}^{-1}$  can be respectively assigned to N-Pb-I stretching mode and Pb-I-NH bending. The wide bend around  $3100\text{ cm}^{-1}$  was assigned to CH-NH stretching vibration [52].

The optical properties were further investigated in terms of light absorption capability because the absorption of light energy is one of the key of photocatalytic processes. Hybrid organic-inorganic perovskite achieves an optical absorbance across the entire visible spectrum as highlighted by Dualeh [53]. Carrier diffusion lengths was found to reach up to  $100\text{ nm}$  for both electrons and holes

in MAIPb via transient photo-luminescence measurements [54,55]. A nearly instantaneous charge generation and dissociations of balanced free charge carriers with high mobility has been observed, and the charges were proved to remain in that state for up to tens of microseconds [56]. From previous literature, it was found that the electronic levels for hybrid perovskites consist of an antibonding hybrid state between the Pb-s and I-p and a non-bonding hybrid state between the Pb-p and I-p orbitals corresponding to highest occupied and lowest unoccupied molecular orbitals, respectively [57]. The electronic properties were not influenced by organic fraction. In particular, Frost et al. showed that VB transition is primarily affected by the ionization potential of halogen ions contribution [58].

In Figure 3B the optical band gap of the perovskite was calculated. From extrapolation of the linear part of the Tauc plot (Kubelka–Munk theory), the optical gap was estimated to be 1.58 eV, which is in close agreement with previous reports [18,21,59–62].

XPS measurements were performed in order to investigate the chemical bonding states of the element in the envisaged catalyst Figure 4A. According to Navas et al. [18], peaks at 143 and 138.1 eV can be assigned to Pb 4f (Figure 5B); peaks around 412 eV, showed in Figure 4B, were assigned to Pb 4d<sub>5/2</sub>. The bigger peaks can be associated with the Pb component in the halide hybrid perovskite structure, while the smaller to metallic Pb probability decomposed from PbI during the synthesis [63]. Peak corresponding to 401 eV peak were assigned to N1s Figure 4D. In accordance with the studies performed by Chen et al. [64], N state may vary and the associated peaks can be found at different BE. Different peaks positions were found in a range of 396–404 eV in agreement with Nakamura and Mrowetz et al. [65]. Conforming to the study of Navas et al. [18], the peaks shown in Figure 4C belong to I 3d<sub>3/2</sub> and I 3d<sub>5/2</sub>. It was further shown that the spectrum shows well separated spin–orbit components, separation of around 11.4–11.5 eV was recorded as typical evidence of the presence of I<sup>0</sup> [18]. Figure 4E shows peak belongs to C1s around 285 eV. Shen et al. [54], in their interesting research on hybrid organic-inorganic perovskite for solar cell application, assigned this peak to the methyl group. The conclusion obtained here agrees well with that reported by previous literature confirming the achievement of the synthesis processes [18,63–66].

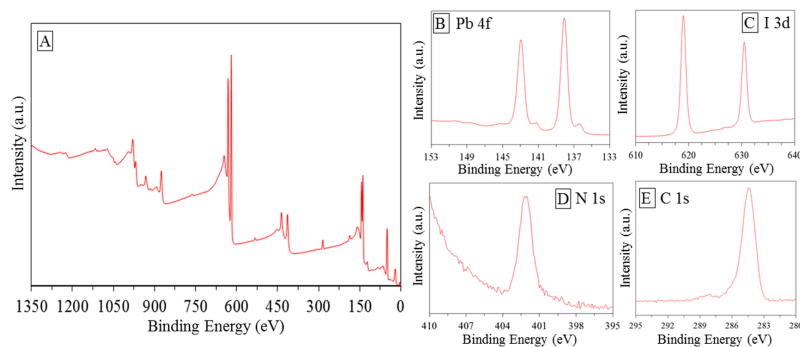


**Figure 4.** X-ray photoelectron spectroscopy (XPS) spectra of the as-prepared MAIPb: (A) general spectrum, (B–E) zooming on specific binding energy range.

### 3.2. Photocatalytic Activity

Among the persistent contaminants, organic dye molecules are toxic and their uncontrolled discharge from various industries into the water can have a huge impact on the environment [67]. In our study, the photocatalytic activity of the synthesized nano-catalyst was examined on RhB removal, which is considered as one of the most abundant dyes in the textile industries effluents and commonly chosen as model pollutant for photocatalytic treatment [68,69]. The photocatalytic performance of investigated material was evaluated as the decrease of the relative concentrations of RhB ( $C/C_0$ ) plotted over time in different conditions. The removal efficiency achieved by photolysis

was found to be negligible. This fact suggests that the chosen pollutant owns excellent photo-stability, as highlighted by Drexhage et al. and Beija et al. [70,71]. Control experiment in dark conditions was evaluated. The results showed moderate affinity between the halide perovskite and RhB molecules in terms of adsorption in darkness. The result are in accordance with the low surface area measured by BET analysis. As expected, significant improvement on RhB removal efficiency was observed during the photocatalytic experiments Figure 5A. After 3 h of irradiation, the concentration of RhB greatly decreased with respect to the initial concentration, proving the activity of the as-synthesized photocatalyst. The UV-vis spectra indicate that the main absorbance peak was reduced as a function of irradiation time and the dye molecules were decolorized. On the other hand, the peak position was found to be invariable and the diminishing intensity suggested that the fused aromatic ring structures and dye chromophores were destroyed (Figure S5). Kibombo et al. achieved similar results during their researches on optimization of photocatalysts for persistent organic pollutant remediation in wastewater management [72]. In their work it was deeply explained how the reactive oxygen species attack the auxochromic groups, induce N-de-ethylation of the alkyl amine group and how photogenerated holes can degrade both RhB suspended molecules and N-de-ethylated products. As depicted in Figure 5, the removal efficiency appeared at the very first interval (15 min), this is in accordance with the ROS generation that is higher at the earlier step of irradiation [73–75].

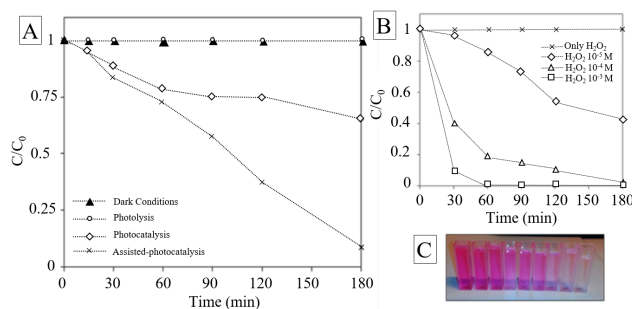


**Figure 5.** (A) Degradation of Rhodamine B (RhB) in dark condition, photolysis, photocatalysis, assisted-photocatalysis; (B) degradation of RhB under different  $\text{H}_2\text{O}_2$  concentration conditions  $10^{-4}$ ,  $10^{-3}$ ,  $10^{-5}$   $\text{mol}\cdot\text{L}^{-1}$ ; (C) picture of color extinction of RhB as function of time.

The potential of the as-prepared material in photodegradation of a different organic compound was further investigated. In particular, methylene blue (MB) was chosen as the target contaminant. Methylene blue could be successfully removed by the assisted photocatalytic reaction after 60 min under visible-light irradiation. The results were compared with blank experiments to demonstrate the photocatalytic nature of the reaction. The results and the comparison are shown in Supporting Information (Figure S6).

The photocatalytic activity of the as-prepared nanoparticles showed higher photocatalytic efficiency for MB dye compared to RhB. The differences in the recorded efficiencies can be attributed to the chemical structures of the organic dyes and the nature of the functional groups present on their surfaces.

### 3.3. Effect of $\text{H}_2\text{O}_2$ on the Photocatalysis Treatment

Many techniques have been applied to reduce the effect of recombination of charges and to enhance the heterogenous photocatalysis performance. Among these techniques, the assistance of external electron acceptor such as hydrogen peroxide ( $\text{H}_2\text{O}_2$ ) in the photocatalytic process has gained more and more attention. The effect of  $\text{H}_2\text{O}_2$  on photocatalytic oxidation of RhB in aqueous suspensions of the as-synthesized material was investigated. Various concentrations of oxidant were used. Test without the presence of a photocatalyst was performed. In addition, the photocatalytic degradation of RhB was found to follow the pseudo first-order reaction model:

$$\ln(C/C_0) = -kt \quad (2)$$

The degradation rate constant  $k$  and the correlation coefficient of the curve  $R^2$  were obtained using regression analysis. The value of  $R^2$  were higher than 0.92, thus it was assumed that the regression line fits well with the data (Table 1).

**Table 1.** Degradation rate constant  $k$  and the correlation coefficient.

Experiment	Rate (s <sup>-1</sup> )	R <sup>2</sup>
Assisted photocatalysis H <sub>2</sub> O <sub>2</sub> 10 <sup>-5</sup> mol·L <sup>-1</sup>	0.0045	0.94
Assisted photocatalysis H <sub>2</sub> O <sub>2</sub> 10 <sup>-3</sup> mol·L <sup>-1</sup>	0.0215	0.92
Assisted photocatalysis H <sub>2</sub> O <sub>2</sub> 10 <sup>-3</sup> mol·L <sup>-1</sup>	0.1087	0.92

The reaction rate increased with H<sub>2</sub>O<sub>2</sub> dosages. For the highest concentration of oxidant (10<sup>-3</sup> mol·L<sup>-1</sup>), the kinetic rate was found to be almost 25 times higher than the lowest concentration and 5 times higher than the average concentration. For practical application and considering the cost of hydrogen peroxide, 10<sup>-4</sup> mol·L<sup>-1</sup> was considered as the optimal value. The combination of halide perovskite and H<sub>2</sub>O<sub>2</sub> under visible-light illumination was found to greatly enhance the degradation rates of RhB. When H<sub>2</sub>O<sub>2</sub> concentration increases, more hydroxyl radicals are produced thus the oxidation rate increases. ROS were considered as dominant mechanism in the photocatalytic process. The first hypothesis is a direct photolysis of H<sub>2</sub>O<sub>2</sub> by visible light that may generate free radicals at a wavelength of 405 nm [76]. A second minor mechanism proposed by Ollis et al. [77] and Ilisz et al. [78] suggested that H<sub>2</sub>O<sub>2</sub> may partially contribute to the rate enhancement of photo-catalytic process behaving as an electron acceptor. According to these theories, H<sub>2</sub>O<sub>2</sub> cannot only generate ·OH but also as electron acceptor, reduce the electrons-holes recombination increasing the photocatalytic efficiency. On the other hand Dionysiou et al. [79] in their studies on assisted-H<sub>2</sub>O<sub>2</sub>-photocatalysis showed that high concentrations of hydrogen peroxide may decrease the degradation rates because of the consumption of hydroxyl radicals.

#### 3.4. Effect of Catalyst Loading

The effect of catalyst load on the ability to remove RhB in aqueous solution is shown in Figure 6A. The results suggest that the removal performance increased with the catalyst load up to 0.5 g·L<sup>-1</sup> and decreased when the load is higher. This is in agreement with the case observed in heterogeneous photo-catalysis reaction. This behavior can be rationalized both in terms of availability of active sites on material surface and light penetration of photo-activating light into the system. The availability of active sites increased with catalyst loading, but on contrary the light penetration and, hence, the photo-activated volume of particles decreased [80]. Moreover, higher amount of catalyst may induce the deactivation of particles by collision with ground state molecules reducing the rate of reaction [81]. The trade-off of these effects was studied by considering also the organic contaminant concentration.

#### 3.5. Effect of Initial Concentration of RhB

The effect of RhB initial concentration is an important parameter to consider [82]. Figure 6B depicts the effect of RhB initial concentration on its removal. The result reveals that the increase of the RhB concentration decreases the removal, corresponding to those from literature [1].

At higher RhB concentration, the generation of radicals on the surface of catalyst may be reduced by the competition of the active sites covered by RhB ions. Moreover, with the increase in the concentration the photons may be intercepted before they can reach the catalyst surface, decreasing the absorption of photons by the catalyst [83]. Higher concentration of RhB may also cause aggregation and even surface dimerization and have consequentially an effect on the degradation rates [42].

### 3.6. Effect of Initial pH

The pH of the dye solution was altered by adding incremental amounts of either dilute HCl or diluted NaOH in order to study the effect of pH on dye removal. Previously, it was confirmed that none of the salts used had any effect on the dye spectra in the absence of light. The solution was subjected to irradiation and change in absorbance value was noted.

The removal rate was found to increase in acidic media as shown in Figure 6C. The photolytic dye degradation appeared to be the best at pH 3 and it decreased when pH was increased. The results implied that in alkaline medium new oxidizing species, such as hydroperoxy anion can be formed. The new species can react with both the reactive oxygen species such as hydroxyl radicals as well as H<sub>2</sub>O<sub>2</sub> molecules. This can consequently lower the dye contaminant removal rate. Future studies will be required to clarify the effect of pH on dye discoloration.

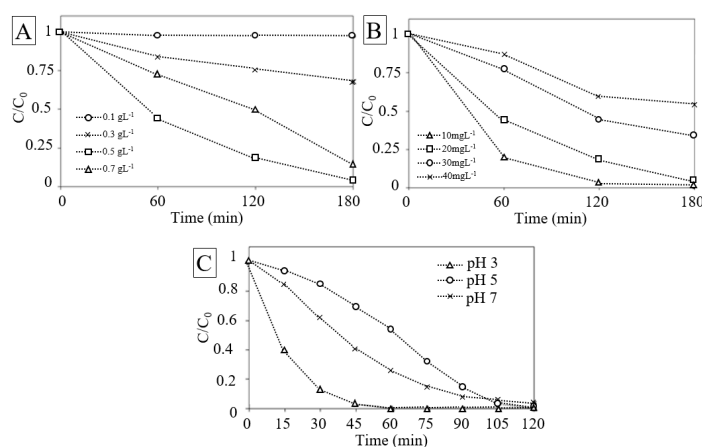


**Figure 6.** (A) Effect of catalyst load. (B) Effect of RhB initial concentration. (C) Effect of RhB initial pH value.

### 3.7. Effect of Temperature on H<sub>2</sub>O<sub>2</sub>-Assisted Photo-Catalysis

According to Wang et al. [84], temperature is another parameter that affects the heterogenous photo-catalysis. Therefore, in this study, 25 °C, 35 °C, 45 °C were selected to examine the effect of temperature on photo-catalysis under visible light irradiation. As the temperature increased from 25 to 45 °C, the first-order rate constant  $k_1$  increased almost 40% (Table 2). This behavior was associated to a decrease in the viscosity and to an enhanced diffusion of the sorbate molecule [85].

**Table 2.** Impact of temperature on the RhB removal kinetic rate under the CH<sub>3</sub>NH<sub>3</sub>PbI<sub>3</sub>/visible irradiation system, experimental conditions RhB: (20 mg·L<sup>-1</sup>), H<sub>2</sub>O<sub>2</sub> (10<sup>-4</sup> M), photo-catalyst (0.5 g·L<sup>-1</sup>), pH 5.

Temperature (°C)	Kinetic rate (min <sup>-1</sup> )	R <sup>2</sup>
25	0.0328	0.9632
35	0.0499	0.9143
45	0.0840	0.8526

The Arrhenius equation was used to determine the activation energy as follows:

$$K = A \cdot \exp(-Ea/RT) \quad (3)$$

where  $K$  is the constant rate that controls the entire process,  $A$  is the Arrhenius constant,  $T$  the solution temperature in  $K$ ,  $E_a$  apparent activation energy ( $\text{kJ}\cdot\text{mol}^{-1}$ ), and  $R$  the ideal gas constant  $0.0083 \text{ kJ mol}^{-1}\cdot\text{K}^{-1}$ . The data are fitted using a linear regression ( $R^2 = 0.9935$ ). From the Arrhenius-type plot (Figure 7).  $E_a$  value was calculated as  $36.96 \text{ kJ}\cdot\text{mol}^{-1}$ . Mcheik and El Jamal found similar result in their study on removal of RhB with persulfate and iron activation [86]. The reaction appeared to be activated also at room temperature and proceeded with relatively low energy barrier.

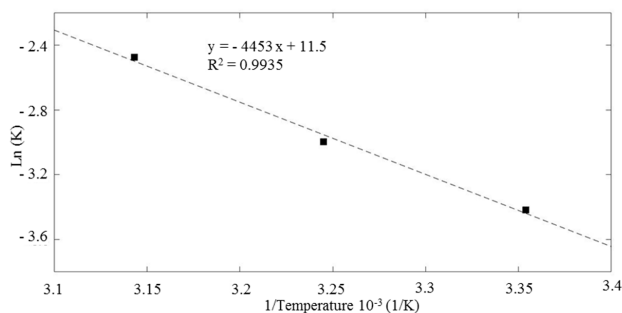


Figure 7. Arrhenius-type plot for the evaluation of the activation energy of the reaction.

### 3.8. Recyclability of the $\text{H}_2\text{O}_2$ -Assisted Photo-Catalysis System

Recyclability of the photocatalyst represents one of the most important advantages of a heterogeneous application. Thus, the recyclability of the synthesized material was evaluated by using  $\text{H}_2\text{O}_2$  to activate the process for multiple cycles. Figure 8 shows three cycles of the RhB removal using the  $\text{H}_2\text{O}_2$ -hybrid organic-inorganic perovskite system irradiated under visible light. It can be seen that after 3 cycles, the system showed a stable and effective catalytic activity on the removal of the selected dye, and the activity loss was negligible. RhB degradation efficiency showed slight decrease from 93% to 80% after 120 min of the third treatment. The results obtained may be caused by active sites saturation. Moreover, the recycle was performed in series, thus a slight decrease in photocatalyst content should be considered. It must be mentioned that the main aim of the former study is to investigate the potential of HOIPs in photocatalytic processes. Further development on material and process technology should be applied.

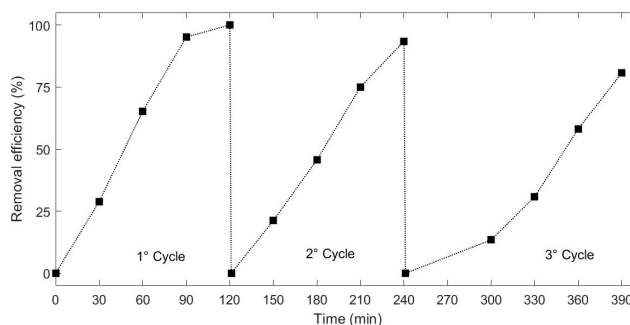


Figure 8. Degradation profile of RhB under assisted visible light photo-catalysis for three cycles.

### 3.9. Active Species and Possible Mechanism

In a typical photocatalytic application, when a semiconductor is irradiated with equivalent or greater light-energy, the electrons ( $e^-$ ) in the valence band (VB) are excited into the conduction band (CB) leaving holes ( $h^+$ ) in the VB. The photo-generated electrons and holes trigger the redox reaction.

When the bottoms of the CB is below the reduction potential of  $H^+$  to  $H_2$  (0 V vs. NHE), and the tops of the VB must be located more positively than the oxidation potential of  $H_2O$  to  $O_2$  (1.23 V vs. NHE) both oxidation and reduction sites are created [87]. The electron/hole pairs and reactive oxygen species (ROS), including  $O_2^{\cdot-}$ , and  $\cdot OH$ , are widely considered the main active species responsible for photocatalytic degradation of organic contaminants [88,89].

As deeply studied by Han et al. [90], the electron spin resonance (ESR) spin-trap technique confirms the presence of free radicals. DMPO and TEMP were used as spin trap for superoxide or hydroxide radicals anions ( $O_2^{\cdot-}$ ,  $\cdot OH$ ) and singlet oxygen species ( $^1O_2$ ), respectively.

In detail, upon visible light photo-excitation of the mixture of the organo-halide perovskite and diamagnetic 2,2,6,6-tetramethylpiperidine (TEMP), three lines with equal intensities were observed in the recorded spectrum in Figure 9. This indicates the capture of singlet oxygen ( $^1O_2$ ) generated by TEMP, leading to the formation of the TEMPO radical. The irradiation period was set at 5 min, a signal of  $g = 2.0001$  appeared confirming photo-generation of radicals. The time of irradiation increased and the intensity of peaks decreased, after half-hour of irradiation the resulting spectrum is shown in Figure 9A. The decrease in spectrum intensity of peaks suggests that  $^1O_2$  radical generation occurred in the very first intervals of the photo-catalytic process that is mainly due to their nano-second lifetime [46,91,92]. 5,5-dimethylpyrroline N-oxide (DMPO) was utilized as superoxide and hydroxide radical anions ( $O_2^{\cdot-}$ ,  $\cdot OH$ ) spin trap. Four typical peaks appeared in the ESR spectrum revealing the presence of the radicals,  $g$  factor was found equal to 1.9985. Later, the sampling period was increased, and the lower peaks were recorded, indicating that radical generation belongs to the initial period of irradiation. Figure 9B shows the radical peaks after 5 min of irradiation. The signal recorded after 30 min shows a decrease in the intensity of peaks implying that no more radicals are present in the solution.

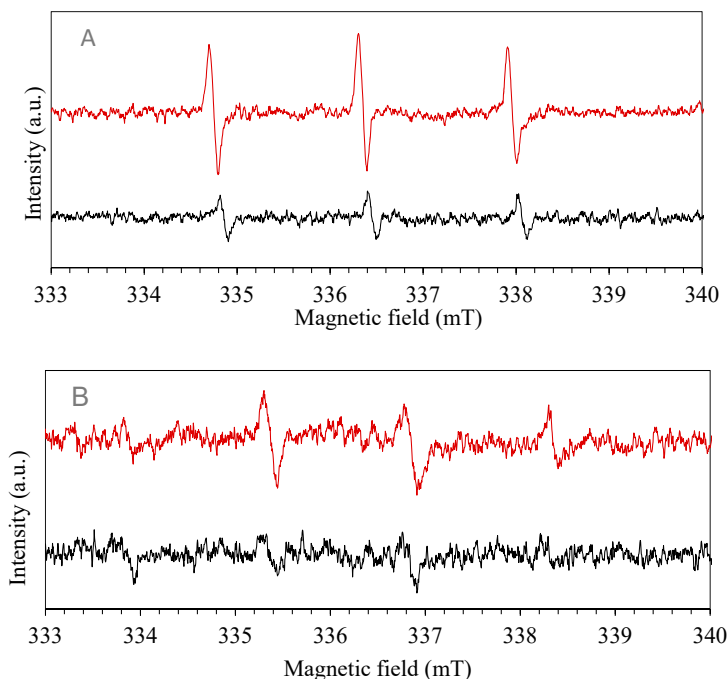


**Figure 9.** Electron paramagnetic resonance (EPR) spectra using as spin-trap: (A) TEMP, red for 5 min, black for 30 min; (B) DMPO, red for 5 min, black for 30 min.

Finally, to evaluate also the effect of RhB in the production of radicals, a solution of equal content (100  $\mu\text{L}$ ) of RhB (20  $\text{mg}\cdot\text{L}^{-1}$ ) and DMPO (100 mM) was prepared and irradiated in the presence of photo-catalyst. After an irradiation time of 5 min, the ESR spectrum was recorded revealing the presence of  $\cdot\text{OH}$  radicals (Figure 10). Four typical peaks were recorded also in presence of RhB, revealing a potential synergetic effect between photo-catalyst and organic dye in the production of hydroxyl and superoxide species. A mixed solution of RhB and DMPO was also prepared in the absence of photo-catalyst to confirm the absence of the radicals.

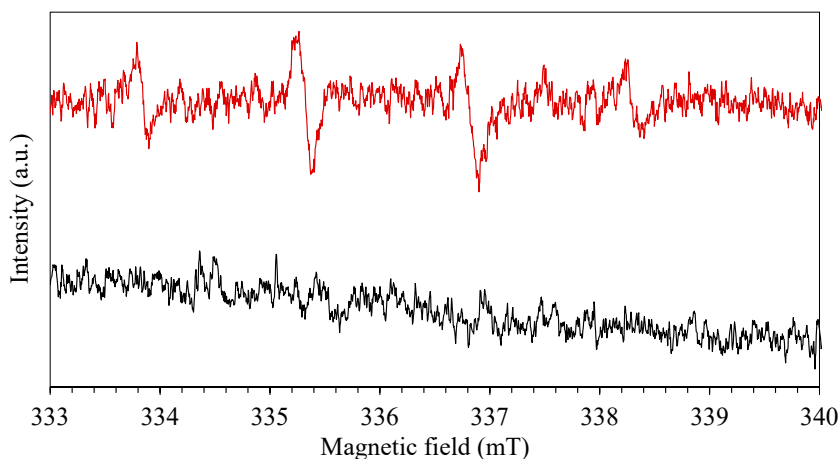


**Figure 10.** EPR spectra using DMPO as spin-trap in presence of RhB, red with catalyst and black without catalyst.

From the results described above, it may be concluded that both  $^1\text{O}_2$ ,  $\text{O}_2^{\cdot-}$  and  $\cdot\text{OH}$  radicals were produced during the visible-light photo-catalyst treatment of RhB [93,94].

The photocatalytic degradation process proceeds through excitation, transportation, and degradation pathways. As highlighted by Yin et al. [19], during the investigation mechanism of photocatalytic degradation of RhB by  $\text{TiO}_2/\text{Eosin-Y}$  system under visible light, dye molecules transfer electrons onto conduction bands (CB) of catalyst leading to the formation of dye cationic radicals. Then the involved electrons generate a series of active oxygen species such as  $\text{O}_2^{\cdot-}$ ,  $\cdot\text{OH}$ , and  $^1\text{O}_2$  which are considered to be involved in the organic contaminant degradation. In a similar study performed by Dutta et al. [95], two main mechanisms were proposed to promote dye degradation, one governed by dye sensitization and the other by the photo-catalyst excitation. In the self-sensitized dye degradation, the photo-induced electrons flow from the dyes to photo-catalyst surface as suggested by their potential energy values. In particular, Lv et al. [96], with their respective co-authors, deeply described the direction of the charge flow; the difference in the potential energy between the CBs induces the electrons to transfer from higher energy level of the photo-excited dye to the lower ones of catalyst. On the other hand, visible light excitation of MAIPb structures could also generate holes in the valance band (VB) and electrons in the CB. Egger et al. studied the tunability of VB (ionization potential) and CB (electron affinity) energies by the atomic orbitals of the anions and cations in different organohalide perovskite [97]. Band energy and band gap engineering of these organic-inorganic solids are indeed possible to be controlled by the chemical composition, and iodine presence was found to upshift the VB and generally narrowing the band gap, favorable condition for bleaching organic compound in aqueous solutions.

The CB transported electrons in both the materials may react with the dissolved oxygen in the water to produce a reactive oxygen species, main responsible for the oxidative dye degradation under



visible light irradiation. As confirmed by an interesting study on nanosized  $\text{Bi}_2\text{WO}_6$  performed under visible light by Fu et al. [98], the presence of oxygen is responsible for the activation of photo-catalysis process. In their experiments, they confirmed the importance of the presence of dissolved oxygen in the treated solution, since its effect is primarily to act as an efficient  $e^-$  trap, leading to the generation of reactive oxygen species and preventing the recombination of charges. Furthermore, Dutta et al. highlighted a similar conclusion in their study on ternary nano-composite based on cadmium sulphide ( $\text{CdS}$ ),  $\text{TiO}_2$ , and graphene oxide. Herein, they proved how generated electrons react with the dissolved oxygen in water to produce a reactive oxidizing agent initially in the specific form of oxygen radical anion  $\text{O}_2^{\cdot-}$ , responsible for the oxidative dye degradation under visible light irradiation [95].

Based on the previous discussion, a possible mechanism of RhB is depicted in Figure 11. After self-sensitization of RhB and the excitation of organohalide perovskite, separation of charges occurs, and transport of electron is promoted. On the other hand, dissolved oxygen can act as an electron acceptor, and can be reduced by the promoted electron in the conduction band to form a superoxide specie  $\text{O}_2^{\cdot-}$  (3). The  $\text{O}_2^{\cdot-}$  can subsequently re-oxidize to  $^1\text{O}_2$  or, in the presence of water and  $\text{H}_2\text{O}_2$ , it can form  $\cdot\text{OH}$ . The strong oxidation power of the hole enables a one-electron oxidation step with water to produce a hydroxyl radical  $\cdot\text{OH}$ . These radicals are highly ROS, able to oxidize directly organic contaminant. In our study, the generation of  $\text{O}_2^{\cdot-}$  and  $\cdot\text{OH}$  was confirmed by the ESR spectra by using DMPO as the spin trap reagent [45], instead, TEMP was used to detect singlet oxygen and it proved electrons and holes generation during visible light irradiation [46].

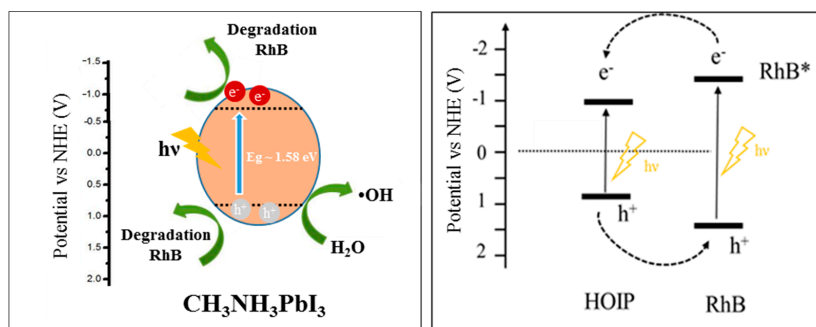


Figure 11. Proposed band gap energy diagram and charge transfer between RhB and photo-catalyst.

#### 4. Conclusions

In conclusion, bare MAIPb were easily synthesized for the photocatalytic degradation of organic dye pollutants. The degradation performance study suggested that RHB was completely degraded after 180 min of treatment assisted by  $\text{H}_2\text{O}_2$ -MAIPb system under visible light irradiation. In this work, we have shown that the outstanding optoelectronic properties of MAIPb can be addressed for photocatalytic degradation of organic compounds. The results constitute a significant step forward in the application of hybrid halide perovskite for solar-driven catalytic processes. It is important to mention that the systematic evaluation of the environmental conditions must be deeply studied.

**Supplementary Materials:** The supplementary materials are available online at <http://www.mdpi.com/2079-4991/10/1/115/s1>.

**Author Contributions:** B.-M.B. as author of research and editor of manuscript, S.B.H. as co-supervisor, M.S. as supervisor and funding provider. All authors have read and agreed to the published version of the manuscript.

**Funding:** This research was funded by Maa-ja vesiteknikaan tuki Foundation.

**Conflicts of Interest:** The authors declare no conflict of interest.

## References

1. Chakrabarti, S.; Dutta, B.K. Photocatalytic degradation of model textile dyes in wastewater using ZnO as semiconductor catalyst. *J. Hazard. Mater.* **2004**, *112*, 269–278. [[CrossRef](#)] [[PubMed](#)]
2. Crake, A.; Christoforidis, K.C.; Godin, R.; Moss, B.; Kafizas, A.; Zafeiratos, S.; Durrant, J.R.; Petit, C. Titanium dioxide/carbon nitride nanosheet nanocomposites for gas phase CO<sub>2</sub> photoreduction under UV-visible irradiation. *Appl. Catal. B Environ.* **2019**, *242*, 369–378. [[CrossRef](#)]
3. Fujishima, A.; Zhang, X.; Tryk, D.A. Heterogeneous photocatalysis: From water photolysis to applications in environmental cleanup. *Int. J. Hydrog. Energy* **2007**, *32*, 2664–2672. [[CrossRef](#)]
4. Hoffmann, M.R.; Martin, S.T.; Choi, W.; Bahnemann, D.W. Environmental Applications of Semiconductor Photocatalysis. *Chem. Rev.* **1995**, *95*, 69. [[CrossRef](#)]
5. Huang, J.H.; Huang, K.L.; Liu, S.Q.; Wang, A.T.; Yan, C. Adsorption of Rhodamine B and methyl orange on a hypercrosslinked polymeric adsorbent in aqueous solution. *Colloids Surfaces A Physicochem. Eng. Asp.* **2008**, *330*, 55–61. [[CrossRef](#)]
6. Lefebvre, O.; Moletta, R. Treatment of organic pollution in industrial saline wastewater: A literature review. *Water Res.* **2006**, *40*, 3671–3682. [[CrossRef](#)]
7. Teng, F.; Liu, Z.; Zhang, A.; Li, M. Photocatalytic Performances of Ag<sub>3</sub>PO<sub>4</sub> Polypods for Degradation of Dye Pollutant under Natural Indoor Weak Light Irradiation. *Environ. Sci. Technol.* **2015**, *49*, 9489–9494. [[CrossRef](#)]
8. Spasiano, D.; Marotta, R.; Malato, S.; Fernandez-Ibañez, P.; di Somma, I. Solar photocatalysis: Materials, reactors, some commercial, and pre-industrialized applications. A comprehensive approach. *Appl. Catal. B Environ.* **2015**, *170–171*, 90–123. [[CrossRef](#)]
9. Patrocínio, A.O.T.; Schneider, J.; França, M.D.; Santos, L.M.; Caixeta, B.P.; Machado, A.E.H.; Bahnemann, D.W. Charge carrier dynamics and photocatalytic behavior of TiO<sub>2</sub> nanopowders submitted to hydrothermal or conventional heat treatment. *RSC Adv.* **2015**, *5*, 70536–70545. [[CrossRef](#)]
10. Natarajan, T.S.; Bajaj, H.C.; Tayade, R.J. Enhanced direct sunlight photocatalytic oxidation of methanol using nanocrystalline TiO<sub>2</sub> calcined at different temperature. *J. Nanopart. Res.* **2014**, *16*, 2713. [[CrossRef](#)]
11. Kou, J.; Lu, C.; Wang, J.; Chen, Y.; Xu, Z.; Varma, R.S. Selectivity Enhancement in Heterogeneous Photocatalytic Transformations. *Chem. Rev.* **2017**, *117*, 1445–1514. [[CrossRef](#)] [[PubMed](#)]
12. Zhang, X.; Wang, Y.; Hou, F.; Li, H.; Yang, Y.; Zhang, X.; Yang, Y.; Wang, Y. Effects of Ag loading on structural and photocatalytic properties of flower-like ZnO microspheres. *Appl. Surf. Sci.* **2017**, *391*, 476–483. [[CrossRef](#)]
13. Zhang, X.; Yang, Y.; Huang, W.; Yang, Y.; Wang, Y.; He, C.; Liu, N.; Wu, M.; Tang, L. g-C<sub>3</sub>N<sub>4</sub>/UiO-66 nanohybrids with enhanced photocatalytic activities for the oxidation of dye under visible light irradiation. *Mater. Res. Bull.* **2018**, *99*, 349–358. [[CrossRef](#)]
14. Geng, X.; Li, W.; Xiao, F.; Wang, D.; Yang, L. Effect of in situ Fe(II)/Fe(III)-doping on the visible light-Fenton-like catalytic activity of Bi/BiOBr hierarchical microspheres. *Catal. Sci. Technol.* **2017**, *7*, 658–667. [[CrossRef](#)]
15. Takanebe, K. Photocatalytic Water Splitting: Quantitative Approaches toward Photocatalyst by Design. *ACS Catal.* **2017**, *7*, 8006–8022. [[CrossRef](#)]
16. Kojima, A.; Teshima, K.; Shirai, Y.; Miyasaka, T. Organometal Halide Perovskites as Visible-Light Sensitizers for Photovoltaic Cells. *J. Am. Chem. Soc.* **2009**, *131*, 6050–6051. [[CrossRef](#)]
17. Tang, H.; He, S.; Peng, C. A Short Progress Report on High-Efficiency Perovskite Solar Cells. *Nanoscale Res. Lett.* **2017**, *12*, 410. [[CrossRef](#)]
18. Navas, J.; Sánchez-Coronilla, A.; Gallardo, J.J.; Hernández, N.C.; Piñero, J.C.; Alcántara, R.; Fernández-Lorenzo, C.; de los Santos, D.M.; Aguilar, T.; Martín-Calleja, J. New insights into organic-inorganic hybrid perovskite CH<sub>3</sub>NH<sub>3</sub>PbI<sub>3</sub> nanoparticles. An experimental and theoretical study of doping in Pb<sup>2+</sup> sites with Sn<sup>2+</sup>, Sr<sup>2+</sup>, Cd<sup>2+</sup> and Ca<sup>2+</sup>. *Nanoscale* **2015**, *7*, 6216–6229. [[CrossRef](#)]
19. Yin, W.J.; Shi, T.; Yan, Y. Unique properties of halide perovskites as possible origins of the superior solar cell performance. *Adv. Mater.* **2014**, *26*, 4653–4658. [[CrossRef](#)]
20. Hantusch, M.; Bessergenev, V.; Mateus, M.C.; Knupfer, M.; Burkel, E. Electronic properties of photocatalytic improved Degussa P25 titanium dioxide powder. *Catal. Today* **2018**, *307*, 111–118. [[CrossRef](#)]
21. Kim, H.-S.; Lee, C.-R.; Im, J.-H.; Lee, K.-B.; Moehl, T.; Marchioro, A.; Moon, S.-J.; Humphry-Baker, R.; Yum, J.-H.; Moser, J.E.; et al. Lead Iodide Perovskite Sensitized All-Solid-State Submicron Thin Film Mesoscopic Solar Cell with Efficiency Exceeding 9%. *Sci. Rep.* **2012**, *2*, 591. [[CrossRef](#)] [[PubMed](#)]
22. Mauro, J.C. Topological constraint theory of glass. *Am. Ceram. Soc. Bull.* **2011**, *90*, 31–37. [[CrossRef](#)]

23. Stranks, S.D.; Stranks, S.D.; Eperon, G.E.; Grancini, G.; Menelaou, C.; Alcocer, M.J.P.; Leijtens, T.; Herz, L.M.; Petrozza, A.; Snaith, H.J. Electron-Hole Diffusion Lengths Exceeding. *Science* **2014**, *342*, 341–344. [[CrossRef](#)] [[PubMed](#)]
24. Chen, Q.; de Marco, N.; Yang, Y.; Song, T.B.; Chen, C.C.; Zhao, H.; Hong, Z.; Zhou, H.; Yang, Y. Under the spotlight: The organic-inorganic hybrid halide perovskite for optoelectronic applications. *Nano Today* **2015**, *10*, 355–396. [[CrossRef](#)]
25. Xing, G.; Mathews, N.; Sun, S.; Lim, S.S.; Lam, Y.M.; Gratzel, M.; Mhaisalkar, S.; Sum, T.C. Long-Range Balanced Electron- and Hole-Transport Lengths in Organic-Inorganic  $\text{CH}_3\text{NH}_3\text{PbI}_3$ . *Science* **2013**, *342*, 344–347. [[CrossRef](#)] [[PubMed](#)]
26. Singh, T.; Kulkarni, A.; Ikegami, M.; Miyasaka, T. Effect of Electron Transporting Layer on Bismuth-Based Lead-Free Perovskite ( $\text{CH}_3\text{NH}_3$ ) $_3$   $\text{Bi}_2\text{I}_9$  for Photovoltaic Applications. *ACS Appl. Mater. Interfaces* **2016**, *8*, 14542–14547. [[CrossRef](#)]
27. Butler, K.T.; Frost, J.M.; Walsh, A. Band alignment of the hybrid halide perovskites  $\text{CH}_3\text{NH}_3\text{PbCl}_3$ ,  $\text{CH}_3\text{NH}_3\text{PbBr}_3$  and  $\text{CH}_3\text{NH}_3\text{PbI}_3$ . *Mater. Horiz.* **2015**, *2*, 228–231. [[CrossRef](#)]
28. Jeon, N.J.; Noh, J.H.; Yang, W.S.; Kim, Y.C.; Ryu, S.; Seo, J.; Seok, S.I. Compositional engineering of perovskite materials for high-performance solar cells. *Nature* **2015**, *517*, 476–480. [[CrossRef](#)]
29. Zhou, H.; Shen, Q.; Li, G.; Luo, S.; Song, T.; Duan, H.-S.; Hong, Z.; You, J.; Liu, Y.; Yang, Y. Interface engineering of highly efficient perovskite solar cells. *Science* **2014**, *345*, 542–546. [[CrossRef](#)]
30. Liu, M.; Johnston, M.B.; Snaith, H.J. Efficient planar heterojunction perovskite solar cells by vapour deposition. *Nature* **2013**, *501*, 395–398. [[CrossRef](#)]
31. Burschka, J.; Pellet, N.; Moon, S.-J.; Humphry-Baker, R.; Gao, P.; Nazeeruddin, M.K.; Grätzel, M. Sequential deposition as a route to high-performance perovskite-sensitized solar cells. *Nature* **2013**, *499*, 316–319. [[CrossRef](#)] [[PubMed](#)]
32. Niu, G.; Guo, X.; Wang, L. Review of recent progress in chemical stability of perovskite solar cells. *J. Mater. Chem. A* **2015**, *3*, 8970–8980. [[CrossRef](#)]
33. Acik, M.; Darling, S.B. Graphene in perovskite solar cells: Device design, characterization and implementation. *J. Mater. Chem. A* **2016**, *4*, 6185–6235. [[CrossRef](#)]
34. Gupta, A.K.; Pal, A.; Sahoo, C. Photocatalytic degradation of a mixture of Crystal Violet (Basic Violet 3) and Methyl Red dye in aqueous suspensions using  $\text{Ag}^+$  doped  $\text{TiO}_2$ . *Dye. Pigment* **2006**, *69*, 224–232. [[CrossRef](#)]
35. Girija, K.; Thirumalairajan, S.; Mastelaro, V.R.; Mangalaraj, D. Photocatalytic degradation of organic pollutants by shape selective synthesis of  $\beta$ - $\text{Ga}_2\text{O}_3$  microspheres constituted by nanospheres for environmental remediation. *J. Mater. Chem. A* **2015**, *3*, 2617–2627. [[CrossRef](#)]
36. McKinnon, N.K.; Reeves, D.C.; Akabas, M.H. 5-HT $_3$  receptor ion size selectivity is a property of the transmembrane channel, not the cytoplasmic vestibule portals. *J. Gen. Physiol.* **2011**, *138*, 453–466. [[CrossRef](#)]
37. Im, J.-H.; Chung, J.; Kim, S.-J.; Park, N.-G. Synthesis, structure, and photovoltaic property of a nanocrystalline 2H perovskite-type novel sensitizer ( $\text{CH}_3\text{CH}_2\text{NH}_3$ ) $\text{PbI}_3$ . *Nanoscale Res. Lett.* **2012**, *7*, 353. [[CrossRef](#)]
38. Umari, P.; Mosconi, E.; de Angelis, F. Relativistic GW calculations on  $\text{CH}_3\text{NH}_3\text{PbI}_3$  and  $\text{CH}_3\text{NH}_3\text{SnI}_3$  Perovskites for Solar Cell Applications. *Sci. Rep.* **2015**, *4*, 4467. [[CrossRef](#)]
39. Green, M.A.; Ho-Baillie, A.; Snaith, H.J. The emergence of perovskite solar cells. *Nat. Photonics* **2014**, *8*, 506–514. [[CrossRef](#)]
40. Bernal, C.; Yang, K. First-principles hybrid functional study of the organic-inorganic perovskites  $\text{CH}_3\text{NH}_3\text{SnBr}_3$  and  $\text{CH}_3\text{NH}_3\text{SnI}_3$ . *J. Phys. Chem. C* **2014**, *118*, 24383–24388. [[CrossRef](#)]
41. Noel, N.K.; Stranks, S.D.; Abate, A.; Wehrenfennig, C.; Guarnera, S.; Haghighirad, A.-A.; Sadhanala, A.; Eperon, G.E.; Pathak, S.K.; Johnston, M.B.; et al. Lead-free organic-inorganic tin halide perovskites for photovoltaic applications. *Energy Environ. Sci.* **2014**, *7*, 3061–3068. [[CrossRef](#)]
42. Rochkind, M.; Pasternak, S.; Paz, Y. Using dyes for evaluating photocatalytic properties: A critical review. *Molecules* **2015**, *20*, 88–110. [[CrossRef](#)] [[PubMed](#)]
43. Liu, N.; Huang, W.; Tang, M.; Yin, C.; Gao, B.; Li, Z.; Tang, L.; Lei, J.; Cui, L.; Zhang, X. In-situ fabrication of needle-shaped MIL-53(Fe) with 1T-MoS $_2$  and study on its enhanced photocatalytic mechanism of ibuprofen. *Chem. Eng. J.* **2019**, *359*, 254–264. [[CrossRef](#)]
44. Liu, N.; Huang, W.; Zhang, X.; Tang, L.; Wang, L.; Wang, Y.; Wu, M. Ultrathin graphene oxide encapsulated in uniform MIL-88A(Fe) for enhanced visible light-driven photodegradation of RhB. *Appl. Catal. B Environ.* **2018**, *221*, 119–128. [[CrossRef](#)]

45. Gross, J.J. HHS Public Access. *Free Radic. Res. Commun.* **2016**, *34*, 352–359.
46. Li, Z.; Han, Y.; Gao, Z.; Wang, F. Supramolecular Engineering of Discrete Pt(II)···Pt(II) Interactions for Visible-Light Photocatalysis. *ACS Catal.* **2017**, *7*, 4676–4681. [[CrossRef](#)]
47. Li, D.; Wang, G.; Cheng, H.-C.; Chen, C.-Y.; Wu, H.; Liu, Y.; Huang, Y.; Duan, X. Size-dependent phase transition in methylammonium lead iodide perovskite microplate crystals. *Nat. Commun.* **2016**, *7*. [[CrossRef](#)]
48. Zhang, X.; Yang, Y.; Lv, X.; Wang, Y.; Liu, N.; Chen, D.; Cui, L. Adsorption/desorption kinetics and breakthrough of gaseous toluene for modified microporous-mesoporous UiO-66 metal organic framework. *J. Hazard. Mater.* **2019**, *366*, 140–150. [[CrossRef](#)]
49. Grabowska, E. Selected perovskite oxides: Characterization, preparation and photocatalytic properties—A review. *Appl. Catal. B Environ.* **2016**, *186*, 97–126. [[CrossRef](#)]
50. Pérez-Osorio, M.A.; Milot, R.L.; Filip, M.R.; Patel, J.B.; Herz, L.M.; Johnston, M.B.; Giustino, F. Vibrational Properties of the Organic-Inorganic Halide Perovskite  $\text{CH}_3\text{NH}_3\text{PbI}_3$  from Theory and Experiment: Factor Group Analysis, First-Principles Calculations, and Low-Temperature Infrared Spectra. *J. Phys. Chem. C* **2015**, *119*, 25703–25718. [[CrossRef](#)]
51. Que, C.J.; Mo, C.J.; Li, Z.Q.; Zhang, G.L.; Zhu, Q.Y.; Dai, J. Perovskite-Like Organic-Inorganic Hybrid Lead Iodide with a Large Organic Cation Incorporated within the Layers. *Inorg. Chem.* **2017**, *56*, 2467–2472. [[CrossRef](#)] [[PubMed](#)]
52. Kumar, V.B.; Gouda, L.; Porat, Z.; Gedanken, A. Sonochemical synthesis of  $\text{CH}_3\text{NH}_3\text{PbI}_3$  perovskite ultrathin nanocrystal sensitizers for solar energy applications. *Ultrason. Sonochem.* **2016**, *32*, 54–59. [[CrossRef](#)] [[PubMed](#)]
53. Dualeh, A.; Moehl, T.; Tétreault, N.; Teuscher, J.; Gao, P.; Nazeeruddin, M.K.; Grätzel, M. Impedance spectroscopic analysis of lead iodide perovskite-sensitized solid-state solar cells. *ACS Nano* **2014**, *8*, 362–373. [[CrossRef](#)] [[PubMed](#)]
54. Shen, P.-S.; Chiang, Y.-H.; Li, M.-H.; Guo, T.-F.; Chen, P. Research Update: Hybrid organic-inorganic perovskite (HOIP) thin films and solar cells by vapor phase reaction. *APL Mater.* **2016**, *4*, 91509. [[CrossRef](#)]
55. Liu, J.; Liu, Y.; Liu, N.; Han, Y.; Zhang, X.; Huang, H.; Lifshitz, Y.; Lee, S.; Zhong, J.; Kang, Z. Metal-free efficient photocatalyst for stable visible water splitting via a two-electron pathway. *Science* **2015**, *6709*, 1–6.
56. Ponceca, C.S.; Savenije, T.J.; Abdellah, M.; Zheng, K.; Yartsev, A.; Pascher, T.; Harlang, T.; Chabera, P.; Pullerits, T.; Stepanov, A.; et al. Organometal halide perovskite solar cell materials rationalized: Ultrafast charge generation, high and microsecond-long balanced mobilities, and slow recombination. *J. Am. Chem. Soc.* **2014**, *136*, 5189–5192. [[CrossRef](#)]
57. Brivio, F.; Walker, A.B.; Walsh, A. Structural and electronic properties of hybrid perovskites for high-efficiency thin-film photovoltaics from first-principles. *APL Mater.* **2013**, *1*, 9–14. [[CrossRef](#)]
58. Frost, J.M.; Butler, K.T.; Brivio, F.; Hendon, C.H.; van Schilfgaarde, M.; Walsh, A. Atomistic origins of high-performance in hybrid halide perovskite solar cells. *Nano Lett.* **2014**, *14*, 2584–2590. [[CrossRef](#)]
59. Chatterjee, S.; Pal, A.J. Introducing  $\text{Cu}_2\text{O}$  Thin Films as a Hole-Transport Layer in Efficient Planar Perovskite Solar Cell Structures. *J. Phys. Chem. C* **2016**, *120*, 1428–1437. [[CrossRef](#)]
60. Zhao, Y.; Zhu, K. Charge Transport and Recombination in Perovskite ( $\text{CH}_3\text{NH}_3$ ) $\text{PbI}_3$  Sensitized  $\text{TiO}_2$  Solar Cells. *J. Phys. Chem. Lett.* **2013**, 2880–2884. [[CrossRef](#)]
61. Noh, J.H.; Im, S.H.; Heo, J.H.; Mandal, T.N.; Seok, S.I. Chemical Management for Colorful, Efficient, and Stable Inorganic–Organic Hybrid Nanostructured Solar Cells. *Nano Lett.* **2013**, *13*, 1764–1769. [[CrossRef](#)] [[PubMed](#)]
62. Zhao, Y.; Zhu, K. Optical bleaching of perovskite ( $\text{CH}_3\text{NH}_3$ ) $\text{PbI}_3$  through room-temperature phase transformation induced by ammonia. *Chem. Commun.* **2014**, *50*, 1605–1607. [[CrossRef](#)] [[PubMed](#)]
63. Xie, H.; Liu, X.; Lyu, L.; Niu, D.; Wang, Q.; Huang, J.; Gao, Y. Effects of Precursor Ratios and Annealing on Electronic Structure and Surface Composition of  $\text{CH}_3\text{NH}_3\text{PbI}_3$  Perovskite Films. *J. Phys. Chem. C* **2015**. [[CrossRef](#)]
64. Chen, J.; He, Z.; Li, G.; An, T.; Shi, H.; Li, Y. Visible-light-enhanced photothermocatalytic activity of  $\text{ABO}_3$ -type perovskites for the decontamination of gaseous styrene. *Appl. Catal. B Environ.* **2017**, *209*, 146–154. [[CrossRef](#)]
65. Mrowetz, M.; Balcerski, W.; Colussi, A.J.; Hoffmann, M.R. Oxidative power of nitrogen-doped  $\text{TiO}_2$  photocatalysts under visible illumination. *J. Phys. Chem. B* **2004**, *108*, 17269–17273. [[CrossRef](#)]
66. Nakamura, R.; Tanaka, T.; Nakato, Y. Mechanism for visible light responses in anodic photocurrents at N-doped  $\text{TiO}_2$  film electrodes. *J. Phys. Chem. B* **2004**, *108*, 10617–10620. [[CrossRef](#)]

67. Dutta, S.; Sarkar, S.; Ray, C.; Pal, T. Benzoin derived reduced graphene oxide (rGO) and its nanocomposite: Application in dye removal and peroxidase-like activity. *RSC Adv.* **2013**, *3*, 21475. [[CrossRef](#)]
68. Sinha, A.K.; Pradhan, M.; Sarkar, S.; Pal, T. Large-scale solid-state synthesis of Sn-SnO<sub>2</sub> nanoparticles from layered SnO by sunlight: A material for dye degradation in water by photocatalytic reaction. *Environ. Sci. Technol.* **2013**, *47*, 2339–2345. [[CrossRef](#)]
69. Ray, C.; Dutta, S.; Sarkar, S.; Sahoo, R.; Roy, A.; Pal, T. A facile synthesis of 1D nano structured selenium and Au decorated nano selenium: Catalysts for the clock reaction. *RSC Adv.* **2013**, *3*, 24313. [[CrossRef](#)]
70. Drexhage, K.H.H. Fluorescence efficiency of laser dyes. *J. Res. Natl. Bur. Stand. Sect. A Phys. Chem.* **1976**, *80*, 421. [[CrossRef](#)]
71. Beija, M.; Afonso, C.A.M.; Martinho, J.M.G. Synthesis and applications of Rhodamine derivatives as fluorescent probes. *Chem. Soc. Rev.* **2009**, *38*, 2410. [[CrossRef](#)] [[PubMed](#)]
72. Kibombo, H.S.; Rasalingam, S.; Koodali, R.T. Facile template free method for textural property modulation that enhances adsorption and photocatalytic activity of aperiodic titania supported silica materials. *Appl. Catal. B Environ.* **2013**, *142*, 119–128. [[CrossRef](#)]
73. Chen, H.; Xu, X. Ruddlesden-Popper compounds in the double-perovskite family Sr<sub>2</sub>FeTaO<sub>6</sub>(SrO)<sub>n</sub> (n = 0, 1 and 2) and their photocatalytic properties. *Appl. Catal. B Environ.* **2017**, *206*, 35–43. [[CrossRef](#)]
74. Xin, B.; Jing, L.; Ren, Z.; Wang, B.; Fu, H. Effects of simultaneously doped and deposited Ag on the photocatalytic activity and surface states of TiO<sub>2</sub>. *J. Phys. Chem. B* **2005**, *109*, 2805–2809. [[CrossRef](#)] [[PubMed](#)]
75. Yang, J.; Bai, H.; Tan, X.; Lian, J. IR and XPS investigation of visible-light photocatalysis-Nitrogen-carbon-doped TiO<sub>2</sub> film. *Appl. Surf. Sci.* **2006**, *253*, 1988–1994. [[CrossRef](#)]
76. Chu, W.; Choy, W.K. The mechanisms of rate enhancing and quenching of trichloroethene photodecay in the presence of sensitizer and hydrogen sources. *Water Res.* **2002**, *36*, 2525–2532. [[CrossRef](#)]
77. Ollis, D.F.; Pelizzetti, E.; Serpone, N. Destruction of water contaminants. *Environ. Sci. Technol.* **1991**, *25*, 1522–1529. [[CrossRef](#)]
78. Ilisz, I.; Föglein, K.; Dombi, A. The photochemical behavior of hydrogen peroxide in near UV-irradiated aqueous TiO<sub>2</sub> suspensions. *J. Mol. Catal. A Chem.* **1998**, *135*, 55–61. [[CrossRef](#)]
79. Dionysiou, D.D.; Suidan, M.T.; Bekou, E.; Baudin, I.; Lainé, J.M. Effect of ionic strength and hydrogen peroxide on the photocatalytic degradation of 4-chlorobenzoic acid in water. *Appl. Catal. B Environ.* **2000**, *26*, 153–171. [[CrossRef](#)]
80. Nagaveni, K.; Sivalingam, G.; Hegde, M.S.; Madras, G. Solar photocatalytic degradation of dyes: High activity of combustion synthesized nano TiO<sub>2</sub>. *Appl. Catal. B Environ.* **2004**, *48*, 83–93. [[CrossRef](#)]
81. Toor, A.T.; Verma, A.; Jotshi, C.K.; Bajpai, P.K.; Singh, V. Photocatalytic degradation of Direct Yellow 12 dye using UV/TiO<sub>2</sub> in a shallow pond slurry reactor. *Dyes Pigments* **2006**, *68*, 53–60. [[CrossRef](#)]
82. Konstantinou, I.K.; Albanis, T.A. TiO<sub>2</sub>-assisted photocatalytic degradation of azo dyes in aqueous solution: Kinetic and mechanistic investigations: A review. *Appl. Catal. B Environ.* **2004**, *49*, 1–14. [[CrossRef](#)]
83. Grzechulska, J.; Morawski, A.W. Photocatalytic decomposition of azo-dye acid black 1 in water over modified titanium dioxide. *Appl. Catal. B Environ.* **2002**, *36*, 45–51. [[CrossRef](#)]
84. Wang, X.; Wang, J.; Guo, P.; Guo, W.; Li, G. Chemical effect of swirling jet-induced cavitation: Degradation of rhodamine B in aqueous solution. *Ultrason. Sonochem.* **2008**, *15*, 357–363. [[CrossRef](#)] [[PubMed](#)]
85. Tang, S.K.; Teng, T.T.; Alkarkhi, A.F.M.; Li, Z. Sonocatalytic Degradation of Rhodamine B in Aqueous Solution in the Presence of TiO<sub>2</sub> Coated Activated Carbon. *APCBEE Procedia* **2012**, *1*, 110–115. [[CrossRef](#)]
86. Mcheik, H.A.; Jamal, M.M. Kinetic study of the discoloration of rhodamine B with persulfate, Iron activation. *J. Univ. Chem. Technol. Metall.* **2013**, *48*, 357–365.
87. Sap, K.A.; Demmers, J.A.A. World's largest Science, Technology & Medicine Open Access book publisher c. *Intech* **2016**, *6*, 111–133. [[CrossRef](#)]
88. Martha, S.; Sahoo, P.C.; Parida, K.M. An overview on visible light responsive metal oxide based photocatalysts for hydrogen energy production. *RSC Adv.* **2015**, *5*, 61535–61553. [[CrossRef](#)]
89. Tak, Y.; Kim, H.; Lee, D.; Yong, K. Type-II CdS nanoparticle–ZnO nanowire heterostructure arrays fabricated by a solution process: Enhanced photocatalytic activity. *Chem. Commun.* **2008**, 4585. [[CrossRef](#)]
90. Han, S.K.; Hwang, T.M.; Yoon, Y.; Kang, J.W. Evidence of singlet oxygen and hydroxyl radical formation in aqueous goethite suspension using spin-trapping electron paramagnetic resonance (EPR). *Chemosphere* **2011**, *84*, 1095–1101. [[CrossRef](#)]

91. Zhang, Y.; Barnes, A.N.; Zhu, X.; Campbell, N.F.; Gao, R. Quantification of thiopurine/UVA-induced singlet oxygen production. *J. Photochem. Photobiol. A Chem.* **2011**, *224*, 16–24. [[CrossRef](#)] [[PubMed](#)]
92. Jovanović, S.P.; Syrgiannis, Z.; Marković, Z.M.; Bonasera, A.; Kepić, D.P.; Budimir, M.D.; Milivojević, D.D.; Spasojević, V.D.; Dramićanin, M.D.; Pavlović, V.B.; et al. Modification of Structural and Luminescence Properties of Graphene Quantum Dots by Gamma Irradiation and Their Application in a Photodynamic Therapy. *ACS Appl. Mater. Interfaces* **2015**, *7*, 25865–25874. [[CrossRef](#)] [[PubMed](#)]
93. Li, L.; Liu, S.; Zhu, T. Application of activated carbon derived from scrap tires for adsorption of Rhodamine B. *J. Environ. Sci.* **2010**, *22*, 1273–1280. [[CrossRef](#)]
94. Gao, H.; Sun, Y.; Zhou, J.; Xu, R.; Duan, H. Mussel-inspired synthesis of polydopamine-functionalized graphene hydrogel as reusable adsorbents for water purification. *ACS Appl. Mater. Interfaces* **2013**, *5*, 425–432. [[CrossRef](#)] [[PubMed](#)]
95. Dutta, S.; Sahoo, R.; Ray, C.; Sarkar, S.; Jana, J.; Negishi, Y.; Pal, T. Biomolecule-mediated CdS-TiO<sub>2</sub>-reduced graphene oxide ternary nanocomposites for efficient visible light-driven photocatalysis. *Dalton Trans.* **2014**, *44*, 193–201. [[CrossRef](#)] [[PubMed](#)]
96. Lv, T.; Pan, L.; Liu, X.; Lu, T.; Zhu, G.; Sun, Z.; Sun, C.Q. One-step synthesis of CdS-TiO<sub>2</sub>-chemically reduced graphene oxide composites via microwave-assisted reaction for visible-light photocatalytic degradation of methyl orange. *Catal. Sci. Technol.* **2012**, *2*, 754. [[CrossRef](#)]
97. Egger, D.A.; Rappe, A.M.; Kronik, L. Hybrid Organic-Inorganic Perovskites on the Move. *Acc. Chem. Res.* **2016**, *49*, 573–581. [[CrossRef](#)]
98. Fu, H.; Pan, C.; Yao, W.; Zhu, Y. Visible-light-induced degradation of rhodamine B by nanosized Bi<sub>2</sub>WO<sub>6</sub>. *J. Phys. Chem. B* **2005**, *109*, 22432–22439. [[CrossRef](#)]



© 2020 by the authors. Licensee MDPI, Basel, Switzerland. This article is an open access article distributed under the terms and conditions of the Creative Commons Attribution (CC BY) license (<http://creativecommons.org/licenses/by/4.0/>).



## **Publication II**

Bresolin, B.M., Ben Hammouda, S., and Sillanpää, M.

**Methylammonium iodo bismuthate perovskite (CH<sub>3</sub>NH<sub>3</sub>)<sub>3</sub>Bi<sub>2</sub>I<sub>9</sub> as new effective visible light-responsive photocatalyst for degradation of environment pollutants**

Reprinted with permission from  
*Journal of Photochemistry & Photobiology A: Chemistry*  
Vol. 376, pp. 116-126, 2019  
© 2019, Elsevier

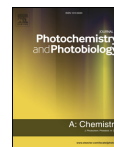






Contents lists available at ScienceDirect

Journal of Photochemistry &amp; Photobiology A: Chemistry

journal homepage: [www.elsevier.com/locate/jphotochem](http://www.elsevier.com/locate/jphotochem)

# Methylammonium iodo bismuthate perovskite (CH<sub>3</sub>NH<sub>3</sub>)<sub>3</sub>Bi<sub>2</sub>I<sub>9</sub> as new effective visible light-responsive photocatalyst for degradation of environment pollutants

Bianca-Maria Bresolin<sup>a,\*</sup>, Samia Ben Hammouda<sup>a</sup>, Mika Sillanpää<sup>a,b</sup><sup>a</sup> Laboratory of Green Chemistry, School of Engineering Science, Lappeenranta University of Technology, Sammonkatu 12, 50130, Mikkeli, Finland<sup>b</sup> Department of Civil and Environmental Engineering, Florida International University, Miami, FL-33174, USA

## ARTICLE INFO

## Keywords:

Visible light photocatalysis  
Hybrid organic-inorganic perovskite  
Dye contaminant  
Halogen lamp

## ABSTRACT

In this work, the photocatalytic activity of a new visible light-responsive (CH<sub>3</sub>NH<sub>3</sub>)<sub>3</sub>Bi<sub>2</sub>I<sub>9</sub> hybrid organic-inorganic perovskite (HOIP) was addressed for the very first time in the treatment of aqueous solutions of model organic dyes. The photocatalyst was successfully prepared by a low temperature solvo-thermal method, easily reproducible. The catalyst was characterized by Fourier-transform infrared spectroscopy (FT-IR), X-ray diffraction spectrometer (XRD), scanning electron microscopy (SEM), energy dispersive X-ray (EDS), X-ray photoelectron spectroscopy (XPS) techniques and UV diffuse reflectance spectrum. The efficiency of photocatalyst was tested for the removal of different type of dyes: fluorone dye (rhodamine B), thiazine dye (methylene blue) and azo dye (reactive Blue 4). Moreover, a multi-contaminated solution, with methylene blue and crystal violet (triarylmethane dye), was used to simulate a real industrial wastewater effluent. The results highlighted an increase of the photocatalytic activity respect the pristine precursor, bismuth iodide. The experiments showed that the values of removal was higher for rhodamine B respect the other dyes, with a removal of 98% after three hours under visible light irradiation. The efficiency of the photocatalyst was also confirmed under optimal conditions with high pressure liquid chromatography (HPLC). The gradual disappearance of rhodamine B peak accompanied by the appearance of by-products peaks was investigated. The stability of the photocatalyst was tested for three consecutive re-cycles. Analysis on different visible light sources was performed: halogen provided higher efficiency respect LED lamp. The outcomes of the present work aim to open the possibility of considering HOIP as a new potential photocatalyst for contaminants treatment.

## 1. Introduction

Water pollution is definitively a current and global issue, it has a huge and negative impact on ecosystems, environment and humans. Water contaminants are mostly driven by industrial wastes related to various industries such as petroleum refinery, textile, paper, pharmaceutical, paint, plastic, etc. [1]. Dyes from dyeing, textile, tanning and paint factories are one of the main sources of water pollution, and a considerable amount of researches has been conducted on this topic. More than 10,000 different dyes with an estimated global annual production of 800,000 tons are commercially available worldwide [1,2]. About 12% of the textile dyes used each year are lost during operations machining, 20% of these lost residues it is estimated to be found in industrial wastewater and then in the environment [3]. The majority of the dyes have good solubility in water, thus these are common water pollutants very harmful also for aquatic animals and plants. Moreover,

most of these dyes are recalcitrant and resist to conventional chemical and biological treatments. There are no doubts about the serious threat that these contaminants can cause to the environment and human health: respiratory problem, asthma, dermatitis, mutagenicity, cancer, etc. [4,5]. Based on data obtained for 250 different dyes, Rochkind et al. [6] divided the most studied dyes in different groups. The selection is dominated by the thiazine dyes (as methylene blue), it is followed by the xanthenes (as rhodamine B) and, despite their dominance in global production (50%–70% of the market), the azo dyes (such as reactive blue 4) appeared as fourth group, hence their dominance in contributing to the environmental challenge.

Various types of conventional methods were used for dyes degradation. Among the traditional methods, many limitations was found: operating cost, non-biodegradable products, time-consuming processes, stability of the dyes on the treatments. On the other hand, advanced oxidation processes (AOPs) is recommended as efficient

\* Corresponding author.

E-mail address: [Bianca.maria.Bresolin@lut.fi](mailto:Bianca.maria.Bresolin@lut.fi) (B.-M. Bresolin).<https://doi.org/10.1016/j.jphotochem.2019.03.009>

Received 6 September 2018; Received in revised form 27 February 2019; Accepted 5 March 2019

Available online 07 March 2019

1010-6030/© 2019 Elsevier B.V. All rights reserved.

decontamination technique. Among AOPs methods, photocatalytic degradation using semiconductors has been gaining increasing attention in the last decade as a sustainable and environment friendly alternative [7]. Heterogeneous photocatalysis combines the utilization of a solid dispersed catalyst (e.g. a semiconductor) irradiated by an appropriate light source for the generation of highly reactive oxygen species (ROS). Some ROS produced in water treatments are: superoxide anion radical ( $\cdot\text{O}_2^-$ ), hydrogen peroxide ( $\text{H}_2\text{O}_2$ ), singlet oxygen ( $^1\text{O}_2$ ), and hydroxyl radical ( $\cdot\text{OH}$ ) [8]. Many studies have demonstrated that these species are the main responsible of degradation of organics [9,10]. There are several advantages that make this green technology very interesting: ambient operating conditions, low working costs, complete mineralization of organic contaminants without any secondary pollution [11]. However, some disadvantages faced during heterogeneous photocatalytic processes are: fast recombination rate of the charge carriers (photo-generated hole–electron), low light absorption range, and poisoning of the active sites on the surface of photocatalyst [7].

The majority of the literature studies are focused on the use of  $\text{TiO}_2$  as photocatalyst because it is cheap, chemically stable and harmful. Nevertheless, this photocatalyst owns some limitations such as low adsorption capacity for hydrophobic contaminants resulting in slow photocatalytic degradation rates, low quantum yield of excitons due to the fast electrons–holes recombination [12]. Moreover,  $\text{TiO}_2$  band gap (above 3.0 eV for rutile and 3.2 eV for anatase) restrains applications to the UV–A region of the electromagnetic spectrum ( $\lambda \leq 387.5$  nm) [13,14]. This article explores the potential of a new effective photocatalyst as alternative to  $\text{TiO}_2$ .

Recently, hybrid organic–inorganic perovskites (HOIPs) have generated considerable interest for optoelectronic applications [15]. The general formula of this class of compounds is  $\text{ABX}_3$ , where A is an organic cation, B an inorganic metal, and X is a halogen element. Compositional, structural, optical, and charges transportation properties are commonly observed in these materials and the interplay of their characteristics makes them great promising candidates for photocatalytic applications [16]. Thus, the properties that may make HOIPs a very good photocatalyst are: a high electron and hole mobility, a large absorption coefficients, a favourable band gap, a strong defect tolerance, shallow point defects, a benign grain boundary recombination effects, a reduced surface recombination and long electron–hole diffusion length [17,18]. Moreover, they can be produced by low cost solution processes [19]. Among the different composition methylammonium lead halide perovskites ( $\text{CH}_3\text{NH}_3\text{PbI}_3$ ) show the better properties in solar cell applications [20]. Unfortunately, this compound contains  $\text{Pb}^{2+}$ , which is a toxic bioavailable cation [15]. According to previous studies, bismuth based perovskites promise good moisture and water stability [21,22]. In this study, in an attempt to replace lead by a non-toxic heavy p-block metal, organic–inorganic methylammonium iodobismuthate perovskite ( $\text{CH}_3\text{NH}_3\text{BiI}_3$ ) (MBI) was prepared via solvo-thermal treatment at low temperature.

In the present study, it was attempted to determine the feasibility of the degradation of some dyes having different chemical structures by MBI, as a new effective photocatalyst activated by visible light irradiation. The photocatalytic ability was investigated on rhodamine B (RhB, fluorone dye), methylene blue (MB, thiazine dye), reactive Blue (RBL, double Azo dye). The most of the photocatalytic studies are based on single dye solution [23], but industrial effluents contain a mixture of dyes. In our study, the photocatalytic treatment of mixed MB and crystal violet (CV, triarylmethane dye) was set to simulated real textile industrial wastewater. These two dyes are extensively used in industries and medicines, both are mutagen, mitotic poisons and suspected carcinogen [24].

At our knowledge, this is the first paper about investigation on the use of bismuth based hybrid organic inorganic perovskite in a photocatalytic system for the removal of different classes of dyes under visible light irradiation.

**Table 1**  
Characteristics of the investigated dyes.

Name	Structure	$\lambda_{\text{max}}$ (nm)	MW (g/mol)
Rhodamine B		554	479.01
Methylene Blue		664	319.85
Crystal Violet		583	407.98
Reactive Blue 4		598	637.44

## 2. Experimental

### 2.1. Materials

Methylamine ( $\text{CH}_3\text{NH}_2$ , 33 wt% in ethanol), hydroiodic acid distilled (HI 57 wt% in water), diethyl ether (DE purity  $\geq 99.8\%$ ), bismuth (III) iodide ( $\text{BiI}_3$  purity 99%), *N,N*-dimethylformamide (DMF purity 99.8%), Rhodamine B (RhB,  $\text{C}_{28}\text{H}_{31}\text{ClN}_2\text{O}_3$ ), methylene blue (MB,  $\text{C}_{16}\text{H}_{18}\text{ClN}_3\text{S}$ ), crystal violet (CV,  $\text{C}_{25}\text{H}_{30}\text{N}_3\text{Cl}$ ) were purchased from Sigma Aldrich. Reactive Blue 4 (RBL,  $\text{C}_{22}\text{H}_{14}\text{Cl}_2\text{N}_3\text{O}_6\text{S}_2$ ) was obtained by Alfa Aesar. The dyes used are listed in Table 1. All chemicals were used without any further purification. Deionized water was used throughout this study.

The VisiLight halogen cold light source CL150 (VWR) was used as light source in the current treatments. The source was equipped by 150 W halogen bulb with 3270 K color temperature. The passively cooled VisiLight LED3 was used as second light source for comparison. The lamp assure environmentally friendly LED technology with flicker-free illumination, 36 W power consumption, 730 lm luminous intensity.

### 2.2. Catalyst preparation and characterization

Hybrid organic–inorganic perovskite was prepared using a easily reproducible method suggested by Navas et al. [25]. Initially, the organic precursors ( $\text{CH}_3\text{NH}_2$ ) and HI were stirred in ice bath under controlled temperature of  $0^\circ\text{C}$  for two hours. The resulted solution was evaporated at  $50^\circ\text{C}$  until a white fine powder was obtained. The as synthesized powder was washed three times with DE and then dried at  $50^\circ\text{C}$  on a hot plate until complete evaporation of the liquid.  $\text{CH}_3\text{NH}_2\text{I}$  and  $\text{BiI}_3$  were mixed in DMF in a molar ration 2:3. The resultant solution was stirred at 400 rpm and heated at  $60^\circ\text{C}$  until complete evaporation of the liquid.

The functional groups present on the photocatalyst surface were characterized by Fourier transform infrared spectra (FT-IR) in a region between 400 and  $4000\text{ cm}^{-1}$  at room temperature using Horiba FT-730 FT-IR spectrometer. The X-ray powder diffraction (XRD) spectrum of the photocatalyst was recorded by PANalytical Empyrean diffractometer with  $\text{Co-K}\alpha$  ( $\lambda = 1.7809\text{ \AA}$ ) radiation source, 40 kV generator voltage and 40 mA tube current. The surface composition and the electronic states of elements in the valence-band region were determined by ESCALAB 250 X-ray photoelectron spectroscopy (XPS) with  $\text{Al-K}\alpha$  (1486.6 eV) as the X-ray source. Light absorption spectra were measured with a PerkinElmer Lambda 1050 spectrophotometer (UV–vis) to establish the absorption spectrum and band gap of the sample. The microstructure and morphology of the material were

defined using Scanning electron microscope (SEM). Energy Dispersive Spectroscopy (EDS) detected the elemental composition of the pure hybrid organic-inorganic. Brunauer–Emmett–Teller (BET) theory and analysis determined the specific surface area of the synthesized material.

### 2.3. Procedure for photocatalysis

The photocatalytic performances of the prepared material was evaluated by the degradation of four different type of organic dyes in aqueous suspension under visible light irradiation, with continuous supply of air. In a typical experiment, desired amount of catalyst was suspended in 100 mL of solution and allowed to stir for 30 min in dark to achieve the adsorption-desorption equilibrium. The lamp was located at the top of the reactor (three cm from solution surface). All photocatalytic reactions were performed at room temperature (25 °C). At given time intervals, samples of three mL were withdrawn from the reactor and filtered immediately through a 0.2 µm filter (phenomenex) for spectrophotometric analysis (PerkinElmer Lambda 45 UV/vis Spectrometer). The decrease of concentration of pollutants was monitored, after calibration, by measuring the decrease in peak intensity at characteristic wavelength:  $\lambda_{\text{max}} = 554 \text{ nm}$  (RhB),  $\lambda_{\text{max}} = 664 \text{ nm}$  (MB),  $\lambda_{\text{max}} = 583 \text{ nm}$  (CV), and  $\lambda_{\text{max}} = 598 \text{ nm}$  (RBL). The degradation efficiencies of the photocatalyst were compared assuming a pseudo-first order kinetic reaction. The following equation was applied:

$$-\ln\left(\frac{C}{C_0}\right) = k \cdot t \quad (1)$$

Where  $C_0$  is the contaminant concentration at the initial time,  $C$  the contaminant concentration at time  $t$ , and  $k$  is the pseudo first-order reaction rate constant.

Moreover, in the case of RhB, by-products were analysed by a Shimadzu High Performance Liquid Chromatography equipped with UV detection (HPLC-UV). Samples were separated using a reversed-phase C18 column (150–4.6 mm) at 550 nm. The column temperature was maintained at 35 °C. The optimized mobile phase consisted of methanol and water with the volume ratio at 70:30, the flow rate was set at 0.5 mL/min and 20 µL of sample were injected. Results and Discussion are presented in APPENDIX A.

The reusability tests were performed to check the stability of the material. After each run, the catalyst was filtrated, washed with deionized water, and then dried for reuse under similar experimental conditions.

Experiments involving radicals capture were conducted. Before the standard photocatalytic tests, 10 mM of  $\text{AgNO}_3$ , 10 mM of KI, 0.1 mL isopropanol (IPA), and 0.01 mmol benzoquinone (BQ) into RhB (20 mg/L, 100 mL) were added as scavengers for  $e^-$ ,  $h^+$ ,  $\cdot\text{OH}$  and  $\text{O}_2^{\cdot-}$  respectively [26–28].

## 3. Results and discussion

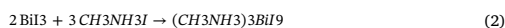
### 3.1. Catalyst characterization

#### 3.1.1. Structural parameters

Synthesis of the bismuth-based organo-halide perovskite can be accomplished using a variety of approaches; in our study, in accordance to our purpose, a low temperature solvo-thermal method was applied [25]. The FT-IR spectroscopy results of the precursors ( $\text{BiI}_3$  and MAI) and the final MBI are shown in Fig. 1. The spectrum shows broad N–H (from 2800 to 3200  $\text{cm}^{-1}$ ) vibrations with the characteristic feature of a hydrogen bond that overlaps with the C–H vibrations [29]. The bands at 1410 and 1450  $\text{cm}^{-1}$  suggest the existence of C–C bending modes and carbonate, respectively [30]. The characteristic peaks occur for N–H stretching vibration at 3097  $\text{cm}^{-1}$ , C–H stretching vibration at 2935  $\text{cm}^{-1}$ , N–H bending at 1577  $\text{cm}^{-1}$ , and peaks at 1461 and 1421  $\text{cm}^{-1}$  belong to C–H bending vibration [31]. The weak band at

1420  $\text{cm}^{-1}$  is related to  $\text{NH}^+$  [30]. The weak and broad peak at around 3500  $\text{cm}^{-1}$  is related to O–H stretching vibrations probable as consequence of the measurements performed under ambient conditions [32]. As shown in Fig. 1, transmittance of MBI increased corresponding to the N–H bonds wavelength ranges. This suggests the presence of hydrogen bonds. The bismuth-based hybrid organic inorganic perovskite structure consists of isolated metal halide dimer units of  $\text{Bi}_2\text{I}_9^{3-}$  anions surrounded by  $\text{CH}_3\text{NH}_3^+$  cations. The clusters are interconnected via N–H...I hydrogen bonding interactions [33–36].

Fig. 2 shows that the color of the as-prepared powder was significantly affected by the addition of MAI. During the synthesis, the color changed from black ( $\text{BiI}_3$ ) to red, implying that certain reaction occurred after addition of the organic fraction. Four main peaks of  $\text{BiI}_3$  from 10 to 60° were observed. For what concerns MBI, all diffraction peaks were consistent with literature reports suggesting that MBI belongs to the hexagonal system with the P63/mmc space group [37–39]. The results agreed well with the hexagonal morphology of MBI single crystals as shown Fig. 3 (SEM). In addition, the diffraction peaks of  $\text{BiI}_3$  were not detectable in the MBI pattern, this fact indicates that almost all  $\text{BiI}_3$  has been transformed completely into MBI. Finally, MAI phase was not observed in the final product, suggesting that a chemical reaction occurred between MAI and  $\text{BiI}_3$  as follows [37]:



According to literature,  $\text{BiI}_3$  consists of small grains with relatively low crystallization [39]. The morphology of the complete MBI powder is presented by the SEM macroscopic image in Fig. 3. The powder exhibit smooth, compact, and polygonal crystal morphology. Average grain sizes reach up to 50–200 nm. As already discussed in XRD results showed above (Fig. 2), the introduction of MAI significantly improved the powder crystallization thus the quality of the synthesized material. Energy dispersive X-ray spectrometry was used to determine the stoichiometric ratio by detecting the ratios in between C, N, Bi, and I atoms. The weight ratios of the atoms was found to be consistent to the stoichiometry of MBI. The slightly higher value of C and the presence of Al can be attributed to the background holder.

#### 3.1.2. Optical parameters

The surface chemical species and their oxidation states were examined by (XPS) and the results are presented in Fig. 4a. The binding energy peaks confirm the presence of dominant elements: C, N, Bi and I. The peaks at binding energies of 285 eV, 402 eV and 533 eV corresponding to the photoelectron peaks of C 1s, N 1s and O 1s, respectively. Scans of the C 1s core level binding energy revealed the presence of two peaks, corresponding to C–C (lower energy eV) and C–N (higher energy eV) (Fig. 4b). XPS core level spectra for N 1s are presented in Fig. 4d. From the N 1s core level spectra one mainly peak present around 402.5 eV corresponding to the existence of N–C bond and free amine group  $\text{NH}_2$  singly bonded to carbon [40]. The doublet peaks of I and Bi are located around 621 eV and 164 eV, respectively. Interestingly, the small peak at lower binding energy of about 283.8 eV (Fig. 4a, zoomed window) is referred to carburet, confirming the formation of Bi–C bonds [41]. Bi 4f scans indicated that Bi species exist both in the 3+ oxidation state and a small amount as  $\text{Bi}^0$  (Fig. 4c). The presence of metallic Bismuth is suggested to be induced in part during measurement of the XPS spectra [42]. Conforming to the study of Navas et al. [25], the peaks 630.2 eV belong to I 3d3/2 and the ones at 619.6 eV belongs to I 3d5/2 (Fig. 4e). The spectrum shows other peaks, the shift to higher binding energy is associated with the loss of an iodide ion through methylammonium iodide evaporation leaving the  $\text{I}^{2-}$  anion from  $\text{BiI}_3$ . Additional broadening of the I 3d spectra indicate the presence an additional peak at 621 eV, this peak is credited to the oxidation of iodine at the surface which forms the  $\text{I}^{2+}$  cation and the iodite ( $\text{IO}_2^-$ ) anion [43].

MBI was found to have excellent absorbing properties. Absorption spectra measured between 380 and 800 nm. As confirmed by other

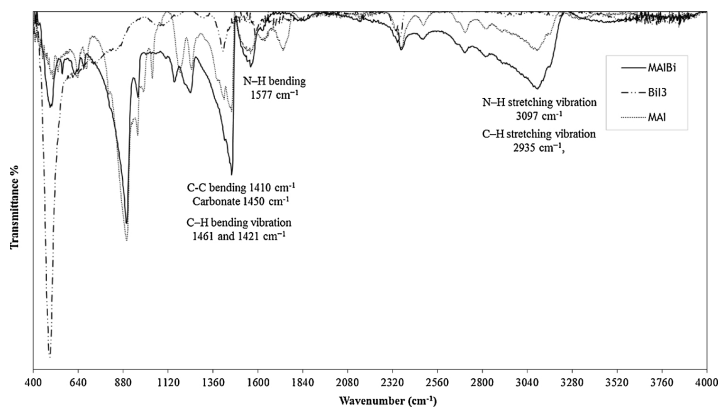


Fig. 1. FTIR spectrum for precursor (BiI<sub>3</sub> and MAI) and (MBI).

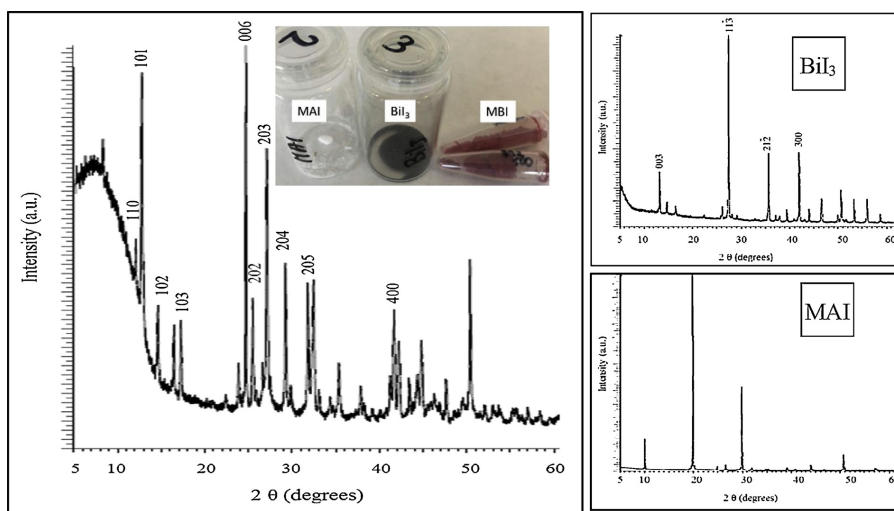


Fig. 2. XRD patterns of the as-prepared hybrid perovskites MBI and precursor, photographs the powders.

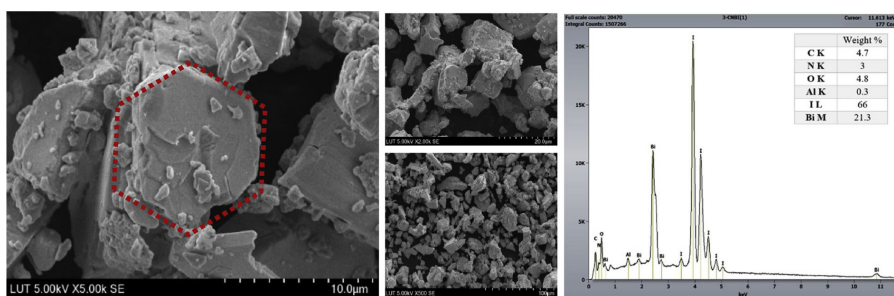


Fig. 3. SEM image and EDX analysis of the as-prepared hybrid perovskites MBI.

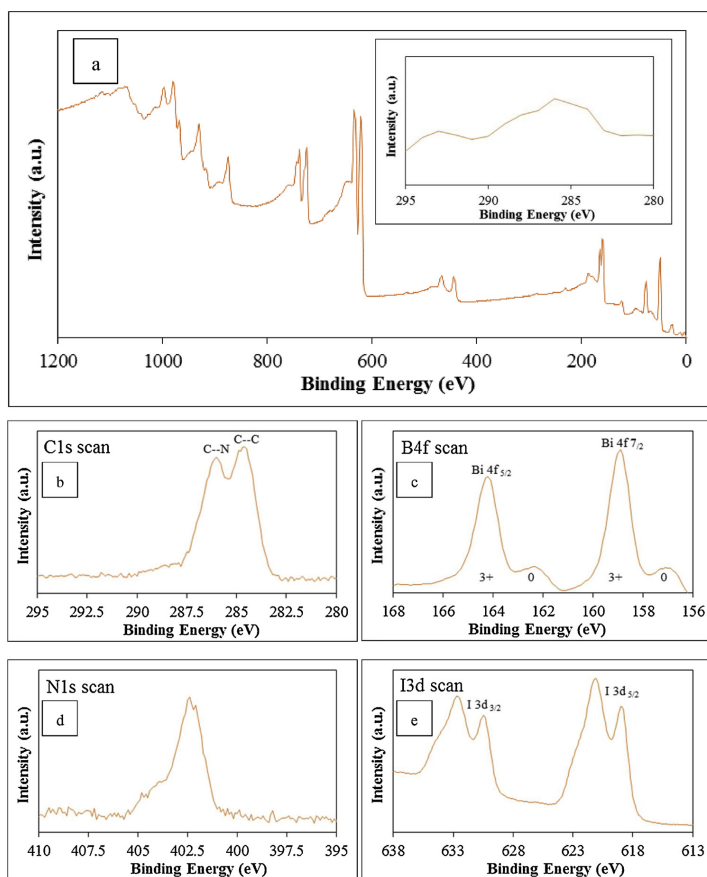


Fig. 4. MBI XPS spectra (MBI): (a) general spectrum, (b–e) specific binding energy for C1 s, B4f, N1 s and I3d respectively.

studies, the absorption onsets varied with MBI precursor ratio, demonstrating a phenomenon called multi-absorptions due to multi-absorption effects [39]. The results reveal an optical bandgap of the material at about 1.94 eV as it was derived from a Tauc plot (Fig. 5). The Tauc equation is reported below (Eq. (3)):

$$\alpha h\nu = A \times (h\nu - E_g)^n \quad (3)$$

Where  $\alpha$  is the absorption coefficient,  $A$  is a constant and  $n = 1/2$  or two for indirect allowed transition [44]. Absorption spectrum measured reveals an optical bandgap of the material at 1.94 eV as it was derived from a Tauc

plot. The result was found to be comparable with literature [45].

### 3.2. Performance of photocatalysis

#### 3.2.1. Mono-contaminated water solutions: RhB

The effect of visible light was firstly tested on RhB as model fluorone dyes. Fig. 6a shows that the direct photolysis of RhB can be neglected. After three hours of irradiation, no relevant decrease in the concentration was recorded. This result suggests that the organic dye owns excellent photo-stability, as highlighted by other authors [46,47].

Adsorption is a primordial step in the photocatalytic processes [48,49]. Adsorption experiment in dark condition was conducted. The results showed moderate affinity between MBI and RhB molecules with a maximum removal of 35% considering 3 h reaction (Fig. 6b). The photocatalytic ability of MBI to remove RhB was evaluated under visible light irradiation. Extinction spectrum using Halogen lamp is shown in Fig. 6c. The results show a remarkable decrease in RhB concentration in presence of MBI and irradiation. The kinetic behavior of the present system was evaluated with a pseudo-first order kinetic model. The first-order kinetic rate was found to be  $0.0221 \text{ min}^{-1}$  with  $R^2$  equal to 0.96. After three hours the extinction peak of RhB was almost disappeared implying the efficacy of the photocatalytic treatment.

#### 3.2.2. Mono-contaminated water solutions (other type of dyes): MB, RBL

The photocatalyst was further used to degrade MB, as sample of thiazine dye. The as contaminated water solution was treated under the same conditions, to investigate the wide applications of the as synthesized catalyst under visible light irradiation. About 89% MB was degraded within 120 min. Fig. 6d display the UV–vis extinction spectrum for the degradation of MB solution under visible light irradiation over time irradiation. The evaluation of first-order kinetic model shows a

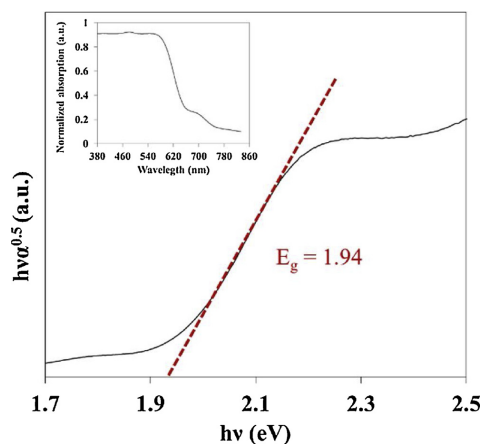


Fig. 5. Diffuse reflectance UV-vis spectra for powder synthesized (MBI): general spectrum, derived plot from Kubelka-Munk.

reaction rate of  $0.0129 \text{ min}^{-1}$ . The MB reaction rate degradation was found to be 42% lower in respect RhB, this result may be the consequence of lower adsorption affinity inbetween the material used and the pollutant.

RBL is an azo dyes, this family is composed by complex aromatic compounds with a structure that provides a high degree of stability. Moreover, they are the most widely used dyes especially in textile dyestuffs [50]. Fig. 6e displays the UV-vis extinction spectrum recorded over different periods of treatment exposure. The evaluation of first-order kinetic model shows a reaction rate of  $0.0006 \text{ min}^{-1}$ . The rate of RBL degradation was found to be extremely lower in respect the other dyes employed during the study. The stability and hardness of the structural bonds of the RBL molecule made the degradation slower and harder in respect the other investigated pollutants. In particular, the difference in chemical structure of RBL may result in difference in adsorption characteristics, in susceptibility to photodegradation and ability in absorption of light photon [51].

Table 2

First order reaction rate and correlation coefficients for the different dyes analyzed.

Dye	Catalyst	Dye concentration (mg/L)	catalyst load (g/L)	first kinetic rate ( $\text{min}^{-1}$ )	$R^2$
RhB	$\text{BiI}_3$	20	0.5	0.0048	0.9534
RhB	MBI	20	0.5	0.0221	0.9825
MB	MBI	20	0.5	0.0129	0.9698
RBL	MBI	20	0.5	0.0006	0.9768
mixed dyes:	MBI	10	0.5	0.0044	0.8945
MB		10		0.0070	0.8606
CV					

### 3.2.3. Multi-contaminated water solution

It is hardly possible that a wastewater stream consists in a single dye contaminant. Therefore, the photocatalytic degradation was applied to a mixture of two different dyes. The purpose of this test is to simulate a real wastewater belonging to textile or printing industries. The absorption spectra of mixed aqueous CV and MB is shown in Fig. 6f. It is evident that the two characteristic absorption peak ( $\lambda_{\text{max}}$ ) do not change when mixed in water. Therefore, the degradation of the mixture was studied separately for the two dyes on the treated solutions. The first-order kinetic rate was applied. The reaction rate was found to be  $0.0044$  and  $0.0070 \text{ min}^{-1}$  for MB and CV. The low  $R^2$  coefficient suggested that the reaction did not follow the pseudo-first order kinetic in this particular case. However, the lower efficiency, and the need of change kinetic model may be due to the competition of the two contaminants for the adsorption sites on the photocatalyst surface. First order reaction rate and correlation coefficients in different conditions are reported in Table 2.

The improvement of the efficiency of MBI respect the bare precursor ( $\text{BiI}_3$ ) may be correlated to the presence of carbon and nitrogen present on the sample surface, as highlighted in XPS and FT-IR analysis. The presence of carbon may increase the surface acidity and decrease the number of defects as inhibiting factors for electrons-holes recombination. Moreover, the carbon may further broaden the visible-light absorbance enhancing the photoenergy used. In addition, the carbon atoms on the surface may lead to the formation of efficient active sites enhancing the activity of the photocatalyst. On the other hand, also the nitrogen presence can involve several crucial factors: a selective type of surface species, a restricted number of lattice defects that may promote

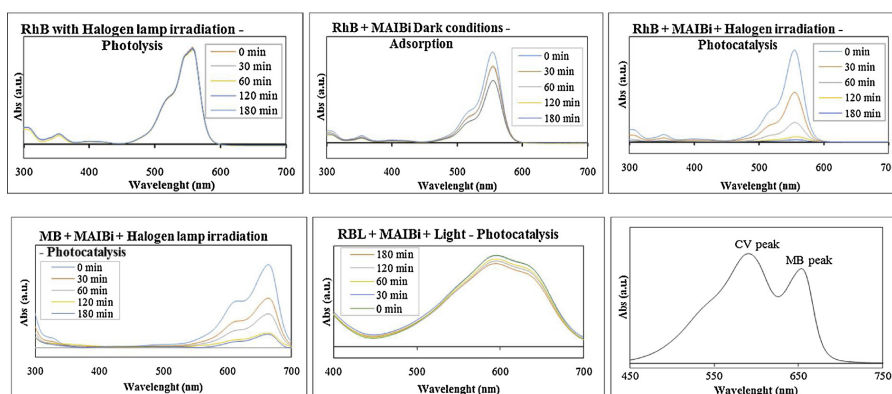


Fig. 6. (a) Extinction spectrum of RhB under visible light irradiation (halogen lamp); (b) extinction spectrum in dark conditions, (c) extinction spectrum under photocatalytic conditions (halogen lamp); (d) extinction spectrum of MB under photocatalytic conditions (halogen lamp); (e) extinction spectrum of RBL under photocatalytic conditions (halogen lamp); (f) extinction spectrum of mixed solution of MB and CV under photocatalytic conditions (halogen lamp).

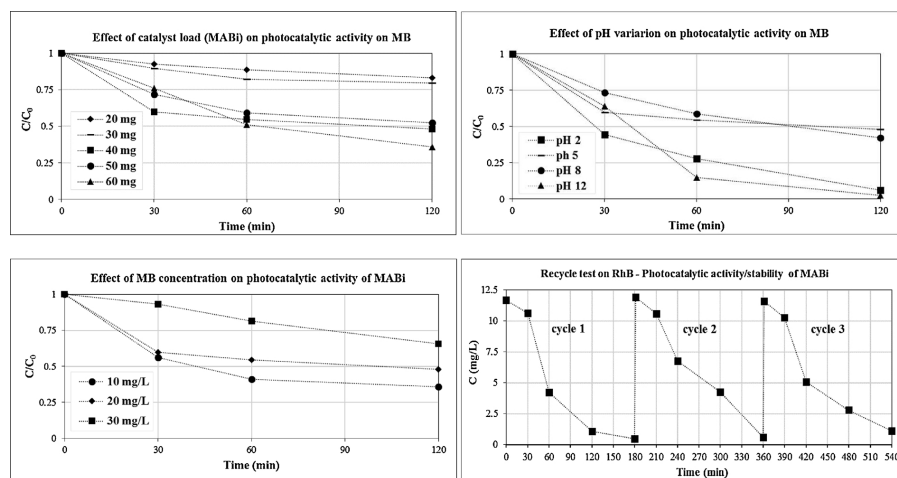
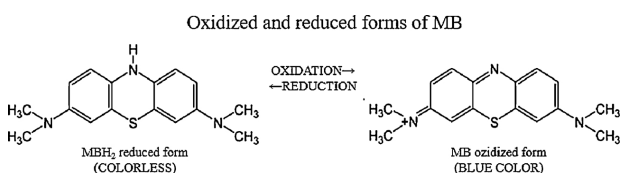


Fig. 7. (a) Effect of catalyst load (MABI, mg on 60 mL of MB solution) on photocatalytic activity in terms of  $C/C_0$ ; (b) pH impact on the MB photocatalytic degradation; (c) effect of MB concentration (mg/L) on photocatalytic activity in terms of  $C/C_0$ ; (d) degradation profile of RhB under visible light photocatalysis for three cycles.



Scheme 1. Oxidized and reduced forms of MB.

charge diffusion. Thus, both carbon and nitrogen were expected to influence the process.

### 3.2.4. Effect of catalyst loading

The concentration of catalyst has been varied from 0.3 to 1 g/L. The results are depicted in Fig. 7a; they show that with increase in catalyst load the initial reaction rate increases. It has been observed that after 120 min about 62% of degradation has been achieved using 60 mg (triangles), about 52% for 50 and 40 mg (squares and circles) and lower than 25% for 30 and 20 mg (lines and diamonds). The increase fact may be due because of the availability of active sites on catalyst surface for photocatalytic reactions. The number of available active sites rises with increase in catalyst loading. Nevertheless, at higher concentrations, other parameters affect the photocatalytic activity. For example, penetration of light may be hindered or even reflected (scattered) due to a light shielding of particles, this may affect the activity of portions of the photosensitive area. Subsequently, a reduction of photons may lead to even a decrease in the rate of degradation.

### 3.2.5. Effect of pH

Many possible reaction mechanisms contribute to variation of contaminants degradation depending mainly by the substrate nature and pH. It is well established that the adsorption of ions modifies the surface charge and the diffuse layer potential and that these quantities may strongly vary with ionic strength and pH. These parameters thus regulate the properties inbetween adsorbate and adsorbent interfaces [52]. Moreover, it must be considered the pH-dependency of electron transfer, such as dye injection, and back electron transfer [53].

The initial pH value of the MB solution was varied in order to study

the effect on the organic dye photodegradation. The natural pH of the solutions (20 ppm) was found to be five and it was varied from two to 12 using the required amount of HCl or NaOH solutions, respectively. Fig. 7b shows the photocatalytic results achieved at different initial pH values: the best degradation results of about 95% were achieved at extreme pH values of 12 and two. In basic conditions, the benefit effect was probably due to the presence of large quantities of OH<sup>-</sup> ions in the reaction medium. The hydroxide favors the formation of ROS, which is now widely accepted as the principal oxidizing specie responsible for the organic contaminants removal process. Moreover, under alkaline conditions, the concentration of MB could be directly reduced by OH<sup>-</sup> ions, thus blue colored MB could be transformed into colorless leucomethylene blue (MBH<sub>2</sub>) (Scheme 1).

At highly acidic pH the enhancement in degradation efficiency may depends on the zero point charge of the catalyst. The adsorption behavior of the photocatalyst can be influenced by the pH value. The point of zero charge (pH<sub>zpc</sub>) was evaluated in order to get the pH value at which the MBI exhibits zero net electrical charge on the surface [54]. The pH<sub>zpc</sub> of the MBI was found to be 2.5, below these pH is most suitable the adsorption of anionic dye, such as MB [55]. It must be mentioned that in acidic condition the aromatic structure of organic dyes may also be easily cleaved by photocatalysis.

### 3.2.6. Effect of dye concentration

The concentration of MB has been varied from 10 to 30 mg/L maintaining constant the other parameters. As can be seen in Fig. 7c, after 120 min the degradation of MB at 10, 20 and 30 mg/L decreases respectively from 62%, 51% to 37%. When the organic contaminant concentration is increased, higher number of molecules are adsorbed on



the catalyst surface. Since huge amount of reactive species are required for the degradation of pollutant if the concentration of target pollutant is high, radicals may be not sufficient for the degradation of pollutant. That fact may ultimately results in decrease in the degradation rate of pollutant as the concentration increases.

### 3.3. Recycle test

The recyclability of the as synthesized material was evaluated for multiple cycles. Recyclability represents one of the most important advantages for heterogeneous catalyst. Fig. 7d displays the data for all the three cycles performed on the pollutant. After three cycles, the system still showed an effective activity on removal of RhB dye, the activity loss was negligible. RhB degradation efficiency showed a removal of 96%, 95% to 91% at the first, second and third cycle, respectively. The decrease observed after reuse may be caused by active sites saturation. It can be concluded that the synthesized material show stable recyclability and thus can be considered as promising heterogeneous catalyst for visible light photo-catalysis.

### 3.4. Alternative visible light source

Nowadays, not only environmental pollution but also the energy demands is considered serious problems all over the world [56]. The demand for energy is increasing dramatically due to the continuous growing of world population, this fact poses a great risk to the environment. The supply of sustainable and clean energy sources as well as the environment protection are key factors to develop green technology and preserve life on our planet. Among the main alternative, solar energy, because of its availability, accessibility, and cleanliness is being considered as an ultimate source of energy, which could address both energy and environmental issues [57,58]. Visible light is portion of solar spectrum, it is non-toxic, it does not generate waste, and it is a renewable source of energy. Among of the available sources for visible light irradiation Halogen and LED bulbs technology were selected in this study. Two visible light units were employed: halogen lamps (Visilight CL150) and LED (Visilight LED 3), both of them were supply by VWR. A comparison between the main characteristics of the two kind of lamps are shown in Table 3.

Fig. 8 illustrates the spectrum differences between halogen and cold light LED. Light sources can generally be divided into thermal light sources such as sunlight, halogen and incandescent light, and non-thermal light sources such as LED and fluorescent lights. LED and halogen light can produce only visible range light in the spectrum of 380 nm–780 nm. Halogen and LED lamps cover the same wavelength range, but they show different intensities. Halogen lamp shows a region of omogenous higher intensity at between 550 and 650 nm, LED lamp shows two relatively isolated peaks respectively at 450 nm and 550 nm.

Halogen and LED lamps were used to compare the photocatalytic behavior of the as sensitized catalyst. Under LED irradiation, the first-order kinetic rate was found to be  $0.0072 \text{ min}^{-1}$ . The value calculated with the use of Halogen irradiation was  $0.0221 \text{ min}^{-1}$ . The LED irradiation give a rate equal to the 35% of the rate reached with the Halogen lamp irradiation. As expected, the halogen lamp was found to be more suitable. Comparing the intensity spectra of the halogen and the LED lamp in Fig. 8 with the adsorption spectrum recorded with the UV/vis Spectrometer in Fig. 5, it can be assumed that the halogen

intensity better fit the adsorption capacity of the MBI. The halogen irradiation source provides a higher intensity respect the LED source. Fig. 9 shows the extinction spectrum of removal of RhB in aqueous solution under LED irradiation.

### 3.5. Possible mechanism for the enhanced photocatalytic activity

In general, the degradation of dyes in the presence of visible-light photocatalysts can be initiated through two main processes known as direct semiconductor excitation and indirect dye sensitization [59]. Indeed, the degradation of RhB can be associated also to self-sensitized mechanisms [60–62]. Thus, electron transfer can be induced under illumination from the dye molecules to the catalyst. On the other side, also the electrons in the photocatalyst can be excited and produce electron-hole pairs. Generally, both the mechanisms can produce reactive radical species and initialize the photocatalytic reaction. Currently, MBI has been widely studied for its remarkable properties such as: high electron and hole mobility, a large absorption coefficient, a favourable band gap, a strong defect tolerance, shallow point defects, a benign grain boundary recombination effect, a reduced surface recombination and long electron-hole diffusion length. These characteristics are in accordance with the requirements of a good visible-light photocatalyst. Herein, the optical data were combined with information assumed by other research studies to build a hypothetical energy band diagram and a possible dye removal mechanism [63–65]. Visible light irradiation promoted generation of electron-hole pairs that can later be transported through the surface of the catalyst. The low recombination rate avoids the recombination of the charges enhancing the photocatalytic activity [66]. The generated holes enable a one-electron oxidation step with water to produce a hydroxyl radicals ( $\cdot\text{OH}$ ). Several researchers have reported  $\cdot\text{OH}$  to be one of the main responsible for oxidation reaction [67]. Free  $\cdot\text{OH}$  radicals, more reactive than the surface-bound analogues, are well known to be primary oxidants in the photocatalytic degradation of organic pollutants because of their reorganization energy [68]. On the other hand, after excitation the electrons could flow from the dye ( $\text{RhB}^*$ ) to the catalyst, enhancing the efficiency of degradation. According to the position of the energy levels of the material, not only the electrons can flow from the excited dye to the inorganic perovskite but also the holes may flow on the other way. The photoexcited holes and electrons can be well separated to restrict charge recombination, and thus the photogenerated charge carriers can be used more efficiently, favouring higher efficiencies by modulating the charge diffusion and transfer dynamics [69]. In photocatalytic process, it is important to investigate the main active species. Trapping agents, such as  $\text{AgNO}_3$ , KI, IPA and BPQ have been used to capture free  $e^-$ , free  $h^+$ , hydroxyl free radicals ( $\cdot\text{OH}$ ) and superoxide radical anions ( $\text{O}_2^{\cdot-}$ ) respectively [26–28]. As shown in Fig. 10, the addition of  $\text{AgNO}_3$  and BPQ has no obvious effect on the degradation of RhB. This suggests that  $e^-$  and  $\text{O}_2^{\cdot-}$  are not the primary active species involved in the process. On contrary, when KI or IPA were added the photodegradation efficiency decrease under two hours of visible-light irradiation. It can be concluded that  $h^+$  and  $\cdot\text{OH}$  are the primary active species in the photodegradation of RhB over the as synthesized photocatalyst. The potentials of the conduction band (CB) and valence band (VB) edges of are represented in energy level diagram of Fig. 10 on the basis of the measurements and previous reports [45,70–72]. On the base of the above results, one can conclude that there are two factors

**Table 3**  
Main characteristics of Halogen and LED lamp.

Lamp	Power consumption (W)	Luminous efficacy (lumens/watt)	Colour temperature (K)	Average Lifespan (hours)
Visilight CL150	150	16–24	3270	1.000
Visilight LED 3	36	80–100	5700	55.000

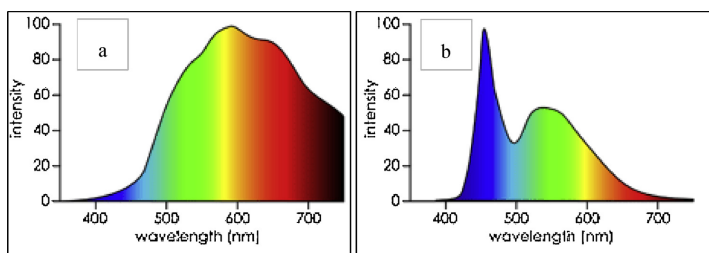


Fig. 8. (a) Halogen lamps emission spectrum, (b) LED lamps emission spectrum.

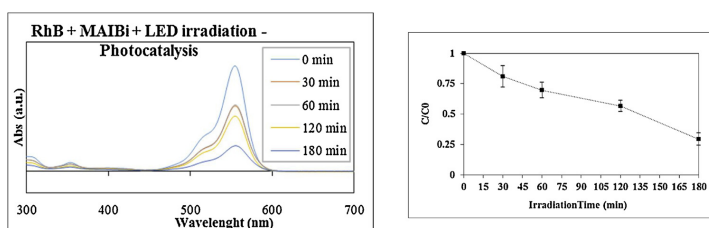


Fig. 9. Extinction spectrum and of RhB under photocatalytic conditions (LED lamp), dynamics degradation ( $C/C_0$ ) during photocatalytic reactions, error bars represent standard deviations from 3 replicates.

contributing to the visible-light photocatalytic activity of MBI. First, the absorption spectrum shifted to visible region resulting in photocatalytic degradation of RhB under visible-light irradiation. Secondly, the effective structure and morphology of MBI allowed highly efficient charges generation and separation in one hand and low charges recombination rate in the other hand. In general, reactive oxygen species such as  $O_2^{\cdot-}$  and  $\cdot OH$  can easily degrade RhB to smaller organic substances or even  $CO_2$  and  $H_2O$  [73]. In our case, after excitation, an electron in the valence band is excited in the conduction band of the photocatalyst (2). The electron and holes are transported through the surface of the catalyst. The holes can be consumed to directly oxidize RhB dye as proved by trapping agent experiments. On the other side, the hole, on the valence band, enables a one-electron oxidation step with water to produce a hydroxyl radical  $\cdot OH$ . Meanwhile, it should be mentioned that it is also possible a contribution of electrons that can

reduce oxygen present in water into the oxidizing species ( $\cdot O_2^-$ ). As explained before, the electron of the organic dye might be transferred from the dye ( $RhB^*$ ) to the catalyst, enhancing the efficiency of degradation by ROS production. According to the position of the energy levels assumed, not only the electrons can flow from the excited dye to the MBI but also the holes may flow from the catalyst to the dye, increasing the degradation efficiency.

Finally, two degradation pathways for RhB degradation are presented in Fig. 10. A first possible degradation occurs by de-ethylation of  $RhB^{*+}$  by the attack on the N-ethyl group leading to the formation of de-ethylated intermediates (N,N,N'-tri-ethylated rhodamine, N,N'-di-ethylated rhodamine, N-ethylated rhodamine and rhodamine). A second pathway involves the degradation of RhB chromophore by the attack of  $\cdot OH$  radicals on the chromophoric structure leading to the formation of organic acids and alcohols intermediates and finally to

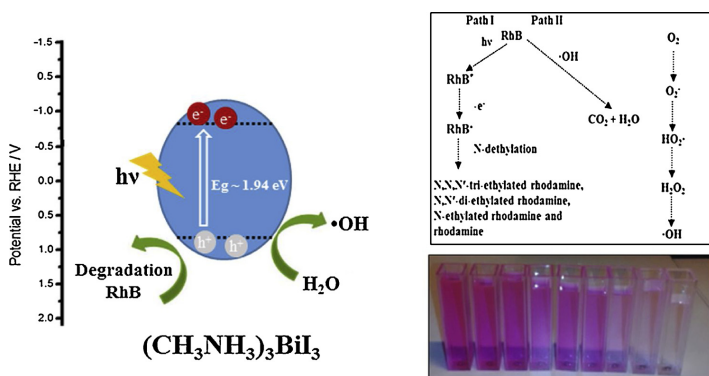


Fig. 10. Hypothesized mechanisms of degradation of RhB.

CO<sub>2</sub> and H<sub>2</sub>O [74,75]. According to the results of trapping agent, one may conclude that the second path is probably the one that occurred in the present case.

#### 4. Conclusions

In summary, the HOIP lead-free perovskite was successfully synthesized via a low temperature wet-chemical method. To the best of our knowledge, it could be the first report in photocatalytic application using MBL. Under visible-light illumination, the material show a remarkable activity for the degradation of the model compounds chosen. This ability was probably due to two specific features of the synthesized material: the visible-light optical absorption capacity and the reduced recombination of photogenerated electron-hole pairs. The present work provides a new type of material that may make full use of solar energy in practice for environmental applications.

#### Acknowledgement

MVTT Foundation is gratefully acknowledged for the financial support.

#### Appendix A. Supplementary data

Supplementary material related to this article can be found, in the online version, at doi:<https://doi.org/10.1016/j.jphotochem.2019.03.009>.

#### References

- [1] A. Helal, F.A. Harraz, A.A. Ismail, T.M. Sami, I.A. Ibrahim, Hydrothermal synthesis of novel heterostructured Fe<sub>2</sub>O<sub>3</sub>/Bi<sub>2</sub>S<sub>3</sub> nanorods with enhanced photocatalytic activity under visible light, *Appl. Catal. B Environ.* 213 (2017) 18–27, <https://doi.org/10.1016/j.apcatb.2017.05.009>.
- [2] C.I. Pearce, J.R. Lloyd, J.T. Guthrie, The removal of colour from textile wastewater using whole bacterial cells: a review, *Dyes Pigm.* 58 (2003) 179–196, [https://doi.org/10.1016/S0143-7208\(03\)00064-0](https://doi.org/10.1016/S0143-7208(03)00064-0).
- [3] S. Rani, M. Aggarwal, M. Kumar, S. Sharma, D. Kumar, Removal of methylene blue and rhodamine B from water by zirconium oxide/graphene, *Water Sci. Technol.* 166 (2012) 51–60, <https://doi.org/10.1016/j.wst.2016.04.001>.
- [4] G.S. Nyanhongo, J. Gomes, G.M. Gübitz, R. Zvauya, J. Read, W. Steiner, Decolorization of textile dyes by laccases from a newly isolated strain of *Trametes modesta*, *Water Res.* 36 (2002) 1449–1456, [https://doi.org/10.1016/S0043-1354\(01\)00365-7](https://doi.org/10.1016/S0043-1354(01)00365-7).
- [5] S. Song, J. Yao, Z. He, J. Qiu, J. Chen, Effect of operational parameters on the decolorization of C.I. Reactive Blue 19 in aqueous solution by ozone-enhanced electrocoagulation, *J. Hazard. Mater.* 152 (2008) 204–210, <https://doi.org/10.1016/j.jhazmat.2007.06.104>.
- [6] M. Rochkind, S. Pasternak, Y. Paz, Using dyes for evaluating photocatalytic properties: A critical review, *Molecules* 20 (2015) 88–110, <https://doi.org/10.3390/molecules20010088>.
- [7] P.T. Anastas, M.M. Kirchhoff, Origins, current status, and future challenges of green chemistry, *Acc. Chem. Res.* 35 (2002) 686–694, <https://doi.org/10.1021/ar010065m>.
- [8] J.M. Burns, W.J. Cooper, J.L. Ferry, D.W. King, B.P. DiMento, K. McNeill, C.J. Miller, W.L. Miller, B.M. Peake, S.A. Rusak, A.L. Rose, T.D. Waite, Methods for reactive oxygen species (ROS) detection in aqueous environments, *Aquat. Sci. Technol.* 54 (2012) 683–734, <https://doi.org/10.1007/s00027-012-0251-x>.
- [9] M.N. Chong, B. Jin, C.W.K. Chow, C. Saint, Recent developments in photocatalytic water treatment technology: a review, *Water Res.* 44 (2010) 2997–3027, <https://doi.org/10.1016/j.watres.2010.02.039>.
- [10] V. Augugliaro, M. Bellardita, V. Loddo, G. Palmisano, L. Palmisano, S. Yurdakal, Overview on oxidation mechanisms of organic compounds by TiO<sub>2</sub> in heterogeneous photocatalysis, *J. Photochem. Photobiol. C Photochem. Rev.* 13 (2012) 224–245, <https://doi.org/10.1016/j.jphotochem.2012.04.003>.
- [11] S. Ahmed, M.G. Rasul, W.N. Martens, R. Brown, M.A. Hashib, Advances in heterogeneous photocatalytic degradation of phenols and dyes in wastewater: a review, *Water Air Soil Pollut.* 215 (2011) 3–29, <https://doi.org/10.1007/s11270-010-0456-3>.
- [12] H. Dong, G. Zeng, L. Tang, C. Fan, C. Zhang, X. He, Y. He, An overview on limitations of TiO<sub>2</sub> <math>2 </math>-based particles for photocatalytic degradation of organic pollutants and the corresponding countermeasures, *Water Res.* 79 (2015) 128–146, <https://doi.org/10.1016/j.watres.2015.04.038>.
- [13] V. Etacheri, C. Di Valentin, J. Schneider, D. Bahnemann, S.C. Pillai, Visible-light activation of TiO<sub>2</sub> photocatalysts: Advances in theory and experiments, *J. Photochem. Photobiol. C Photochem. Rev.* 25 (2015) 1–29, <https://doi.org/10.1016/j.jphotochem.2015.08.003>.
- [14] C. a Gouvêa, F. Wypych, S.G. Moraes, N. Durán, N. Nagata, P. Peralta-Zamora, Semiconductor-assisted photocatalytic degradation of reactive dyes in aqueous solution, *Chemosphere* 40 (2000) 433–440, [https://doi.org/10.1016/S0045-6535\(99\)00313-6](https://doi.org/10.1016/S0045-6535(99)00313-6).
- [15] R.L.Z. Hoyer, R.E. Brandt, A. Oshero, V. Stevanovic, S.D. Stranks, M.W.B. Wilson, H. Kim, A.J. Akey, J.D. Perkins, R.C. Kurchin, J.R. Poindexter, E.N. Wang, M.G. Bawendi, V. Bulovic, T. Buonassisi, Methylammonium bismuth iodide as a lead-free, stable hybrid organic-inorganic solar absorber, *Chem. A Eur. J.* 22 (2016) 2605–2610, <https://doi.org/10.1002/chem.201505055>.
- [16] J.C. Colmenares, Heterogeneous Photocatalysis, (2016), [https://doi.org/10.1007/978-3-662-48719-8\\_7](https://doi.org/10.1007/978-3-662-48719-8_7).
- [17] Q. Chen, N. De Marco, Y. Yang, T. Bin Song, C.C. Chen, H. Zhao, Z. Hong, H. Zhou, Y. Yang, Under the spotlight: the organic-inorganic hybrid halide perovskite for optoelectronic applications, *Nano Today* 10 (2015) 355–396, <https://doi.org/10.1016/j.nantod.2015.04.009>.
- [18] S.D. Stranks, S.D. Stranks, G.E. Eperon, G. Grancini, C. Menelaou, M.J.P. Alcocer, T. Leijtens, L.M. Herz, A. Petrozza, H.J. Snaith, Electron-hole diffusion lengths exceeding 1 μm in an organic-inorganic hybrid perovskite, *Science* 342 (2014) 341–344, <https://doi.org/10.1126/science.1243982>.
- [19] T. Singh, A. Kulkarni, M. Ikegami, T. Miyasaka, Effect of electron transporting layer on bismuth-based lead-free perovskite (CH<sub>3</sub>NH<sub>3</sub>)<sub>3</sub>Bi<sub>2</sub>I<sub>9</sub> for photovoltaic applications, *ACS Appl. Mater. Interfaces* 8 (2016) 14542–14547, <https://doi.org/10.1021/acsmi.6b02843>.
- [20] E. Edri, S. Kirmayer, D. Cahen, G. Hodes, High open-circuit voltage solar cells based on organic-inorganic lead bromide perovskite, *J. Phys. Chem. Lett.* 4 (2013) 897–902, <https://doi.org/10.1021/jz400348q>.
- [21] H. Li, C. Wu, Y. Yan, B. Chi, J. Pu, J. Li, S. Priya, Fabrication of lead-free (CH<sub>3</sub>NH<sub>3</sub>)<sub>3</sub>Bi<sub>2</sub>I<sub>9</sub> perovskite photovoltaics in ethanol solvent, *ChemSusChem* 10 (2017) 3994–3998, <https://doi.org/10.1002/cssc.201701470>.
- [22] M. Lyu, J.H. Yun, M. Cai, Y. Jiao, P.V. Bernhardt, M. Zhang, Q. Wang, A. Du, H. Wang, G. Liu, L. Wang, Organic-inorganic bismuth (III)-based material: a lead-free, air-stable and solution-processable light-absorber beyond organolead perovskites, *Nano Res.* 9 (2016) 692–702, <https://doi.org/10.1007/s12274-015-0948-y>.
- [23] V. Vaiano, M. Matarangolo, O. Sacco, D. Sannino, Photocatalytic treatment of aqueous solutions at high dye concentration using praseodymium-doped ZnO catalysts, *Appl. Catal. B Environ.* 209 (2017) 621–630, <https://doi.org/10.1016/j.apcatb.2017.03.015>.
- [24] A.K. Gupta, A. Pal, C. Sahoo, Photocatalytic degradation of a mixture of Crystal Violet (Basic Violet 3) and Methyl Red dye in aqueous suspensions using Ag + doped TiO<sub>2</sub>, *Dyes Pigm.* 69 (2006) 224–232, <https://doi.org/10.1016/j.dyepig.2005.04.001>.
- [25] J. Navas, A. Sánchez-Coronilla, J.J. Gallardo, N. Cruz Hernández, J.C. Piñero, R. Alcántara, C. Fernández-Lorenzo, D.M. De los Santos, T. Aguilar, J. Martín-Call, ejaNew insights into organic-inorganic hybrid perovskite CH<sub>3</sub>NH<sub>3</sub>PbI<sub>3</sub> nanoparticles. An experimental and theoretical study of doping in Pb 2+ sites with Sn 2+, Sr 2+, Cd 2+ and, *Nanoscale*. 7 (2015) 6216–6229, <https://doi.org/10.1039/C5NR00041F>.
- [26] M. Jaffer, S. Mohamed, D.K. Bhat, Novel ZnWO<sub>4</sub> / RGO nanocomposite as high performance photocatalyst, *RSC Adv.* 4 (2017) 158–171, <https://doi.org/10.3934/matersci.2017.1.158>.
- [27] J. Zhang, H. Liu, Z. Ma, Flower-like Ag<sub>2</sub>O / Bi<sub>2</sub>MoO<sub>6</sub> p-n heterojunction with enhanced photocatalytic activity under visible light irradiation *Journal of Molecular Catalysis A : chemical flower-like Ag<sub>2</sub>O / Bi<sub>2</sub>MoO<sub>6</sub> p-n heterojunction with enhanced photocatalytic activity under visible light irradiation*, *J. Mol. Catal. A Chem.* 424 (2016) 37–44, <https://doi.org/10.1016/j.molcata.2016.08.009>.
- [28] X. Yuan, H. Wang, Y. Wu, G. Zeng, One-pot Self-Assembly and Photoreduction Synthesis of Silver Nanoparticle-Decorated Reduced Graphene Oxide / MIL-125 (Ti) Photocatalyst With Improved Visible Light Photocatalytic Activity 2016 (2016), <https://doi.org/10.1002/aoc.3430>.
- [29] J. Idigoras, A. Todinova, J.R. Sánchez-Valencia, A. Barranco, A. Borrás, J.A. Anta, The interaction between hybrid organic-inorganic halide perovskite and selective contacts in perovskite solar cells: an infrared spectroscopy study, *Phys. Chem. Chem. Phys.* 18 (2016) 13583–13590, <https://doi.org/10.1039/C6CP01265E>.
- [30] S.M. El-Sheikh, T.M. Khedr, A. Hakki, A.A. Ismail, W.A. Badawy, D.W. Bahnemann, Visible light activated carbon and nitrogen co-doped mesoporous TiO<sub>2</sub> as efficient photocatalyst for degradation of ibuprofen, *Sep. Purif. Technol.* 173 (2017) 258–268, <https://doi.org/10.1016/j.seppur.2016.09.034>.
- [31] A. Shit, A.K. Nandi, Interface engineering of hybrid perovskite solar cells with poly (3-thiophene acetic acid) under ambient conditions, *Phys. Chem. Chem. Phys.* 18 (2016) 10182–10190, <https://doi.org/10.1039/C6CP00502K>.
- [32] C. Müller, T. Glaser, M. Plogmeyer, M. Sendner, S. Döring, A.A. Bakulin, C. Brzuska, R. Scheer, M.S. Pshenichnikov, W. Kowalsky, A. Pucci, R. Lovrincić, Water Infiltration in Methylammonium Lead Iodide Perovskite: Fast and Inconspicuous, *Chem. Mater.* 27 (2015) 7835–7841, <https://doi.org/10.1021/acs.chemmater.5b03883>.
- [33] S.F. Hoefler, G. Trimmel, Progress on lead-free metal halide perovskites for photovoltaic applications : a review, *Monatshfte Für Chemie - Chem. Mon.* 148 (2017) 795–826, <https://doi.org/10.1007/s00706-017-1933-9>.
- [34] H. Damak, A. Yangui, S. Triki, Y. Abid, H. Feki, Structural characterization, vibrational, optical properties and DFT investigation of a new luminescent organic-inorganic material, *J. Lumin.* 161 (2015) 214–220, <https://doi.org/10.1016/j.jlumin.2015.01.010>.
- [35] S. Sourisseau, N. Louvain, W. Bi, N. Mercier, D. Rondeau, F. Boucher, J. Buzare, C. Legein, L. De Chimie, B.V. La, I. Mate, J. Rouxel, A.V. Oli, V. Messiaen, L.M. Cedex, R.V. October, Reduced band gap hybrid perovskites resulting from

- combined hydrogen and halogen bonding at the organic-inorganic interface, *Chem. Mater.* 45 (2007) 600–607, <https://doi.org/10.1021/cm062380e>.
- [36] P. Dey, V. Khorwal, P. Sen, K. Biswas, T. Maiti, Spectral studies of lead-free organic-inorganic hybrid potential photo absorbers, *energy technol. Environ. Sci.* 4 (2018) 794–800, <https://doi.org/10.1002/sltc.201702745>.
- [37] Z. Zhang, X. Li, X. Xia, Z. Wang, Z. Huang, B. Lei, Y. Gao, High-quality (CH<sub>3</sub>NH<sub>3</sub>)<sub>3</sub>Bi<sub>2</sub>I<sub>9</sub> film-based solar cells: pushing efficiency up to 1.64%, *J. Phys. Chem. Lett.* 8 (2017) 4300–4307, <https://doi.org/10.1021/acs.jpcclett.7b01952>.
- [38] M. Kong, H. Hu, L. Wan, M. Chen, Y. Gan, J. Wang, F. Chen, B. Dong, D. Eder, S. Wang, Nontoxic (CH<sub>3</sub>NH<sub>3</sub>)<sub>3</sub>Bi<sub>2</sub>I<sub>9</sub> perovskite solar cells free of hole conductors with an alternative architectural design and a solution-processable approach, *RSC Adv.* 7 (2017) 35549–35557, <https://doi.org/10.1039/c7ra04924b>.
- [39] C. Lan, J. Luo, S. Zhao, C. Zhang, W. Liu, S. Hayase, T. Ma, Effect of lead-free (CH<sub>3</sub>NH<sub>3</sub>)<sub>3</sub>Bi<sub>2</sub>I<sub>9</sub> perovskite addition on spectrum absorption and enhanced photovoltaic performance of bismuth triiodide solar cells, *J. Alloys Compd.* 701 (2017) 834–840, <https://doi.org/10.1016/j.jallcom.2017.01.169>.
- [40] V. Zardetto, B.L. Williams, A. Perrotta, F. Di Giacomo, M.A. Verheijen, R. Andriessen, W.M.M. Kessels, M. Creatore, Atomic layer deposition for perovskite solar cells: research status, opportunities and challenges, *Sustain. Energy Fuels* 1 (2017) 30–55, <https://doi.org/10.1039/C6SE00076B>.
- [41] J. Hou, K. Jian, M. Shen, R. Wei, X. Wu, F. Idrees, C. Cao, Micro and nano hierarchical structures of BiOI / activated carbon for efficient visible-light- photocatalytic reactions, *Nature* (2017) 2–11, <https://doi.org/10.1038/s41598-017-12266-x>.
- [42] D.M. Fabian, S. Ardo, Hybrid organic-inorganic solar cells based on bismuth iodide and 1,6-hexanediammonium dication, *J. Mater. Chem. A* 4 (2016) 6837–6841, <https://doi.org/10.1039/C6TA00517A>.
- [43] C. Rocks, V. Svrcek, P. Maguire, D. Mariotti, Understanding surface chemistry during MAPbI<sub>3</sub> spray deposition and its effect on photovoltaic performance, *J. Mater. Chem. C* 5 (2017) 902–916, <https://doi.org/10.1039/C6TC04864A>.
- [44] J. Tauc, Optical properties and electronic structure of amorphous Ge and Si, *Mater. Res. Bull.* 3 (1968) 37–46, [https://doi.org/10.1016/0025-5408\(68\)90023-8](https://doi.org/10.1016/0025-5408(68)90023-8).
- [45] K. Eckhardt, V. Bon, J. Grothe, F.M. Wisser, S. Kaskel, As A Potential Absorber for Photovoltaics †, (2016), pp. 3058–3060, <https://doi.org/10.1039/C5CC10455F>.
- [46] K.H.H. Drekhage, Fluorescence efficiency of laser dyes, *J. Res. Natl. Bur. Stand. Sect. A Phys. Chem.* 80A (1976) 421, <https://doi.org/10.6028/jres.080A.044>.
- [47] M. Beija, C.A.M. Afonso, J.M.G. Martinho, Synthesis and applications of Rhodamine derivatives as fluorescent probes, *Chem. Soc. Rev.* 38 (2009) 2410, <https://doi.org/10.1039/b901612k>.
- [48] V. Belessi, D. Lambropoulou, I. Konstantinou, R. Zboril, J. Tucek, D. Jancik, T. Albanis, D. Petridis, Structure and photocatalytic performance of magnetically separable titania photocatalysts for the degradation of propachlor, *Appl. Catal. B Environ.* 87 (2009) 181–189, <https://doi.org/10.1016/j.apcatb.2008.09.012>.
- [49] A. Lee, H. Nikraz, BOD: COD ratio as an Indicator for river pollution, *Int. Proc. Chem. Biol. Environ. Eng.* 51 (2015) 139–142, <https://doi.org/10.7763/IPCBE.2015.05.012>.
- [50] N. Turkten, Z. Cinar, Photocatalytic decolorization of azo dyes on TiO<sub>2</sub>: prediction of mechanism via conceptual DFT, *Catal. Today* 287 (2017) 169–175, <https://doi.org/10.1016/j.cattod.2017.01.019>.
- [51] N.M. Julkapli, S. Bagheri, S. Bee, A. Hamid, Recent Advances in Heterogeneous Photocatalytic Decolorization of Synthetic Dyes 2014 (2014), <https://doi.org/10.1155/2014/692307>.
- [52] G. Trefalt, S.H. Behrens, M. Borkovec, Charge regulation in the electrical double layer: ion adsorption and surface interactions, *Langmuir* 32 (2016) 380–400, <https://doi.org/10.1021/acs.langmuir.5b03611>.
- [53] S.G. Yan, J.T. Hupp, Semiconductor-based interfacial electron-transfer reactivity: decoupling kinetics from pH-dependent band energetics in a dye-sensitized titanium dioxide/aqueous solution system, *J. Phys. Chem.* 100 (1996) 6867–6870, <https://doi.org/10.1021/jp953180l>.
- [54] N. Fiol, I. Villaescusa, Determination of sorbent point zero charge: usefulness in sorption studies, *Environ. Chem. Lett.* 7 (2009) 79–84, <https://doi.org/10.1007/s10311-008-0139-0>.
- [55] D.L. Postai, C.A. Demarchi, F. Zanatta, D.C.C. Melo, C.A. Rodrigues, Adsorption of rhodamine B and methylene blue dyes using waste of seeds of *Aleurites Moluccana*, a low cost adsorbent, *Alexandria Eng. J.* 55 (2016) 1713–1723, <https://doi.org/10.1016/j.aej.2016.03.017>.
- [56] W. Zhang, Q. Zhao, X. Wang, X. Yan, J. Xu, Z. Zeng, Lead-free organic-inorganic hybrid perovskite heterojunction composites for photocatalytic applications, *Catal. Sci. Technol.* 7 (2017) 2753–2762, <https://doi.org/10.1039/C7CY00389G>.
- [57] W. Wang, M.O. Tadé, Z. Shao, Research progress of perovskite materials in photocatalysis- and photovoltaics-related energy conversion and environmental treatment, *Chem. Soc. Rev.* 44 (2015) 5371–5408, <https://doi.org/10.1039/C5CS00113G>.
- [58] G. Zhang, G. Liu, L. Wang, J.T.S. Irvine, Inorganic perovskite photocatalysts for solar energy utilization, *Chem. Soc. Rev.* 45 (2016) 5951–5984, <https://doi.org/10.1039/C5CS00769K>.
- [59] T. Wu, G. Liu, J. Zhao, H. Hidaka, N. Serpone, Photoassisted degradation of dye pollutants. V. self-photosensitized oxidative transformation of Rhodamine B under visible light irradiation in aqueous TiO<sub>2</sub> dispersions, *J. Phys. Chem. B* 102 (1998) 5845–5851, <https://doi.org/10.1021/jp980922c>.
- [60] N. Huang, J. Shu, Z. Wang, M. Chen, C. Ren, W. Zhang, One-step pyrolytic synthesis of ZnO nanorods with enhanced photocatalytic activity and high photostability under visible light and UV light irradiation, *J. Alloys Compd.* 648 (2015) 919–929, <https://doi.org/10.1016/j.jallcom.2015.07.039>.
- [61] L. Pan, J.J. Zou, X. Zhang, L. Wang, Water-mediated promotion of dye sensitization of TiO<sub>2</sub> under visible light, *J. Am. Chem. Soc.* 133 (2011) 10000–10002, <https://doi.org/10.1021/ja2035927>.
- [62] G. Xing, C. Tang, B. Zhang, L. Zhao, Y. Su, X. Wang, A highly uniform ZnO/NaTaO<sub>3</sub> nanocomposite: enhanced self-sensitized degradation of colored pollutants under visible light, *J. Alloys Compd.* 647 (2015) 287–294, <https://doi.org/10.1016/j.jallcom.2015.06.095>.
- [63] A. Kumar, V. Sharma, S. Kumar, A. Kumar, V. Krishnan, Towards utilization of full solar light spectrum using green plasmonic Au-TiO<sub>2</sub> photocatalyst at ambient conditions, *Surf. Interfaces* 11 (2018) 98–106, <https://doi.org/10.1016/j.surfin.2018.03.005>.
- [64] A.J. Lehner, D.H. Fabiani, H.A. Evans, C.A. Hébert, S.R. Smock, J. Hu, H. Wang, J.W. Zwaniger, M.L. Chabinyr, R. Seshadri, Crystal and electronic structures of complex bismuth iodides A<sub>3</sub>Bi<sub>2</sub>I<sub>9</sub> (A = K, Rb, Cs) related to perovskite: aiding the rational design of photovoltaics, *Chem. Mater.* 27 (2015) 7137–7148, <https://doi.org/10.1021/acs.chemmater.5b03147>.
- [65] M. Aamir, Z.H. Shah, M. Sher, A. Iqbal, N. Revaprasadu, M.A. Malik, J. Akhtar, Enhanced photocatalytic activity of water stable hydroxyl ammonium lead halide perovskites, *Mater. Sci. Semicond. Process.* 63 (2017) 6–11, <https://doi.org/10.1016/j.mssp.2017.01.001>.
- [66] B.W. Park, B. Philippe, X. Zhang, H. Rensmo, G. Boschloo, E.M.J. Johansson, Bismuth Based Hybrid Perovskites A<sub>3</sub>Bi<sub>2</sub>I<sub>9</sub> (A = Methylammonium or Cesium) for Solar Cell Application, *Adv. Mater.* 27 (2015) 6806–6813, <https://doi.org/10.1002/adma.201501978>.
- [67] R. Andreozzi, V. Caprio, A. Insola, R. Marotta, Advanced oxidation processes (AOP) for water purification and recovery, *Catal. Today* 53 (1999) 51–59, [https://doi.org/10.1016/S0920-5861\(99\)00102-9](https://doi.org/10.1016/S0920-5861(99)00102-9).
- [68] X. Li, J. Yu, M. Jaroniec, Hierarchical photocatalysts, *Chem. Soc. Rev.* 45 (2016) 2603–2636, <https://doi.org/10.1039/c5cs00838g>.
- [69] S. Liu, K. Yin, W. Ren, B. Cheng, J. Yu, Tandem photocatalytic oxidation of Rhodamine B over surface fluorinated bismuth vanadate crystals, *J. Mater. Chem.* 22 (2012) 17759–17767, <https://doi.org/10.1039/c2jm33337f>.
- [70] J. Huang, Z. Gu, X. Zhang, G. Wu, H. Chen, Lead-free (CH<sub>3</sub>NH<sub>3</sub>)<sub>3</sub>Bi<sub>2</sub>I<sub>9</sub> perovskite solar cells with fluorinated PDI film as organic electron transport layer, *J. Alloys Compd.* 767 (2018) 870–876, <https://doi.org/10.1016/j.jallcom.2018.07.185>.
- [71] K. Ahmad, N. Ansari, K. Natarajan, S.M. Mobin, A (CH<sub>3</sub>NH<sub>3</sub>)<sub>3</sub>Bi<sub>2</sub>I<sub>9</sub> Perovskite Based on a Two-step Deposition Method: Lead-free, Highly Stable, and With Enhanced Photovoltaic Performance, (2019), pp. 1192–1198, <https://doi.org/10.1002/celc.201801322>.
- [72] Z. Zhang, X. Li, X. Xia, Z. Wang, Z. Huang, B. Lei, Y. Gao, High-Quality (CH<sub>3</sub>NH<sub>3</sub>)<sub>3</sub>Bi<sub>2</sub>I<sub>9</sub> Film-Based Solar Cells: Pushing Efficiency up to 1.64%, (2017), pp. 3–10, <https://doi.org/10.1021/acs.jpcclett.7b01952>.
- [73] L. Hu, H. Yuan, L. Zou, F. Chen, X. Hu, Adsorption and visible light-driven photocatalytic degradation of Rhodamine B in aqueous solutions by Ag@AgBr/SBA-15, *Appl. Surf. Sci.* 355 (2015) 706–715, <https://doi.org/10.1016/j.apsusc.2015.04.166>.
- [74] S.K. Yadav, P. Jeevanandam, Synthesis of Ag<inf>2</inf>-TiO<inf>2</inf> nanocomposites and their catalytic activity towards rhodamine B photodegradation, *J. Alloys Compd.* 649 (2015) 483–490, <https://doi.org/10.1016/j.jallcom.2015.07.184>.
- [75] K. Yu, S. Yang, H. He, C. Sun, C. Gu, Y. Ju, Visible Light-Driven Photocatalytic Degradation of Rhodamine B over NaBiO<sub>3</sub>: Pathways and Mechanism, *J. Phys. Chem. A* 113 (2009) 10024–10032, <https://doi.org/10.1021/jp905173e>.



## **Publication III**

Bresolin, B.M., Günnemann, C., Bahnemann, D.W., and Sillanpää, M.  
**Pb-Free Cs<sub>3</sub>Bi<sub>2</sub>I<sub>9</sub> Perovskite as a Visible-Light-Active Photocatalyst for Organic  
Pollutant Degradation**

Reprinted with permission from  
*Nanomaterials*  
Vol. 10 (763), pp. 1-13, 2020  
© 2020, MDPI



Article

# Pb-Free Cs<sub>3</sub>Bi<sub>2</sub>I<sub>9</sub> Perovskite as a Visible-Light-Active Photocatalyst for Organic Pollutant Degradation

Bianca-Maria Bresolin <sup>1,\*</sup>, Carsten Günnemann <sup>2</sup>, Detlef W. Bahnemann <sup>2,3,4</sup> and Mika Sillanpää <sup>5,6,7</sup>

<sup>1</sup> Department of Separation Science, School of Engineering Science, Lappeenranta University of Technology, Sammonkatu 12, 50130 Mikkeli, Finland

<sup>2</sup> Institute of Technical Chemistry, Leibniz University Hannover, Callinstraße 3, D-30167 Hannover, Germany; guennemann@iftc.uni-hannover.de (C.G.); Bahnemann@iftc.uni-hannover.de (D.W.B.)

<sup>3</sup> Laboratory of Nano- and Quantum-Engineering (LNQE), Gottfried Wilhelm Leibniz University Hannover, Schneiderberg 39, D-30167 Hannover, Germany

<sup>4</sup> Laboratory "Photoactive Nanocomposite Materials", Saint-Petersburg State University, Ulyanovskaya str. 1, Peterhof, 198504 Saint-Petersburg, Russia

<sup>5</sup> Institute of Research and Development, Duy Tan University, De Nang 550000, Vietnam; mikaesillanpaa@gmail.com

<sup>6</sup> Faculty of Environmental and Chemical Engineering, Duy Tan University, De Nang 550000, Vietnam

<sup>7</sup> School of Civil Engineering and Surveying, Faculty of Health, Engineering and Science, University of Southern Queensland, West Street, Toowoomba, QLD 4350, Australia

\* Correspondence: biancabresolin@yahoo.it or Bianca.Maria.Bresolin@lut.fi

Received: 14 March 2020; Accepted: 11 April 2020; Published: 16 April 2020



**Abstract:** In our work, we employed Cs<sub>3</sub>Bi<sub>2</sub>I<sub>9</sub> as a visible-light-active photocatalyst, synthesized with a low-temperature solvothermal method. The morphological and structural properties of the as-prepared perovskite were investigated, and the results were compared to previous studies to confirm its nature and the quality of the synthesis procedure. Transient absorption spectroscopy was applied in order to investigate the generation and lifetime of photogenerated charge carriers, revealing their formation after visible light excitation. The potential photocatalytic activity of the as-prepared metal halide perovskite was applied for the removal of Rhodamine B in aqueous solution, demonstrating an excellent activity of 93% after 180 min under visible-light irradiation. The current research aims to provide insights into the design of a new visible-light-active photocatalyst, Cs<sub>3</sub>Bi<sub>2</sub>I<sub>9</sub>, selected for its high application value in the field of advanced materials for light harvesting.

**Keywords:** halide perovskite; laser photolysis; charge carrier separation; visible light activity

## 1. Introduction

The recent developments in industrialization have caused simultaneously remarkable energy and environmental challenges. This increasing global environmental pollution has become a pivotal issue; thus, sustainable technologies to solve the problem for human society should be developed [1]. On the other hand, the extensive employment of alternative renewable energy sources is also required for a sustainable future of our planet and its ecosystems.

Among the possible alternatives, heterogeneous photocatalysis has emerged as a promising technology holding the key for the future in environmental decontamination and renewable energy generation. One of its main advantages is the use of light energy, a sustainable source available all over the world [2–5]. Light energy is definitively considered one of the most promising sustainable sources, providing an environmentally friendly supply, and with its worldwide availability, it can be considered as one of the main candidates to overcome the future energy crisis [6,7].



In recent years, the use of light-activated photocatalysts emerged in heterogeneous advanced oxidation as great technology for environmental remediation and light energy conversion [8,9]. Some of the merits of these materials include the absence of fouling, the lack of mass transfer limitations, applicability at ambient conditions, and the ability to mineralize many organic pollutants into non-toxic compounds, such as water, carbon dioxide, and inorganic ions [10]. Among different photocatalysts, Titanium Oxide (TiO<sub>2</sub>) has attracted particular attention for many reasons, such as high stability, resistance to different pH conditions, non-toxicity, strong redox reaction potentiality, low cost, and availability in the market [2,11]. Unfortunately, with its wide bandgap (3.2 eV), conventional TiO<sub>2</sub> could be mainly utilized under UV illumination that only accounts for a small fraction of the sun's energy (5%) [12,13]. On the other hand, visible light accounts for almost 45% of the available solar radiation. Therefore, by exploiting novel visible-light-using active photocatalysts, sunlight would be more efficiently used, and the overall applications based on solar radiation would be greatly improved [14–17]. Thus, it seems profitable to design new and highly efficient visible-light-active photocatalysts for practical applications.

Recently, perovskite materials emerged for their record-breaking properties, in particular, their attractive light-harvesting ability [18–20]. Among them, lead halide perovskites have garnered a lot of attention for their remarkable performance, especially in photovoltaic devices. Unfortunately, their toxicity and instability remain two gaps to overcome for environmental applications [21–23]. In contrast, inorganic perovskite materials display much better stability [24–26]. Particularly, bismuth-based halide perovskites have gained attention by solving both the stability and toxicity issues related to lead-based materials [27–29]. Bismuth is known as an abundant metal on the earth's crust; it can be recovered as a byproduct of other metals' refining, and its price is quite stable and relatively low [30]. Several scientists have investigated ternary cesium bismuth halide (Cs<sub>3</sub>Bi<sub>2</sub>I<sub>9</sub>) as a new material for high-performance photovoltaic applications [27,31–34]. The Cs<sub>3</sub>Bi<sub>2</sub>I<sub>9</sub> structure consists of identical perovskite-like fragments described by a general formula A<sub>3</sub>Bi<sub>2</sub>I<sub>9</sub>, with alternating edge-sharing [BiI<sub>6</sub>]<sup>3-</sup> octahedral layers, where the voids are filled with Cs<sup>+</sup> cations [35,36]. The tuneable structure and morphology have a great influence on the intrinsic electronic and optical properties that make this material so interesting in photocatalytic applications [37]. Many pioneers in photovoltaic technology have already experienced its advantages, such as excellent photoluminescence intensity suppression and significantly less toxicity than lead halides [31,33,34,37–42]. Intense research has been reported on Cs<sub>3</sub>Bi<sub>2</sub>I<sub>9</sub> due to its attractive and impressive optical and electronic properties, such as excellent carrier transport behavior, high defect tolerance, and extremely low-density defects. However, several characteristics and potential applications of such an interesting material are still unrevealed.

The development of visible-light-active photocatalysts to tackle environmental contamination using a sustainable approach has been addressed as imperative, taking into consideration that visible light makes up the substantial fraction of the solar spectrum. In this work, we focused on Cs<sub>3</sub>Bi<sub>2</sub>I<sub>9</sub> powder, prepared with an easily reproducible and low-temperature procedure. In particular, the visible-light-induced photogenerated charges were studied by laser flash photolysis revealing their mobility and dynamics effects.

Dyes are one of the main sources of water pollution [43–47]; in textile industries, around 12% of dyes used are found to be lost during operations every year, and 20% of their residues are estimated to be released directly in the environment [48]. High contamination has been reported for xanthene dyes, such as Rhodamine B (RhB), [49] which was found to be very harmful not only for the aquatic animals and plants, but also for humans, causing respiratory problems, asthma, dermatitis, mutagenicity, cancer, etc. [50]. Dyes show good solubility in water, and they are strongly resistant to the majority of conventional chemical and biological methods [51,52].

In our work, the as-synthesized metal halide perovskite was characterized by different techniques, and its photocatalytic activity was tested by studying the degradation of Rhodamine B in aqueous suspension under visible-light irradiation.

The aim of our work is, besides the characterization of the as-synthesized material, to investigate the ability of the perovskite to generate trapped charge carriers after excitation with visible light. Laser flash photolysis measurements were applied to determine the primary photochemical processes: the photogeneration of electrons and holes charge carriers. The reactivity of the trapped charge carriers was tested by the photodegradation of RhB.

The structure of the as-synthesized material is depicted in Figure 1. Based on our comprehensive study, we have proposed  $\text{Cs}_3\text{Bi}_2\text{I}_9$  as a potential visible-light photocatalyst justified by the investigated criteria, such as proper bandgap, suitable optical properties, and charge carriers' dynamics.

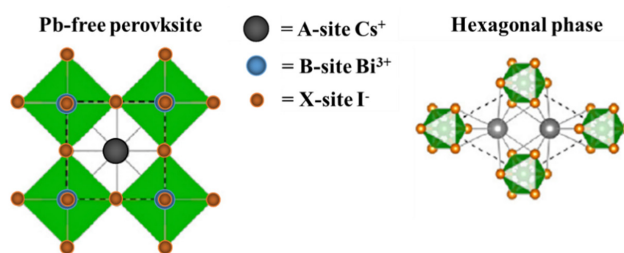


**Figure 1.** Illustrations depicting the crystal structures of the conventional perovskite and the hexagonal-phase-ordered-vacancy perovskite structure adopted by  $\text{Cs}_3\text{Bi}_2\text{I}_9$ .

## 2. Materials and Methods

### 2.1. Photocatalyst Preparation

$\text{Cs}_3\text{Bi}_2\text{I}_9$  perovskite was synthesized from cesium iodide (CsI, 99.9% trace metals basis) and bismuth iodide ( $\text{BiI}_3$ , purity 99%) using dimethylformamide (anhydrous, 99.8%, DMF) as the solvent. All chemicals were purchased from Sigma Aldrich (Darmstadt, Germany) and used without further purification. In a typical synthesis, CsI and  $\text{BiI}_3$  were mixed in dimethylformamide in a molar ratio of 3:2 and heated at 60 °C overnight for the evaporation of the solvent. Diethyl ether (purity  $\geq 99.8\%$ , Sigma Aldrich, Darmstadt, Germany) was used to wash the sample three times in order to remove DMF residues. Finally, the sample was dried in an oven at 60 °C overnight. The obtained material was finally ground in a mortar in order to obtain a fine powder.

### 2.2. Photocatalyst Characterization

The crystal phases and lattice parameters of the sample and its precursors were determined by powder X-ray diffraction using a D8 Advance diffractometer (Bruker, Solna, Sweden) provided with a Cu  $K\alpha$  radiation source. The UV-Vis diffuse reflectance spectrum of the as-synthesized perovskite was recorded with a Cary-100 Bio Spectrophotometer (Agilent, Santa Clara, CA, USA), equipped with an integrating sphere, at room temperature, within a wavelength range between 300 and 800 nm, and employing barium sulfate as the reflection standard. The optical bandgap energies were investigated using the Kubelka–Munk function [33]. The specific surface area of the sample was evaluated with Brunauer–Emmett–Teller (BET) measurements. The analysis was performed by a single point through adsorption of nitrogen at  $-196$  °C, using a Chemisorb 2300 apparatus (Micro metrics Instrument). Information about the elemental composition of the powder and chemical state of the species on the surface of the sample was analyzed using X-ray photoelectron spectroscopy (XPS-Leybold Heraeus, Mellon, Toronto, ON, Canada) with 300 W  $\text{AlK}\alpha$  radiation (20 eV pass energy with energy resolution 0.6 eV and 0.1 eV steps; modified Shirley background subtraction and modified Scofield relative sensitivity factors library were used in the quantification; data were processed with the advantage XPS analysis SW). Electrochemical measurements were performed in a three-electrode electrochemical cell provided with a Pt counter electrode and an  $\text{Ag}/\text{AgCl}/3 \text{ mol}\cdot\text{L}^{-1} \text{ NaCl}$  reference electrode. Thin films of the  $\text{Cs}_3\text{Bi}_2\text{I}_9$  were prepared on top of fluoride-doped tin oxide (FTO)-coated

glasses (Sigma Aldrich,  $\approx 8 \Omega \text{ sq}^{-1}$ ) by the screen printing method [53]. The elemental composition was confirmed by means of energy dispersive spectroscopy (EDS). Transmission electron microscopy analysis was performed with a TECNAI FEI G2 microscope.

### 2.3. Laser Flash Photolysis Measurements

Transient absorption spectroscopy measurements (TAS) were performed with an Applied Photophysics LKS 80 Laser Flash Photolysis Spectrometer. In order to analyze the light absorption of the photogenerated transient species, the powder was excited with an Nd-YAG laser (Quantel; Brilliant B; 2nd harmonic, 532 nm) and analyzed with a pulsed xenon lamp (Osram XBO, 150 W; Austin, TX, USA). The diffusely reflected light was led to a monochromator and then to a photomultiplier as a detector (Hamamatsu PMT R928, Japan). Excitations energy densities of  $3 \text{ mJ cm}^{-2}$  per pulse were used and monitored by a Maestro energy meter (Gentec-EO). Resistance of  $100 \Omega$  was used for the connection between detector and oscilloscope. Before each experiment, the  $\text{Cs}_3\text{Bi}_2\text{I}_9$  powder sample was placed in a quartz flat cuvette flushed with nitrogen or methanol for 30 min according to the purpose of the measurements. The change in the reflectance  $\Delta J$  was obtained from the measured absorbance (Abs) values according to Equation (1), where  $I_0$  and  $I$  are the intensities of the reflected light before and after excitation, respectively.

$$\Delta J = 1 - 10^{-\text{Abs}} = \frac{I - I_0}{I_0} \quad (1)$$

For each measurement, the average of 15 shots was considered, and the data points were reduced to 200.

### 2.4. Measurement of the Photocatalytic Reactivity

For the determination of the photocatalytic activity of the as-prepared sample, the photocatalytic conversion of Rhodamine B in aqueous solution was investigated at ambient temperature under visible-light irradiation. The experiments were performed in a 250 mL flask, with 100 mg of the photocatalyst powder that was dispersed into 100 mL of an RhB solution (20 mg/L). After a period to reach the adsorption equilibration in dark conditions (30 min), the surface of the solution was irradiated with a 150 W halogen lamp (Visilight CL150, Lutterworth, UK) with emission in the visible range (380–400 nm, Figure S1); more information is available in the Supplementary Materials. The lamp was located at the top of the reactor at two centimeters from the surface of the solution. The decrease in the concentration of the target pollutant was monitored at constant intervals of time by a PerkinElmer Lambda (Waltham, MA, USA) 1050 UV—visible spectrophotometer.

## 3. Results and Discussion

### 3.1. Morphological Characterization

Figure 2 shows the recorded XRD pattern of the as-prepared material, which agrees with the reference pattern (01-070-0666 (I)—cesium bismuth iodide). Furthermore, no peaks corresponding to precursor materials were present (Supplementary Materials, Figure S2), confirming the purity of the as-synthesized powder. The obtained lattice parameters are  $a = 8.404 \text{ \AA}$ ,  $b = 8.404 \text{ \AA}$ , and  $c = 21.183 \text{ \AA}$ , which are in good agreement with previous studies [31,37]. More details are presented in our previous report [54].

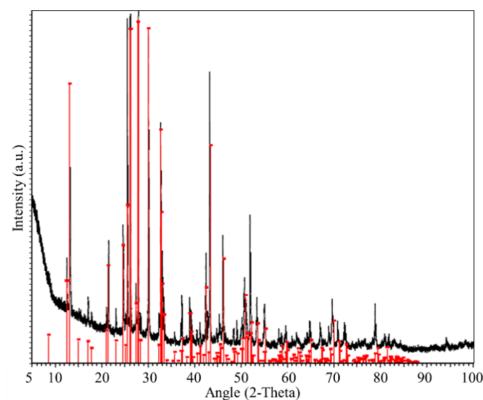


Figure 2. XRD pattern of  $\text{Cs}_3\text{Bi}_2\text{I}_9$  perovskite powder.

The morphology of the  $\text{Cs}_3\text{Bi}_2\text{I}_9$  powder was investigated by means of transmission electron microscopy (TEM and SEM). Transmission electron microscopy images (Figure 3a,b) of  $\text{Cs}_3\text{Bi}_2\text{I}_9$  depict that the particles exhibited hexagonal shapes with an average size in the order of a hundred nanometers. From the SEM images, the  $\text{Cs}_3\text{Bi}_2\text{I}_9$  powder shows a typical 3D structure of particles with rough surfaces; further details are shown in our previous report [54]. The growth of well-defined crystals is important to highlight, because a high crystallinity, which is confirmed by the XRD as well, is one important factor for the efficient separation and transport of photogenerated charge carriers [55]. The charge recombination is affected by the presence of defects in crystals that behave as trap sites [56]. The present powder exhibits large but well-separated crystallized grains. These properties may facilitate the diffusion of free carriers and thus increase the efficiency of charge carriers under illumination [57]. Energy-dispersive X-ray spectroscopy (EDX) measurements were taken to verify the composition of the as-synthesized material (Figure 3c). According to the measurement, the element contents (I: 40.5%, Cs:12.4%, and Bi: 8.1%) were found to be in good agreement with the expected percentage [41].

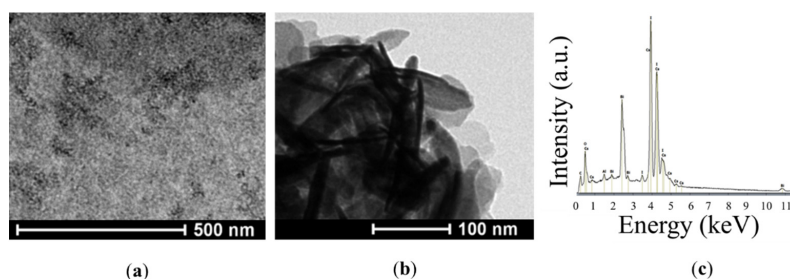


Figure 3. TEM images (a,b) and EDX analysis (c) of the as-synthesized  $\text{Cs}_3\text{Bi}_2\text{I}_9$  powder.

The results of the XPS analysis of the as-synthesized  $\text{Cs}_3\text{Bi}_2\text{I}_9$  powder are shown in Figure 4, where the resulting overview survey is displayed. The spectrum shows mainly perovskite core peaks, but it includes some other contributions probably due to surface impurities and the contribution of the sample holder. As an example, the peaks around 293.5 and 287.2 eV can be associated with carbon or the two peaks around 550 eV are ascribable to oxygen. However, core-level spectra for Bi 4f, I 3d, and Cs 3d have been detected. The contribution of Bi 4f was detected in a range between 168.0 and 155.0 eV [58]. The smaller peak at the lower binding energy (157.2 eV) indicates the presence of a metallic Bi component, probably induced in part during the measurements [59]. Two intense peaks

appear in the XPS spectrum related to the core level I 3d. According to previous studies, they can be associated with the doublets  $3d_{5/2}$  and  $3d_{3/2}$  with the lower binding component located at 618.9 eV and assignable to triiodide  $I_3^-$ . The additional broadening of the I 3d peak at 622.3 eV may indicate the presence of oxidized species of iodine at the surface, which forms the  $I_2^+$  cation and the iodite anion ( $IO_2^-$ ) [60]. The Cs  $3d_{5/2}$  and Cs  $3d_{3/2}$  peaks are observed at about 724.6 and 738.4 eV, respectively. The satellite broad peaks at higher binding energies of the main photoemission peaks, which may be identified as plasmons, arise from the excitation of plasma oscillations of the valence band electrons by the motion of photoelectrons in the solid. This feature was already shown in previous reports [61]. The XPS analysis further results in atomic percentages (I: 51.4%, Cs: 22.4%, and Bi: 9.9%) that agree well with the percentages obtained by the EDX analysis.

Further details are presented in our previous report [54].

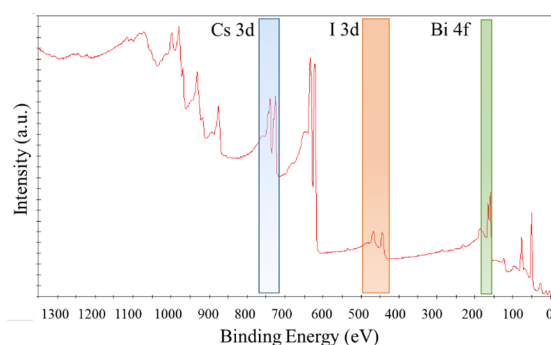


Figure 4. XPS survey spectrum.

The BET surface area of the  $Cs_3Bi_2I_9$  powder was measured based on nitrogen adsorption to be  $5.6 \text{ m}^2 \cdot \text{g}^{-1}$ .

As shown in the photograph (Figure 5), bare  $BiI_3$  displays a dark black color, whereas  $Cs_3Bi_2I_9$  is red. This evident color change strongly supports the formation of a  $BiI_3$  coordination complex,  $Cs_3Bi_2I_9$ , when the precursors were dissolved in DMF [62,63].

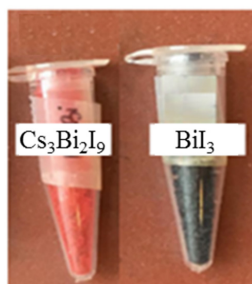
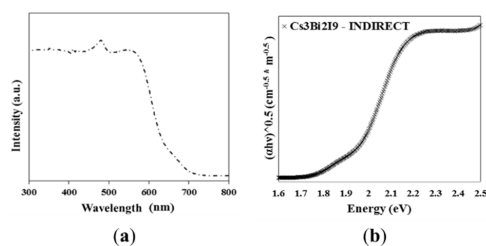


Figure 5. Dark bare  $BiI_3$  and red coordination complex  $Cs_3Bi_2I_9$ .

### 3.2. Optical Characterization

UV–Vis diffuse reflectance spectra were recorded to quantify the light absorption ability and the optical bandgaps of the  $Cs_3Bi_2I_9$  powder; the results are shown in Figure 6a. The absorption starts at around 630 nm with an additional peak observed near 485 nm.  $Cs_3Bi_2I_9$  exhibits a strong excitonic behavior even at room temperature; the excitonic absorption peak at 2.56 eV (485 nm) may be related to the strong quantum confinement effect due to the 0D nature of the  $[Bi_2I_9]^{3-}$  bioctahedra [39].

The bandgap of the powder was calculated from the Tauc plot and was found to be indirect and equal to 1.95 eV (Figure 6b). Previous studies showed similar observations confirming the results herein obtained [28,31,57]. Moreover, a potential advantage is suggested in the use of  $\text{Cs}_3\text{Bi}_2\text{I}_9$  due to its ability to absorb light in the visible region. For example,  $\text{TiO}_2$ , which is the most common photocatalyst, absorbs only in the UV region ( $\lambda < 400 \text{ nm}$ ) [64].



**Figure 6.** UV-Vis spectrum of  $\text{Cs}_3\text{Bi}_2\text{I}_9$  (a) and the Kubelka–Munk function for the determination of the bandgap energy of  $\text{Cs}_3\text{Bi}_2\text{I}_9$  (b).

### 3.3. TAS

In order to get information about the processes occurring upon illumination, TAS measurements were performed in the microsecond time scale, which allows us to study the reaction dynamics of the photogenerated charges carriers. Because  $\text{Cs}_3\text{Bi}_2\text{I}_9$  was found to have a bandgap of 1.95 eV, the excitation was therefore performed with a 532 nm laser pulse. The measurements were performed in  $\text{N}_2$  atmosphere and in a mixture of  $\text{N}_2$  and methanol. In  $\text{N}_2$  atmosphere, the lifetime of the photogenerated carriers is maximized by preventing the reaction with donor or acceptor molecules, which are present in the air or adsorbed to the surface of the powder. When no electron donor or acceptor is present in the medium, the observed decay of the transient signals can be related to the internal recombination of charge carriers [65]. The addition of methanol, as a hole scavenger, makes it possible to identify at which wavelengths the trapped species (electrons and holes) absorb. The spectra in both atmospheres are shown in Figure 7a at 100 ns after the excitation. Both spectra have a similar shape and maximum, which can be observed at 620 nm in  $\text{N}_2$  atmosphere and in the presence of methanol at 640 nm. In general, the addition of methanol has a clearly visible effect on the  $\Delta J$  values, which are related to the number of photogenerated charge carriers, independent of the considered wavelength. In the range of 560 to 620 nm, the  $\Delta J$  values decrease after the addition of methanol, and thus, at these wavelengths, holes can be detected. Contrarily, between 640 and 740 nm, all  $\Delta J$  values increase in the presence of methanol, which is an indication for the presence of electrons at this wavelength range. The increase and the decrease of the  $\Delta J$  values for decay at a specific wavelength are not only detectable at a certain time point, but also present in the whole considered time scale, as can be seen for the decay at 640 nm (Figure 7b) and at 620 nm (Figure 7c), for example. It was reported for photocatalytic active materials such as  $\text{TiO}_2$  that 10 ns after the excitation, 90% of the electron–hole pairs were recombined and that the trapping of the charge carriers happened in the ps or fs time scale [66,67]. Because trapped charge carriers usually initiate photocatalytic redox reactions, the detection of trapped electrons and holes clearly supports the ability of  $\text{Cs}_3\text{Bi}_2\text{I}_9$  as a suitable material for photocatalytic reactions.

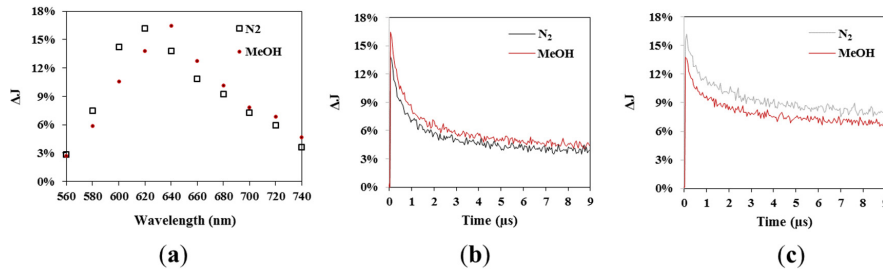


**Figure 7.** Transient absorption spectra in  $N_2$  and in methanol atmosphere at  $0.1 \mu s$  after the excitation (a). Transient absorption signal measured in  $N_2$  and MeOH atmosphere at  $640 \text{ nm}$  (b) and at  $620 \text{ nm}$  (c).

### 3.4. Photocatalytic Activity

To confirm the visible-light photocatalytic activity, which was proposed by the TAS measurements, the degradation of RhB as a model organic pollutant was studied. Figure 8a shows the change of the concentration of RhB as a function of the irradiation time for the blank experiment, the photocatalyst without light (dark), and the photocatalyst with visible light illumination (light). Without the presence of  $Cs_3Bi_2I_9$ , only a negligible degradation of the dye can be observed in the considered time domain of 3 h. This is supported by the reported stability of RhB in aqueous solution under visible-light irradiation [68]. In the presence of the perovskite, but in the absence of light, only the adsorption of the dye molecules to the photocatalyst will take place. Within three hours, approximately 34% of the dye in the aqueous solution was adsorbed to the surface. The low amount of adsorbed dye molecules might be explained by the low surface area of the material. In contrast, in the presence of the perovskite and during visible-light illumination, a nearly complete degradation (93%) of the dye can be observed (Figure 8b).

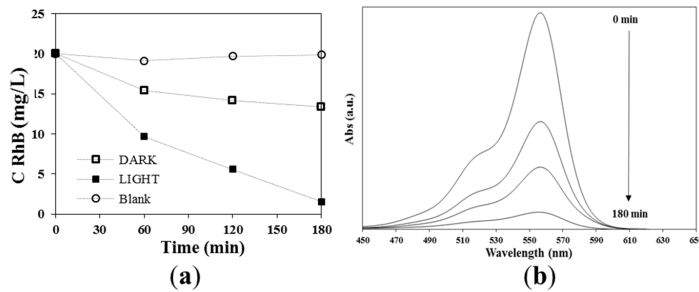


**Figure 8.** (a) Change in the concentration of Rhodamine B (RhB) at different conditions; (b) change in the absorption spectra of RhB during its photodegradation in the presence of  $Cs_3Bi_2I_9$  nanoparticles under visible-light irradiation.

For the application of a photocatalyst, recyclability is an important factor that needs to be considered as well. In Figure 9, the degradation of RhB is shown for three cycles, showing a degradation after 180 min of illumination of 93%, 92%, and 92% after the first, second, and third cycle, respectively. Just a small activity loss is present after three cycles with the perovskite material, which confirms the suitability of  $Cs_3Bi_2I_9$  for being used as a photocatalyst under visible-light illumination.

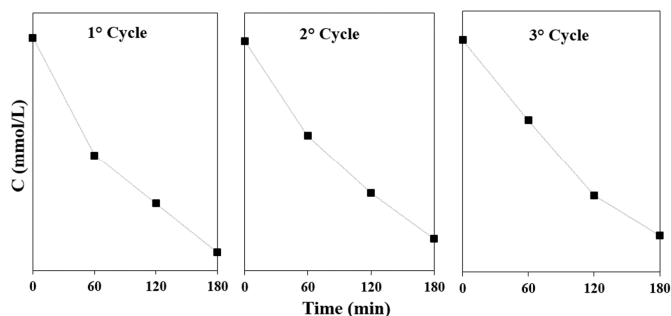


Figure 9. Recyclability test of the as-synthesized nanoparticles for RhB removal under visible-light irradiation.

#### 4. Conclusions

The present work describes the successful synthesis of  $\text{Cs}_3\text{Bi}_2\text{I}_9$  by a low-temperature and easily reproducible method, confirmed by an extensive morphological and optical characterization.

TAS measurements were applied in order to investigate the creation of photogenerated charge carriers, confirming that the material is not only absorbing visible light, but that the illumination also leads to the generation of electron–hole pairs, which can be trapped afterwards. The proposed activity was confirmed by an efficient degradation of RhB (93% after 180 min) during the illumination with visible light, confirming its potential as photocatalyst. After a recyclability test including three cycles, just a small activity loss was observed, which demonstrates the stability of the perovskite. All in all,  $\text{Cs}_3\text{Bi}_2\text{I}_9$  was shown to be a stable photocatalytic material under visible-light illumination, which is able to degrade RhB, making the perovskite an interesting material to investigate for the degradation of other compounds, as well. The aim of this study was to provide insights on a new photocatalyst by taking into account how environmentally friendly visible-light-responsive materials can offer the opportunity to revolutionize photocatalytic processes due to the major utilization of the potential solar spectrum.

**Supplementary Materials:** The following are available online at <http://www.mdpi.com/2079-4991/10/4/763/s1>, Figure S1: Irradiance spectrum of a Halogen lamp (3200 K) compared to the solar irradiance on a surface per unit wavelength with emphasis on visible light range, Figure S2: XRD patterns of  $\text{CsI}$  and  $\text{BiI}_3$ .

**Author Contributions:** B.-M.B. as author of research and editor of manuscript, C.G. as editor of the manuscript and performer of TAS analysis, D.W.B. as supervisor and M.S. funding provider. All authors have read and agree to the published version of the manuscript.

**Funding:** This research was funded by Maa-ja vesiteknikaan tuki Foundation.

**Acknowledgments:** We further thank the Laboratory of Nano and Quantum Engineering (LNQE), in particular Luis Granone for performing the XRD analysis.

**Conflicts of Interest:** The authors declare no conflict of interest

#### References

- Hoffmann, M.R.; Martin, S.T.; Choi, W.; Bahnemann, D.W. Environmental Applications of Semiconductor Photocatalysis. *Chem. Rev.* **1995**, *95*, 69–96. [[CrossRef](#)]
- Alam, U.; Khan, A.; Raza, W.; Khan, A.; Bahnemann, D.W.; Muneer, M. Highly efficient Y and V co-doped ZnO photocatalyst with enhanced dye sensitized visible light photocatalytic activity. *Catal. Today* **2017**, *284*, 169–178. [[CrossRef](#)]
- Saravanan, R.; Khan, M.M.; Gupta, V.K.; Mosquera, E.; Gracia, F.; Narayanan, V.; Stephen, A. ZnO/Ag/CdO nanocomposite for visible light-induced photocatalytic degradation of industrial textile effluents. *J. Colloid Interface Sci.* **2015**, *452*, 126–133. [[CrossRef](#)] [[PubMed](#)]



4. Zhang, S.; Gu, P.; Ma, R.; Luo, C.; Asiri, A.M.; Zhao, G.; Cheng, W.; Wang, X. Recent developments in fabrication and structure regulation of visible-light-driven g-C<sub>3</sub>N<sub>4</sub>-based photocatalysts towards water purification: A critical review. *Catal. Today* **2019**, *335*, 65–77. [[CrossRef](#)]
5. Herrmann, J.-M.; Guillard, C.; Pichat, P. Heterogeneous photocatalysis: An emerging technology for water treatment. *Catal. Today* **1993**, *17*, 7–20. [[CrossRef](#)]
6. Kabir, E.; Kumar, P.; Kumar, S.; Adelodun, A.A.; Kim, K.-H. Solar energy: Potential and future prospects. *Renew. Sustain. Energy Rev.* **2018**, *82*, 894–900. [[CrossRef](#)]
7. Spasiano, D.; Marotta, R.; Malato, S.; Fernández-Ibáñez, P.; Di Somma, I. Solar photocatalysis: Materials, reactors, some commercial, and pre-industrialized applications. A comprehensive approach. *Appl. Catal. B Environ.* **2015**, *170*, 90–123. [[CrossRef](#)]
8. Gao, H.; Zhao, S.; Cheng, X.; Wang, X.; Zheng, L. Removal of anionic azo dyes from aqueous solution using magnetic polymer multi-wall carbon nanotube nanocomposite as adsorbent. *Chem. Eng. J.* **2013**, *223*, 84–90. [[CrossRef](#)]
9. Zhou, C.; Lai, C.; Zhang, C.; Zeng, G.; Huang, D.; Cheng, M.; Hu, L.; Xiong, W.; Chen, M.; Wang, J.; et al. Semiconductor/boron nitride composites: Synthesis, properties, and photocatalysis applications. *Appl. Catal. B Environ.* **2018**, *238*, 6–18. [[CrossRef](#)]
10. Mamba, G.; Mishra, A.K. Graphitic carbon nitride (g-C<sub>3</sub>N<sub>4</sub>) nanocomposites: A new and exciting generation of visible light driven photocatalysts for environmental pollution remediation. *Appl. Catal. B Environ.* **2016**, *198*, 347–377. [[CrossRef](#)]
11. Vaiano, V.; Sacco, O.; Matarangolo, M. Photocatalytic degradation of paracetamol under UV irradiation using TiO<sub>2</sub>-graphite composites. *Catal. Today* **2018**, *315*, 230–236. [[CrossRef](#)]
12. Zhang, G.; Zhang, Y.C.; Nadagouda, M.; Han, C.; O’Shea, K.; El-Sheikh, S.M.; Ismail, A.A.; Dionysiou, D.D. Visible light-sensitized S, N and C co-doped polymorphic TiO<sub>2</sub> for photocatalytic destruction of microcystin-LR. *Appl. Catal. B Environ.* **2014**, *144*, 614–621. [[CrossRef](#)]
13. Wei, N.; Cui, H.; Song, Q.; Zhang, L.; Song, X.; Wang, K.; Zhang, Y.; Li, J.; Wen, J.; Tian, J. Ag<sub>2</sub>O nanoparticle/TiO<sub>2</sub> nanobelt heterostructures with remarkable photo-response and photocatalytic properties under UV, visible and near-infrared irradiation. *Appl. Catal. B Environ.* **2016**, *198*, 83–90. [[CrossRef](#)]
14. Zhu, X.; Wang, P.; Huang, B.; Ma, X.; Qin, X.; Zhang, X.; Dai, Y. Synthesis of novel visible light response Ag<sub>10</sub>Si<sub>4</sub>O<sub>13</sub> photocatalyst. *Appl. Catal. B Environ.* **2016**, *199*, 315–322. [[CrossRef](#)]
15. Kato, H.; Kudo, A. Visible-Light-Response and Photocatalytic Activities of TiO<sub>2</sub> and SrTiO<sub>3</sub> Photocatalysts Codoped with Antimony and Chromium. *J. Phys. Chem. B* **2002**, *106*, 5029–5034. [[CrossRef](#)]
16. Li, H.; Su, Z.; Hu, S.; Yan, Y. Free-standing and flexible Cu/Cu<sub>2</sub>O/CuO heterojunction net: A novel material as cost-effective and easily recycled visible-light photocatalyst. *Appl. Catal. B Environ.* **2017**, *207*, 134–142. [[CrossRef](#)]
17. Grätzel, M.; Park, N.-G. Organometal halide perovskite photovoltaics: A diamond in the rough. *Nano* **2014**, *9*, 1440002. [[CrossRef](#)]
18. Snaith, H.J. Perovskites: The Emergence of a New Era for Low-Cost, High-Efficiency Solar Cells. *J. Phys. Chem. Lett.* **2013**, *4*, 3623–3630. [[CrossRef](#)]
19. Burschka, J.; Pellet, N.; Moon, S.-J.; Humphry-Baker, R.; Gao, P.; Nazeeruddin, M.K.; Grätzel, M. Sequential deposition as a route to high-performance perovskite-sensitized solar cells. *Nature* **2013**, *499*, 316–319. [[CrossRef](#)]
20. Mesquita, I.; Andrade, L.; Mendes, A. Perovskite solar cells: Materials, configurations and stability. *Renew. Sustain. Energy Rev.* **2018**, *82*, 2471–2489. [[CrossRef](#)]
21. Noel, N.K.; Stranks, S.D.; Abate, A.; Wehrenfennig, C.; Guarnera, S.; Haghighirad, A.-A.; Sadhanala, A.; Eperon, G.E.; Pathak, S.K.; Johnston, M.B.; et al. Lead-free organic–inorganic tin halide perovskites for photovoltaic applications. *Energy Environ. Sci.* **2014**, *7*, 3061–3068. [[CrossRef](#)]
22. Qin, K.; Dong, B.; Wang, S. Improving the stability of metal halide perovskite solar cells from material to structure. *J. Energy Chem.* **2019**, *33*, 90–99. [[CrossRef](#)]
23. Kojima, A.; Teshima, K.; Shirai, Y.; Miyasaka, T. Organometal Halide Perovskites as Visible-Light Sensitizers for Photovoltaic Cells. *J. Am. Chem. Soc.* **2009**, *131*, 6050–6051. [[CrossRef](#)] [[PubMed](#)]
24. Kulbak, M.; Gupta, S.; Kedem, N.; Levine, I.; Bendikov, T.; Hodes, G.; Cahen, D. Cesium Enhances Long-Term Stability of Lead Bromide Perovskite-Based Solar Cells. *J. Phys. Chem. Lett.* **2015**, *7*, 167–172. [[CrossRef](#)] [[PubMed](#)]

25. Liang, J.; Zhu, G.; Wang, C.; Zhao, P.; Wang, Y.; Hu, Y.; Ma, L.; Tie, Z.; Liu, J.; Jin, Z. An all-inorganic perovskite solar capacitor for efficient and stable spontaneous photocharging. *Nano Energy* **2018**, *52*, 239–245. [[CrossRef](#)]
26. Ren, J.; Li, T.; Zhou, X.; Dong, X.; Shorokhov, A.; Semenov, M.B.; Krevchik, V.D.; Wang, Y. Encapsulating all-inorganic perovskite quantum dots into mesoporous metal organic frameworks with significantly enhanced stability for optoelectronic applications. *Chem. Eng. J.* **2019**, *358*, 30–39. [[CrossRef](#)]
27. Saparov, B.; Hong, F.; Sun, J.-P.; Duan, H.-S.; Meng, W.; Cameron, S.; Hill, I.; Yan, Y.; Mitzi, D.B. Thin-Film Preparation and Characterization of Cs<sub>3</sub>Sb<sub>2</sub>I<sub>9</sub>: A Lead-Free Layered Perovskite Semiconductor. *Chem. Mater.* **2015**, *27*, 5622–5632. [[CrossRef](#)]
28. Lehner, A.J.; Fabini, D.; Evans, H.A.; Hébert, C.-A.; Smock, S.R.; Hu, J.; Wang, H.; Zwanziger, J.W.; Chabiniyc, M.L.; Seshadri, R. Crystal and Electronic Structures of Complex Bismuth Iodides A<sub>3</sub>Bi<sub>2</sub>I<sub>9</sub> (A = K, Rb, Cs) Related to Perovskite: Aiding the Rational Design of Photovoltaics. *Chem. Mater.* **2015**, *27*, 7137–7148. [[CrossRef](#)]
29. Ma, Z.; Peng, S.; Wu, Y.; Fang, X.; Chen, X.; Jia, X.; Zhang, K.; Yuan, N.-Y.; Ding, J.; Dai, N. Air-stable layered bismuth-based perovskite-like materials: Structures and semiconductor properties. *Phys. B Condens. Matter* **2017**, *526*, 136–142. [[CrossRef](#)]
30. Vesborg, P.C.K.; Jaramillo, T.F. Addressing the terawatt challenge: Scalability in the supply of chemical elements for renewable energy. *RSC Adv.* **2012**, *2*, 7933–7947. [[CrossRef](#)]
31. Park, B.-W.; Philippe, B.; Zhang, X.; Rensmo, H.; Boschloo, G.; Johansson, E.M.J. Bismuth Based Hybrid Perovskites A<sub>3</sub>Bi<sub>2</sub>I<sub>9</sub>(A: Methylammonium or Cesium) for Solar Cell Application. *Adv. Mater.* **2015**, *27*, 6806–6813. [[CrossRef](#)] [[PubMed](#)]
32. Ghosh, B.; Wu, B.; Mulmudi, H.K.; Guet, C.; Weber, K.; Sum, T.C.; Mhaisalkar, S.G.; Mathews, N. Limitations of Cs<sub>3</sub>Bi<sub>2</sub>I<sub>9</sub> as Lead-Free Photovoltaic Absorber Materials. *ACS Appl. Mater. Interfaces* **2018**, *10*, 35000–35007. [[CrossRef](#)] [[PubMed](#)]
33. Nila, A.; Baibarac, M.; Matea, A.; Mitran, R.-A.; Baltog, I. Exciton-phonon interactions in the Cs<sub>3</sub>Bi<sub>2</sub>I<sub>9</sub> crystal structure revealed by Raman spectroscopic studies. *Phys. Status Solidi* **2016**, *254*, 1552805. [[CrossRef](#)]
34. Hong, K.-H.; Kim, J.; Debbichi, L.; Kim, H.; Im, S.H. Band Gap Engineering of Cs<sub>3</sub>Bi<sub>2</sub>I<sub>9</sub> Perovskites with Trivalent Atoms Using a Dual Metal Cation. *J. Phys. Chem. C* **2016**, *121*, 969–974. [[CrossRef](#)]
35. Hu, Y.; Zhang, S.; Miao, X.; Su, L.; Bai, F.; Qiu, T.; Liu, J.; Yuan, G. Ultrathin Cs<sub>3</sub>Bi<sub>2</sub>I<sub>9</sub> Nanosheets as an Electronic Memory Material for Flexible Memristors. *Adv. Mater. Interfaces* **2017**, *4*, 1700131. [[CrossRef](#)]
36. Chai, W.-X.; Wu, L.-M.; Li, J.-Q.; Chen, L. Silver Iodobismuthates: Syntheses, Structures, Properties, and Theoretical Studies of [Bi<sub>2</sub>Ag<sub>2</sub>I<sub>10</sub>]<sup>2-</sup> and [Bi<sub>4</sub>Ag<sub>2</sub>I<sub>16</sub>]<sup>4-</sup>. *Inorg. Chem.* **2007**, *46*, 1042–1044. [[CrossRef](#)] [[PubMed](#)]
37. Pal, J.; Bhunia, A.; Chakraborty, S.; Manna, S.; Das, S.; Dewan, A.; Datta, S.; Nag, A. Synthesis and Optical Properties of Colloidal M<sub>3</sub>Bi<sub>2</sub>I<sub>9</sub> (M = Cs, Rb) Perovskite Nanocrystals. *J. Phys. Chem. C* **2018**, *122*, 10643–10649. [[CrossRef](#)]
38. Hoye, R.L.Z.; Brandt, R.E.; Oshero, A.; Stevanović, V.; Stranks, S.D.; Kim, H.; Akey, A.J.; Perkins, J.D.; Kurchin, R.C.; Poindexter, J.R.; et al. Methylammonium Bismuth Iodide as a Lead-Free, Stable Hybrid Organic-Inorganic Solar Absorber. *Chem. A Eur. J.* **2016**, *22*, 2605–2610. [[CrossRef](#)]
39. Cuhadar, C.; Kim, S.-G.; Yang, J.-M.; Seo, J.-Y.; Lee, D.; Park, N.-G. All-Inorganic Bismuth Halide Perovskite-Like Materials A<sub>3</sub>Bi<sub>2</sub>I<sub>9</sub> and A<sub>3</sub>Bi<sub>1.8</sub>Na<sub>0.2</sub>I<sub>8.6</sub> (A = Rb and Cs) for Low-Voltage Switching Resistive Memory. *ACS Appl. Mater. Interfaces* **2018**, *10*, 29741–29749. [[CrossRef](#)]
40. Slavney, A.H.; Hu, T.; Lindenberg, A.M.; Karunadasa, H.I. A Bismuth-Halide Double Perovskite with Long Carrier Recombination Lifetime for Photovoltaic Applications. *J. Am. Chem. Soc.* **2016**, *138*, 2138–2141. [[CrossRef](#)]
41. Bai, F.; Hu, Y.; Hu, Y.; Qiu, T.; Miao, X.; Zhang, S. Lead-free, air-stable ultrathin Cs<sub>3</sub>Bi<sub>2</sub>I<sub>9</sub> perovskite nanosheets for solar cells. *Sol. Energy Mater. Sol. Cells* **2018**, *184*, 15–21. [[CrossRef](#)]
42. Mel'nikova, S.V.; Zaitsev, A.I. Ferroelectric phase transition in Cs<sub>3</sub>Bi<sub>2</sub>I<sub>9</sub>. *Phys. Solid State* **1997**, *39*, 1652–1654. [[CrossRef](#)]
43. Nidheesh, P.; Zhou, M.; Oturan, M.A. An overview on the removal of synthetic dyes from water by electrochemical advanced oxidation processes. *Chemosphere* **2018**, *197*, 210–227. [[CrossRef](#)] [[PubMed](#)]
44. Namasivayam, C.; Kavitha, D. Removal of Congo Red from water by adsorption onto activated carbon prepared from coir pith, an agricultural solid waste. *Dyes Pigments* **2002**, *54*, 47–58. [[CrossRef](#)]

45. Yang, X.; Al-Duri, B. Kinetic modeling of liquid-phase adsorption of reactive dyes on activated carbon. *J. Colloid Interface Sci.* **2005**, *287*, 25–34. [[CrossRef](#)]
46. Rocher, V.; Siaugue, J.-M.; Cabuil, V.; Bée, A. Removal of organic dyes by magnetic alginate beads. *Water Res.* **2008**, *42*, 1290–1298. [[CrossRef](#)]
47. Helal, A.; Harraz, F.A.; Ismail, A.A.; Sami, T.M.; Ibrahim, I. Hydrothermal synthesis of novel heterostructured Fe<sub>2</sub>O<sub>3</sub>/Bi<sub>2</sub>S<sub>3</sub> nanorods with enhanced photocatalytic activity under visible light. *Appl. Catal. B Environ.* **2017**, *213*, 18–27. [[CrossRef](#)]
48. Rani, S.; Aggarwal, M.; Kumar, M.; Sharma, S.; Kumar, D. Removal of methylene blue and rhodamine B from water by zirconium oxide/graphene. *Water Sci. Technol.* **2016**, *30*, 51–60. [[CrossRef](#)]
49. Rochkind, M.; Pasternak, S.; Paz, Y. Using Dyes for Evaluating Photocatalytic Properties: A Critical Review. *Molecules* **2014**, *20*, 88–110. [[CrossRef](#)]
50. Nyanhongo, G.S.; Gomes, J.; Gübitz, G.M.; Zvauya, R.; Read, J.; Steiner, W. Decolorization of textile dyes by laccases from a newly isolated strain of *Trametes modesta*. *Water Res.* **2002**, *36*, 1449–1456. [[CrossRef](#)]
51. Huang, J.-H.; Huang, K.-L.; Liu, S.; Wang, A.-T.; Yan, C. Adsorption of Rhodamine B and methyl orange on a hypercrosslinked polymeric adsorbent in aqueous solution. *Colloids Surf. A Physicochem. Eng. Asp.* **2008**, *330*, 55–61. [[CrossRef](#)]
52. Zhang, S.; Li, J.; Zeng, M.; Zhao, G.; Xu, J.; Hu, W.; Wang, X. In Situ Synthesis of Water-Soluble Magnetic Graphitic Carbon Nitride Photocatalyst and Its Synergistic Catalytic Performance. *ACS Appl. Mater. Interfaces* **2013**, *5*, 12735–12743. [[CrossRef](#)] [[PubMed](#)]
53. Ito, S.; Chen, P.; Comte, P.; Nazeeruddin, M.K.; Liska, P.; Péchy, P.; Grätzel, M. Fabrication of screen-printing pastes from TiO<sub>2</sub> powders for dye-sensitised solar cells. *Prog. Photovolt. Res. Appl.* **2007**, *15*, 603–612. [[CrossRef](#)]
54. Bresolin, B.-M.; Balayeva, N.O.; Granone, L.I.; Dillert, R.; Bahnemann, D.W.; Sillanpää, M. Anchoring lead-free halide Cs<sub>3</sub>Bi<sub>2</sub>I<sub>9</sub> perovskite on UV100–TiO<sub>2</sub> for enhanced photocatalytic performance. *Sol. Energy Mater. Sol. Cells* **2020**, *204*, 110214. [[CrossRef](#)]
55. Sun, C.; Guo, Y.; Fang, B.; Guan, L.; Duan, H.; Chen, Y.; Li, H.; Liu, H. Facile preparation of high-quality perovskites for efficient solar cells via a fast conversion of wet PbI<sub>2</sub> precursor films. *RSC Adv.* **2017**, *7*, 22492–22500. [[CrossRef](#)]
56. Sherkar, T.S.; Momblona, C.; Gil-Escrig, L.; Ávila, J.; Sessolo, M.; Bolink, H.J.; Koster, L.J.A. Recombination in Perovskite Solar Cells: Significance of Grain Boundaries, Interface Traps, and Defect Ions. *ACS Energy Lett.* **2017**, *2*, 1214–1222. [[CrossRef](#)]
57. Liang, P.-W.; Liao, C.-Y.; Chueh, C.-C.; Zuo, F.; Williams, S.T.; Xin, X.-K.; Lin, J.-J.; Jen, A. Additive Enhanced Crystallization of Solution-Processed Perovskite for Highly Efficient Planar-Heterojunction Solar Cells. *Adv. Mater.* **2014**, *26*, 3748–3754. [[CrossRef](#)]
58. Phuyal, D.; Jain, S.M.; Philippe, B.; Johansson, M.B.; Pazoki, M.; Kullgren, J.; Kvashnina, K.O.; Klintonberg, M.; Johansson, E.M.J.; Karis, O.; et al. The electronic structure and band interface of cesium bismuth iodide on a titania heterostructure using hard X-ray spectroscopy. *J. Mater. Chem. A* **2018**, *6*, 9498–9505. [[CrossRef](#)]
59. Fabian, D.M.; Ardo, S. Hybrid organic–inorganic solar cells based on bismuth iodide and 1,6-hexanediammonium dication. *J. Mater. Chem. A* **2016**, *4*, 6837–6841. [[CrossRef](#)]
60. Rocks, C.; Svrcek, V.; Maguire, P.; Mariotti, D. Understanding surface chemistry during MAPbI<sub>3</sub> spray deposition and its effect on photovoltaic performance. *J. Mater. Chem. C* **2017**, *5*, 902–916. [[CrossRef](#)]
61. Deepa, M.; Salado, M.; Calió, L.; Kazim, S.; Shivaprasad, S.M.; Ahmad, S. Cesium power: Low Cs+ levels impart stability to perovskite solar cells. *Phys. Chem. Chem. Phys.* **2017**, *19*, 4069–4077. [[CrossRef](#)] [[PubMed](#)]
62. Nørby, P.; Jørgensen, M.R.V.; Johnsen, S.; Iversen, B.B. Bismuth Iodide Hybrid Organic-Inorganic Crystal Structures and Utilization in Formation of Textured BiI<sub>3</sub> Film. *Eur. J. Inorg. Chem.* **2016**, *2016*, 1389–1394. [[CrossRef](#)]
63. Zhang, Y.; Yin, J.; Parida, M.R.; Ahmed, G.; Pan, J.; Bakr, O.M.; Brédas, J.-L.; Mohammed, O.F. Direct-Indirect Nature of the Bandgap in Lead-Free Perovskite Nanocrystals. *J. Phys. Chem. Lett.* **2017**, *8*, 3173–3177. [[CrossRef](#)] [[PubMed](#)]
64. Huang, K.; Chen, L.; Liao, M.; Xiong, J. The Photocatalytic Inactivation Effect of Fe-Doped TiO<sub>2</sub> Nanocomposites on Leukemic HL60 Cells-Based Photodynamic Therapy. *Int. J. Photoenergy* **2012**, *2012*, 1–8. [[CrossRef](#)]

65. Bahnemann, D.W.; Hilgendorff, M.; Memming, R. Charge Carrier Dynamics at TiO<sub>2</sub> Particles: Reactivity of Free and Trapped Holes. *J. Phys. Chem. B* **1997**, *101*, 4265–4275. [[CrossRef](#)]
66. Serpone, N.; Lawless, D.; Khairutdinov, R.; Pelizzetti, E. Subnanosecond Relaxation Dynamics in TiO<sub>2</sub> Colloidal Sols (Particle Sizes  $R_p = 1.0$ –13.4 nm). Relevance to Heterogeneous Photocatalysis. *J. Phys. Chem.* **1995**, *45*, 16655–16661. [[CrossRef](#)]
67. Schneider, J.; Matsuoka, M.; Takeuchi, M.; Zhang, J.; Horiuchi, Y.; Anpo, M.; Bahnemann, D.W. Understanding TiO<sub>2</sub> Photocatalysis: Mechanisms and Materials. *Chem. Rev.* **2014**, *114*, 9919–9986. [[CrossRef](#)]
68. Liu, S.; Yin, K.; Ren, W.; Cheng, B.; Yu, J. Tandem photocatalytic oxidation of Rhodamine B over surface fluorinated bismuth vanadate crystals. *J. Mater. Chem.* **2012**, *22*, 17759. [[CrossRef](#)]



© 2020 by the authors. Licensee MDPI, Basel, Switzerland. This article is an open access article distributed under the terms and conditions of the Creative Commons Attribution (CC BY) license (<http://creativecommons.org/licenses/by/4.0/>).



## **Publication IV**

Bresolin, B.M., Balayeva, N.O., Granone, L.I., Dillert, R., Bahnemann, D.W., and Sillanpää, M.

**Anchoring lead-free halide Cs<sub>3</sub>Bi<sub>2</sub>I<sub>9</sub> perovskite on UV100–TiO<sub>2</sub> for enhanced photocatalytic performance**

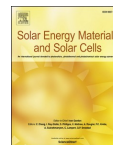
Reprinted with permission from  
*Solar Energy Materials & Solar Cells*  
Vol. 204 (110214), pp. 1-11, 2020  
© 2020, Elsevier





Contents lists available at ScienceDirect

## Solar Energy Materials and Solar Cells

journal homepage: <http://www.elsevier.com/locate/solmat>Anchoring lead-free halide Cs<sub>3</sub>Bi<sub>2</sub>I<sub>9</sub> perovskite on UV100–TiO<sub>2</sub> for enhanced photocatalytic performanceBianca-Maria Bresolin<sup>a,\*</sup>, Narmina O. Balayeva<sup>b</sup>, Luis I. Granone<sup>b,c</sup>, Ralf Dillert<sup>b,c</sup>, Detlef W. Bahnemann<sup>b,c,d</sup>, Mika Sillanpää<sup>a,e</sup><sup>a</sup> Laboratory of Green Chemistry, School of Engineering Science, Lappeenranta University of Technology, Sammonkatu 12, 50130, Mikkeli, Finland<sup>b</sup> Institut für Technische Chemie, Leibniz Universität Hannover, Callinstr. 3, D-30167, Hannover, Germany<sup>c</sup> Laboratory of Nano- and Quantum-Engineering (LNQE), Gottfried Wilhelm Leibniz University Hannover, Schneiderberg 39, D-30167, Hannover, Germany<sup>d</sup> Laboratory "Photoactive Nanocomposite Materials", Saint-Petersburg State University, Ulyanovskaya Str. 1, Peterhof, 198504, Saint-Petersburg, Russia<sup>e</sup> Department of Civil and Environmental Engineering, Florida International University, Miami, FL, 33174, USA

## ARTICLE INFO

## Keywords:

Photocatalysis  
Heterostructure  
Perovskite  
Titanium dioxide  
Visible light

## ABSTRACT

Halide perovskites have shown great potential in photocatalytic applications. In order to enhance the charge transportation efficiency, the chemical stability, and the light absorption ability, we anchored a lead-free halide perovskite (Cs<sub>3</sub>Bi<sub>2</sub>I<sub>9</sub>) on UV100–TiO<sub>2</sub> nanoparticles to build a visible-light active photocatalysts. The as-prepared material exhibited excellent stability and a remarkable yield for photocatalytic oxidation of methanol to formaldehyde under visible light irradiation. The photocatalyst was characterized using X-ray diffraction, scanning electron microscopy, energy-dispersive X-ray spectroscopy, Transmission electron microscopy, X-ray photoelectron spectroscopy, ultraviolet–visible diffuse reflectance spectroscopy, Brunauer–Emmett–Teller surface area measurement, and photoelectrochemical properties. The analyses confirmed a remarkable improvement of visible-light absorption, a favorable decrease in the recombination of photoinduced charge carriers, and a suitable bandgap for visible-light photocatalytic applications. Recycle experiments showed that the composites still presented significant photocatalytic activity after three successive cycles. A possible underlying mechanism of the composite accounting for the enhanced photocatalytic activity under visible light irradiation was proposed.

Our study aims to open new possibilities of using lead-free halide perovskites for photocatalytic applications.

## 1. Introduction

Environmental pollution and energy demand are without any doubts among the biggest challenges of the new century [1,2]. In recent years, it has been reported a steady increase of water pollution in many parts of the world caused by the accelerated release of pollutants due to the combination of a growing population and a rapid industrial development [3–6]. Moreover, efficient and sustainable technologies for remediation of wastewater remain a current issue and great challenge for scientists [7]. On the other hand, it is equally urgent to find a renewable energy resource to answer the increasing energy demand and mitigate the negative effect of global warming [8–11]. Therefore, the development of highly efficient and eco-friendly methods for wastewater treatment based on renewable energy sources has become an imperative task.

Among different technologies, photocatalysis appears to be a promising way to solve simultaneous environmental and energy issues [12–15]. The initiating event in photocatalysis is the absorption of the radiation emitted by the sun and the formation of electron-hole pairs in the empty conduction band (CB) and the filled valence band (VB), respectively. To the extent that not all the electrons and holes after recombine, some of them may attenuate to the surface reacting with bounded groups, water or adsorbed molecules. Generally, highly reactive oxygen species (ROS) are formed by interfacial transfer of electrons and holes to oxygen molecules dissolved in water and water adsorbed on the catalyst surface [16,17]. The strong oxidizing power of ROS induces the degradation and mineralization of many organic and inorganic wastewater pollutants [18,19]. As a sustainable technology, a photocatalytic process can operate at room temperature utilizing clean and renewable solar light as driving force for the abatement of contaminants

\* Corresponding author.

E-mail addresses: [biancabresolin@yahoo.it](mailto:biancabresolin@yahoo.it), [bianca-maria.bresolin@lut.fi](mailto:bianca-maria.bresolin@lut.fi), [Bianca.Maria.Bresolin@lut.fi](mailto:Bianca.Maria.Bresolin@lut.fi) (B.-M. Bresolin).<https://doi.org/10.1016/j.solmat.2019.110214>

Received 15 July 2019; Received in revised form 1 October 2019; Accepted 7 October 2019

Available online 24 October 2019

0927-0248/© 2019 Elsevier B.V. All rights reserved.



with any production of hazardous residues after complete mineralization [20]. Among the studied photocatalysts,  $\text{TiO}_2$  is definitively the most investigated material due to its high oxidative efficiency, chemical stability, nontoxicity, and low-cost [21–23]. Unfortunately, the photocatalytic efficiency of  $\text{TiO}_2$  is still low, mainly due to the slow reactions and the low solar energy absorption capacity [24,25]. Charge generation and separation process are one of the factors that affect reaction rate employing  $\text{TiO}_2$  as a photocatalyst because the recombination process is usually found to be much faster than the interfacial charge carrier transfer [26,27]. Moreover,  $\text{TiO}_2$  exhibits a wide bandgap and thus it can only be excited by photons with wavelengths in the UV range, which accounts for around 5% of the solar radiation energy [28]. Therefore, enhancing the efficiency of the photocatalytic process and extending the light absorption range of  $\text{TiO}_2$  represent a current challenge for researchers.

In our research, we studied the formation of semiconductor heterostructures with improved electron dynamics and enhanced light absorption ability. In recent years, significant advances have been made to design various kinds of semiconductor-based heterostructures for many potential applications such as biomedicine, nanodevices, and photocatalysis [29,30]. In the past decades, semiconductor heterostructures have been extensively studied for their ability to enhance the photo-induced charge separation efficiency [31,32]. In general, a type-II heterojunction is formed when both the VB and the CB energetic positions are more positive or more negative in one of the semiconductors. In this case, the band bending may induce the photogenerated charges carriers to migrate from one semiconductor to the other resulting in a spatial separation of the electrons and holes on different sides of the heterojunction. This mechanism highly reduces the recombination rate of the charge carriers enhancing the charge separation efficiency, increasing the carrier lifetime, and consequentially improving the photocatalytic efficiency [33–36]. Moreover, by coupling a UV-active semiconductor, such as  $\text{TiO}_2$ , with a visible light-active semiconductor, the synergic absorption ability of the two semiconductors extends the light response range improving the solar energy utilization [37].

Furthermore, among important technological developments of the current decade, perovskite material has achieved outstanding performances showing high power conversion efficiency, especially in photovoltaic applications [38–41]. In particular, organic-inorganic hybrid halide perovskites (HOIP) have become promising candidates due to their remarkable properties [42,43]. Unfortunately, the ambient instability and the easy decomposition of the labile organic components should be overcome in order to develop HOIP materials for environmental remediation. Moreover, the most efficient HOIPs usually contain lead, being a serious toxic disadvantage that limits commercial applications. On the other hand, among the inorganic perovskites, Bi-based halide perovskites have gained much attention solving the stability and toxicity issues related to lead-based perovskite materials [41,44,45]. In particular, cesium bismuth iodide ( $\text{Cs}_3\text{Bi}_2\text{I}_9$ ) is new low toxicity and air-stable compound belonging to the perovskite family that exhibits remarkable and promising qualities.  $\text{Cs}_3\text{Bi}_2\text{I}_9$  is characterized by a dark cherry red color, and it can be easily synthesized at low temperature. Although the phase transitions of these compounds have been well studied [46–48], the optoelectronic properties of the ternary inorganic bismuth halides have not been explored extensively [41].  $\text{Cs}_3\text{Bi}_2\text{I}_9$  has been reported to have bandgap energy of about 2 eV. Due to its narrow bandgap, it has a wide range of optical absorption, and it can be assumed to be suitable for applications in photocatalysis [49–51].

In our research,  $\text{Cs}_3\text{Bi}_2\text{I}_9$  perovskite and anatase  $\text{TiO}_2$  as new heterostructure material was coupled to improve the performance in photocatalytic applications. In particular, joining a wider bandgap semiconductor having a more positive conduction band edge potential (vs. RHE) to form a heterojunction structure may be a way to allow the inhibition of recombination of electron-hole pairs. On the other hand, the presence of  $\text{Cs}_3\text{Bi}_2\text{I}_9$  inorganic perovskite was addressed to improve

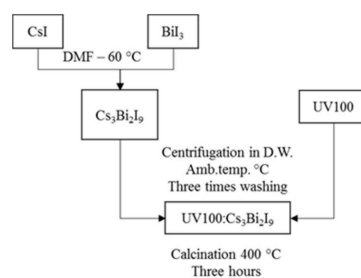


Fig. 1. Schematic illustration of the preparation pathway of the  $\text{Cs}_3\text{Bi}_2\text{I}_9/\text{TiO}_2$  composites.

Table 1  
List of synthesized materials.

Name of material	$\text{Cs}_3\text{Bi}_2\text{I}_9$ wt%
$\text{Cs}_3\text{Bi}_2\text{I}_9$	–
UV100-0.5	0.50
UV100-0.25	0.25
UV100-0.1	0.10
UV100-0.05	0.05
UV100	–

the light absorption capacity of  $\text{TiO}_2$  and further enhance its photocatalytic activity. To our knowledge, this is the first report that employed UV100: $\text{Cs}_3\text{Bi}_2\text{I}_9$  composites for photocatalytic water treatment.

## 2. Materials and methods

### 2.1. Materials

$\text{TiO}_2$  Hombikat UV100 powder (250  $\text{m}^2\text{g}^{-1}$  specific surface area, particle size  $\sim 10$  nm [52]) was kindly provided by Sachtleben Chemie GmbH (now Venator Germany GmbH, Germany). Cesium iodide CsI (99.9%, trace metals basis), bismuth iodide  $\text{BiI}_3$  (99%), diethyl ether (99.8%), and dimethylformamide (DMF, anhydrous, 99.8%) were purchased from Sigma-Aldrich and used without further purification.

### 2.2. Photocatalyst synthesis

Perovskite  $\text{Cs}_3\text{Bi}_2\text{I}_9$  was synthesized from CsI and  $\text{BiI}_3$  using DMF as a solvent. In a typical synthesis, CsI and  $\text{BiI}_3$  were mixed in DMF (20 mL) in a molar ratio of 3:2, at 60 °C under continuous stirring overnight. After the complete evaporation of DMF, the material was washed three times with diethyl ether to remove any DMF residue and dried [53]. The  $\text{Cs}_3\text{Bi}_2\text{I}_9/\text{TiO}_2$  composites were synthesized following a simple impregnation method.  $\text{TiO}_2$  and  $\text{Cs}_3\text{Bi}_2\text{I}_9$  were suspended in deionized water (Milli-Q, 18.2  $\text{M}\Omega\text{cm}$ ) and sonicated for 1 h. The suspension was centrifuged three times with deionized water and the obtained solid was subsequently calcined (400 °C) to form the  $\text{Cs}_3\text{Bi}_2\text{I}_9/\text{TiO}_2$  composites. The obtained materials were finally ground into fine powders. The schematic illustration of the multi-step preparation pathway is presented in Fig. 1. The four synthesized composites with different weight ratios were named as UV100-0.05, UV100-0.1, UV100-0.25, UV100-0.5, where the numbers demonstrate the weight percentage of  $\text{Cs}_3\text{Bi}_2\text{I}_9$  in respect to  $\text{TiO}_2$  (Table 1).

### 2.3. Photocatalyst characterization

The crystal phases and lattice parameters of the samples were

determined by powder X-ray diffraction using a D8 Advance diffractometer (Bruker) provided with a Cu K $\alpha$  radiation source. Diffuse reflectance UV–Vis spectroscopy was employed using a spectrophotometer (Varian Spectrophotometer Cary-100 Bio, Agilent technologies). Barium sulfate was used as a standard for 100% reflection. For the bare perovskite, the bandgap was deduced from Tauc plot [54]. Brunauer–Emmett–Teller (BET) measurements were performed to determine the specific surface area of the precursors and the synthesized powders. The analysis was performed by a single-point measurement of physisorption of molecular nitrogen at  $-196^\circ\text{C}$  using a Chemisorb 2300 apparatus (Micromeritics Instrument). Information on the elemental composition and the chemical state of the species composing the sample surfaces were recorded using X-ray photoelectron spectroscopy (XPS-Leybold Heraeus) with 300 W Al K $\alpha$  radiation. The morphology of the materials was further defined using scanning electron microscopy (SEM). Field emission scanning electron microscopy (FESEM) images were obtained in a Jeol JSM 6700 F microscopy at 2.0 kV acceleration voltage. The elemental composition was determined by energy dispersive spectroscopy (EDS). Electrochemical measurements were performed in a three-electrode electrochemical cell provided with a Pt counter electrode and Ag/AgCl (3 M saturated solution of NaCl) as a reference electrode. Thin films of the  $\text{Cs}_3\text{Bi}_2\text{I}_9/\text{TiO}_2$  composites were prepared on top of fluoride-doped tin oxide (FTO) coated glasses (Sigma Aldrich,  $\approx 8\ \Omega/\text{sq}$ ) by the doctor blade technique. A paste consisting of 200 mg of the composite, 50  $\mu\text{l}$  of Triton X-100 (Sigma-Aldrich, laboratory-grade), 100 mg of polyethylene glycol 10000 (Merck, for synthesis), 400  $\mu\text{l}$  of deionized water, and ethanol was used for the film preparation. A final calcination step at  $400^\circ\text{C}$  for 2 h was applied in order to remove the organic materials. The as-prepared films were used as working electrodes for impedance measurements at 10 Hz in 0.1 mol/L  $\text{KNO}_3$  using a ZENNIUM Electrochemical Workstation (Zahner-Elektrik GmbH & Co. KG). A solar simulator equipped with a xenon lamp (300 W, 678 W·m $^{-2}$ ) and an AM-1.5 G filter was employed for the photo-electrochemical measurements.

#### 2.4. Set-up for photocatalytic evaluation in aqueous phase

In this study, methanol ( $\text{CH}_3\text{OH}$ ) was used as a model of organic pollutant in order to quantify the photocatalytic potential of the  $\text{Cs}_3\text{Bi}_2\text{I}_9/\text{TiO}_2$  composite materials [55]. A closed quartz photoreactor was filled with 75 mL of a 100 mM methanol aqueous solution. Single wavelength LED irradiation was used with two different light sources M455L3 (blue LED 455 nm), and M365L2 (UV LED 365 nm) purchased from Thorlab and equipped with a collimating lens. The emission spectra of the light sources are shown in the Supporting Information (Fig. S1). The irradiation of the composite suspensions (1 g/L) started after 30 min in the dark to ensure that the adsorption-desorption equilibrium was established. Liquid samples were withdrawn at regular time intervals. The catalyst was removed from the liquid phase by filtration through an RC membrane with a 0.2- $\mu\text{m}$  pore size (Phenomenex). The amount of photogenerated formaldehyde was determined after the oxidation of methanol by taking 300  $\mu\text{l}$  after specific illumination intervals. After addition of 600  $\mu\text{l}$  of the Nash reagent (0.02 M acetylacetone, 0.05 M acetic acid, and 2 M ammonium acetate), the yellow-colored diacetylaldihydrolutidine (DDL) is formed and detected by fluorescence spectroscopy [55,56]. At an excitation wavelength of 405 nm, the characteristic emission of DDL appears at 510 nm. The fluorescence of DDL was measured in a well plate (Nunclon Delta Surface, Thermo Fisher Scientific Inc., USA) sample holder. The analysis was performed employing an F-7000 Fluorescence Spectrophotometer Hitachi equipped with a Xenon Lamp (FL parameter: 700 V PMT voltage, 5 nm excitation and emission slits, 2400 nm min $^{-1}$  scan speed, 315 nm excitation wavelength, luminosity spectrum of 410–650 nm emission wavelength recorded).

Moreover, the reaction rate of the different photocatalysts was determined by considering a first-order kinetic model according to the

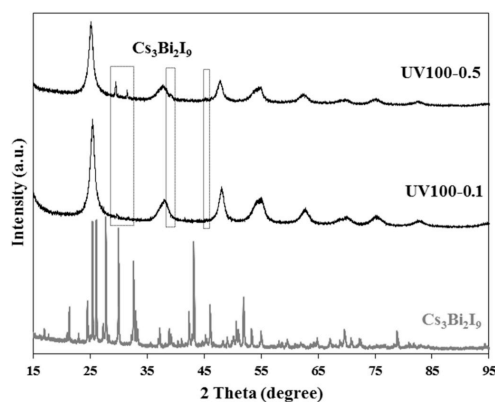


Fig. 2. XRD patterns for precursors and synthesized materials.

following equation Eq. (1):

$$k = -\frac{d[A]}{[A]} \quad (1)$$

where  $[A]$  is the concentration of the model pollutant and  $k$  is the reaction rate.

The detection of hydroxyl radicals was performed by the use of terephthalic acid, which reacts with photogenerated hydroxyl radicals, yielding the fluorescent 2-hydroxyterephthalic acid (2-HTA) [57]. Aqueous terephthalic acid solution (0.5 mM) was mixed with 1 g/L of catalyst, and the pH was adjusted to basic using NaOH solution (2 mM). The solution was stirred for 30 min and then irradiated with a LED lamp. Sample from the solution were collected at different time intervals and filtrated to separate the catalyst. Finally, the fluorescence of the filtrate was measured by exciting at 315 nm.

### 3. Results and discussion

#### 3.1. Catalyst characterization

The XRD patterns of UV100 and the as-synthesized composites are shown in Fig. 2. The UV100 diffraction pattern was compared with the JCDs-ICSD standards, and it was indexed to the tetragonal  $\text{TiO}_2$  anatase phase (JCPDS Card no. 21–1272). The peaks observed at  $2\theta$  values of  $25.4^\circ$ ,  $38.5^\circ$ ,  $48.2^\circ$ ,  $54.4^\circ$ ,  $55.4^\circ$ , and  $62.7^\circ$  correspond to the (101), (004), (200), (105), (211), and (204) crystal planes [58]. Additional XRD patterns of the starting materials ( $\text{BiI}_3$  and  $\text{CsI}_2$ ) and the  $\text{Cs}_3\text{Bi}_2\text{I}_9$  perovskite are shown in the Supporting Information. The XRD pattern of  $\text{Cs}_3\text{Bi}_2\text{I}_9$  exhibits a hexagonal crystallographic phase with space group  $P63/mmc$  [53,59,60]. In the XRD pattern of  $\text{Cs}_3\text{Bi}_2\text{I}_9$ , closely spaced peaks convolute into a single broad peak, sometimes with an asymmetric shape. These complexities, together with the usual uncertainties arising from inhomogeneity in the size and shape of nanocrystals, made the determination of the crystallite size of  $\text{Cs}_3\text{Bi}_2\text{I}_9$  challenging. The XRD patterns obtained for the heterostructures after calcination show peaks of the pristine anatase- $\text{TiO}_2$  (UV100) crystal phase without any changes. This result confirms that the perovskite nanoparticles, which are present in only low quantity ( $<0.5\ \text{wt}\%$ ), are dispersed on the  $\text{TiO}_2$  surface. No shift was measured in the peaks of the calcined samples confirming high thermal stability of the crystal structure. The presence of  $\text{Cs}_3\text{Bi}_2\text{I}_9$  was detected on the UV100–0.5 sample at  $2\theta$  equal to  $29.6^\circ$ ,  $31.5^\circ$ ,  $38.7^\circ$ , and  $44.9^\circ$ . In the as-synthesized heterostructures is diffraction peak was probability hidden by the high intensity of the  $\text{TiO}_2$  diffraction peak at

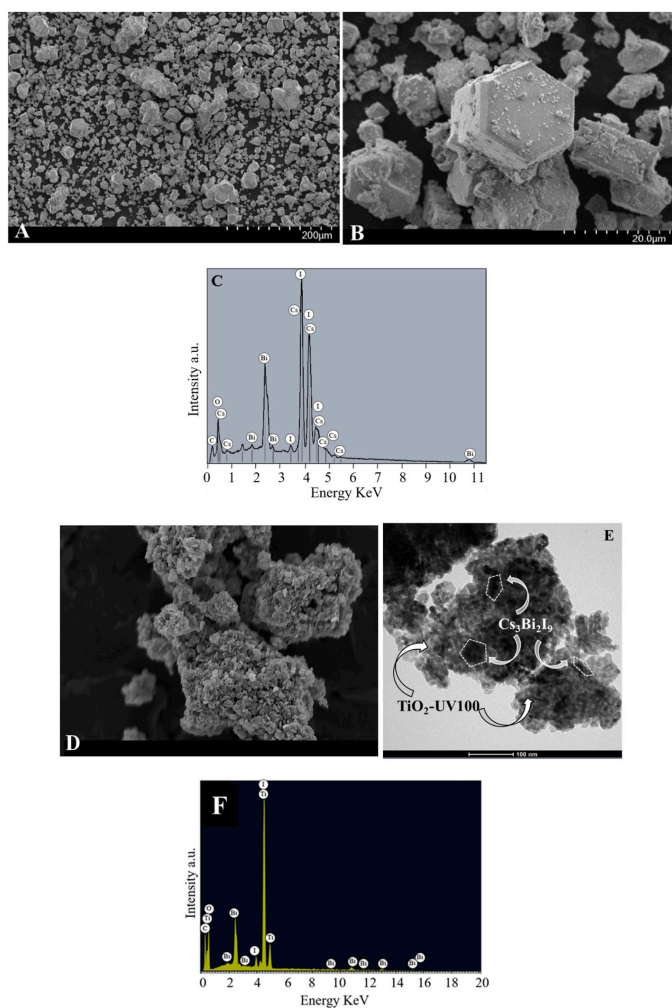


**Fig. 3.** A and B) SEM images for bare perovskite  $\text{Cs}_3\text{Bi}_2\text{I}_9$ , C) EDX analysis for bare perovskite  $\text{Cs}_3\text{Bi}_2\text{I}_9$ , D) SEM images for composite UV100-0.1 E) EDX analysis for composite UV100-0.1.

$2\theta = 25.4^\circ$  (see Fig. 3).

The optical bandgap of the materials was determined using UV-vis diffuse reflectance spectroscopy. The optical properties of the UV100-0.1 and UV100-0.5 composites were characterized by UV-vis spectroscopy at room temperature and compared with commercial UV100, used as a reference (Fig. S3). The results exhibit that both the UV100-0.1 and UV100-0.5 composites show a redshift of the absorption. The absorption edge of the bare UV100 was found to be 400 nm, for UV100-0.1 and UV100-0.5 composites were about 580 and 630 nm, respectively. This optical absorption may be responsible for driving the degradation reaction more efficiently under visible light illumination [61]. Unlike traditional semiconductors,  $\text{Cs}_3\text{Bi}_2\text{I}_9$  exhibits strong excitonic behavior even at room temperature. The excitonic absorption peak

at 2.56 eV (485 nm) is shown in Fig. S3. The peak is usually related to the strong quantum confinement effect due to the 0D nature of  $[\text{Bi}_2\text{I}_9]^{3-}$  bi-octahedra [40]. The calculated bandgap from the Tauc plot of the absorbance data of  $\text{Cs}_3\text{Bi}_2\text{I}_9$  is reported in Supporting Information.

BET adsorption analysis was performed to detect the specific surface area of the employed materials. In general, Hombikat UV100 particles are mainly formed by small homogenous sub-particles highly agglomerated, and the surface of the particles is full of pores producing a high specific surface area [62]. On the contrary, the perovskite has a very small surface area around  $5 \text{ m}^2/\text{g}$  which is more than 50 times lower than  $\text{TiO}_2$ . In the UV100-0.5 sample, containing 0.5 wt%  $\text{Cs}_3\text{Bi}_2\text{I}_9$ , the surface area decreased to  $74.4 \text{ m}^2/\text{g}$ . However, while reducing the content of perovskite to 0.1 wt%, the surface area slightly increased to

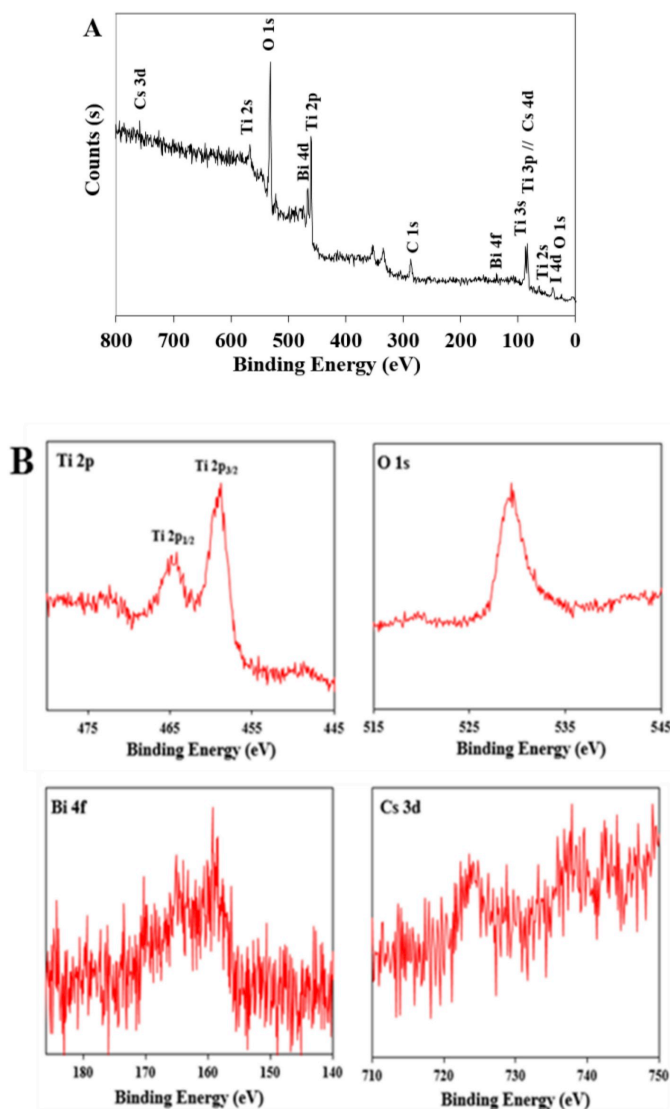


Fig. 4. A) XPS survey spectrum of the UV100-0.1 heterostructure B) T 2p, O 1s, Bi 4f, and Cs 3d spectra, respectively.

82.6 m<sup>2</sup>/g, nearly three times less than the commercial UV100 (284.98 m<sup>2</sup>/g). The formation of perovskite nanoclusters on the surface of the composites might result in a decrease in specific BET surface area of titanium by creating an excessive agglomeration on the surface of the UV100. Consequently, all the perovskite-based heterostructures presented a significantly smaller surface area respect the pristine TiO<sub>2</sub>. In order to observe the morphology of the as-synthesized powders, the SEM was used. Fig. 3A–C report the SEM images and the EDX analysis of the as-synthesized inorganic perovskite Cs<sub>2</sub>Bi<sub>3</sub>I<sub>9</sub>. The morphology was likely

to be induced by a slow crystal growth rate since the synthesis was performed at low temperature (60 °C) and the DMF was slowly evaporated. The image clearly shows hexagonal structures in agreement with the XRD pattern (Fig. S1) (see Fig. 5).

The characteristic SEM images of the as-prepared microcrystals show particles of various size ranging from 10 to 15 μm (Fig. 3A). While the smaller particles exhibit irregular crystal shapes, the larger are hexagonal (Fig. 3B). Energy-dispersive X-ray spectroscopy (EDX) measurements were performed to verify the percentage of elements in the

sample, all showing prominent peaks (Fig. 3C) [63]. Fig. 3D–F show SEM images and EDX analysis for the UV100-0.5 composite with  $\text{Cs}_3\text{Bi}_2\text{I}_9$  content of 0.5%. In general, Hombikat UV100 nanoparticles clusters exhibit a narrow range of homogeneous particles in shape and size. The surface of the particles, usually full of pores, may produce high specific surface area herein in agreement with the observations made with BET measurements [64]. Moreover, this marked porosity may facilitate the implant of functional species [62]. The presence of  $\text{Cs}_3\text{Bi}_2\text{I}_9$  in a composite emerge many insular aggregates and the surfaces of  $\text{TiO}_2$  become rough as revealed in Fig. 3D. In order to obtain an understanding of the interfacial interaction between UV100 and halide perovskite, the heterostructure was characterized by TEM. TEM images confirmed that the composites exhibit similar morphology of pristine material, indicating the structure of the singular materials remains unchanged after the solvent treatment. The TEM picture in Fig. 3E shows different lattice fringes of the as-synthesized halide perovskite on the UV100, revealing the formation of heterostructure after the as performed synthesis. Fig. 3F displayed the EDX analysis of the as synthesized composite. These data confirm the coexistence of  $\text{TiO}_2$  and  $\text{Cs}_3\text{Bi}_2\text{I}_9$  without exhibiting any remarkable contamination by other chemical species.

X-ray photoelectron spectroscopy (XPS) was performed to confirm the elemental composition and the valence of the single elements on the surface of the samples. The specific survey spectrum of the halide perovskite is discussed in the Supporting Information (Fig. S5). According to the survey spectrum of the as-synthesized composite, the detected elements include Ti, Bi, I, Cs, and O (Fig. 6). The silver peak can be ascribed to the elemental composition of the holder of the instrument. The carbon peak at 284.9 eV is attributable to the atmospheric carbon, introduced during the sample preparation and measurement. The XPS proves the successful preparation of composition between  $\text{TiO}_2$  and  $\text{Cs}_3\text{Bi}_2\text{I}_9$ . The obtained binding energy peaks confirm the presence of dominant elements: Ti and O. Fig. 4B show a high-resolution XPS spectrum of the Ti 2p region. The core level of the binding energy of Ti  $2p_{3/2}$  and Ti  $2p_{1/2}$  was found at 458.8 eV and 464.8 eV, respectively. It must be noted that the peaks of Ti  $2p_{1/2}$  and Bi  $4d_{3/2}$  may partially overlapped. The XPS peak at 465.4 eV can also be assigned to Bi  $4d_{3/2}$ . The peak located at 530.4 eV is shown in Fig. 4B, indicates the presence of the main component corresponding to metal oxide bond Ti–O. It may also be considered the presence of adsorbed  $\text{OH}^-$  and  $\text{CO}_3^{2-}$  ions which correspond to 532 eV signal [65]. Since the intensity of the carbon peak indicated a very small amount of C, the component in the O 1s spectra were mainly assigned to  $\text{OH}^-$ . As expected, the peaks belonging to the perovskite elements were found to be very weak and noisy because of the low content in the composite. However, the presence of bismuth, cesium, and iodine was confirmed as depicted in Fig. 4B. The peak of Bi located around 160 eV indicates that Bi species exists in the  $3^+$  oxidation state. Furthermore, the high-resolution XPS spectra of Cs reveals the binding energy curves of Cs  $3d_{3/2}$  and Cs  $3d_{5/2}$  at 738.7 and 724.8 eV, respectively.

The photocatalytic activity is not only related to the light absorption capacity of the photocatalyst, but also to its ability to separate the photogenerated charge carriers and to catalyze the reduction and oxidation reactions [66]. Thus, it is important not only to evaluate the structural and optical properties but also the electronic properties of a semiconductor in order to understand the observed photocatalytic performance. The position of Fermi level and flat band potential ( $V_{fb}$ ) in the illuminated semiconductor electrode, relative to the redox potential of electrolyte, is interesting information that plays a key role in the application of semiconductor. For an n-doped semiconductor,  $V_{fb}$  lies close to the conduction band edge. Thus, the band edge energetic position of the conduction band can be estimated from the  $V_{fb}$  value [67]. Capacitance-voltage measurements of films in electrolyte solutions are frequently used to construct Mott-Schottky plots, from which  $V_{fb}$  of the semiconductor can be extracted. This method provides a direct measurement of the energetic interfacial alignment [68]. Herein, the

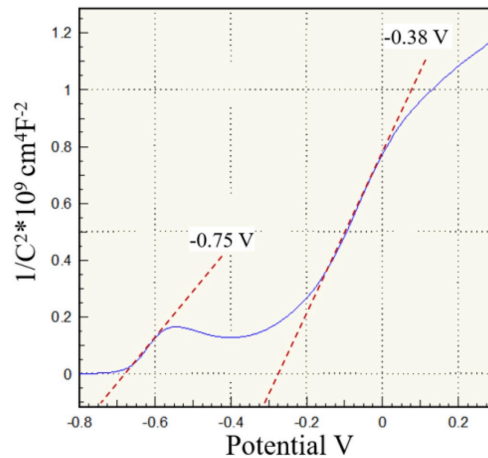


Fig. 5. Mott-Schottky plot for UV100-0.1 composite films on FTO.

Mott-Schottky results were conducted to confirm the relationship between the energetic levels at the semiconductor-electrolyte interface and the observed photocatalytic activity of the  $\text{Cs}_3\text{Bi}_2\text{I}_9/\text{TiO}_2$  heterostructures in aqueous oxidation processes. Fig. 5 shows the results obtained for the capacitance-voltage measurements. The analysis was performed employing  $\text{Cs}_3\text{Bi}_2\text{I}_9/\text{TiO}_2$  film deposited on top of FTO glass,  $\text{KNO}_3$  was used as an electrolyte. In general, the extrapolation of the linear fit of the straight portion of the curve to  $1/(C/A)^2 = 0$  gives an approximated value of the conduction band position  $\approx V_{fb}$ . The energetic position of the valence band ( $E_{vb}$ ) can be calculated when the value of the bandgap energy ( $E_g$ ) is known:

$$E_{vb} = E_{cb} + E_g \quad (2)$$

There are many factors that may affect the  $V_{fb}$  measurements, including defects induced during the synthetic process. For example, it is well known that for anatase  $\text{TiO}_2$  a frequency dependence in the Mott-Schottky plots may be caused by the inhomogeneity of the donor density near the surface [69]. Such effects might also influence the measurements performed for the  $\text{Cs}_3\text{Bi}_2\text{I}_9/\text{TiO}_2$  heterostructures. Thus, the obtained  $V_{fb}$  results were considered in a qualitative rather than quantitative manner. The positive slope of the straight line indicates that the as-synthesized material was an n-type semiconductor. However, in the case of the as-synthesized heterostructures, it is interesting to note both the results confirm the feature characteristic of an n-junction, where with three flat band potential values  $-0.37$  V for UV100 [70,71],  $-0.75$  V for the UV100-0.1 heterostructure. The Mott-Schottky plots for the bare perovskite are presented in Supporting Information. The energetic position of the  $V_{fb}$  can be considered similar to the position of the conduction band; it can be assumed that the electrons of the conduction band of the heterostructure have higher reductive power respect to the bare UV100. Thus, the reduction of  $\text{O}_2$  to  $\text{O}_2^\bullet$  and  $\text{H}^+$  to  $\text{H}_2$  by photogenerated electrons was found to be thermodynamically more favored for the heterostructure than for the bare UV100, resulting in a higher photocatalytic activity. Another possible explanation of the results is the transfer of the excited electrons from one material to the other, resulting in a decrease of recombination rate.

Moreover, the heterojunction formation should be considered a key factor to enhance the activity of the material. In semiconductor heterojunctions, the transfer direction of the photogenerated charge carriers depends on the position of the energetic levels (CB and VB). In general, when  $\text{TiO}_2$  is coupled with another semiconductor, spatial charge

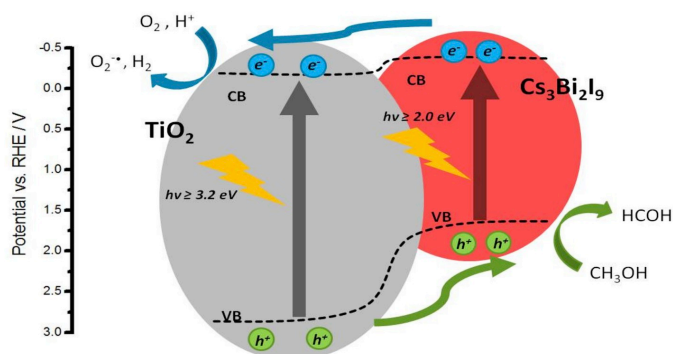


Fig. 6. Band alignment in the UV100:Cs<sub>3</sub>Bi<sub>2</sub>I<sub>9</sub> heterostructures.

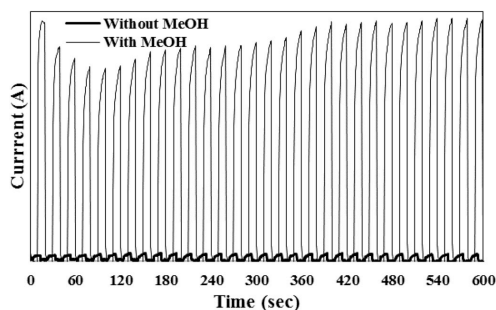


Fig. 7. Time-resolved current measurement, UV100-0.1 composite on FTO, in a presence and absence of MeOH.

separation may occur [72]. In the Cs<sub>3</sub>Bi<sub>2</sub>I<sub>9</sub>:TiO<sub>2</sub> heterostructure, the energetic position of TiO<sub>2</sub> and Cs<sub>3</sub>Bi<sub>2</sub>I<sub>9</sub> are shown in Fig. 6. Due to this energy band alignment, photogenerated electrons are transferred from

the CB of Cs<sub>3</sub>Bi<sub>2</sub>I<sub>9</sub> into the CB of TiO<sub>2</sub>, while photogenerated holes can be transferred from the VB of TiO<sub>2</sub> into the CB of Cs<sub>3</sub>Bi<sub>2</sub>I<sub>9</sub>. This allows a more efficient charge separation in the Cs<sub>3</sub>Bi<sub>2</sub>I<sub>9</sub>:TiO<sub>2</sub> heterojunction than in TiO<sub>2</sub> or Cs<sub>3</sub>Bi<sub>2</sub>I<sub>9</sub> alone.

TiO<sub>2</sub> and Cs<sub>3</sub>Bi<sub>2</sub>I<sub>9</sub> form a type II heterojunction allowing a more efficient charge separation than TiO<sub>2</sub> or Cs<sub>3</sub>Bi<sub>2</sub>I<sub>9</sub> alone. Photogenerated electrons were transferred into the CB of TiO<sub>2</sub> while photogenerated holes were transferred into the VB of Cs<sub>3</sub>Bi<sub>2</sub>I<sub>9</sub>. In aerobic reaction condition the CB electrons might react with O<sub>2</sub> to yield O<sub>2</sub><sup>•-</sup> or in anaerobic reaction condition H<sup>+</sup> to H<sub>2</sub>, while VB holes might oxidize methanol into formaldehyde.

Photocurrent measurements under solar simulator, with and without methanol, were conducted in order to evaluate the relevant properties and illustrate the enhanced electron transfer in the composites. Fig. 7 shows the current density as a function of time by switching on and off the light at 20 s intervals. In the absence of methanol, the current density was found to be extremely small. On the contrary, the current density increased when methanol was added to the electrolyte. In particular, the current density rose subsequently when the light was on and then gradually increased to a steady state. Afterward, the current density decreased instantly as the light was turned off. The current density on the composite deposited on FTO was clearly higher during illumination.

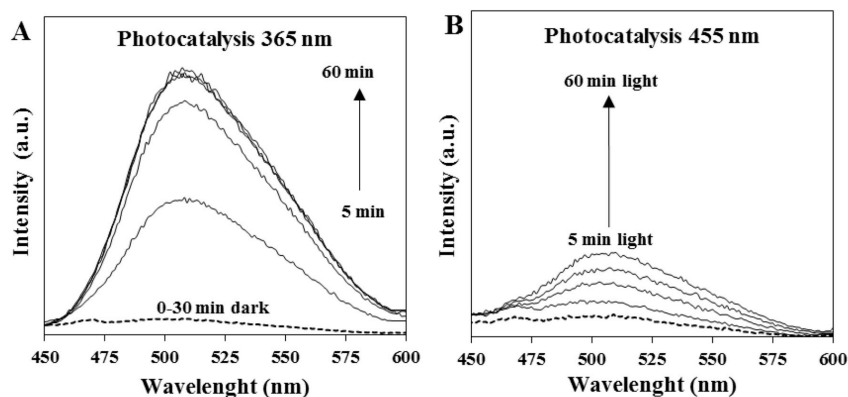


Fig. 8. A) Photocatalytic evolution in PL spectra of methanol oxidation as a function of irradiation time under 365 nm-light irradiation over UV100-0.1, B) Photocatalytic evolution in PL spectra as a function of irradiation time under 455 nm-light irradiation over UV100-0.1.

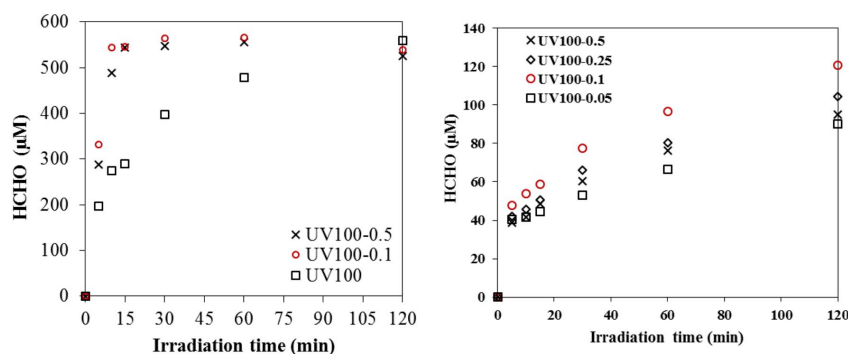


Fig. 9. A) Photocatalytic oxidation of MeOH to the HCHO under UV-light irradiation, B) Photocatalytic oxidation of MeOH to the HCHO under visible-light irradiation.

### 3.2. Performance of photocatalysis

#### 3.2.1. MeOH oxidation into formaldehyde

The photocatalytic reforming of methanol into formaldehyde lately leads to oxidizing to formic acid and finally to CO<sub>2</sub> and water [73]. When the semiconductor absorbs a photon with an energy equal to or higher than its bandgap, the electrons migrate from the valence band (VB) into the conduction band (CB). This results in the formation of holes (h<sup>+</sup><sub>vb</sub>) and electrons (e<sup>-</sup><sub>cb</sub>) in the VB and CB, respectively. The photogenerated holes, when do not recombine with e<sup>-</sup><sub>cb</sub>, react with surface hydroxyl groups (-OH) or adsorbed water molecules to produce hydroxyl (•OH) radicals. Hydroxyl radicals are strong and non-selective oxidizing agents in photocatalytic reactions [11]. The radicals rapidly react with surface adsorbed methanol that is oxidized primarily into formaldehyde and then into other species. In addition, the photogenerated e<sup>-</sup><sub>cb</sub> can react with electron acceptors, such as O<sub>2</sub>, dissolved in the solution or adsorbed on the surface of the semiconductor. The reaction with O<sub>2</sub> produce superoxide radical anions (O<sub>2</sub><sup>•-</sup>) or hydrogen peroxide (H<sub>2</sub>O<sub>2</sub>), that may be utilized for the oxidation of methanol through the intermediate formation of •OH radicals [10]. The photocatalytic oxidation of methanol into formaldehyde was expressed in terms of the increase of the intensity of the peaks corresponding to DDL, as a function of time of irradiation. It has been reported by Nash [56] that 2 mol of acetylacetone react with 1 mol of formaldehyde to give 1 mol of DDL. The characteristic emission peak of DDL, corresponding at the formation of formaldehyde, was found to be at 510 nm. The peaks corresponding to DDL increase in intensity as a function of time of irradiation indicating the conversion of methanol to formaldehyde, which was quantified by calibration.

Previously, two control experiments were performed. Initially, the effect of light was tested on methanol as a model contaminant. Direct photolysis of methanol upon UV and visible light was found to be negligible. Similar results were reported in other studies before [55,73]. A second control experiment was conducted in dark conditions and in the presence of the composite catalyst (UV100-0.1). Any degradation was recorded. In general, 30 min of dark absorption was performed before switch on the light in order to reach adsorption-desorption equilibrium. The results highlight three main points. First, the enhancement of peak at 510 nm in both Fig. 8A and B means that formaldehyde appeared as an oxidation product of methanol. Moreover, the peaks appeared to increase along time of irradiation. Therefore, the results confirm the oxidation of methanol into formaldehyde during the photocatalytic experiments. Finally, Fig. 8A–B are evident that photocatalysis under UV irradiation shows remarkable higher efficiency respect to the visible light irradiation.

Table 2

Reaction rates of photocatalytic oxidation MeOH under UV and visible light irradiation.

	UV100-0.1	UV100-0.5	UV100
$k$ (min <sup>-1</sup> ) – 365 nm	1.51	1.72	0.84
$R^2$	0.99	0.99	0.95
$k$ (min <sup>-1</sup> ) – 455 nm	0.05	0.03	–
$R^2$	0.95	0.98	–

The reforming of methanol to formaldehyde was performed in water solution under UV and visible-light irradiation. Fig. 9A and B show the variation in formaldehyde concentration during light irradiation for the different photocatalysts under UV and visible-light irradiation, respectively. Under UV light irradiation (Fig. 9A), the observed photocatalytic activity can be primarily attributed to the transition of electrons from the valence band to the conduction band of TiO<sub>2</sub> due to the absorption of UV radiation having energy higher than the bandgap energy. The photocatalytic activities of the heterostructures UV100-0.1 and UV100-0.5 were found to be relatively higher when compared with the activity reported for commercial UV100. It must be noticed that after 15 min the concentration of formaldehyde starts to be constant, this may be associated to complete conversion of methanol. Moreover, the UV100-0.1 composite showed the best photocatalytic activity under visible light irradiation respect all the other synthesized composites, as shown in Fig. 9B. In particular, when the load of perovskite introduced in the composite was enhanced, the photodegradation was reduced. The decrease may be associated with the possibility of a different degree of aggregation according to the amount of the perovskite present in the composite. Finally, this effect may also be related to the fact that perovskite may occupy the adsorption site on TiO<sub>2</sub> surface by decreasing the adsorption rate of the reactant.

Moreover, the efficiencies in methanol degradation process of the as-synthesized composites were compared using the calculated rate of reaction, as shown in Eq. (1). The results are listed in Table 2. The results show that the UV100-0.1 and UV100-0.5 heterostructures exhibited improved photocatalytic activity both under visible and UV-light irradiation. In this evaluation, the reaction rate was applied in the first 10 min of experiments where the reaction shows a linear behavior. The degradation appeared to be considerably faster under UV light irradiation in comparison with the visible-light irradiation. The UV100-0.5 and UV100-0.1 composites showed a reaction rate of 50% and 44% higher in comparison with the bare UV100, respectively. Moreover, the methanol was almost completely converted within 15 min, under UV-light irradiation with UV100-0.5 and UV100-0.1 composites. On the contrary,

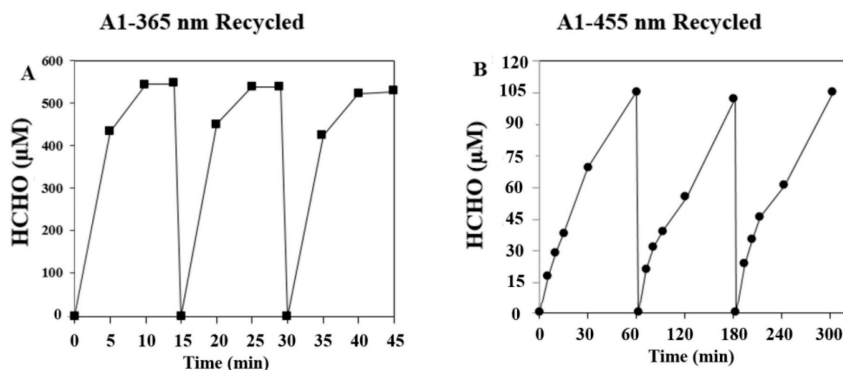


Fig. 10. Recycling test for UV100-0.1 under UV and visible-light irradiation.

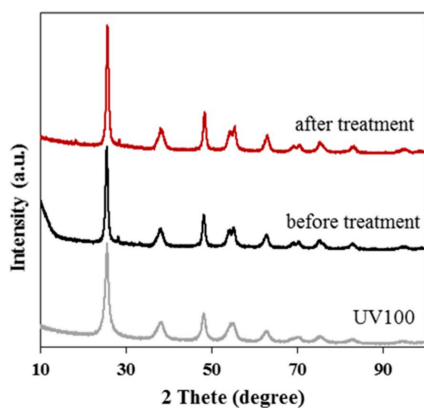


Fig. 11. XRD patterns of the as synthesized composite before and after treatment and the bare UV100 as reference.

UV100 nanoparticles irradiated under UV-light showed the complete removal of methanol after 120 min. Since the photon energy is lower than the bandgap energy of UV100 nanoparticles under 455 nm, visible light illumination and the transfer of electrons from the valence band to the conduction band was not expected to occur. In this case, the perovskite acts as a photosynthesizer, and it can harvest the visible light. Charge carriers can be photogenerated on perovskite surface under visible-light illumination as shown in DRS light-absorption measurement. In this case, the photocatalytic activity of TiO<sub>2</sub> can be extended to the visible light range when combined with the narrower bandgap.

Moreover, the photocatalytic performance was also expected to be improved within the heterojunction interface because of the two materials allowed the migration of the charge carriers, which hinder also their fast recombination. Under visible light irradiation, remarkably superior efficiency was achieved by the UV100-0.1 respect to all the other prepared composites.

In addition, the recyclability test of UV100-0.1 composite has been evaluated for three times without observing any significant loss in the efficiency (Fig. 10). The results demonstrate that UV100-0.1 composite has great potential and good stability and may be considered as new photocatalytic material to use in water treatment.

In order to ensure the photocatalytic stability of the as prepared nanocomposite, the XRD patterns before and after reaction were

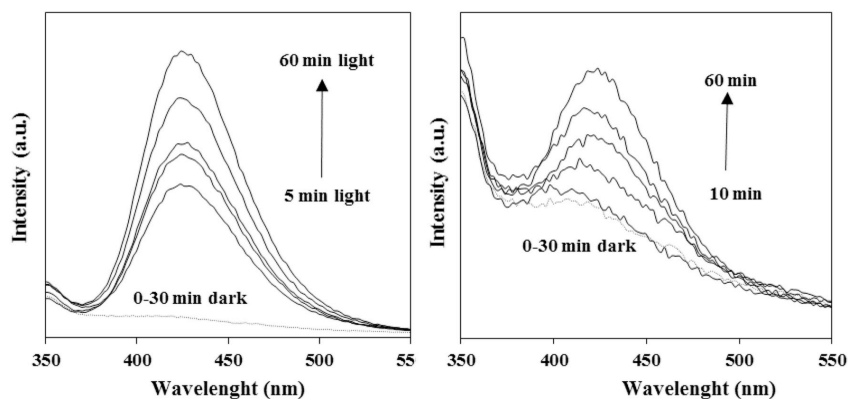


Fig. 12. Fluorescence spectral changes with UV and visible-light irradiation time in a solution of terephthalic acid with UV100-0.1 under UV and visible light.



recorded. Fig. 11 displays the patterns for the as-prepared composite, before and after treatment; the pattern of pristine UV100 is also shown as a reference. As visible from the figure, the XRD peaks after photocatalytic reaction are similar to that before reaction. It indicates that the structure of the as-prepared material does not change during the photocatalytic process, and the stability of photocatalytic activity is depended on the stability of the structure.

### 3.2.2. Formation of hTA: •OH evaluation

As already mentioned, •OH plays an important role in the organic pollutants abatements in wastewater treatments. In aqueous solutions, the direct measurement of •OH is highly difficult due to its low concentration and short lifetime. Terephthalic acid (TA) has proven to be suitable for the •OH quantification [74–76]. The fluorescence method analyses carried out to detect the 2-hydroxyterephthalic acid (hTA) As an oxidation product of TA. TA was found to be more stable with respect to other probes used such as benzene, nitrobenzene [57]. The formation of hydroxyl radicals •OH under irradiation was detected by the fluorescence-technique using terephthalic acid as a fluorescence probe molecule (Fig. 12). The gradual increase in the PL intensity was observed at about 425 nm, which indicates the formation of 2-hydroxyterephthalic acid produced by a chemical reaction between TA and •OH formed during irradiation of the photocatalytic process.

## 4. Conclusions

In summary, the heterostructure  $\text{Cs}_3\text{Bi}_2\text{I}_9/\text{TiO}_2$  composites were successfully synthesized via a simple wet-chemical method and applied for the photocatalytic decomposition of methanol. Under UV and visible-light illumination, the composites, especially UV100-0.1 and UV100-0.5 were found to have a higher photocatalytic activity than pure Hombikat UV100  $\text{TiO}_2$ . According to the optical measurements and the electrochemical studies, the heterostructures benefit not only of an extended light-harvesting in the visible light region but also of increased charge separation. The increased photocatalytic activity under UV light irradiation may be ascribed to the simultaneous contribution of the perovskite and UV-100, acting as light-absorbing heterojunction. On the other hand, the activity under visible light irradiation can be mainly addressed to perovskite material which as like redox mediator.

## Acknowledgements

Maa-ja vesiteknikaan tuki ry (MVTI Foundation), Finland is gratefully acknowledged for the financial support. Moreover, we thank Luis I. Granone and the Laboratory of Nano and Quantum Engineering (LNQE) for providing electrochemical and XRD measurements.

## Appendix A. Supplementary data

Supplementary data to this article can be found online at <https://doi.org/10.1016/j.solmat.2019.110214>.

## References

- [1] W. Zhang, S. Yang, J. Li, W. Gao, Y. Deng, W. Dong, C. Zhao, G. Lu, Visible-to-ultraviolet Upconversion: energy transfer, material matrix, and synthesis strategies, *Appl. Catal. B Environ.* 206 (2017) 89–103, <https://doi.org/10.1016/j.apcatb.2017.01.023>.
- [2] P. Lianos, Review of recent trends in photoelectrocatalytic conversion of solar energy to electricity and hydrogen, *Appl. Catal. B Environ.* 210 (2017) 235–254, <https://doi.org/10.1016/j.apcatb.2017.03.067>.
- [3] O. Lefebvre, R. Moletta, Treatment of organic pollution in industrial saline wastewater: a literature review, *Water Res.* 40 (2006) 3671–3682, <https://doi.org/10.1016/j.watres.2006.08.027>.
- [4] D. Wang, S.C. Pillai, S.H. Ho, J. Zeng, Y. Li, D.D. Dionysiou, Plasmonic-based nanomaterials for environmental remediation, *Appl. Catal. B Environ.* 237 (2018) 721–741, <https://doi.org/10.1016/j.apcatb.2018.05.094>.
- [5] C. Yang, H. Chen, G. Zeng, G. Yu, S. Luo, Biomass accumulation and control strategies in gas biofiltration, *Biotechnol. Adv.* 28 (2010) 531–540, <https://doi.org/10.1016/j.biotechadv.2010.04.002>.
- [6] S. Suárez, M. Yates, A.L. Petre, J.A. Martín, P. Avila, J. Blanco, Development of a new Rh/TiO<sub>2</sub>-sepiolite monolithic catalyst for N<sub>2</sub>O decomposition, *Appl. Catal. B Environ.* 64 (2006) 302–311, <https://doi.org/10.1016/j.apcatb.2005.12.006>.
- [7] F. Teng, Z. Liu, A. Zhang, M. Li, Photocatalytic performances of Ag<sub>3</sub>PO<sub>4</sub>Polypods for degradation of dye pollutant under natural indoor weak light irradiation, *Environ. Sci. Technol.* 49 (2015) 9489–9494, <https://doi.org/10.1021/acs.est.5b00735>.
- [8] A.O.T. Patrocínio, J. Schneider, M.D. França, L.M. Santos, B.P. Caixeta, A.E. H. Machado, D.W. Bahnemann, Charge carrier dynamics and photocatalytic behavior of TiO<sub>2</sub> nanopowders submitted to hydrothermal or conventional heat treatment, *RSC Adv.* 5 (2015) 70536–70545, <https://doi.org/10.1039/c5ra13291f>.
- [9] D. Spasiano, R. Marotta, S. Malato, P. Fernandez-Ibanez, I. Di Somma, Solar photocatalysis: materials, reactors, some commercial, and pre-industrialized applications. A comprehensive approach, *Appl. Catal. B Environ.* 170–171 (2015) 90–123, <https://doi.org/10.1016/j.apcatb.2014.12.050>.
- [10] T.S. Natarajan, H.C. Bajaj, R.J. Tayade, Enhanced direct sunlight photocatalytic oxidation of methanol using nanocrystalline TiO<sub>2</sub> calcined at different temperature, *J. Nanoparticle Res.* 16 (2014) 2713, <https://doi.org/10.1007/s11051-014-2713-7>.
- [11] J. Kou, C. Lu, J. Wang, Y. Chen, Z. Xu, R.S. Varma, Selectivity enhancement in heterogeneous photocatalytic transformations, *Chem. Rev.* 117 (2017) 1445–1514, <https://doi.org/10.1021/acs.chemrev.6b00396>.
- [12] A. Kudo, Photocatalysis, *Appl. Catal. B Environ.* 46 (2003) 703, <https://doi.org/10.1016/j.apcatb.2003.08.002>.
- [13] C. Martínez, S. Vilarinho, M.I. Fernández, J. Faria, M.L. Canle, J.A. Santaballa, Mechanism of degradation of ketoprofen by heterogeneous photocatalysis in aqueous solution, *Appl. Catal. B Environ.* 142–143 (2013) 633–646, <https://doi.org/10.1016/j.apcatb.2013.05.018>.
- [14] S.A.A. Nakhli, K. Ahmadizadeh, M. Fereshtehnejad, M.H. Rostami, M. Safari, S. M. Borghei, Biological removal of phenol from saline wastewater using a moving bed biofilm reactor containing acclimated mixed consortia, *SpringerPlus* 3 (2014) 1–10, <https://doi.org/10.1186/2193-1801-3-112>.
- [15] J. Saïen, H. Nejati, Enhanced photocatalytic degradation of pollutants in petroleum refinery wastewater under mild conditions, *J. Hazard Mater.* 148 (2007) 491–495, <https://doi.org/10.1016/j.jhazmat.2007.03.001>.
- [16] S. Loeb, R. Hofmann, J.H. Kim, Beyond the pipeline: assessing the efficiency limits of advanced technologies for solar water disinfection, *Environ. Sci. Technol. Lett.* 3 (2016) 73–80, <https://doi.org/10.1021/acs.estlett.6b00023>.
- [17] H. Sun, G. Li, X. Nie, H. Shi, P.K. Wong, H. Zhao, T. An, Systematic approach to in-depth understanding of photoelectrocatalytic bacterial inactivation mechanisms by tracking the decomposed building blocks, *Environ. Sci. Technol.* 48 (2014) 9412–9419, <https://doi.org/10.1021/es502471h>.
- [18] S. Huang, Y. Xu, Q. Liu, T. Zhou, Y. Zhao, L. Jing, H. Xu, H. Li, Enhancing reactive oxygen species generation and photocatalytic performance via adding oxygen reduction reaction catalysts into the photocatalysts, *Appl. Catal. B Environ.* 218 (2017) 174–185, <https://doi.org/10.1016/j.apcatb.2017.06.030>.
- [19] W. Wang, Y. Yu, T. An, G. Li, H.Y. Yip, J.C. Yu, P.K. Wong, Visible-light-driven photocatalytic inactivation of E. coli K-12 by bismuth vanadate nanotubes: bactericidal performance and mechanism, *Environ. Sci. Technol.* 46 (2012) 4599–4606, <https://doi.org/10.1021/es2042977>.
- [20] N. Muhd Julkapli, S. Bagheri, S. Bee Abd Hamid, Recent advances in heterogeneous photocatalytic decolorization of synthetic dyes, *Sci. World J.* (2014), <https://doi.org/10.1155/2014/692307>, 2014.
- [21] A. Fujishima, T.N. Rao, D.A. Tryk, Titanium dioxide photocatalysis, *J. Photochem. Photobiol. C Photochem. Rev.* 1 (2000) 1–21, [https://doi.org/10.1016/S1389-5567\(00\)00002-2](https://doi.org/10.1016/S1389-5567(00)00002-2).
- [22] K.I. Hadjiivanov, D.G. Klissurski, Surface chemistry of titania (anatase) and titania-supported catalysts, *Chem. Soc. Rev.* 25 (1996) 61, <https://doi.org/10.1039/cs9962500061>.
- [23] D. Friedmann, C. Mendive, D. Bahnemann, TiO<sub>2</sub> for water treatment: parameters affecting the kinetics and mechanisms of photocatalysis, *Appl. Catal. B Environ.* 99 (2010) 398–406, <https://doi.org/10.1016/j.apcatb.2010.05.014>.
- [24] T. Salthammer, S. Mentese, R. Marutzky, Formaldehyde in the indoor environment, *Chem. Rev.* 110 (2010) 2536–2572, <https://doi.org/10.1021/cr800399g>.
- [25] J.C. Yu, L. Zhang, Z. Zheng, J. Zhao, Synthesis and characterization of phosphated mesoporous titanium dioxide with high photocatalytic activity, *Chem. Mater.* 15 (2003) 2280–2286, <https://doi.org/10.1021/cm0340781>.
- [26] S.B. Kim, S.C. Hong, Kinetic study for photocatalytic degradation of volatile organic compounds in air using thin film TiO<sub>2</sub> photocatalyst, *Appl. Catal. B Environ.* 35 (2002) 305–315, [https://doi.org/10.1016/S0926-3373\(01\)00274-0](https://doi.org/10.1016/S0926-3373(01)00274-0).
- [27] X.Z. Li, F.B. Li, Study of Au/Au<sup>3+</sup>-TiO<sub>2</sub> photocatalysts toward visible photooxidation for water and wastewater treatment, *Environ. Sci. Technol.* 35 (2001) 2381–2387, <https://doi.org/10.1021/es001752w>.
- [28] A. Kumar, V. Sharma, S. Kumar, A. Kumar, V. Krishnan, Towards utilization of full solar light spectrum using green plasmonic Au-TiO<sub>2</sub> photocatalyst at ambient conditions, *Surf. Interfaces* 11 (2018) 98–106, <https://doi.org/10.1016/j.surfin.2018.03.005>.
- [29] Y. Zheng, L. Zheng, Y. Zhan, X. Lin, Q. Zheng, K. Wei, Ag/ZnO heterostructure nanocrystals: synthesis, characterization, and photocatalysis, *Inorg. Chem.* 46 (2007) 6980–6986, <https://doi.org/10.1021/ic700688f>.
- [30] X. Zhang, Y. Wang, B. Liu, Y. Sang, H. Liu, Heterostructures construction on TiO<sub>2</sub>nanobelts: a powerful tool for building high-performance photocatalysts,

- Appl. Catal. B Environ. 202 (2017) 620–641, <https://doi.org/10.1016/j.apcatb.2016.09.068>.
- [31] Y. Wang, Q. Wang, X. Zhan, F. Wang, M. Safdar, J. He, Visible light driven type II heterostructures and their enhanced photocatalysis properties: a review, *Nanoscale* 5 (2013) 8326–8339, <https://doi.org/10.1039/c3nr01577g>.
- [32] R. Wang, G. Jiang, Y. Ding, Y. Wang, X. Sun, X. Wang, W. Chen, Photocatalytic activity of heterostructures based on TiO<sub>2</sub> and halloysite nanotubes, *ACS Appl. Mater. Interfaces* 3 (2011) 4154–4158, <https://doi.org/10.1021/am201020q>.
- [33] H. McDaniel, P.E. Heil, C.L. Tsai, K. Kim, M. Shim, Integration of type II nanorod heterostructures into photovoltaics, *ACS Nano* 5 (2011) 7677–7683, <https://doi.org/10.1021/nn2029988>.
- [34] D.C. Lee, I. Robel, J.M. Pietryga, V.I. Klimov, Infrared-active heterostructured nanocrystals with ultralong carrier lifetimes, *J. Am. Chem. Soc.* 132 (2010) 9960–9962, <https://doi.org/10.1021/ja102716p>.
- [35] C.J. Dooley, S.D. Dimitrov, T. Fiebig, Ultrafast electron transfer dynamics in CdSe/CdTe donor-acceptor nanorods, *J. Phys. Chem. C* 112 (2008) 12074–12076, <https://doi.org/10.1021/jp804040r>.
- [36] G.D. Scholes, M. Jones, S. Kumar, Energetics of photoinduced electron-transfer reactions decided by quantum confinement, *J. Phys. Chem. C* 111 (2007) 13777–13785, <https://doi.org/10.1021/jp0745583>.
- [37] Z. Jiang, Q. Qian, C. Zhu, H. Sun, W. Wan, J. Xie, H. Li, P.K. Wong, S. Yuan, Carbon nitride coupled with CdS-TiO<sub>2</sub> nanodots as 2D/0D ternary composite with enhanced photocatalytic H<sub>2</sub> evolution: a novel efficient three-level electron transfer process, *Appl. Catal. B Environ.* 210 (2017) 194–204, <https://doi.org/10.1016/j.apcatb.2017.03.069>.
- [38] X. Zeng, T. Zhou, C. Leng, Z. Zang, M. Wang, W. Hu, X. Tang, S. Lu, L. Fang, M. Zhou, Performance improvement of perovskite solar cells by employing a CdSe quantum dot/PCBM composite as an electron transport layer, *J. Mater. Chem. A* 5 (2017) 17499–17505, <https://doi.org/10.1039/c7ta02033c>.
- [39] Y. Huangping, Zhou, Chen Qi, Li Gang, Song Luo, Song Tze-bing, Duan Hsin-Sheng, Hong Zirou, You Jingbi, Liu Yongsheng, Yang, Interface engineering of highly efficient perovskite solar cells, *Science* 345 (2014) 542–546, <https://doi.org/10.1126/science.1254050>, 80.
- [40] C. Cuhadar, S.G. Kim, J.M. Yang, J.Y. Seo, D. Lee, N.G. Park, All-inorganic bismuth halide perovskite-like materials A<sub>3</sub>Bi<sub>2</sub>I<sub>9</sub> and A<sub>3</sub>Bi<sub>1.8</sub>Na<sub>0.2</sub>I<sub>8.6</sub> (A = Rb and Cs) for low-voltage switching resistive memory, *ACS Appl. Mater. Interfaces* 10 (2018) 29741–29749, <https://doi.org/10.1021/acsami.8b07103>.
- [41] A.J. Lehner, D.H. Fabini, H.A. Evans, C.A. Hébert, S.R. Smock, J. Hu, H. Wang, J. W. Zwanziger, M.L. Chabinyr, R. Seshadri, Crystal and electronic structures of complex bismuth iodides A<sub>3</sub>Bi<sub>2</sub>I<sub>9</sub> (A = K, Rb, Cs) related to perovskite: aiding the rational design of photovoltaics, *Chem. Mater.* 27 (2015) 7137–7148, <https://doi.org/10.1021/acs.chemmater.5b03147>.
- [42] N.G. Park, Perovskite solar cells: an emerging photovoltaic technology, *Mater. Today* 18 (2015) 65–72, <https://doi.org/10.1016/j.mattod.2014.07.007>.
- [43] S. Heo, G. Seo, Y. Lee, D. Lee, M. Seol, J. Lee, J.-B. Park, K. Kim, D.-J. Yun, Y. S. Kim, J.K. Shin, T.K. Ahn, M.K. Nazeeruddin, Deep level trapped defect analysis in CH<sub>3</sub>NH<sub>3</sub>PbI<sub>3</sub> perovskite solar cells by deep level transient spectroscopy, *Energy Environ. Sci.* 10 (2017) 1128–1133, <https://doi.org/10.1039/c7ee00303j>.
- [44] R.L.Z. Hoyer, R.E. Brandt, A. Osherov, V. Stevanovic, S.D. Stranks, M.W.B. Wilson, H. Kim, A.J. Akey, J.D. Perkins, R.C. Kurchin, J.R. Poindexter, E.N. Wang, M. G. Bawendi, V. Bulovic, T. Buonassisi, Methylammonium bismuth iodide as a lead-free, stable hybrid organic-inorganic solar absorber, *Chem. Eur J.* 22 (2016) 2605–2610, <https://doi.org/10.1002/chem.201505055>.
- [45] A.H. Slavney, T. Hu, A.M. Lindenberg, H.I. Karunadasa, A bismuth-halide double perovskite with long carrier recombination lifetime for photovoltaic applications, *J. Am. Chem. Soc.* 138 (2016) 2138–2141, <https://doi.org/10.1021/jacs.5b13294>.
- [46] S.V. Mel'nikova, A.I. Zaitsev, Ferroelectric phase transition in Cs<sub>3</sub>Bi<sub>2</sub>I<sub>9</sub>, *Phys. Solid State* 39 (1997) 1652–1654, <https://doi.org/10.1134/1.1129882>.
- [47] O. Lindqvist, G. Johansson, F. Sandberg, T. Norin, The crystal structure of cesium bismuth iodide, Cs<sub>3</sub>Bi<sub>2</sub>I<sub>9</sub>, *Acta Chem. Scand.* 22 (1968) 2943–2952, <https://doi.org/10.3891/acta.chem.scand.22.2943>.
- [48] I.P. Aleksandrov, A.F. Bovina, O.A. Ageev, A.A. Sukhovskii, Incommensurate phase in the layered hexagonal crystal Cs<sub>3</sub>Bi<sub>2</sub>I<sub>9</sub>, *Phys. Solid State* 39 (1997) 991–994, <https://doi.org/10.1134/1.1130118>.
- [49] G.E. Eperon, S.D. Stranks, C. Menelaou, M.B. Johnston, L.M. Herz, H.J. Snaith, Formamidinium lead trihalide: a broadly tunable perovskite for efficient planar heterojunction solar cells, *Energy Environ. Sci.* 7 (2014) 982–988, <https://doi.org/10.1039/c3ee43822h>.
- [50] N.K. Noel, S.D. Stranks, A. Abate, C. Wehrenfennig, S. Guarnera, A.A. Highghirad, A. Sadhanala, G.E. Eperon, S.K. Pathak, M.B. Johnston, A. Petrozza, L.M. Herz, H. J. Snaith, Lead-free organic-inorganic tin halide perovskites for photovoltaic applications, *Energy Environ. Sci.* 7 (2014) 3061–3068, <https://doi.org/10.1039/c4ee01076k>.
- [51] B. Lee, C.C. Stoumpos, N. Zhou, F. Hao, C. Malliakas, C.Y. Yeh, T.J. Marks, M. G. Kanatzidis, R.P.H. Chang, Air-stable molecular semiconductor iodosalts for solar cell applications: Cs<sub>2</sub>Snl<sub>6</sub> as a hole conductor, *J. Am. Chem. Soc.* 136 (2014) 15379–15385, <https://doi.org/10.1021/ja508464w>.
- [52] D.W. Bahnemann, Solar Water Detoxification: Novel TiO<sub>2</sub> Powders as Highly Active Photocatalysts, vol. 119, 2016.
- [53] B.W. Park, B. Philippe, X. Zhang, H. Rensmo, G. Boschloo, E.M.J. Johansson, Bismuth based hybrid perovskites A<sub>3</sub>Bi<sub>2</sub>I<sub>9</sub> (A: methylammonium or cesium) for solar cell application, *Adv. Mater.* 27 (2015) 6806–6813, <https://doi.org/10.1002/adma.201501978>.
- [54] A. Nilå, M. Baibarac, A. Matea, R. Mitran, I. Baltog, Exciton-phonon interactions in the Cs<sub>3</sub>Bi<sub>2</sub>I<sub>9</sub> crystal structure revealed by Raman spectroscopic studies, *Phys. Status Solidi Basic Res.* 254 (2017), <https://doi.org/10.1002/psb.201552805>.
- [55] A.A. Ismail, S.A. Al-Sayari, D.W. Bahnemann, Photodeposition of precious metals onto mesoporous TiO<sub>2</sub> nanocrystals with enhanced their photocatalytic activity for methanol oxidation, *Catal. Today* 209 (2013) 2–7, <https://doi.org/10.1016/j.cattod.2012.09.027>.
- [56] T. Nash, The colorimetric estimation of formaldehyde by means of the hantzsch reaction, *Nature* 170 (1952) 976–977.
- [57] Y. Son, V. Mishin, W. Welsh, S.E. Lu, J.D. Laskin, H. Kipen, Q. Meng, A novel high-throughput approach to measure hydroxyl radicals induced by airborne particulate matter, *Int. J. Environ. Res. Public Health* 12 (2015) 13678–13695, <https://doi.org/10.3390/ijerph121113678>.
- [58] W. Li, R. Liang, A. Hu, Z. Huang, Y.N. Zhou, Generation of oxygen vacancies in visible light activated one-dimensional iodine TiO<sub>2</sub> photocatalysts, *RSC Adv.* 4 (2014) 36959–36966, <https://doi.org/10.1039/c4ra04768k>.
- [59] J. Pal, A. Bhunia, S. Chakraborty, S. Manna, S. Das, A. Dewan, S. Datta, A. Nag, Synthesis and optical properties of colloidal M<sub>3</sub>Bi<sub>2</sub>I<sub>9</sub> (M=Cs, Rb) perovskite nanocrystals, *J. Phys. Chem. C* 122 (2018), <https://doi.org/10.1021/acs.jpcc.8b03542>.
- [60] G.M. Paternò, N. Mishra, A.J. Barker, Z. Dang, G. Lanzani, L. Manna, A. Petrozza, Broadband defects emission and enhanced ligand Raman scattering in 0D Cs<sub>3</sub>Bi<sub>2</sub>I<sub>9</sub> colloidal nanocrystals, *Adv. Funct. Mater.* 29 (2019) 0–19, <https://doi.org/10.1002/adfm.201805299>.
- [61] M. Miyayachi, H. Irie, M. Liu, X. Qiu, H. Yu, K. Sumada, K. Hashimoto, Visible-light-sensitive photocatalysts: nanocluster-grafted titanium dioxide for indoor environmental remediation, *J. Phys. Chem. Lett.* 7 (2016) 75–84, <https://doi.org/10.1021/acs.jpclett.5b02041>.
- [62] F. Gao, Y. Yang, T. Wang, Preparation of porous TiO<sub>2</sub>/Ag heterostructure films with enhanced photocatalytic activity, *Chem. Eng. J.* 270 (2015) 418–427, <https://doi.org/10.1016/j.cej.2015.02.048>.
- [63] F. Bai, Y. Hu, Y. Hu, T. Qiu, X. Miao, S. Zhang, Lead-free, air-stable ultrathin Cs<sub>3</sub>Bi<sub>2</sub>I<sub>9</sub> perovskite nanosheets for solar cells, *Sol. Energy Mater. Sol. Cells* 184 (2018) 15–21, <https://doi.org/10.1016/j.solmat.2018.04.032>.
- [64] G. Colon, M.C. Hidalgo, J.A. Navio, Photocatalytic deactivation of commercial TiO<sub>2</sub> samples during simultaneous photoreduction of Cr(VI) and photooxidation of salicylic acid, *J. Photochem. Photobiol. A Chem.* 138 (2001) 79–85.
- [65] F. Ungureanu, R. Medianu, R. V. Ghita, C.C. Negrilă, P. Ghita, A.S. Manea, M. F. Lazarescu, P.O.B. Mg., Properties of TiO<sub>2</sub> Thin Films Prepared by Different Techniques, vol. 9, 2007, pp. 1457–1461.
- [66] H. Yan, X. Wang, M. Yao, X. Yao, Band structure design of semiconductors for enhanced photocatalytic activity: the case of TiO<sub>2</sub>, *Prog. Nat. Sci. Mater. Int.* 23 (2013) 402–407, <https://doi.org/10.1016/j.pnsc.2013.06.002>.
- [67] K. Sayama, H. Arakawa, Photocatalytic decomposition of water and photocatalytic reduction of carbon dioxide over zirconia catalyst, *J. Phys. Chem.* 97 (1993) 531–533, <https://doi.org/10.1021/j100105a001>.
- [68] W.P. Cardon, F. Gomes, On the determination of the flat-band potential of a semiconductor in contact with a metal or an electrolyte from the Mott-Schottky plot, *J. Phys. D Appl. Phys.* 11 (1978) 63–67.
- [69] Y. Nosaka, A.Y. Nosaka, Reconsideration of intrinsic band Alignments within anatase and rutile TiO<sub>2</sub>, *J. Phys. Chem. Lett.* 7 (2016) 431–434, <https://doi.org/10.1021/acs.jpclett.5b02804>.
- [70] W. Zhang, Z. Chen, S. Li, Dye-sensitized solar cells based on Bi<sub>4</sub>Ti<sub>3</sub>O<sub>12</sub>, *Int. J. Photoenergy* 2011 (2011) 3–8, <https://doi.org/10.1155/2011/821045>.
- [71] R. Beranek, (Photo)electrochemical methods for the determination of the band edge positions of TiO<sub>2</sub>-based nanomaterials, *Adv. Phys. Chem.* (2011), <https://doi.org/10.1155/2011/786759>, 2011.
- [72] O. Ola, M.M. Maroto-Valer, Review of material design and reactor engineering on TiO<sub>2</sub> photocatalysis for CO<sub>2</sub> reduction, *J. Photochem. Photobiol. C Photochem. Rev.* 24 (2015) 16–42, <https://doi.org/10.1016/j.jphotochemrev.2015.06.001>.
- [73] J.R. Guimarães, C.R. Turato Farah, M.G. Maniero, P.S. Fadini, Degradation of formaldehyde by advanced oxidation processes, *J. Environ. Manag.* 107 (2012) 96–101, <https://doi.org/10.1016/j.jenvman.2012.04.024>.
- [74] X. Fang, G. Mark, C. Von Sonntag, OH radical formation by ultrasound in aqueous solutions: Part I: the chemistry underlying the terephthalate dosimeter, *Ultrason. Sonochem.* 3 (1996) 57–63, [https://doi.org/10.1016/1350-4177\(95\)00032-1](https://doi.org/10.1016/1350-4177(95)00032-1).
- [75] D.H. Gonzalez, X.M. Kuang, J.A. Scott, G.O. Rocha, S.E. Paulson, Terephthalate probe for hydroxyl radicals: yield of 2-hydroxyterephthalic acid and transition metal interference, *Anal. Lett.* 51 (2018) 1–10, <https://doi.org/10.1080/00032719.2018.1431246>.
- [76] M. Sahni, B.R. Locke, Quantification of hydroxyl radicals produced in aqueous phase pulsed electrical discharge reactors, *Ind. Eng. Chem. Res.* 45 (2006) 5819–5825, <https://doi.org/10.1021/ie0601504>.



## **Publication V**

Bresolin, B.M., Sgarbossa, P., Bahnemann, D.W., and Sillanpää, M.  
**Cs<sub>3</sub>Bi<sub>2</sub>I<sub>9</sub>/g-C<sub>3</sub>N<sub>4</sub> as a new binary photocatalyst for efficient visible-light photocatalytic processes**

Reprinted with permission from  
*Separation and Purification Technology*  
Vol. 251 (117320), pp. 1-12, 2020  
© 2020, Elsevier





Contents lists available at ScienceDirect

## Separation and Purification Technology

journal homepage: [www.elsevier.com/locate/seppur](http://www.elsevier.com/locate/seppur)

## Cs<sub>3</sub>Bi<sub>2</sub>I<sub>9</sub>/g-C<sub>3</sub>N<sub>4</sub> as a new binary photocatalyst for efficient visible-light photocatalytic processes

Bianca-Maria Bresolin<sup>a,\*</sup>, Paolo Sgarbossa<sup>b</sup>, Detlef W. Bahnemann<sup>c,d,e</sup>, Mika Sillanpää<sup>f,g,h</sup>

<sup>a</sup> Laboratory of Green Chemistry, School of Engineering Science, Lappeenranta University of Technology, Sammonkatu 12, 50130 Mikkeli, Finland

<sup>b</sup> Dipartimento di Ingegneria Industriale, Università di Padova, Via Marzolo 9, 35131 Padova, Italy

<sup>c</sup> Institut für Technische Chemie, Leibniz Universität Hannover, Callinstr. 3, D-30167 Hannover, Germany

<sup>d</sup> Laboratory of Nano- and Quantum-Engineering (LNQE), Gottfried Wilhelm Leibniz University Hannover, Schneiderberg 39, D-30167 Hannover, Germany

<sup>e</sup> Laboratory "Photoactive Nanocomposite Materials", Saint-Petersburg State University, Ulyanovskaya str. 1, Peterhof, 198504 Saint-Petersburg, Russia

<sup>f</sup> Institute of Research and Development, Duy Tan University, De Nang 550000, Viet Nam

<sup>g</sup> Faculty of Environmental and Chemical Engineering, Duy Tan University, De Nang 550000, Viet Nam

<sup>h</sup> School of Civil Engineering and Surveying, Faculty of Health, Engineering and Science, University of Southern Queensland, West Street, Toowoomba 4350, QLD, Australia



## ARTICLE INFO

## Keywords:

Perovskite

Photocatalysis

Lead-free halide perovskite

Visible light

## ABSTRACT

Recently lead-free halide perovskite have shown great performances, especially in solar cell applications. On the other hand, graphitic carbon nitride g-C<sub>3</sub>N<sub>4</sub> materials have been rising interest thanks to the tunable electronic structure and excellent physicochemical stability, which could serve as an excellent candidate for photocatalytic applications. In our research, we tried to overcome the low charge transportation efficiency and chemical instability anchoring a cesium/bismuth-based perovskite on g-C<sub>3</sub>N<sub>4</sub> nanosheets to prepare composite photocatalyst based on nitrogen-iodine chemical bonding. Among different lead-free halide perovskite loads, the CNCSBI001 composite (g-C<sub>3</sub>N<sub>4</sub>:Cs<sub>3</sub>Bi<sub>2</sub>I<sub>9</sub> 10:0.1 w%) showed the better stability and an outstanding yield for photocatalytic degradation of organic compound in water solution under visible light irradiation. Hydrogen evolution test were also perform to test the activity of the synthesized compound under simulated solar light irradiation. The former study aim to provide insights on the use of halide perovskite-based Z-scheme photocatalyst for different photocatalytic applications.

## 1. Introduction

In the last centuries, the rapid development of urbanization and industrialization have led to two significant issues: an increase of global energy demand and a remarkable release of toxic and harmful chemical pollutants into the environment. To date, scientist have put enormous efforts to advance in sustainable and clean energy technologies to solve the aforementioned crises [1–5].

Among different technologies, photocatalytic processes over semiconductor surfaces have attracted particular attention in recent years as potentially efficient, environmentally friendly and low cost methods for environment remediation [6–9] as well as for renewable hydrogen production [8,10–12].

Light can be considered an ideal reagent for 'green' chemical processes due to its non-toxicity, it does not produce any waste, and it can be obtained from renewable sources. For this reason solar energy has attracted much interest because it is the most abundant and clean

source of energy, thus built artificial photosynthetic systems able to convert solar energy into chemical energy may be desirable.

Recently, graphitic carbon nitride (g-C<sub>3</sub>N<sub>4</sub>) has been worldwide labelled as a suitable candidate to be investigated as a potential next-generation materials for sustainable energy conversion and catalytic applications [13–15]. Among the advantageous properties of the g-C<sub>3</sub>N<sub>4</sub> nanostructures one can mention: the high surface area, the quantum efficiency, the separation and transport of the interfacial charge and the ease of modification through the formation of composites or the incorporation of surface functional groups [16]. Considering these outstanding features, there is a remarkable scientific effort seeking to couple it with other semiconductors to fabricate nanocomposites with excellent photocatalytic performance toward environmental remediation by improving charge carrier separation and transportation, prolonging the charge carrier lifetime, enlarging specific surface area and enhancing adsorption sites.

Recently, halide perovskite materials have attracted remarkable

\* Corresponding author at: Laboratory of Green Chemistry, School of Engineering Science, Lappeenranta University of Technology, Sammonkatu 12, 50130 Mikkeli, Finland.

E-mail address: [Bianca-maria.Bresolin@lut.fi](mailto:Bianca-maria.Bresolin@lut.fi) (B.-M. Bresolin).

<https://doi.org/10.1016/j.seppur.2020.117320>

Received 3 December 2019; Received in revised form 25 June 2020; Accepted 26 June 2020

Available online 03 July 2020

1383-5866/ © 2020 Elsevier B.V. All rights reserved.

interest in particular in photovoltaics and optoelectronic applications due to their unique efficiency. Some of the remarkable properties that make these materials promising candidates for photocatalytic applications are large absorption coefficients due to the favourable band gap, point defects, grain boundary and long electron-hole diffusion length that reduced electron-hole pair recombination [17]. Moreover, the synthesis of these materials is easily reproducible and low cost. In the past, lead halide perovskite showed the better efficiency as harvester of solar energy [18–23]. Unfortunately, this material showed instability especially in high humidity, the possible leaching of  $Pb^{2+}$  as bioavailable cation, make the lead-based material toxic and unsuitable especially for wastewater treatment. On contrary, bismuth-based perovskites promise good moisture and water stability [18,24–26].

In recent years, lead based halide perovskite/carbon based-materials such as graphene oxide or  $g-C_3N_4$  composites were found to be particularly active for photocatalytic  $CO_2$  reduction [23,27]. Built up composite photocatalysts by anchoring semiconductor-materials on  $g-C_3N_4$  is based on some important considerations. The band alignment between the interfaces of materials can facilitate charge separation and transportation [28,29]. Secondly,  $g-C_3N_4$  surface functionalization may enhance the interaction of particles with other materials. Thus, amino or carboxyl groups can perform strong chemical interactions stronger than physical adsorption. Moreover, the halide perovskite particles passivated by the graphitic carbon nitride surface is expected to be more stable in photoreaction [30,31]. This can be address to overcome instability towards water that is a challenge for common practical applications of halide perovskites.

So far, for fabrication of efficient modified photocatalysts, different strategies have been employed, especially, they have been addressed to increase the visible-light activity. Among them, much efforts have been spent in heterojunction construction and coupling synthesis of bismuth based nano-materials, but their potential has still to be thoroughly explored. Even though major advancements have been made to improve photocatalytic activity of Bi-based photocatalysts more efforts are still necessary [32].

In our work, we investigate a new potential composite photocatalyst  $g-C_3N_4/Cs_3Bi_2I_9$  for photocatalytic applications under visible light irradiation. Herein, we report a facile self-assembly synthesis of a  $g-C_3N_4/Cs_3Bi_2I_9$  Heterogeneous photocatalyst through their electrostatic interactions that facilitate the spontaneous assembly of the two charged components.

To the best of our knowledge, this is the first time that a  $g-C_3N_4/Cs_3Bi_2I_9$  hybrid structure is prepared and tested in photocatalytic application under visible light irradiation.

## 2. Materials and methods

### 2.0.1. Materials

All chemicals including dicyandiamide (99%), melamine (99%), Urea (> 99.5%), CsI (99.999%),  $BiI_3$  (99%), N,N-dimethylformamide (DMF, anhydrous, 99.8%) were purchased from Sigma-Aldrich and used without further purification. Deionized water was used during the preparation.

### 2.0.2. Preparation of $Cs_3Bi_2I_9$

The synthesis method of  $Cs_3Bi_2I_9$  is consistent with previous report [25]. Briefly,  $BiI_3$  and CsI were mixed (2:3 M ration) into a round bottom flask in DMF. The mixture was heated at 60 °C under magnetic stirring to the total evaporation of the solvent. Subsequently, the solid was washed three times with diethyl ether and water, dried to remove the residue of DMF. A shining red powder was obtained and kept in dark for further use. The elemental analysis of the dried sample indicated that very low C and N contents (2.1 wt% and 1.6 wt% respectively) were remaining in the final sample, implying that solvent

**Table 1**  
g- $C_3N_4$  synthesis yield.

Precursor	temperature °C/time h	name	yield $w_{final}/w_{initial}$ (%)
Urea	550 / 4	U/ $g-C_3N_4$	9.2
Melamine	550 / 4	M/ $g-C_3N_4$	54.6
Dicyanamide	550 / 4	D/ $g-C_3N_4$	52.6

molecules were largely removed.

### 2.0.3. Preparation of $g-C_3N_4$

The  $g-C_3N_4$  was synthesized according to previous reports [33,34]. In general,  $g-C_3N_4$  can be readily fabricated through a traditional thermal condensation. Different low-cost N-rich organic solid precursors can be used, such as urea, thiourea, melamine, dicyandiamide or cyanamide at 500–600°C in air or inert atmosphere. Herein,  $g-C_3N_4$  was prepared by heating directly in ceramic crucible. Briefly, the precursor was calcined for 2 h at 550 °C in a covered ceramic crucible. The U/ $g-C_3N_4$ , M/ $g-C_3N_4$  and D/ $g-C_3N_4$  were prepared as reported with urea, melamine or dicyanamide as precursors, respectively. All the yellow products were weighed before and after to measure the synthesis yield (Table 1).

The yields were evaluated to compare the efficiencies of the synthesis as optimization parameter. Thus, melamine was selected as precursor due to its higher synthesis yield.

### 2.0.4. Preparation of $Cs_3Bi_2I_9/g-C_3N_4$

Approximately 10 g of  $g-C_3N_4$  powder were dispersed in an appropriate amount of hexane and ultra-sonicated for 15 min. Then, a certain percentage of  $Cs_3Bi_2I_9$  was added to the suspension and ultra-sonicated for 30 min. Finally, the composites were obtained after centrifugation at 6000 rpm for 5 min followed by drying at 40 °C. The weight percentage of  $Cs_3Bi_2I_9$  with respect to  $g-C_3N_4$  was either 1 or 10 wt%, the corresponding sample is denoted as CNCsBI001 or CNCsBI01, respectively. The scheme of synthesis is shown in Fig. 1.

## 3. Characterization of the photocatalyst

### 3.1. Structural characterization

Diffuse reflectance spectra were recorded using a Cary 4000 spectrophotometer (Varian). XRD spectra of samples were collected using a PANalytical  $\theta/\theta$  diffractometer (CuK $\alpha$  radiation; 40 kV and 40 mA). The transmission IR spectra of the samples in KBr pellets are recorded on a Perkin-Elmer Spectrum 100 FTIR spectrophotometer in the region 400–4000  $cm^{-1}$ . Environmental scanning electron microscopy measurements were performed on Philips XL, 30-XRF-EDS embedded. Transmission electron microscopy analysis were performed with TECNAI FEI G2 microscope.

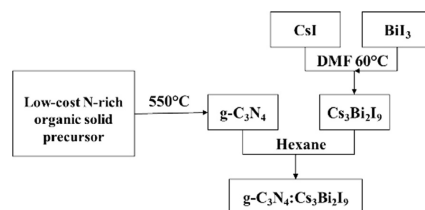


**Fig. 1.** Schematic illustration for the synthesis of the photocatalyst.

### 3.1.1. Photoelectrochemical measurements

The electrochemical and photoelectrochemical measurements were performed using a Zennium potentiostat and a PECC-2 photoelectrochemical cell (Zahner-Elektrik GmbH & Co. KG). The standard three-compartment cell used consisted of the working electrode, a Pt wire counter electrode and an Ag/AgCl reference electrode. 0.1 M Na<sub>2</sub>SO<sub>4</sub> was used as electrolyte solution at pH 7. The working electrode was prepared using doctor blade technique, annealed at 400 °C for 2 h in order to remove organic chemicals. Mott-Schottky measurements were performed at a frequency of 100 Hz and 5 mV of amplitude. During the polarization measurements the illumination source was chopped on and off with a frequency of 250 mHz. The light source was a solar simulator with a 300 W, 678 Wm<sup>-2</sup> Xenon lamp (LOT-Quantum Design GmbH) and an AM-1.5 G filter. IPCE, Incident photon to current conversion efficiency measurements, were carried out using a white LED (TLS, Zahner) coupled with a USB controlled monochromator in a wavelength range of 430–730 nm.

## 4. Photocatalytic application tests

### 4.1. Aqueous phase organic contaminant degradation

Initially, visible-light photocatalytic efficiency was investigated and compared on the treatment of some well known organic contaminants: Rhodamin B (RhB), Methylene Blue (MB), Methyl Orange (MO), and a mix of organic dyes simultaneously (MB and MO). In general, 0.5 g/L of the photocatalyst was suspended in 100 mL of aqueous solution containing different amount of organic contaminant. The suspension was maintained in dark condition for 60 min in order to reach the adsorption-desorption equilibrium. Afterwards, the suspension was irradiated using a **LED-visible light lamp** (A passively cooled VisiLight LED3 was used. The lamp assure environmentally friendly LED technology with flicker free illumination, 36 W power consumption, 730 lm luminous intensity). During the photocatalytic tests, 3 mL of the sample was taken at given time intervals and filtered to separate the catalyst (0.2 μm). The degradation results were monitored using a UV/vis spectrometer (Lambda 25, Perkin Elemer). As well known, dyes absorb visible-light photons (dye sensitization), thus photoexcited electrons may be injected into photocatalyst particles enhancing the photocatalytic activity. For further testing the photocatalytic activity of the as synthesized composite, methanol (MeOH) oxidation was evaluated. In a typical experiment, 1 g/L of catalyst was added in 75 mL of MeOH aqueous solution (100 mM). The suspension was stirred in the dark for 30 min to reach the adsorption-desorption equilibrium. During the photocatalytic tests, performed under **LED visible-lamp irradiation** (M455L3-455 nm, ThorLABS), 0.5 mL of the sample were taken at given time intervals and separated by filtration (0.2 μm) to remove the catalyst. The degradation of methanol was evaluated using the Hantzsch reaction with subsequent fluorescence analysis to quantify the amount of formaldehyde produced in an aqueous solution. This method, known as the Nash method, is widely used to determine formaldehyde concentrations. In brief, formaldehyde condenses with acetylacetone in the presence of an ammonium acetate as buffer, according to the Hantzsch reaction, to form 3,5-diacetyl-1,4-dihydropyridin (DDL). The former compound is fluorescence active and shows a band at 510 nm when excited at 405 nm. The fluorescence of DDL was measured in a well plate (Nunclon Delta Surface, Thermo Fisher Scientific Inc., USA) sample holder using a UV-visible spectrophotometer, 100 Bio, Cary.

#### 4.1.1. Hydrogen evolution

The prepared photocatalyst with Platinum deposit was used to conduct molecular hydrogen evolution photocatalysis under UV light irradiation (355 nm). The photo-deposition technique was applied to deposit 1 wt% platinum (Pt) on the samples. Hexachloroplatinic acid (H<sub>2</sub>PtCl<sub>6</sub> · 6H<sub>2</sub>O) was used as the Pt precursor, methanol was used as a reducing agent (10 vol./vol. % in water). The suspension was

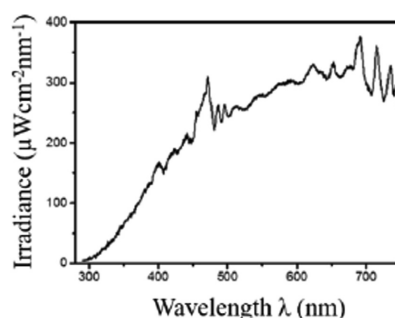


Fig. 2. Irradiance spectrum of the Xe lamp employed in the H<sub>2</sub> evolution measurements.

transferred into a closed reactor and placed under UV-light for 12 h with continuous stirring. The suspension was washed several times with water and subsequently with ethanol to remove non-deposited Pt. The sample was finally dried in an oven for 12 h at 90 °C.

In a typical experimental run, 6 mg of the photocatalyst were added into 6 mL of MeOH solution (10 vol%) used as a hole scavenger in a reactor of 12 mL. The suspension inside the photoreactor was degassed for 15 min with Ar to remove air, stirred for 30 min in the dark. Afterwards, the photoreactor was kept under 450 W Xe lamp equipped with a water-filter and aWG320-filter to block UV-B and UV-C. Samples were withdrawn at intervals of one hour. The spectral irradiance measured by a SprettraRad (BWTEK) irradiance meter is shown in Fig. 2. The increasing hydrogen content was measured hourly by using a gas chromatograph (Shimadzu 8A, Kyoto, Japan) equipped with a TCD detector and a 5 Å molecular sieve packed column. Along the experiments, Ar was used as the carrier gas.

## 5. Results and discussion

### 5.1. Catalyst characterization

Transmission electron microscope (TEM) and environmental scanning electron microscope (ESEM) images confirmed the successful synthesis of the composite photocatalysts and they are presented in Fig. 3.

To obtain an understanding of the interfacial interaction between g-C<sub>3</sub>N<sub>4</sub> and halide perovskite, the material was characterized by TEM. The layered structure of g-C<sub>3</sub>N<sub>4</sub> and the hexagonal structure type of Cs<sub>3</sub>Bi<sub>2</sub>I<sub>9</sub> were both confirmed. The Cs<sub>3</sub>Bi<sub>2</sub>I<sub>9</sub> particles of 45–50 nm in average size have relatively smooth surfaces which become rougher after the anchoring to the g-C<sub>3</sub>N<sub>4</sub> sheets (Fig. 3 A1-A3). The TEM picture of Fig. 3 A1-A3 show different lattice fringes of the as synthesized halide perovskite and the g-C<sub>3</sub>N<sub>4</sub> sheet, revealing the formation of the composite after the as performed synthesis. Moreover, TEM images confirmed that the composites exhibit similar morphology with that of bare g-C<sub>3</sub>N<sub>4</sub> nanosheets, indicating the structure of g-C<sub>3</sub>N<sub>4</sub> remains unchanged after the solvent treatment.

The ESEM images (Fig. 3B) reveal some important information. First, they confirm the presence of the two material, the lighter particles with higher molecular weights (Cs<sub>3</sub>Bi<sub>2</sub>I<sub>9</sub>) and lower (g-C<sub>3</sub>N<sub>4</sub>) in darker colors. The photographs of g-C<sub>3</sub>N<sub>4</sub> and the as prepared material are shown in Fig. 3C. It can be seen that the color of original g-C<sub>3</sub>N<sub>4</sub> is light yellow. However, after composition with the Cs<sub>3</sub>Bi<sub>2</sub>I<sub>9</sub> perovskite, the as-prepared CNCsBIO01 to CNCsBIO1 samples turn purple. This is consistent with the success of the synthesis.

EDS analysis confirm the nature of the darker material, mainly composed by C and N, as g-C<sub>3</sub>N<sub>4</sub>. On the contrary, by the punctual



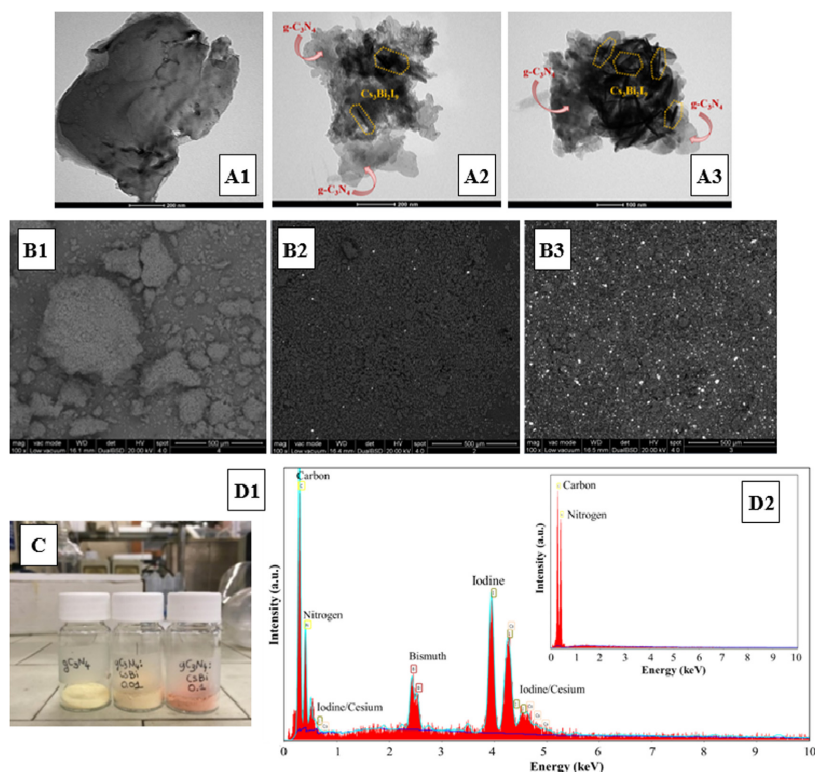


Fig. 3. A1) TEM image of  $g\text{-C}_3\text{N}_4$ , A2) CNCsBi001 and A3) CNCsBi01; B1) ESEM images of  $g\text{-C}_3\text{N}_4$ , B2) CNCsBi001 and B3) CNCsBi01; C) photograph of  $g\text{-C}_3\text{N}_4$ , CNCsBi001 and CNCsBi01; D1) EDS analysis CNCsBi001; D2) EDS analysis  $g\text{-C}_3\text{N}_4$ .

analysis on lighter spots the presence of the  $\text{Cs}_3\text{Bi}_2\text{I}_9$  was established. The elemental analysis are reported for the two material in Fig. 3 D1 and D2,  $g\text{-C}_3\text{N}_4$  and  $\text{Cs}_3\text{Bi}_2\text{I}_9$ , respectively. Secondly, the images clearly show the difference in between CNCsBi001 (Fig. 3 B1) and CNCsBi01 (Fig. 3 B2) in term of halide perovskite content, 1 and 10%, respectively.

XRD measurements reveal the detailed information on the purity and crystallinity of the samples. Fig. 4 shows the XRD patterns of the  $g\text{-C}_3\text{N}_4$ ,  $\text{Cs}_3\text{Bi}_2\text{I}_9$  and the composites in different molar ratios. All the samples were found to be well crystallized. The peaks of  $g\text{-C}_3\text{N}_4$  could be well indexed to reference (JCPDS 87-1526) [35]. Two distinct diffraction peaks at 12.99 and 27.80 and can be assigned to the corresponding (100) and (002) diffraction planes of the graphitic carbon nitride. The XRD pattern of  $\text{Cs}_3\text{Bi}_2\text{I}_9$  shows that all the peaks are well indexed to the orthorhombic hexagonal crystallographic phase with space group  $P63/mmc$  (194) and good crystallinity [25,36]. Moreover, Fig. 4 shows that diffraction peaks of both the halide perovskite and graphitic carbon nitride can be clearly identified in the heterojunction-based photocatalysts and the peak intensities of halide perovskite increase according to its content, 1 and 10%, respectively. The narrow sharp peaks suggest that the products are well crystallized. No impurity peaks were observed, which implies that the two materials were in pure phases in the composites.

Fig. 5A displays the FTIR spectra of the as synthesized materials in order to investigate their chemical bonding and understand the nature

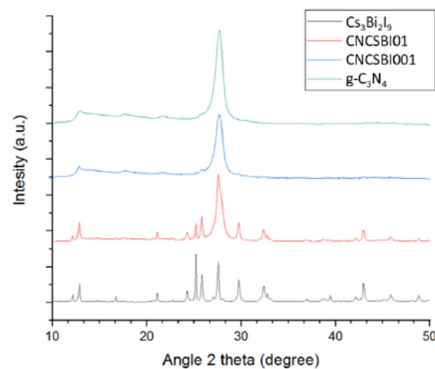


Fig. 4. XRD patterns of  $g\text{-C}_3\text{N}_4$ , CNCsBi001, CNCsBi01 and  $\text{Cs}_3\text{Bi}_2\text{I}_9$ .

of interaction between the two materials. The characteristic vibration peak of the pure graphitic carbon nitride appears at 808, 1245, 1322, 1574, and 1633  $\text{cm}^{-1}$ . The peak at 808  $\text{cm}^{-1}$  can be assigned to the triazine units, while those from 1245 to 1574  $\text{cm}^{-1}$  the stretching vibration of C–N heterocycles. The peaks at 1322  $\text{cm}^{-1}$  and 1633  $\text{cm}^{-1}$

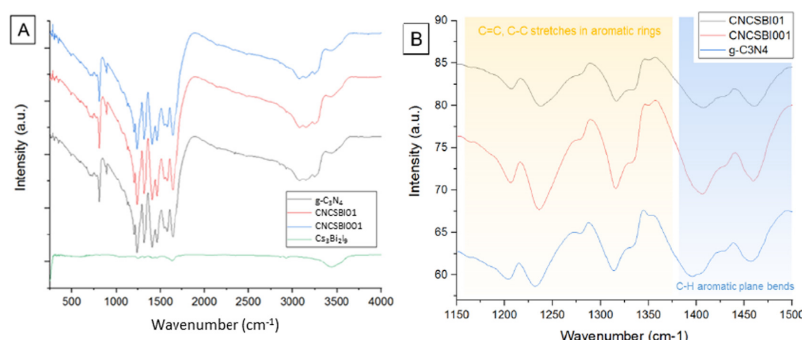


Fig. 5. A) FTIR spectra of  $g\text{-C}_3\text{N}_4$ , CNCsBi001, CNCsBi01 and  $\text{Cs}_3\text{Bi}_2\text{I}_9$ ; B) Zoom on specific regions of FTIR spectra of  $g\text{-C}_3\text{N}_4$ , CNCsBi001, CNCsBi01.

define the stretching mode of C–N and C=N bonds, respectively. The absorption band ranges between  $3000$  and  $3500\text{ cm}^{-1}$  shows the presence of chemical groups such as  $\text{NH}_x$  and OH. The absorption intensity in this range is slightly reduced when the perovskite was added to the system due to the substitutional chemical bonds between the two materials. All the FTIR spectra exhibit the characteristic peaks of  $g\text{-C}_3\text{N}_4$  meaning that no impurity or solvent residue absorption peaks were detected. Moreover, a zoom of the FTIR spectra from  $1150\text{ cm}^{-1}$  to  $1330\text{ cm}^{-1}$  shows systematically shifted of values with the introducing of lead-free perovskite in the graphitic carbon nitride framework (Fig. 5B). The absorption band ranges between  $1000\text{ cm}^{-1}$  and  $1300\text{ cm}^{-1}$  can be assigned to the aromatic plane C–H bending [37,38]. Furthermore, the ranges between  $1400\text{ cm}^{-1}$  and  $1600\text{ cm}^{-1}$  belong to C=C and C–C bond from aromatic rings [39,40]. This can be due to the chemical interactions between  $\text{Cs}_3\text{Bi}_2\text{I}_9$  and the surface of  $g\text{-C}_3\text{N}_4$  that increase the electron density of aromatic heterocycles. This can be considered an indication of bonding between the surface functional groups of the graphitic carbon nitride and the lead-free halide perovskite.

In order to understand the influence of  $\text{Cs}_3\text{Bi}_2\text{I}_9$  perovskite nanoparticles on the surface of  $g\text{-C}_3\text{N}_4$  nanosheets and to investigate the effect of the photocatalytic activity of the heterojunction, the BET surface area of bare  $g\text{-C}_3\text{N}_4$  and the heterojunctions have been investigated. The BET surface area of the as synthesized materials are  $6.30$ ,  $15.06$  and  $17.61\text{ m}^2\text{ g}^{-1}$  for  $g\text{-C}_3\text{N}_4$ , CNCsBi001 and CNCsBi01, respectively. The surface area measured for the bare  $\text{Cs}_3\text{Bi}_2\text{I}_9$  was found to be 10 times lower. However, upon coupling of  $g\text{-C}_3\text{N}_4$  nanosheets with the lead-free halide perovskite, the BET surface area of the resulting composites was enhanced. It can be assumed that, the increase in surface area may be induced by the exfoliation of  $g\text{-C}_3\text{N}_4$  in presence of perovskite material and during the ultrasonication process adopted in the synthesis. Thus, the high surface area of the photocatalysts synthesized can provide more reaction sites for the adsorption and degradation of pollutant molecules resulting in the enhancement of photocatalytic ability [41].

Two important parameters of the electronic structure that may affect the photocatalytic activity of semiconductors are the band gap that determine the photons absorption capacity and the flat band potential that affects the recombination probability. For the sake of understanding the mechanism of the electrocatalytic enhancement of the as synthesized heterojunctions DRS and Mott-Schottky measurements were conducted.

Fig. 6A shows the absorption spectra of the as synthesized materials in the range of  $350\text{--}800\text{ nm}$ . The results for the bare  $g\text{-C}_3\text{N}_4$  exhibited an absorption edge around  $470\text{ nm}$ . The pure  $\text{Cs}_3\text{Bi}_2\text{I}_9$  has a higher light absorption capacity in the visible region with a band edge around  $600\text{ nm}$ . Compared to the pure  $g\text{-C}_3\text{N}_4$ , all the composites exhibit a red

shift and a shoulder on the adsorption edge that means an increase in absorption in the visible region. The  $g\text{-C}_3\text{N}_4$  and  $\text{Cs}_3\text{Bi}_2\text{I}_9$  absorption edge can be clearly noticed in CNCsBi01. As expected, a significant increase light absorption intensity in the visible light can be related to the presence of the lead-free halide perovskite,  $\text{Cs}_3\text{Bi}_2\text{I}_9$ . The band gap was determined by the following equation:

$$\alpha h\nu = A(h\nu - E_g)^{n/2}$$

where  $\alpha$  is the optical absorption coefficient,  $h$  is the Planck constant,  $\nu$  is the light frequency,  $E_g$  is the band gap, and  $A$  is a constant. Both  $g\text{-C}_3\text{N}_4$  and  $\text{Cs}_3\text{Bi}_2\text{I}_9$  possess indirect transition band gaps [25,42,43], thus  $n$  is assigned accordingly. By extrapolating the straight line to the x-axis in this plot, the  $E_g$  of  $g\text{-C}_3\text{N}_4$  and  $\text{Cs}_3\text{Bi}_2\text{I}_9$  were estimated to be about  $2.68\text{ eV}$  and  $1.88\text{ eV}$  (as shown in Fig. 6B), respectively. The two material edges are clearly observed in the measurement performed on CNCsBi001 and CNCsBi01. It is important to mention that in general, the total absorption of the composite can be linked to an increases in the production of electron-hole pairs, resulting in a higher photocatalytic activity.

It is well known that semiconductors with unique band gap structure may have photoelectric properties that could convert light energy electricity. Fig. 7A shows the Mott-Schottky plots for the as synthesized materials. The measured area of the electrode is  $1.0\text{ cm}^2$ . As expected, all of the plots show a positive slope, meaning that all of the material-based electrodes were  $n$ -type semiconductors with electrons as the majority carriers. The intersection points of the potential and linear potential curves give the value of the flat band potential ( $V_{fb}$ ), which are approximately  $-1.21\text{ V}$ ,  $-1.61\text{ V}$  and  $-1.79\text{ V}$  versus Ag/AgCl for the graphitic carbon nitride, the heterojunctions and the bare perovskite, respectively. From the results it is theoretically expected that the as prepared heterojunctions may has a relatively stronger reduction ability, due to the negative shift of  $V_{fb}$ .

In order to investigate the photoactivity of the samples as a function of wavelength, IPCE (%) measurements were performed under illumination by an AM 1.5 G solar simulator. The results are shown in Fig. 7B. Compared with a negligible IPCE obtained for the pure  $g\text{-C}_3\text{N}_4$ , a remarkably increased IPCE was observed for all the materials, with a maximum of  $28\%$  around  $330\text{ nm}$  for CNCsBi01. On the basis of these findings, increased light absorption may not be the only reason for the improved IPCE, and the contribution of heterojunction effect needs also to be considered.

Fig. 7C shows the measured polarization curves of the as synthesized samples under chopped light illumination:  $g\text{-C}_3\text{N}_4$  (red), CNCsBi01 (purple), CNCsBi001 (blue) and  $\text{Cs}_3\text{Bi}_2\text{I}_9$  (grey). All the materials show anodic photocurrent, revealing an  $n$ -type response. In all cases, the photocurrent increases with the applied potential. The photoresponse of the samples increases with the content of lead-free

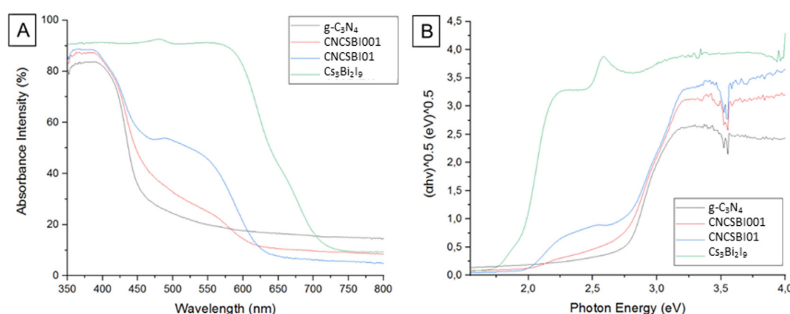


Fig. 6. UV-vis absorption spectra of  $Cs_3Bi_2I_9$ , CNCsBI001, CNCsBI01 and  $g-C_3N_4$ .

halide perovskite. Thus, it is reasonable to conclude that the enhancement of photocurrent measured can be mainly attributed to the presence of perovskite.

The improved charge carrier separation in the photocatalyst was investigated by EIS measurements confirming the effect on the kinetics of interfacial charge transfer between the two materials. The Nyquist plot the smaller arc radius corresponds to a lower charge transfer resistance, thus a better transfer capability. As shown in In Fig. 7D, the Nyquist plots of the as synthesized heterojunctions CNCsBI001 and CNCsBI01 shown smaller arc radius. A lower value of resistance leads to higher efficiency in charge transfer across the electrode/electrolyte interface. In these cases the charge recombination is reduced respect

the bare  $g-C_3N_4$ , thus the photocurrent response is higher. The reason for the more efficient charge transport could be the electron-phonon interaction of the two connected materials. The junction between two material can lead to an increase in charge mobility.

### 5.2. Performance of photocatalysis

Photocatalytic performance of the as synthesized materials were tested in comparison with the pure precursors, respectively  $Cs_3Bi_2I_9$  and  $g-C_3N_4$ . The photocatalytic activities of  $g-C_3N_4/Cs_3Bi_2I_9$  were measured by the degradation of different organic dyes in water solution under LED-visible light irradiation. Initially, the comparative photocatalytic

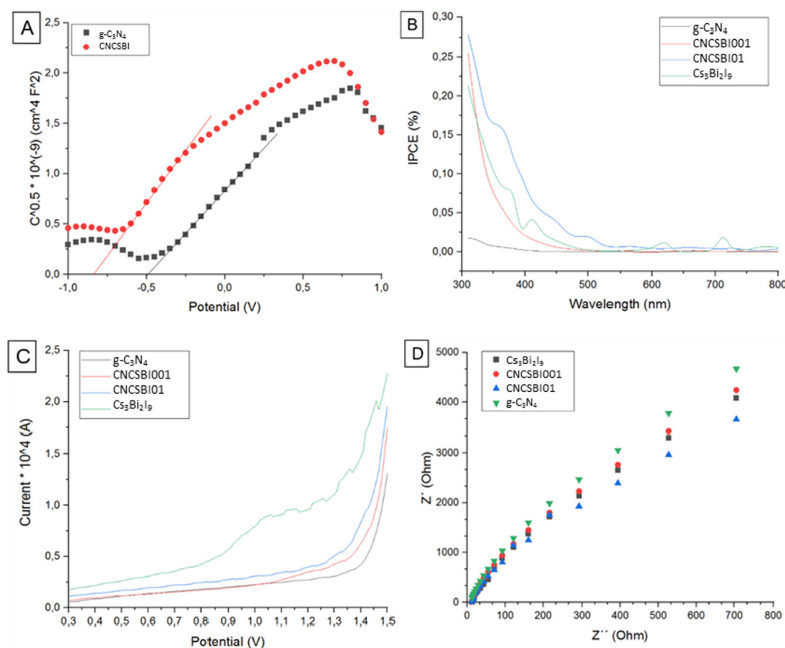
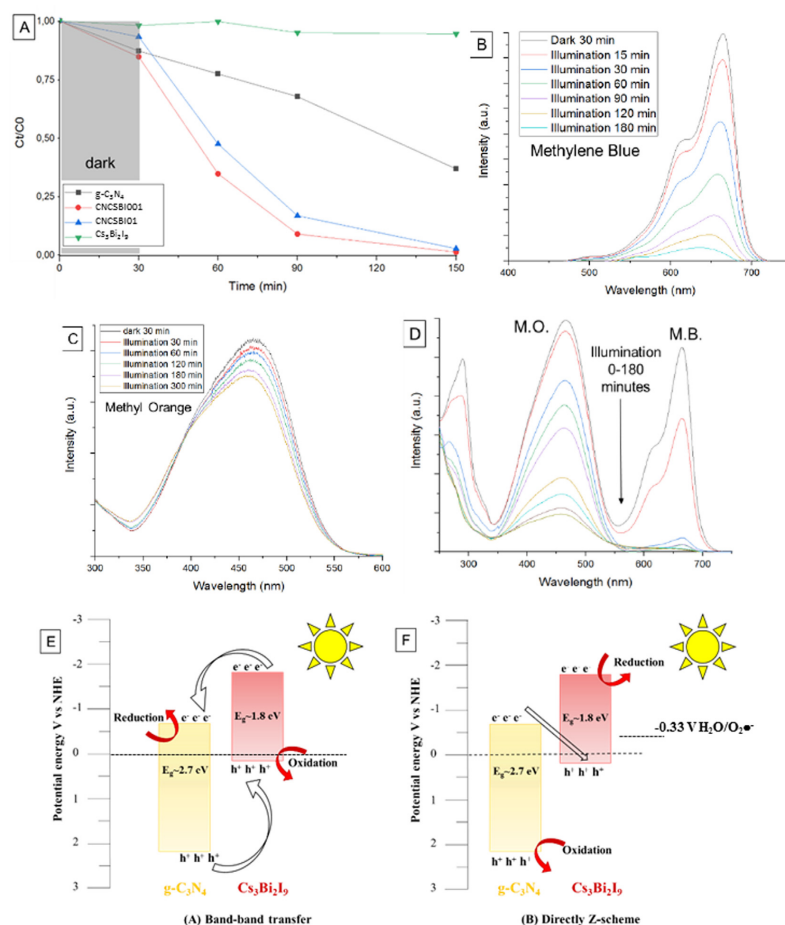


Fig. 7. A) Mott-Schottky analysis based on capacitance–voltage measurements for the samples. B) Incident photons to current efficiency for photoanodes recorded at a bias of 1.23 V vs. RHE for  $g-C_3N_4$ , CNCsBI001, CNCsBI01,  $Cs_3Bi_2I_9$ . C) Polarization curves for  $g-C_3N_4$ , CNCsBI001, CNCsBI01,  $Cs_3Bi_2I_9$  measured under 250 mHz chopped light illumination (under illumination by an AM 1.5 G solar simulator). D) Nyquist plots for  $g-C_3N_4$ , CNCsBI001, CNCsBI01,  $Cs_3Bi_2I_9$ .



**Fig. 8.** A) Comparison of RhB photodegradation by  $g\text{-C}_3\text{N}_4$ , CNCsBI001, CNCsBI01 and  $\text{Cs}_3\text{Bi}_2\text{I}_9$ ; B-C) Photodegradation of MB, and MO by CNCsBI001 under LED-visible light irradiation, respectively; D) Simultaneous photodegradation of MO and MB over CNCsBI001.

performance of the as synthesized materials was tested on RhB as probe-dye as a function of irradiation time. In Fig. 8A can be clearly seen that the CNCsBI001 has the higher efficiency respect the other materials, reaching about 100% of degradation after 120 min of visible-light irradiation. The adsorption ability of the as prepared photocatalysts in dark experiments was also investigated. In all cases, it is clearly noted a remarkable enhance of the adsorption rate of the target pollutant as the light was switched on. Initial adsorption experiments conducted in dark for 30 min demonstrated the adsorption on the surface of the material is minimal and could be neglected under irradiation conditions. When a higher amount of perovskite was loaded, the lower RhB degradation rate can be ascribed to charge recombination at the excessive defect sites on the surface of material that not coordinated to  $g\text{-C}_3\text{N}_4$ . The efficiency of photocatalytic activity of the photocatalyst was observed for a wide range of pollutants. Fig. 8B and C shows time-dependent photocatalytic degradation of MB ( $10\text{ mgL}^{-1}$ ), and MO ( $30\text{ mgL}^{-1}$ ), respectively, using a load of  $1\text{ gL}^{-1}$  of the as prepared

photocatalyst under LED-visible light irradiation. The figures show a total degradation of MB in 180 min and a partial degradation of MO in 300 min. A higher efficiency in MB degradation can be correlated with the type of available catalytic sites and the binding affinity of the substrates towards the selected organic dye. The results confirmed the photocatalytic ability of the material on the degradation of different types of organic dyes under visible-light irradiation. Finally, a mixture of dyes was used to investigate the photocatalytic efficiency of the as synthesized photocatalyst in complex systems. The maximum absorbance values of the chosen organic dyes do not change upon their mixing, allowing the simultaneous detection of the two contaminants [47,48]. Fig. 8D shows time-dependent photocatalytic degradation of MB ( $10\text{ mgL}^{-1}$ ) and MO ( $5\text{ mgL}^{-1}$ ) mixed in water solution. From the results, it was concluded that the mixture of the two organic dyes can be degraded effectively using the as synthesized material under visible-light irradiation in presence. The as described investigation was performed because the real dyes originating from various industries

typically consist of mixture of contaminants along with interfering substances.

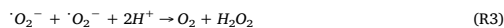
A suitable band structure is the key consideration in choosing coupled semiconductors for constructing effective photocatalysts. Based on the previous results the configuration of valence and conduction bands are presented in Fig. 8E-F. In the composite, the CB position of lead-free perovskite is more negative than that of the carbon-based material, and the graphitic carbon nitride VB has a more negative position. Two types photocatalytic contribution have been considered. If conventional II heterojunction system is considered, it may effectively separate photogenerated electron-hole pairs due to the staggered band structures of the component semiconductors, providing the higher activity respect the bare  $g\text{-C}_3\text{N}_4$  Fig. 8E. As an alternative a Z-scheme could be established where the electrons from the CB of  $g\text{-C}_3\text{N}_4$  combine with the holes from the VB of  $\text{Cs}_3\text{Bi}_2\text{I}_9$ , acting like scavengers Fig. 8F. The former double-charge transfer mechanism favors the charge separation, decreasing the potential energy of electrons and holes [44]. This configuration leads to a great reduction in charges recombination in the composite photocatalyst with the respect to the bare components, as shown in the photocurrent and charge-transfer resistance measurements (Fig. 7C-D). This mechanism is expected to lead to a higher photocatalytic activity [45,46] Fig. 8E.

A possible pathway of photocatalytic degradation of the organic dyes was proposed. As well known, in a typical photocatalytic process, charge carriers (electrons and holes) can be generated under light illumination (R1). When electrons and holes are separated, they can react with the hydroxyl ions and dissolved oxygen to produce hydroxyl free radicals and superoxide free radicals, as respectively reported in equations R(2) and R(3). The superoxide radicals may further react with protons and produce  $\text{H}_2\text{O}_2$  (R4). This reaction can be considered a secondary source for the formation of hydroxyl radicals (R5). The free radicals have a high oxidative capacity, thus and are capable of oxidizing organic compound such as RhB, MB and MO to the complete mineralization with the only release of  $\text{CO}_2$  and  $\text{H}_2\text{O}$  (R6). The system of equations is summarized as follows:

*Photogeneration of charge carriers*



*Formation of oxidative species*



*Mineralization of RhB*

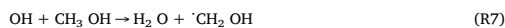


Previously, it has been reported that the  $\cdot\text{O}_2^-$ ,  $h^+$ , and  $\cdot\text{OH}$  are in general the major reactive species in photocatalytic oxidation treatments. In order to investigate the mechanism beyond the photocatalytic RhB degradation of the photocatalyst, different scavengers are used to explore the reactive species involved in the process. When the scavengers are added in the reaction solution they are able to selectively remove one of the reactive species. Therefore, based on the change in the photocatalytic efficiency it is possible to determine the active species in the photocatalytic treatment. It is well known that the ammonium oxalate (AO) can be added to remove hole ( $h^+$ ), iso-propanol (IPA) can be employed to impair the hydroxyl radical ( $\cdot\text{OH}$ ), while p-benzoquinone can be applied to reduce the superoxide radical ( $\cdot\text{O}_2^-$ ) [49–53]. The results of visible-light photocatalytic efficiency on RhB using CNCSBI001 as photocatalyst with various scavengers are shown in Fig. 9A. When the AO or IPA are added in the reaction solution, the photocatalytic efficiency remains almost invariable. Therefore, holes and hydroxyl radicals appear not to be the major reactive species. On the contrary, after the addition of BQ into the reaction solution, the

degradation efficiency of the probe dye remarkably decreases. Thus, based on the previous results, it is clear that  $\cdot\text{O}_2^-$  is the major reactive specie involved in the photocatalytic reaction system irradiated by LED visible-light. By considering the intrinsic and nonselective character of reactive oxygen radicals we attributed the cleavage of the RhB chromophore structure to attack of the dye, or its radical cations, by superoxide radicals. A possible photoreaction mechanism is summarized in Fig. 9B. According to previous study, N-deethylation process of RhB can be mainly induced by the produced superoxide radicals in the lead-free based photocatalytic system [54–56].

In order to investigate the photocatalytic efficiency of the as prepared materials, the formaldehyde concentration during the methanol oxidation was evaluated. The associated fluorescence spectra of the formed DDL are presented in Fig. 10A1. The measurement shows a continuous increase of formaldehyde concentration with reaction time. The longer irradiation time leads to a higher amount of formaldehyde in the bulk suspension. Fig. 10A2 shows the efficiency achieved after 4 h of irradiation with three different lamp: solar simulator, LED 406 nm and LED 455 nm. The maximum efficiency was achieved under solar light simulation irradiation due to the wide spectrum of light and higher intensity of the lamp. As previously reported for the organic dyes degradation (R1-R6), free radicals have been considered for their high oxidative capacity as main factors of methanol oxidation. In particular, the photogenerated free radicals are capable of oxidizing methanol by H-atom abstraction (R7). The resulted hydroxymethyl radicals can be further oxidized by the presence of oxygen and they can form formaldehyde (R8) [57].

## 6. Methanol oxidation to formaldehyde



The efficiency of the as synthesized material was further investigated for photochemical hydrogen production under solar light irradiation. The photocatalytic hydrogen evolution of the platinumized CNCSBI001 was evaluated in methanol:water solution. Under the former conditions, methanol reacts as holes scavenger and the electrons can be transferred to water and produce molecular hydrogen. The experiment was performed up to 6 h of irradiation and samples were withdraw every hour and the amount of evolved hydrogen was measured by gas chromatography at various (Fig. 10B1). As clearly depicted in the figure, continuous hydrogen production occurs from the beginning of the irradiation period.

Fig. 10B2 shows the comparison between pure  $g\text{-C}_3\text{N}_4$  and the as prepared photocatalyst. The pure  $g\text{-C}_3\text{N}_4$  sample shows solar-light photocatalytic activity with  $\text{H}_2$  evolution reaction (HER)  $496.85 \mu\text{mol g}^{-1} \text{h}^{-1}$ , attributable to the moderate bandgap and particular electronic structure of  $g\text{-C}_3\text{N}_4$ . After addition with metal halide perovskite, the photocatalytic activity of CNCSBI001 sample was improved of about 46% with a HER of about  $920.76 \mu\text{mol g}^{-1} \text{h}^{-1}$ . The enhancement of photocatalytic activity was attributed to the improvement of the light absorption and electro-chemical properties of the new designed material.

The consumption of MeOH, as a sacrificial agent, was confirmed by the detection of formaldehyde and a possible mechanism was proposed in the inset of the figure. Finally, in same condition, the hydrogen evolution was further confirmed under visible light irradiation LED 455 nm Fig. 10B3 over 4 h of illumination. The obtained results confirm the potential of the as prepared material in different photocatalytic applications.

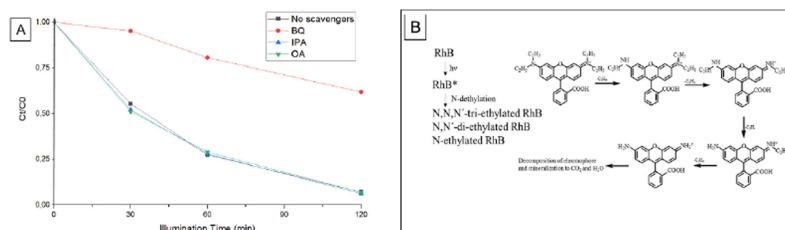


Fig. 9. Effect of the addition of different scavengers on the degradation of RhB over CNCsBI001.

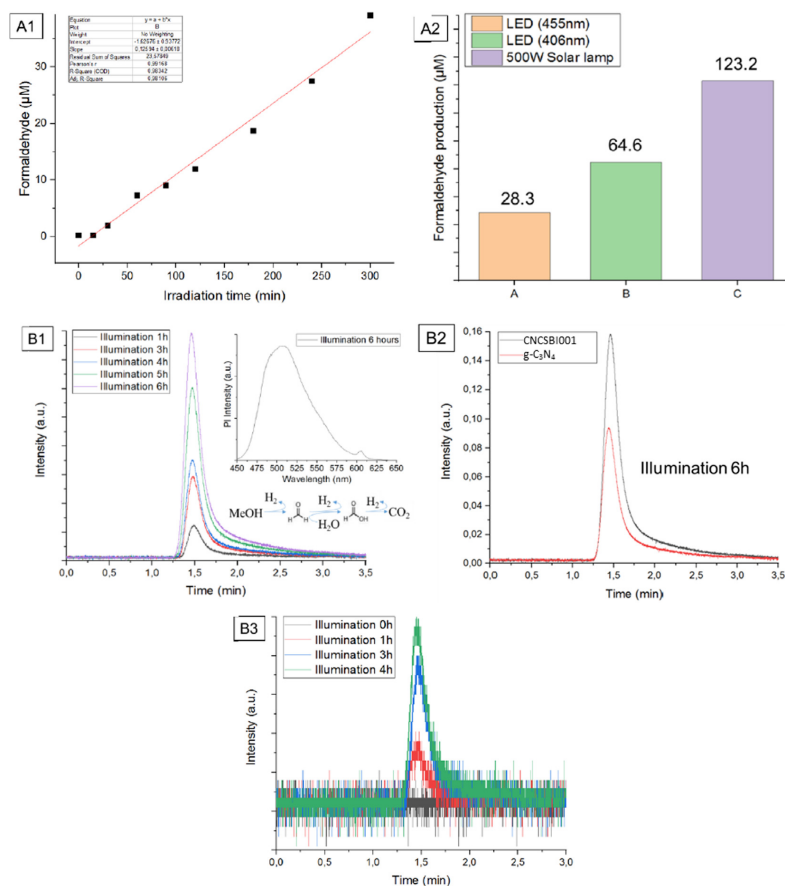


Fig. 10. A1) Oxidation of methanol express as enhance of formaldehyde concentration during visible light photocatalytic experiment under visible light irradiation (455 nm) of CNCsBI001; A2) Comparison of methanol oxidation using three lamps as different energy sources, (inset) Solar energy distribution; B1) Evidence of H<sub>2</sub> evolution, the H<sub>2</sub> peaks produced in GC over 6 h of illumination under solar simulator irradiation; B2) Comparison between activity of pure g-C<sub>3</sub>N<sub>4</sub> and the composite photocatalyst; B3) Evidence of H<sub>2</sub> evolution, the H<sub>2</sub> peaks produced in GC over 4 h of illumination under visible light irradiation LED 455 nm.

### 6.1. Recycle test

Photocatalytic stability of CNCsBI001 halide perovskite-modified graphitic carbon nitride was confirmed by the recycling tests. The

irradiation time of the three subsequent times cycles was performed and the degradation rate change was evaluated. The results shown in Fig. 11A confirm a negligible decrease in the rate of the process. After the last run, the powder was separated and dried, afterwards, the FTIR

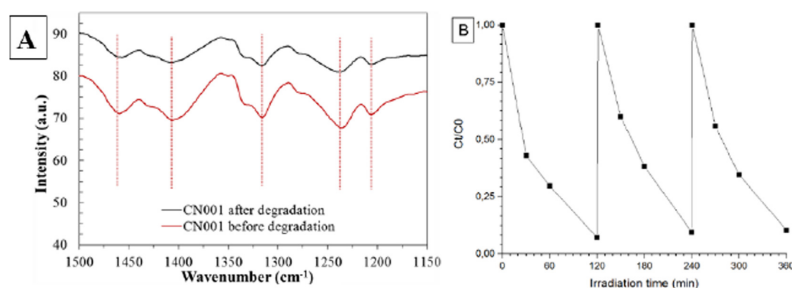


Fig. 11. A) Cycling tests of photocatalytic degradation RhB in CNCSBIO01 under visible light irradiation; B) FTIR spectra before and after degradation of RhB under visible-light irradiation.

spectrum of the samples was collected. As shown in Fig. 11B, the stability of the as synthesized new photocatalyst was confirmed, no significant or drastic change observed in the existing stretching and bending frequencies of spectrum before and after the degradation. The above achievements illustrated that the prepared material exhibited a good stability and high repeatable ability.

## 7. Conclusions

In recent years, designing visible-light-driven  $g\text{-C}_3\text{N}_4$  photocatalysts has been rising due to the tunable electronic structure and excellent physicochemical stability it has been shown that they can be excellent candidates in photocatalytic application. In our research, a new composite photocatalyst based on graphitic carbon nitride and lead-free perovskite  $g\text{-C}_3\text{N}_4/\text{Cs}_3\text{Bi}_2\text{I}_9$  was successfully prepared via a facile and reproducible wet chemical method. The accomplishment of the synthesis was evidenced by the morphological characterization of the composite. The as prepared photocatalyst exhibited enhanced photocatalytic performance in the degradation of RhB, MB, MO as well as for the mixture of selected dyes under LED-visible light illumination. The chemical trapping experiments confirmed that, especially for RhB  $\text{O}_2^{\cdot-}$  was the main active specie in the degradation process under visible light irradiation. Moreover, the as synthesized photocatalyst was found to possess a good stability and recyclability after repeated uses. The as prepared composite was found to be also suitable for visible light degradation of MeOH and  $\text{H}_2$  evolution under solar light illumination. The photocatalysts own a remarkably enhanced absorbance in the visible region, due to the narrow band gap of the lead-free perovskite.

The enhance in separation and transport efficiency of photoinduced electron-hole pairs in the photocatalyst were corroborated by photoelectrochemical measurements. The suppressed charge recombination and efficient charge transfer can be ascribed to the heterojunctions formation. The enhanced photocatalytic performance can be attributed to efficient direct scheme heterojunction with a remarkable high redox ability. The results obtained in this work confirm the feasibility of improving the photocatalytic performance of single semiconductors through the formation of composites. Moreover, our work aims to provide important new insights for fabricating composite photocatalysts based on lead-free perovskite material easy to prepare and with suitable properties for photocatalytic applications.

## CRedit authorship contribution statement

**Bianca-Maria Bresolin:** Conceptualization, Methodology, Validation, Formal analysis, Investigation, Data curation, Writing - original draft, Writing - review & editing, Visualization, Supervision. **Paolo Sgarbossa:** Resources, Writing - review & editing. **Detlef W. Bahnemann:** Resources, Supervision, Funding acquisition. **Mika**

**Sillanpää:** Resources, Supervision, Project administration, Funding acquisition.

## Declaration of Competing Interest

The authors declare that they have no known competing financial interests or personal relationships that could have appeared to influence the work reported in this paper.

## Acknowledgements

Maa-javesiteknikaan tuki foundation is gratefully acknowledged for the financial support. This research was supported by Saint-Petersburg State University via a research Grant ID 32706707. The authors thank the LNQE (Laboratory of Nano and Quantum Engineering, Hannover, Germany) and the Leibniz University for providing technical equipment and technological knowledge. BMB and PS wish to thank the Department of Industrial Engineering, Padova University, for partial financial support through the 'Investimento Strategico di Dipartimento-SID' grant (Progetto SGAR\_SID17\_01).

## Appendix A. Supplementary data

Supplementary data to this article can be found online at <https://doi.org/10.1016/j.seppur.2020.117320>.

## References

- [1] M.R. Hoffmann, S.T. Martin, W. Choi, D.W. Bahnemann, *Environmental Applications of Semiconductor Photocatalysis*, *Chem. Rev.* 95 (1995) 69.
- [2] A.O.T. Patrocínio, J. Schneider, M.D. França, L.M. Santos, B.P. Caixeta, A.E.H. Machado, D.W. Bahnemann, Charge carrier dynamics and photocatalytic behavior of  $\text{TiO}_2$  <math>\langle \text{inf} > 2 < /math>\langle \text{inf} > nanopowders submitted to hydrothermal or conventional heat treatment, *RSC Adv.* 5 (2015) 70536–70545, <https://doi.org/10.1039/c5ra13291f>.
- [3] D. Spasiano, R. Marotta, S. Malato, P. Fernandez-Ibañez, I. Di Somma, Solar photocatalysis: Materials, reactors, some commercial, and pre-industrialized applications. A comprehensive approach, *Appl. Catal. B Environ.* 170–171 (2015) 90–123, <https://doi.org/10.1016/j.apcatb.2014.12.050>.
- [4] T.S. Natarajan, H.C. Bajaj, R.J. Tayade, Enhanced direct sunlight photocatalytic oxidation of methanol using nanocrystalline  $\text{TiO}_2$  calcined at different temperature, *J. Nanoparticle Res.* 16 (2014) 2713, <https://doi.org/10.1007/s11051-014-2713-7>.
- [5] J. Kou, C. Lu, J. Wang, Y. Chen, Z. Xu, R.S. Varma, Selectivity Enhancement in Heterogeneous Photocatalytic Transformations, *Chem. Rev.* 117 (2017) 1445–1514, <https://doi.org/10.1021/acs.chemrev.6b00396>.
- [6] T.P. Yoon, M.A. Ischay, J. Du, Visible light photocatalysis as a greener approach to photochemical synthesis, *Nat. Chem.* 2 (2010) 527–532, <https://doi.org/10.1038/nchem.687>.
- [7] I.K. Konstantinou, T.A. Albanis,  $\text{TiO}_2$ -assisted photocatalytic degradation of azo dyes in aqueous solution: Kinetic and mechanistic investigations: A review, *Appl. Catal. B Environ.* 49 (2004) 1–14, <https://doi.org/10.1016/j.apcatb.2003.11.010>.
- [8] F.K. Kessler, Y. Zheng, D. Schwarz, C. Merschjann, W. Schnick, X. Wang, M.J. Bojdy, Functional carbon nitride materials-design strategies for electrochemical devices, *Nat. Rev. Mater.* 2 (2017), <https://doi.org/10.1038/natrevmats>.

- 2017.30.
- [9] X. Liu, M. Wang, S. Zhang, B. Pan, Application potential of carbon nanotubes in water treatment: A review, *J. Environ. Sci. (China)* 25 (2013) 1263–1280, [https://doi.org/10.1016/S1001-0742\(12\)60161-2](https://doi.org/10.1016/S1001-0742(12)60161-2).
  - [10] S. Chen, T. Takata, K. Domen, Particulate photocatalysts for overall water splitting, *Nat. Rev. Mater.* 2 (2017) 1–17, <https://doi.org/10.1038/natrevmats.2017.50>.
  - [11] J. Ran, W. Guo, H. Wang, B. Zhu, J. Yu, S.Z. Qiao, Metal-Free 2D/2D Phosphorene/g-C<sub>3</sub>N<sub>4</sub> Van der Waals Heterojunction for Highly Enhanced Visible-Light Photocatalytic H<sub>2</sub> Production, *Adv. Mater.* 30 (2018) 2–7, <https://doi.org/10.1002/adma.201800128>.
  - [12] J. Joy, J. Mathew, S.C. George, Nanomaterials for photoelectrochemical water splitting – review, *Int. J. Hydrogen Energy* 43 (2018) 4804–4817, <https://doi.org/10.1016/j.ijhydene.2018.01.099>.
  - [13] H. Zhang, L. Zhao, F. Geng, L.H. Guo, B. Wan, Y. Yang, Carbon dots decorated graphitic carbon nitride as an efficient metal-free photocatalyst for phenol degradation, *Appl. Catal. B Environ.* 180 (2016) 656–662, <https://doi.org/10.1016/j.apcatb.2015.06.056>.
  - [14] P. Qiu, H. Chen, F. Jiang, Cobalt modified mesoporous graphitic carbon nitride with enhanced visible-light photocatalytic activity, *RSC Adv.* 4 (2014) 39969–39977, <https://doi.org/10.1039/c4ra06451h>.
  - [15] S.M. Lam, J.C. Sin, A.R. Mohamed, A review on photocatalytic application of g-C<sub>3</sub>N<sub>4</sub>/semiconductor (CNS) nanocomposites towards the erasure of dyeing wastewater, *Mater. Sci. Semicond. Process.* 47 (2016) 62–84, <https://doi.org/10.1016/j.mssp.2016.02.019>.
  - [16] S. Kumar, S. Karthikeyan, A. Lee, g-C<sub>3</sub>N<sub>4</sub>-Based Nanomaterials for Visible Light-Driven Photocatalysis, *Catalysts* 8 (2018) 74, <https://doi.org/10.3390/catal8020074>.
  - [17] N.G. Park, M. Grätzel, T. Miyasaka, Organic-inorganic halide perovskite photo-voltaics: From fundamentals to device architectures, *Org. Halide Perovskite Photovoltaics From Fundam. to Device Archit.* 3 (2016) 1–366, <https://doi.org/10.1007/978-3-319-35114-8>.
  - [18] B. Lee, C.C. Stoumpos, N. Zhou, F. Hao, C. Malliakas, C.Y. Yeh, T.J. Marks, M.G. Kanatzidis, R.P.H. Chang, Air-stable molecular semiconducting iodosalts for solar cell applications: Cs<sub>2</sub>NiI<sub>6</sub> as a hole conductor, *J. Am. Chem. Soc.* 136 (2014) 15379–15385, <https://doi.org/10.1021/ja508464w>.
  - [19] A. Kojima, K. Teshima, Y. Shirai, T. Miyasaka, Organometal Halide Perovskites as Visible-Light Sensitizers for Photovoltaic Cells, *J. Am. Chem. Soc.* 131 (2009) 6050–6051, <https://doi.org/10.1021/ja809598r>.
  - [20] M.A. Pérez-Osorio, R.L. Milot, M.R. Filip, J.B. Patel, L.M. Herz, M.B. Johnston, F. Giustino, Vibrational Properties of the Organic-Inorganic Halide Perovskite CH<sub>3</sub>NH<sub>3</sub>PbI<sub>3</sub> from Theory and Experiment: Factor Group Analysis, First-Principles Calculations, and Low-Temperature Infrared Spectra, *J. Phys. Chem. C* 119 (2015) 25703–25718, <https://doi.org/10.1021/acs.jpcc.5b07432>.
  - [21] A. Dualeh, T. Moehl, N. Tetreault, J. Teuscher, P. Gao, M.K. Nazeeruddin, M. Grätzel, Impedance spectroscopic analysis of lead iodide perovskite-sensitized solid-state solar cells, *ACS Nano* 8 (2014) 362–373, <https://doi.org/10.1021/nn404323g>.
  - [22] H. Zai, C. Zhu, H. Xie, Y. Zhao, C. Shi, Z. Chen, X. Ke, M. Sui, C. Chen, J. Hu, Q. Zhang, Y. Gao, H. Zhou, Y. Li, Q. Chen, Congenetic Incorporation of CsPbBr<sub>3</sub> Nanocrystals in a Hybrid Perovskite Heterojunction for Photovoltaic Efficiency Enhancement, *ACS Energy Lett.* 3 (2018) 30–38, <https://doi.org/10.1021/acsenenergylett.7b00925>.
  - [23] Y.F. Xu, M.Z. Yang, B.X. Chen, X.D. Wang, H.Y. Chen, D. Bin Kuang, C.Y. Su, A CsPbBr<sub>3</sub> Perovskite Quantum Dot/Graphene Oxide Composite for Photocatalytic CO<sub>2</sub> Reduction, *J. Am. Chem. Soc.* 139 (2017) 5660–5663, <https://doi.org/10.1021/jacs.7b00489>.
  - [24] N.K. Noel, S.D. Stranks, A. Abate, C. Wehrenfennig, S. Guarnera, A.-A. Haghighirad, A. Sadhanala, G.E. Eperon, S.K. Pathak, M.B. Johnston, A. Petrozza, L.M. Herz, H.J. Snaith, Lead-free organic-inorganic tin halide perovskites for photovoltaic applications, *Energy Environ. Sci.* 7 (2014) 3061–3068, <https://doi.org/10.1039/C4EE01076K>.
  - [25] B.W. Park, B. Philippe, X. Zhang, H. Rensmo, G. Boschloo, E.M.J. Johansson, Bismuth Based Hybrid Perovskites A<sub>3</sub>Bi<sub>2</sub>I<sub>9</sub> (A: Methylammonium or Cesium) for Solar Cell Application, *Adv. Mater.* 27 (2015) 6806–6813, <https://doi.org/10.1002/adma.201501978>.
  - [26] C. Cuhadar, S.-G. Kim, J.-M. Yang, J.-Y. Seo, D. Lee, N.-G. Park, All-Inorganic Bismuth Halide Perovskite-Like Materials A<sub>3</sub>Bi<sub>2</sub>I<sub>9</sub> and A<sub>3</sub>Bi<sub>2</sub>Br<sub>9</sub> (A = Rb and Cs) for Low-Voltage Switching Resistive Memory, *ACS Appl. Mater. Interfaces* 10 (35) (2018) 29741–29749, <https://doi.org/10.1021/acsami.8b07103>.
  - [27] M. Ou, W. Tu, S. Yin, W. Xing, S. Wu, H. Wang, S. Wan, Q. Zhong, R. Xu, Amino-Assisted Anchoring of CsPbBr<sub>3</sub> Perovskite Quantum Dots on Porous g-C<sub>3</sub>N<sub>4</sub> for Enhanced Photocatalytic CO<sub>2</sub> Reduction, *Angew. Chemie - Int. Ed.* 57 (2018) 13570–13574, <https://doi.org/10.1002/anie.201808930>.
  - [28] L. Shi, T. Wang, H. Zhang, K. Chang, J. Ye, Electrostatic Self-Assembly of Nanosized Carbon Nitride Nanosheet onto a Zirconium Metal-Organic Framework for Enhanced Photocatalytic CO<sub>2</sub> Reduction, *Adv. Funct. Mater.* 25 (2015) 5360–5367, <https://doi.org/10.1002/adfm.201502253>.
  - [29] W. Tu, Y. Xu, J. Wang, B. Zhang, T. Zhou, S. Yin, S. Wu, C. Li, Y. Huang, Y. Zhou, Z. Zou, J. Robertson, M. Kraft, R. Xu, Investigating the Role of Tunable Nitrogen Vacancies in Graphitic Carbon Nitride Nanosheets for Efficient Visible-Light-Driven H<sub>2</sub> Evolution and CO<sub>2</sub> Reduction, *ACS Sustain. Chem. Eng.* 5 (2017) 7260–7268, <https://doi.org/10.1021/acsschemeng.7b01477>.
  - [30] X. Li, Y. Wang, H. Sun, H. Zeng, Amino-Mediated Anchoring Perovskite Quantum Dots for Stable and Low-Threshold Random Lasing, *Adv. Mater.* 29 (2017) 1–9, <https://doi.org/10.1002/adma.201701185>.
  - [31] J. De Roo, M. Ibáñez, P. Geiregat, G. Nedelcu, W. Walravens, J. Maes, J.C. Martins, I. Van Driessche, M.V. Kovalenko, Z. Hens, Highly Dynamic Ligand Binding and Light Absorption Coefficient of Cesium Lead Bromide Perovskite Nanocrystals, *ACS Nano* 10 (2016) 2071–2081, <https://doi.org/10.1021/acsnano.5b06295>.
  - [32] K. Sharma, V. Dutta, S. Sharma, P. Raizada, A. Hosseini-Bandegharai, P. Thakur, P. Singh, Recent advances in enhanced photocatalytic activity of bismuth oxhyalides for efficient photocatalysis of organic pollutants in water: A review, *J. Ind. Eng. Chem.* 78 (2019) 1–20, <https://doi.org/10.1016/j.jiec.2019.06.022>.
  - [33] M. Zhang, J. Xu, R. Zong, Y. Zhu, Enhancement of visible light photocatalytic activities via porous structure of g-C<sub>3</sub>N<sub>4</sub>, *Appl. Catal. B Environ.* 147 (2014) 229–235, <https://doi.org/10.1016/j.apcatb.2013.09.002>.
  - [34] S.C. Yan, Z.S. Li, Z.G. Zou, Photodegradation performance of g-C<sub>3</sub>N<sub>4</sub> fabricated by directly heating melamine, *Langmuir* 25 (2009) 10397–10401, <https://doi.org/10.1021/la900923z>.
  - [35] N. Tian, H. Huang, Y. He, Y. Guo, Y. Zhang, Novel g-C<sub>3</sub>N<sub>4</sub>/BiO<sub>4</sub> heterojunction photocatalysts: Synthesis, characterization and enhanced visible-light-responsive photocatalytic activity, *RSC Adv.* 4 (2014) 42716–42722, <https://doi.org/10.1039/c4ra05917d>.
  - [36] J. Pal, A. Bhunia, S. Chakraborty, S. Manna, S. Das, A. Dewan, S. Datta, A. Nag, Synthesis and Physical Properties of Colloidal M<sub>3</sub>Bi<sub>2</sub>I<sub>9</sub> (M = Cs, Rb) Perovskite Nanocrystals, *J. Phys. Chem. C* 122 (2018), <https://doi.org/10.1021/acs.jpcc.8b03542>.
  - [37] J.C. Bailar, N. Ch. INFRARED SPECTRA OF 36 (1974).
  - [38] Y. Cai, J. Lv, J. Feng, Spectral Characterization of Four Kinds of Biodegradable Plastics: Poly (Lactic Acid), Poly (Butylenes Adipate-Co-Terephthalate), Poly (Hydroxybutyrate-Co-Hydroxyvalerate) and Poly (Butylenes Succinate) with FTIR and Raman Spectroscopy, *J. Polym. Environ.* 21 (2013) 108–114, <https://doi.org/10.1007/s10924-012-0534-2>.
  - [39] S. Krzemińska, L. Lipińska, M. Woluntarski, M. Oleksy, C. Ślusarczyk, W. Biniś, A. Smejda-Krzewicka, Hybrid XNBR composites with carbon and aluminosilicate nanofillers, (2019). <http://doi.org/10.1007/s00289-019-02825-9>.
  - [40] Y. Joon, J. Joon, Y. Il, J. Kook, H. Na, J. Kim, S. Bin, Oxygen functional groups and electrochemical capacitive behavior of incompletely reduced graphene oxides as a thin-film electrode of supercapacitor, *Electrochim. Acta* 116 (2014) 118–128, <https://doi.org/10.1016/j.electacta.2013.11.040>.
  - [41] P. Shandilya, D. Mittal, M. Soni, P. Raizada, A. Hosseini-Bandegharai, A.K. Saini, P. Singh, Fabrication of fluorine doped graphene and SmVO<sub>4</sub> based dispersed and adsorptive photocatalyst for abatement of phenolic compounds from water and bacterial disinfection, *J. Clean. Prod.* 203 (2018) 386–399, <https://doi.org/10.1016/j.jclepro.2018.08.271>.
  - [42] Y. Yang, W. Guo, Y. Guo, Y. Zhao, X. Yuan, Y. Guo, Fabrication of Z-scheme plasmonic photocatalyst Ag@AgBr/g-C<sub>3</sub>N<sub>4</sub> with enhanced visible-light photocatalytic activity, *J. Hazard. Mater.* 271 (2014) 150–159, <https://doi.org/10.1016/j.jhazmat.2014.02.023>.
  - [43] A.J. Lehner, D.H. Fabin, H.A. Evans, C.A. Hébert, S.R. Smock, J. Hu, H. Wang, J.W. Zwanziger, M.L. Chabiny, R. Seshadri, Crystal and Electronic Structures of Complex Bismuth Iodides A<sub>3</sub>Bi<sub>2</sub>I<sub>9</sub> (A = K, Rb, Cs) Related to Perovskite: Aiding the Rational Design of Photovoltaics, *Chem. Mater.* 27 (2015) 7137–7148, <https://doi.org/10.1021/acs.chemmater.5b03147>.
  - [44] M. Aguirre, Matias; Zhou, Ruixin; Eugene, Alexis; Guzman, Marcelo; Grella, Cu<sub>2</sub>O/TiO<sub>2</sub> heterostructure for CO<sub>2</sub> reduction through a direct Z-scheme: Protecting Cu<sub>2</sub>O from photocorrosion, *Appl. Catal. B Environ.* 217 (2017) 485–493, <https://doi.org/10.1016/j.apcatb.2017.05.058>.
  - [45] P. Raizada, A. Sudhaik, P. Singh, A. Hosseini-Bandegharai, P. Thakur, Converting type II AgBr/VO into ternary Z scheme photocatalyst via coupling with phosphorus doped g-C<sub>3</sub>N<sub>4</sub> for enhanced photocatalytic activity, *Sep. Purif. Technol.* 227 (2019) 115692, <https://doi.org/10.1016/j.seppur.2019.115692>.
  - [46] P. Raizada, A. Sudhaik, P. Singh, P. Shandilya, V.K. Gupta, A. Hosseini-Bandegharai, S. Agrawal, Ag<sub>3</sub>PO<sub>4</sub> modified phosphorus and sulphur co-doped graphitic carbon nitride as a direct Z-scheme photocatalyst for 2, 4-dimethyl phenol degradation, *J. Photochem. Photobiol. A Chem.* 374 (2019) 22–35, <https://doi.org/10.1016/j.jphotochem.2019.01.015>.
  - [47] P. Wongkulasin, S. Chavadej, T. Sreethawong, Photocatalytic degradation of mixed azo dyes in aqueous wastewater using mesoporous-assembled TiO<sub>2</sub> nanocrystal synthesized by a modified sol-gel process, *Colloids Surfaces A Physicochem. Eng. Asp.* 384 (2011) 519–528, <https://doi.org/10.1016/j.colsurfa.2011.05.022>.
  - [48] A.K. Gupta, A. Pal, C. Sahoo, Photocatalytic degradation of a mixture of Crystal Violet (Basic Violet 3) and Methyl Red dye in aqueous suspensions using Ag + doped TiO<sub>2</sub>, *Dye. Pigment.* 69 (2006) 224–232, <https://doi.org/10.1016/j.dyepig.2005.04.001>.
  - [49] S. Chen, Y. Hu, S. Meng, X. Fu, Study on the separation mechanisms of photo-generated electrons and holes for composite photocatalysts g-C<sub>3</sub>N<sub>4</sub>-WO<sub>3</sub>, *Appl. Catal. B Environ.* 150–151 (2014) 564–573, <https://doi.org/10.1016/j.apcatb.2013.12.053>.
  - [50] X. Ding, X. Song, P. Li, Z. Ai, L. Zhang, Efficient visible light driven photocatalytic removal of NO with aerosol flow synthesized Bi<sub>2</sub>N-codoped TiO<sub>2</sub> hollow spheres, *J. Hazard. Mater.* 190 (2011) 604–612, <https://doi.org/10.1016/j.jhazmat.2011.03.099>.
  - [51] Z. He, Y. Shi, C. Gao, L. Wen, J. Chen, S. Song, BiOCl/BiVO<sub>4</sub> p-n Heterojunction with Enhanced Photocatalytic Activity under Visible-Light Irradiation, *J. Phys. Chem. C* 118 (2014) 389–398, <https://doi.org/10.1021/jp409598s>.
  - [52] M. Mousavi, A. Habibi-Yangjeh, Magnetically separable ternary g-C<sub>3</sub>N<sub>4</sub>/Fe<sub>3</sub>O<sub>4</sub>/BiOI nanocomposites: Novel visible-light-driven photocatalysts based on graphitic carbon nitride, *J. Colloid Interface Sci.* 465 (2016) 83–92, <https://doi.org/10.1016/j.jcis.2015.11.057>.



- [53] J. Wang, L. Tang, G. Zeng, Y. Deng, Y. Liu, L. Wang, Y. Zhou, Z. Guo, J. Wang, C. Zhang, *Applied Catalysis B: Environmental* Atomic scale g-C<sub>3</sub>N<sub>4</sub> / Bi<sub>2</sub>WO<sub>6</sub> 2D / 2D heterojunction with enhanced photocatalytic degradation of ibuprofen under visible light irradiation, *Appl. Catal. B, Environ.* 209 (2017) 285–294, <https://doi.org/10.1016/j.apcatb.2017.03.019>.
- [54] J. Jin, Q. Liang, C. Ding, Z. Li, S. Xu, Simultaneous synthesis-immobilization of Ag nanoparticles functionalized 2D g-C<sub>3</sub>N<sub>4</sub> nanosheets with improved photocatalytic activity, *J. Alloys Compd.* 691 (2017) 763–771, <https://doi.org/10.1016/j.jallcom.2016.08.302>.
- [55] H. Liang, S. Liu, H. Zhang, X. Wang, J. Wang, New insight into the selective photocatalytic oxidation of RhB through a strategy of modulating radical generation, *RSC Adv.* 8 (2018) 13625–13634, <https://doi.org/10.1039/c8ra0181810>.
- [56] X. Hu, T. Mohamood, W. Ma, C. Chen, J. Zhao, Oxidative decomposition of rhodamine B dye in the presence of VO<sup>2+</sup> and/or Pt(IV) under visible light irradiation: N-deethylation, chromophore cleavage, and mineralization, *J. Phys. Chem. B.* 110 (2006) 26012–26018, <https://doi.org/10.1021/jp0635588q>.
- [57] C. yi Wang, J. Rabani, D.W. Bahnemann, J.K. Dohrmann, Photonic efficiency and quantum yield of formaldehyde formation from methanol in the presence of various TiO<sub>2</sub> photocatalysts, *J. Photochem. Photobiol. A Chem.* 148 (2002) 169–176, [https://doi.org/10.1016/S1010-6030\(02\)00087-4](https://doi.org/10.1016/S1010-6030(02)00087-4).

## ACTA UNIVERSITATIS LAPPEENRANTAENSIS

909. NEISI, NEDA. Dynamic and thermal modeling of touch-down bearings considering bearing non-idealities. 2020. Diss.
910. YAN, FANGPING. The deposition and light absorption property of carbonaceous matter in the Himalayas and Tibetan Plateau. 2020. Diss.
911. NJOCK BAYOCK, FRANCOIS MITERAND. Thermal analysis of dissimilar weld joints of high-strength and ultra-high-strength steels. 2020. Diss.
912. KINNUNEN, SINI-KAISU. Modelling the value of fleet data in the ecosystems of asset management. 2020. Diss.
913. MUSIKKA, TATU. Usability and limitations of behavioural component models in IGBT short-circuit modelling. 2020. Diss.
914. SHNAI, IULIIA. The technology of flipped classroom: assessments, resources and systematic design. 2020. Diss.
915. SAFAEI, ZAHRA. Application of differential ion mobility spectrometry for detection of water pollutants. 2020. Diss.
916. FILIMONOV, ROMAN. Computational fluid dynamics as a tool for process engineering. 2020. Diss.
917. VIRTANEN, TIINA. Real-time monitoring of membrane fouling caused by phenolic compounds. 2020. Diss.
918. AZZUNI, ABDELRAHMAN. Energy security evaluation for the present and the future on a global level. 2020. Diss.
919. NOKELAINEN, JOHANNES. Interplay of local moments and itinerant electrons. 2020. Diss.
920. HONKANEN, JARI. Control design issues in grid-connected single-phase converters, with the focus on power factor correction. 2020. Diss.
921. KEMPPINEN, JUHA. The development and implementation of the clinical decision support system for integrated mental and addiction care. 2020. Diss.
922. KORHONEN, SATU. The journeys of becoming and being an international entrepreneur: A narrative inquiry of the "I" in international entrepreneurship. 2020. Diss.
923. SIRKIÄ, JUUKA. Leveraging digitalization opportunities to improve the business model. 2020. Diss.
924. SHEMYAKIN, VLADIMIR. Parameter estimation of large-scale chaotic systems. 2020. Diss.
925. AALTONEN, PÄIVI. Exploring novelty in the internationalization process - understanding disruptive events. 2020. Diss.
926. VADANA, IUSTIN. Internationalization of born-digital companies. 2020. Diss.
927. FARFAN OROZCO, FRANCISCO JAVIER. In-depth analysis of the global power infrastructure - Opportunities for sustainable evolution of the power sector. 2020. Diss.

928. KRAINOV, IGOR. Properties of exchange interactions in magnetic semiconductors. 2020. Diss.
929. KARPPANEN, JANNE. Assessing the applicability of low voltage direct current in electricity distribution - Key factors and design aspects. 2020. Diss.
930. NIEMINEN, HARRI. Power-to-methanol via membrane contactor-based CO<sub>2</sub> capture and low-temperature chemical synthesis. 2020. Diss.
931. CALDERA, UPEKSHA. The role of renewable energy based seawater reverse osmosis (SWRO) in meeting the global water challenges in the decades to come. 2020. Diss.
932. KIVISTÖ, TIMO. Processes and tools to promote community benefits in public procurement. 2020. Diss.
933. NAQVI, BILAL. Towards aligning security and usability during the system development lifecycle. 2020. Diss.
934. XIN, YAN. Knowledge sharing and reuse in product-service systems with a product lifecycle perspective. 2020. Diss.
935. PALACIN SILVA, VICTORIA. Participation in digital citizen science. 2020. Diss.
936. PUOLAKKA, TIINA. Managing operations in professional organisations – interplay between professionals and managers in court workflow control. 2020. Diss.
937. AHOLA, ANTTI. Stress components and local effects in the fatigue strength assessment of fillet weld joints made of ultra-high-strength steels. 2020. Diss.
938. METSOLA, JAAKKO. Good for wealth or bad for health? Socioemotional wealth in the internationalisation process of family SMEs from a network perspective. 2020. Diss.
939. VELT, HANNES. Entrepreneurial ecosystems and born global start-ups. 2020. Diss.
940. JI, HAIBIAO. Study of key techniques in the vacuum vessel assembly for the future fusion reactor. 2020. Diss.
941. KAZARNIKOV, ALEXEY. Statistical parameter identification of reaction-diffusion systems by Turing patterns. 2020. Diss.
942. SORMUNEN, PETRI. Ecodesign of construction and demolition waste-derived thermoplastic composites. 2020. Diss.
943. MANKONEN, ALEKSI. Fluidized bed combustion and humidified gas turbines as thermal energy conversion processes of the future. 2020. Diss.
944. KIANI OSHTORJANI, MEHRAN. Real-time efficient computational approaches for hydraulic components and particulate energy systems. 2020. Diss.
945. PEKKANEN, TIIA-LOTTA. What constrains the sustainability of our day-to-day consumption? A multi-epistemological inquiry into culture and institutions. 2021. Diss.
946. NASIRI, MINA. Performance management in digital transformation: a sustainability performance approach. 2021. Diss.





ISBN 978-952-335-619-1  
ISBN 978-952-335-620-7 (PDF)  
ISSN-L 1456-4491  
ISSN 1456-4491  
Lappeenranta 2021